New direction in electrode design for electrochemical energy storage

Daniela Ledwoch

A dissertation submitted in partial fulfilment

of the requirements for the degree of

Doctor of Philosophy

of

University College London.

Department of Chemical Engineering

sponsored by the Royal Commission of the Exhibition of 1851

August 11, 2021

I, Daniela Ledwoch, confirm that the work presented in this thesis is my own. Where information has been derived from other sources, I confirm that this has been indicated in the work.

Abstract

With the electrification of transport, the increase in cordless appliances, and the intention of many countries to switch to renewable energy production, the demand in energy storage, especially in batteries, is rapidly increasing. At present, lithium-ion batteries are used to power most electric cars and portable devices.[1, 2, 3, 4, 5, 6, 7, 8, 9, 10, 11] However, lithium is a rare material with an appearance in the upper earth crust of less than 70 ppm and its primary resources in China and Bolivia.[12] Sodium-ion batteries are discussed as a potential alternative to replace lithium-ion batteries partly.[13, 14, 15, 16, 17, 18] Like lithium-ion batteries, sodium-ion batteries contain transition metal materials on the cathode side, e.g., layered oxide or phosphates, paired with a carbon comprising anode. Graphite cannot be reversibly cycled in sodium-ion batteries when carbonated electrolytes are used, so amorphous hard carbon is the anode of choice for sodium-ion batteries.[13, 19, 20] But improvements in the observed charge rate are required for many potential applications such as power tools, e-mobility and stationary energy storage. An improvement in electrode design is required to enable fast charging of sodium-ion batteries and eliminate metallic dendrite growth on the electrodes. In this work, fundamental research is undertaken to understand the limitations in cell testing design and the influence of testing parameters to build up a reliable and repeatable test regime. The then tested composite electrodes are determined in terms of electrochemical performance and physical properties with the aim to link manufacturing parameters to performance and implement those findings to improve the overall battery performance. The results emphasize the importance and limitations of ionic transport within hard carbon electrodes, and the required optimization between electronic and ionic conductivity for sodium-ion transport in these electrodes. By adding the ionic conductor zeolite to the composite electrode, better rate performance and improved ageing characteristics were observed, which may enable faster charging of sodium-ion batteries.

Impact Statement

The world requires more energy, and the urge for renewable energy production is growing for years. Hence, the public, academia and also the industry is highly interested in developments as to new high capacity materials, cost-savings, and battery safety concepts. Therefore the support either via public funds or industry-sponsored research is massive. So, besides the still growing field of research for lithium-ion batteries, the need for alternatives increases as well. Sodium-ion batterie technology is one of those candidates that, as a drop-in alternative to lithium-ion, are close to commercialisation.

Nonetheless, several obstacles have to be overcome to make this technology suitable for a broader range of applications. Within the last ten years, the scope of research has not changed a lot. Still, the main goal is to look for an all-in-one-solution: a fast charging, light weighted material, that is cheap, highly abundant, and environmentally friendly. Thereby the mismatch of performance between laboratory scale (material) and industrial application (composite electrode) is often neglected. This work targets to close this gap on different levels:

- To challenge and study the parameter settings for testing methods use in the community for years.
- Determining the differences between material and composite electrode testing.
- The methodical approach to link physical characteristics of composite electrodes to their electrochemical performance.

The chosen approach of investigating electrode characteristics in terms of ionic mobility in composite electrodes is novel. And so is the demonstrated solution to add ionic conductors during the electrode preparation process (patent pending).[21] Follow-up research undertaken at University Birmingham regarding the use of ionic conductors during the inking process has also been recently published.[22]

For this study the cell set-up has been extensively studied and improved in order to measure electrode characteristics rather than artefacts. More accurate electrochemical test methods have been evaluated on those cells and the importance and influence of parameter settings has been highlighted. The generated data set will be implemented in teaching tutorials. This will help many researchers to investigate accurate electrode features rather than misinterpret systematic errors as an electrode or material feature.

Further, this work will help replace the expensive approach of trial and error by modelling pathways to electrode optimisation. It will enable the linking of physical characteristics to electrochemical behaviour by combining electrochemical analysis with imaging techniques such as computed tomography or synchrotron X-ray diffraction either in-situ or in-operando. Both techniques are used heavily to study commercial cell characteristics, such as safety (thermal runaway) or defects caused via or during cell manufacturing.

Moreover, as a future aspect many materials for sodium-ion batteries can be sourced nationally: hard carbon can be gained from many organic sources; sodium is much more abundant than Lithium and extractable from seawater. Hence, sodium-ion batteries have a location advantage towards lithium-ion batteries, since from 2024 EU tariffs become effective on automotive batteries comprising less than 50 % local (UK or EU sourced) materials.[23]

Acknowledgements

First of all, I would like to thank my supervisor Prof. Dr Daniel Brett, for his guidance and support, not only technical but also personal. Further thanks to Prof. Dr Paul Shearing supporting me with his intensive knowledge of physical characterisation techniques and encouraging me to think out the ”electrochemical” box. My thanks to Dr Tom Miller and Prof. Dr Maria-Magdalena Titirici for accepting to be in my examination committee. Many thanks to Prof. Dr Emma Kendrick to encourage me to start this journey and support me through all these years as a colleague, industrial supervisor and a friend. I also thank Katherine Smith for stepping in as my industrial supervisor, her guidance and fruitful discussion throughout my thesis work and her massive support while balancing work duties, PhD challenges and negotiating the obstacles during the transfer from Sharp to Johnson Matthey. I also like to thank all of the EIL family, taking me in as a full member although showing up infrequently and helping out with technical struggles and clearing minds during coffee breaks or after-work beer(s). Special thanks to Nive Kulkarni, Fabiola Valdez, Julia Weaving, Drasti Patel, Chun Tan and Sohrab Daemi.

I am very grateful for the team at Sharp Laboratories of Europe, where I started this journey. My former manager Martin Tillin also taught me the balance of technical support and employee guidance by being a good example and role model. I am still feeling honoured about the opportunity given to be by the committee of the Royal Commission of the Exhibition of 1851 and their financial support. I very much hope this thesis and results satisfy their requirements and high standards. Thanks to Nigel, Angela, Amahl and Jenifer for your support and help.

Thanks to Johnson Matthey PLC and Sarah Ball, also in place of the whole materials team, for taking me in as a new colleague and allowing me to continue my PhD studies.

I would like to thank my parents for raising me to a strong and independent woman, always believing in me and always giving me more support than needed, also, to my sister

staying by my side when help or just a chat or glass of gin was needed. Thanks to my friends in Germany, the UK or both, for their help, support, understanding and encouragement during my PhD work. Thanks to my wonderful now-husband for his understanding, support, meals, and back rubs during the sometimes seemingly endless journey, coping with years of air travel between Germany and the UK, change of houses and flatmates. And finally, thanks to my daughter Levke for showing me what is important in life, refocussing and allowing me a little bit of sleep.

Contents

List of Symbols and Abbreviations **17**

1 Introduction and background **20**

1.1 Motivation 20

1.2 Research aims and thesis outline 21

2 Theory and mathematical background **22**

2.1 Electrochemistry 22

2.1.1 Galvanostatic and potentiostatic testing methods 23

2.1.2 Galvanostatic Intermittent Titration Technique 24

2.1.3 CV 25

2.1.4 EIS 28

2.1.5 Electrochemical Potential Spectroscopy 31

2.2 Physical characterisation techniques 32

2.2.1 SEM, FIB and EDX spectroscopy 32

2.2.2 X-ray CT 33

2.3 Batteries: functional principle 38

2.4 Electrode properties 40

2.4.1 Electrode reactions: Intercalation, alloying, and conversion 40

2.4.2 Degradation mechanisms 43

2.4.3 Processing 46

2.5 Anode material: HC for sodium-ion batteries 48

3 Literature review **51**

3.1 Comparison of lithium to sodium-ion batteries: costs and commercialisation 51

3.2 Electrode materials and reactions 55

3.3 Importance and safety of the experimental set-up 56
3.4 Comparison of cell designs for material testing and commercial applications 58
3.5 Electrochemical characterisation 61
3.5.1 OCV 61
3.5.2 Galvanostatic and potentiostatic testing methods 63
3.5.3 GITT, PITT and EPS 63
3.5.4 CV 66
3.5.5 EIS 68
3.6 Physical characterisation 69
3.6.1 Microscopy 69
3.6.2 Porosity measurements 70
3.6.3 Spectroscopy 70
3.7 Summary and Conclusion 72

4 Methodology **74**
4.1 Preparation of HC anodes for sodium-ion batteries 74
4.2 Cell set-up, assembling and optimisation 75
4.2.1 Assembling of different cell set-ups 75
4.2.2 Influence of cell design on stability of long-term OCV 77
4.2.3 Reactivity of sodium metal to carbonates 81
4.2.4 Influence of the temperature on battery testing 83
4.3 Cell connection 83
4.3.1 Parameters for electrochemical characterisation 84
4.4 Sample preparations for SEM 86

5 The Performance of HC in a NIB **88**
5.1 Introduction 88
5.2 Electrochemical analysis 89
5.2.1 Charge and discharge behaviour 89
5.2.2 Rate performance 89
5.2.3 Influence of the electrolyte 91
5.2.4 Resistance changes observed upon cycling 93
5.3 Conclusion 95

6 Determining the apparent diffusion coefficients of HC 97

6.1 Introduction . . . 97

6.2 Electrochemical analysis . . . 98

6.2.1 Apparent diffusion coefficient calculations based on GITT . . . 99

6.2.2 Apparent diffusion coefficient calculations based on EIS . . . 104

6.2.3 Apparent diffusion coefficient calculations based on EPS . . . 108

6.2.4 Comparison and discussion of the results gained from GITT, EIS and EPS . . . 110

6.3 Conclusion and Outlook . . . 117

7 Optimisation of HC electrodes: Porosity 119

7.1 Introduction . . . 119

7.2 Electrochemical analysis . . . 120

7.2.1 Investigation of the ionic and electronic mobility in HC electrodes . 120

7.2.2 Influence of porosity on ionic and electronic mobility . . . 127

7.3 Conclusion . . . 133

8 Optimisation of HC electrodes: ionic conductive additive 136

8.1 Introduction . . . 136

8.2 Results and discussion . . . 137

8.2.1 Electrochemical characterization . . . 137

8.2.2 Physical characterisation . . . 145

8.3 Conclusion . . . 146

9 Conclusions and Outlook 149

A Appendices 153

B Conference Contributions and Publications 167

References 170

List of Figures

2.1 Illustration of two GITT steps. 26
2.2 Cyclic voltammogramm of a reversible redox reaction. 27
2.3 a) Schematic drawing of kinetic processes in lithium-ion batteries; b) Modelled impedance spectrum of an intercalation material 29
2.4 3D representation of the EIS spectra showing Bode and Nyquist plot. 29
2.5 Illustration of different kinds of electrons. 33
2.6 Schematic drawing of the working principle for X-ray CT operation. 34
2.7 X-ray CT artefact overview 37
2.8 Illustration of charge and discharge of a sodium-ion battery. 38
2.9 Overview of the average discharge potentials and specific capacities for all types of lithium-ion electrodes 41
2.10 Overview of the average discharge potentials and specific capacities for all types of electrodes 42
2.11 Approximate range of average discharge potentials and specific capacity of some of the most common conversion-type cathodes and anodes 44
2.12 Schematic of SEI formation on silicon surfaces. 45
2.13 Degradation mechanisms in Na-ion cells. 45
2.14 Illustration of main process steps for electrode manufacturing 46
2.15 Franklin models for isotropic and graphitising carbons. 49
2.16 HC characteristics. 49

3.1 Analysis of the world wide battery market in 2018. 52
3.2 Illustration of capacity and electrochemical reduction potential of reported positive and negative electrode materials for lithium-ion and sodium-ion cells. 55
3.3 Assembling of different cell set-ups as used for research and development on laboratory-scale 58

3.4 Optimisation of the reference electrode diameter. 59
3.5 Photos and schematic drawings of different lithium-ion battery shapes. . . . 61
3.6 Discharge curves for lithium-ion batteries at various C-rates. 64
3.7 Typical GITT voltage trace of the working vs. counter electrode and working vs. reference electrode. 65
3.8 Cyclic voltamogramms of a) bare $LiFePO_4$ and $LiFePO_4$/C at continuous cycling and b) of $LiFePO_4$/C with various scan rates. 66
3.9 Comparison of electrochemical performance of cathodes in half cells using CV. 67
3.10 Nyquist plots for a) graphite at different degrees of lithium intercalation levels and b) carbon materials with a high and low surface area 68
3.11 Operando XRD data of a sodium-ion cathode recorded during galvanostatic cycling. 72

4.1 3-electrode set-up based on a working, counter and reference electrode. . . . 75
4.2 Assembly of a 3-electrode Swagelok Cell 76
4.3 OCV profiles of full cells and HC electrodes. 78
4.4 Picture of an used sodium metal reference. 80
4.5 HC potential versus Na reference before and after replacement 81
4.6 (a) Picture of sodium metal stored in three different electrolytes, initial state; (b) sodium in PC : EC : DEC after three weeks; (c) sodium in PC : DEC after three weeks. 82
4.7 Temperature profile in battery testing lab over 90 days at Sharp Laboratories of Europe prior the installation of an air conditioning system. 83
4.8 WE and cell profile of a HC composite electrode vs. Na metal in a 3-electrode arrangement. 84

5.1 Voltage profile of a HC electrode versus sodium metal in a 3-electrode arrangement. 90
5.2 Voltage profile of a HC electrode vs. sodium metal in a 3-electrode arrangement at different C-rates. 90
5.3 Polarisation of sodium metal during GITT in two different electrolytes . . . 91
5.4 IR drop on sodium metal during GITT in two different electrolytes 92

5.5 Impedance spectra of sodium metal CE for full 2nd and 20th sodiation. 93
5.6 Difference of WE and CE impedance compared to full-cell data. 94

6.1 Full formation cycle of an HC half-cell 99
6.2 GITT profile of the sodiation and desodiation branch of the HC working and sodium metal counter electrode versus time. 101
6.3 Comparison of the determined diffusion coefficients with the literature . . . 102
6.4 EIS spectra versus voltage for the full second cycle. 105
6.5 Impedance data of the second and tenth sodiation and desodiation at 0.457 V. 106
6.6 Apparent diffusion coefficients based on low-frequency impedance data . . . 107
6.7 WE, CE potential and current profile of the EPS cycle 109
6.8 Apparent diffusion coefficients based on EPS data 110
6.9 Comparison of GITT, EIS, and EPS data 111

7.1 GITT and DCIR profiles of HC electrode 122
7.2 GITT and DCIR profiles of HC electrode 125
7.3 GITT and DCIR profiles of HC electrodes at different porosities 128
7.4 GITT and DCIR profiles of cycled HC electrodes at different porosities . . . 131
7.5 Crossection images of FIB cut (15×20 μm) of two electrodes of 30 % porosity. 133

8.1 First and Second cycle of HC electrodes 138
8.2 Average gravimetric capacities for a set of three electrodes each 139
8.3 EIS for HC composite electrodes 142
8.4 Performance graphs of rate testing 143
8.5 Sodiation profiles of three different electrode compositions. 144
8.6 SEM images of uncycled and cycled electrodes 147

A.1 Profile of the attenuation length of PEEK and carbon between 30 eV and 30 keV. 153
A.2 Left: Example for the linear fitting of low-frequency EIS data using a data generated at a potential of 0.457 V. Right: Example fit for calculating the diffusion coefficients from EPS data. 153
A.3 Graphs of EIS data for warburg fitting. 154
A.4 Equivalent circuit as used for fitting 154

A.5 Differential capacity plot for the 2nd cycle of the EPS measurement. 156
A.6 Current profile during the voltage steps between EIS measurements at desodiation. 156
A.7 Current profile during the voltage steps between EIS measurements at desodiation. 157
A.8 Voltage profile of GITT measurement versus square-root of time. Left: whole sodiation and desodiation; Right: zoom in on two desodiation and relaxation steps. 157
A.9 Comparison of two proposed intercalation models. 158
A.10 Photograph and SEM image of cycled electrode 158
A.11 Image of the electrode block prepared for FIB slicing of a cycled Standard Electrode 159
A.12 Average gravimetric capacities for a set of three electrodes each 160
A.13 Results of the DCIR measurements conducted during GITT measurements . 161
A.14 Cross-section micrographs of FIB cuts. 161
A.15 Detailed EDS images by the element of the uncycled electrode 162
A.16 Equivalent Circuit as used to fit EIS data. 163
A.17 Detailed EDS images by the element of the cycled electrode. 164
A.18 SEM micrograph and generated binary picture of a crosssection of an uncycled electrode. 165
A.19 SEM micrograph and generated binary picture of a crosssection of an uncycled electrode. 165
A.20 Results of SEM Image Processing (uncycled electrode) 165
A.21 Results of SEM Image Processing (cycled electrode) 166
A.22 Photographs of an uncycled and two cycled electrodes 166
A.23 SEM micrograph of a cycled electrode. 166

List of Tables

2.1 Electrochemical characteristics of the three classes of insertion compounds . 42

3.1 Prices of electrode and current collector materials for lithium and sodium-ion batteries. 53
3.2 Summary of characteristics and budget costing for different home energy storage systems 54

6.1 Differences in cell building and parameter settings for GITT testing as chosen in this PhD project, Bommier et al. [92], and Wang et al. [99]. 104
6.2 Minimum and maximum values of the apparent diffusion coefficient for sodiation and desodiation, respectively. Values are based on the second cycle, as seen in Figure 6.2, 6.6, and 6.8. 112
6.3 List of parameters for evaluation of the apparent diffusion coefficient for the three techniques used: GITT, EIS, and EPS. 113

8.1 Summary of WE properties to investigate ionic conductive additives 139
8.2 Apparent diffusion coefficients for different electrode compositions 141
8.3 Average desodiation capacities for different electrode compositions 145

A.1 Analysis data of the slope fitting for σ evaluation 154
A.2 Fitting parameters for equivalent circuit of the second cycle during sodiation. 155
A.3 Fitting parameters for equivalent circuit of the second cycle during desodiation. 155
A.4 Summary of porosity and volume fraction calculations 1. 158
A.5 Summary of porosity and volume fraction calculations 2. 159
A.6 Sheet resistance of electrode coatings 160
A.7 Series resistance of the electrode coatings at 0.005 V and 1.0 V vs Na/Na^+ . 162

A.8 Series resistance of the electrode coatings at 0.005 V and 1.0 V vs Na/Na^+ . 162

A.9 EDS map spectrum results of a Standard Electrode 162

List of Symbols and Abbreviations

Symbol	Definition
α	Charge transfer coefficient, dimensionless
ΔE_S	Change in steady-state voltage per GITT step [V]
ΔE_t	Change in cell voltage per GITT step [V]
ΔG	Gibbs energy [V]
η	Activation overpotential (defined as $\eta = E - E_{eq}$ [V]
μ	Mass attenuation coefficient [m^2 kg^{-1}]
ω	Radial frequency [s^{-1}]
ρ	Density [kg m^{-3}]
σ	Warburg coefficient, obtained from graphical analysis [$\Omega s^{-\frac{1}{2}}$]
τ	Applied current time interval [s]
φ_{00}	Free Gibbs energy [V]
φ_0	Equilibrium potential [V]
a_i	Chemical activity, dimensionless
E_{eq}	Equilibrium potential [V]
I_0	Intensity [%]
j_0	Exchange current density [A m−2]
M_{AM}	Atomic weight of the active material [g mol^{-1}]
m_{mol}	Molar mass [g mol^{-1}]
p_S	Specimen pixel size [px]
R_Ω	Resistance, Ohmic [Ohm]
R_{CT}	Resistance, charge transfer [Ohm]
R_{RE}	Resistance, real [Ohm]
V_{mol}	Molar volume [cm^3 mol^{-1}]
b	Blurring size [px]

c	Concentration [mol cm^{-3}]
D	Diffusion coefficient [cm^2 s^{-1}]
E	Photon energy [eV]
E	Electrode potential [V]
F	Faraday's constant [9.65×10^4 C mol^{-1}]
j	current density [A m−2]
L	Diffusion length [m]
M	Magnification, dimensionless
n	Number of electrons per mole of product, dimensionless
P	Probability [%]
R	Ideal gas constant [J K^{-1} mol^{-1}]
S	Surface area [m^2]
T	Temperature [K]
Z	Atomic number, dimensionless

Abbreviation	**Definition**
AFM	Atomic Force Microscopy
ART	Algebraic reconstruction technique
CB	Carbon black
CCCV	Constant Current Constant Voltage
CE	Coulombic efficiency
CEI	Cathode Electrolyte Interphase
CMC	Carboxylmethyl Cellulose
CT	Computed Tomography
CV	Cyclic voltyammetry
DCIR	Direct Current Internal Resistance
DEC	Diethylene carbonate
DFT	Density-functional theory
DMC	Dimethylcarbonate
EC	Ethylene carbonate
EC-AFM	Electrochemical AFM

EDX	Energy Dispersive X-ray
EIS	Electrochemical Impedance Spectroscopy
EPS	Electrochemical Potential Spectroscopy
FBP	Filtered-back projection
FCL	First cycle loss
FIB	Focussed Ion Beam
FOV	Field of view
GEIS	Galvano EIS
GITT	Galvanostatic intermittent Titration Technique
GSM	Gram per square meter
HC	Hard Carbon
LFP	Lithium Iron Phosphate
NMC	Nickel Manganese Cobalt
NMP	N-methyl-2-pyrrolidone
NMR	Nuclear Magnetic Resonance
OCV	Open Circuit Voltage
PC	Propylene carbonate
PEEK	Polyether ether ketone
PEIS	Potentio EIS
PITT	Potentiostatic intermittent Titration Technique
PP	Polypropylene
PVA	Polyvinyl alcohol
PVdF	Polyvinylidene Fluoride
SBR	styrene-butadiene rubber
SEI	Solid Electrolyte Interphase
SEM	Scanning Electron Microscope
SIRT	Statistical image reconstruction technique
SoC	State of Charge
SoH	State of Health
XPS	X-ray Photoelectron Spectroscopy
XRD	X-Ray Diffraction

Chapter 1

Introduction and background

1.1 Motivation

Energy storage is one of the most important research topics nowadays. More applications are becoming powered or cordless like toothbrushes, vacuum cleaners, scooter and electric cars. Additionally, the upcoming climate catastrophe forces society and politics to move to carbon-free energy production. And although forecasts based on wind and solar energy are reliable enough to enable a stable net frequency, the times where power is consumed does not fit the production (day-night mismatch). Therefore energy storage facilities are needed. Different energy storage concepts are in development, including water pump plants, gas storage caverns, fuel cells, redox-flow systems, and batteries. To date, the best known and promoted solution are lithium-ion batteries. The technology is within our lives for nearly 30 years. Especially for small portable appliances lithium-ion batteries are beneficial. Also within the automotive sector lithium-ion batteries seem to be the use of choice. However, the potential shortage in materials used in lithium-ion batteries such as lithium and cobalt pushes prices and dependencies. With sodium being an alternative to lithium-ion batteries, sodium-ion batteries' research is gaining increasing interest within recent years. Sodium is much more abundant than lithium, but the potential lack of power and energy density is a challenge for its application in portable devices. Therefore enhanced material development and improved charge and discharge rates and cycle life are crucial for its commercial use. Hence, most research institutes invest in developing new materials with larger capacities and better rate capability. Nevertheless, the electrodes used in commercial applications are composite materials based on the active material providing the ion storage capacity and additional ingredients to change the electrode's physical characteristics and enhance electrochemical processes and performance. The link between electrode composition and

the active material performance is rather neglected in literature.

1.2 Research aims and thesis outline

In recent years many new materials for electrochemical energy storage have been developed focusing on higher energy and/or power density. These materials' given values are often measured by low rate cycling tests on lab-scale in small cells and do not consider the processing. This PhD project aims to engineer electrodes for next-generation battery devices and identify and understand the main mechanisms of chemical and physical changes in the electrodes. Understanding the fundamental chemical and physical processes will help identify the influences of processing steps on electrodes' final performance characteristics. The combined fundamental studies and empirical process optimisation approach helps design and fabricate engineered electrodes, which exceed the currently available commercial electrodes' performance.

The active material must be processed into an electrode under carefully controlled conditions to produce a good reliable device.[1]This fact is well-known, as displayed by several publications in all fields of energy storage such as flow field studies in redox flow batteries,[24] influence of porosity in batteries,[25] particle size of active material [26] and addition of electronic additives in lithium-ion batteries.[27] The processing optimisation is often done by empirical trial and error. Often no fundamental scientific understanding of the processes and the effect on the output is understood or known. However, to improve and investigate novel battery technologies, a fundamental understanding of the electrochemical mechanisms within an electrode, e.g. charge transport (ions and electrons), phase transitions and microscale investigations to study electrode stabilities are crucial. Hence the first part of this work centres upon the methodology of electrode testing. Different cell designs, test parameters and methods are investigated to determine the most reliable and reproducible testing routine. Based on those results, simple composite electrodes are analysed for their electrochemical and physical properties. Further, the impact of changes within the electrode processing upon cycling performance will be determined. Subsequently, the gained knowledge of the interaction between material characteristics, processing and composite electrode performance will be used to tailor electrodes and will deliver a optimised battery performance.

[1] A famous example is the development of Lithium Iron Phosphate (LFP, $LiFePO_4$). Because of its poor conductivity, it was not used in lithium-ion batteries for years. An increase of the conductivity via carbon coating and particle size decrease made it one of the most used materials in commercial lithium-ion batteries nowadays.

Chapter 2

Fundamentals: Theory and mathematical background

This chapter gives an overview about the theoretical background of sodium-ion batteries, materials, processing and analysis techniques. This first two chapters provide the theoretical and mathematical basics of the electrochemical and physical techniques used for characterisation and data analysis. Further the general working principle of sodium-ion batteries and their degradation mechanisms are discussed, followed by an introduction of hard carbon, the anode material most commonly used in sodium-ion batteries, which is investigated in this thesis.

2.1 Electrochemistry

Electrochemistry can be used to determine and understand fundamental inner processes within battery electrodes. The main techniques to investigate the properties of composite electrodes are:

- Measurement of Open Circuit Voltage (OCV), also named Open Circuit Potential,
- Cyclic voltammetry (CV),
- Galvanostatic and potentiostatic methods, and
- Electrochemical Impedance Spectroscopy (EIS).

This chapter provides detailed information and theoretical background of these methods and their analysis. More specific information regarding the implementation of these techniques can be found in Chapter 3.5.

2.1.1 Galvanostatic and potentiostatic testing methods

Publications stating new materials or improvements in performance often show voltage - capacity profiles for different charge and discharge currents. The current values are either stated as C-rates or in $A \cdot g^{-1}$. Regardless of which denotations is used, it should be clearly stated if capacity calculations are based on electrode weight, electrode material weight or active mass only.

Fast charging or discharging tests help to determine in addition to the available capacity, conductivity, side reactions and ageing mechanisms. Charge and discharge profiles might differ in shape or are shifted from each other. The effects give an indication of the source of inner processes. If curves are shifted towards lower capacities and voltage, a higher internal ohmic resistances can be assumed[1]. If the shape of the curves differ from each other, polarisation effects depending on the state of charge (SoC) are occurring. These effects are, for example, side reactions, surface changes or a lack in conductivity related to the state-of-charge of the material. All mentioned reactions and properties also depend on the state-of-health. Polarisation effects can be spotted easily at the beginning or end of charge and discharge (see Figure 2.16 in Chapter 2.5) within the voltage drop between charge/discharge and OCV state.

Polarisation effects in sodium-ion batteries can be differentiated into resistive, diffusion, and charge transfer. Ohmic overpotentials are caused by the resistance of current collectors, active materials and electrolyte. Therefore, changes in cohesion, adhesion and electrolyte decomposition influence the intensity of overpotentials. Diffusion overpotentials are based on Fick's first and second laws:

$$\text{Fick's first law:} \qquad \vec{J} = -D\nabla c \tag{2.1}$$

$$\text{Fick's second law:} \qquad \frac{\delta c}{\delta t} = -\nabla \vec{J}. \tag{2.2}$$

$\vec{J}$ is the partial current density, D is the diffusion coefficient and c the concentration of the moving species. The charge transfer is based on the Arrhenius and the Butler-Volmer equations. The two terms of the Butler-Volmer equation describe the forward and backward reactions. These are balanced, unless a current is applied which favours one reaction (Bulter-Volmer: $\alpha \neq 0.5$). This leads to diffusion effects to adapt an equilibrium and a mass

[1] In general $V = R \cdot I$, Ohm's law, R - resistance, V - Voltage, I - Current

transfer as a concentration gradient is formed.

The sudden increase and decrease of the electrode potential at the beginning and end of any charge or discharge is caused by the IR drop.

2.1.2 Galvanostatic Intermittent Titration Technique

The Galvanostatic Intermittent Titration Technique (GITT) is conducted to investigate one-dimensional diffusion within electrodes and polarisation effects and diffusion characteristics depending on the state-of-charge of battery materials. GITT is a combination of transient and steady-state measurements.[28] For time τ, a constant current I is applied to the system, followed by a relaxation step while monitoring the voltage (chronopotentiometry). The calculation of the apparent diffusion coefficient D is based on Fick's first and second law. Also, the voltage (IR) drops at each pulse are considered to remove the effect of polarisation form the calculations and can also be utilized to elucidate the change in electronic resistance with SoC.[29, 30, 31, 32]

Diffusion processes occur within liquid and solid material as well as influencing the kinetics of charge transfer. GITT was first introduced by Wen et al. [33] to characterise the electrochemical properties of insertion materials assuming a one-dimensional diffusion in a solid solution electrode, neglecting double-layer charging, phase transformation, charge-transfer kinetics and ohmic potential drop. Based on Fick's laws (see Equations 2.1 and 2.2), the following equation can be used to calculate an apparent diffusion coefficient:

$$\tilde{D} = \frac{4}{\pi}\left(\frac{IV_M}{z_A F S}\right)\left(\frac{dE/d\delta}{dE/d\sqrt{t}}\right)^2, \qquad \left(t \gg \frac{L^2}{\tilde{D}}\right),$$

where I is the time dependent current, V_M the molar volume, z_A the charge number of the electro-active species (for Na ion battery, $z_A = 1$), F the Faraday constant, S is the sample-electrolyte surface area, δ the titration step, L is the characteristic length or thickness of the electrode material, and t in seconds the duration of the pulse. For S the geometrical electrode shape is assumed and L is measured using a film thickness gauge. $\left(\frac{dE}{d\delta}\right)$ and $\left(\frac{dE}{d\sqrt{t}}\right)$ can be obtained from the graphs of the measurements. $\left(\frac{dE}{d\delta}\right)$ can be be measured by plotting the equilibrium electrode voltage against the electroactive material composition after each current pulse, $\left(\frac{dE}{d\sqrt{t}}\right)$ from a plot of the voltage versus the square root of the time during constant current pulse [34]. If small currents and short time intervals are used the transient response of the voltage E is a linear function of the square root of time and Equation 2.1.2

can be simplified to:

$$\tilde{D} = \frac{4}{\pi\tau}\left(\frac{m_{AM}V_M}{M_{AM}S}\right)\left(\frac{\Delta E_S}{\Delta E_t}\right)^2, \qquad \left(\tau \gg \frac{L^2}{\tilde{D}}\right), \tag{2.3}$$

where τ is the applied current time interval, m_{AM} the mass of active material, M_{AM} the atomic weight of the active material, ΔE_s the change in steady state voltage, and ΔE_t the change in cell voltage. As mentioned above, these assumptions are not validated for phase-transforming materials, as ions are not only transported by movement through the interphase boundary, but also by ionic diffusion.[30, 34] Therefore, the calculated diffusion coefficients are *apparent* diffusion coefficients, reflecting the characteristics of the whole composite electrode system including a phase change from a sodium deficient into a sodium rich state (e.g. sodiation of HC (HC)) and the other way around (e.g. desodiation of HC).[34]

For GITT a small current is applied to the system followed by a relaxation step, recording the consequent response measured as a function of time until steady-state is reached. In this work GITT is used to investigate the diffusion coefficients depending on state-of-charge and state-of-health of composite electrodes.

It should be noted that by using graphical data analysis it is possible to exclude the ohmic drop from the diffusion coefficient calculations, as illustrated in Figure 2.1.

2.1.3 CV

CV is a potentiodynamic measurement, where a triangular voltage is applied between working and reference electrode and the resulting current between working and counter electrode is recorded. For analysis, the resulting current between working and counter electrode is plotted versus the applied voltage. This plot is named cyclic voltammogram. Within standard charging and discharging profiles showing voltage versus time, phase changes occur in plateaus regions. The same effects appear in CV plots as peaks. Hence, the voltage at which phase changes occur can be determined. As sodium-ion batteries involve relatively slow solid-state processes, low scan rates are used to capture relevant details (e.g. below $100\,\mu V \cdot s^{-1}$).

Data obtained by CV can by used to analyse the nature of the charge transfer, reversibility of reactions, and orders of magnitudes of diffusion coefficients. When scanning the potential with time, it is important to distinguish two different kinds of current densities: capacitive and Faradaic.

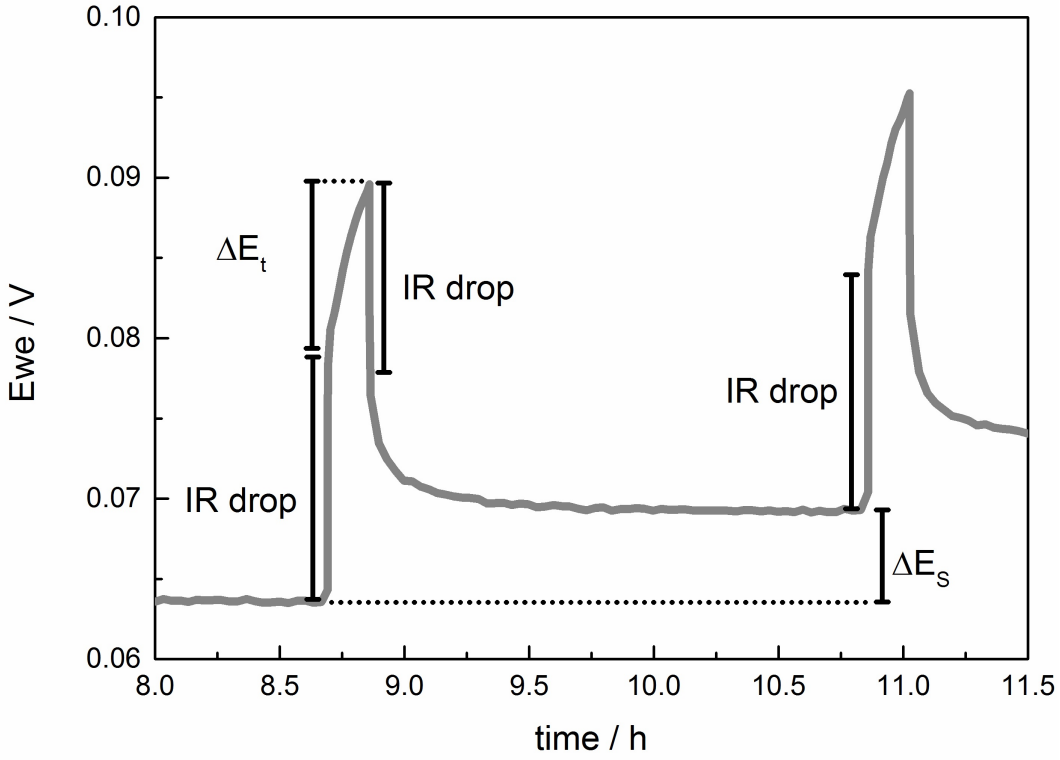

Figure 2.1: Illustration of two GITT steps, visualising Ohmic drop, time interval τ, ΔE_S and ΔE_t.

Capacitive currents derive from the charging of the double-layer. The capacitive current is given by:

$$j_c = C_d \frac{dE}{dt}, \tag{2.4}$$

where j_c is the current density, E the potential, C_d the capacitance, and t the time.

Faradaic currents originate from the charge passed during red-ox reaction and are influenced by charge transfer kinetics and species diffusion. Peaks within a cyclic voltammogramm appear due to ratio changes of mass transport and surface reaction control. Within the nonfaradaic region of the cyclic voltammogram the active species are transported towards the electrode surface. When the electrode potential is close to a reaction potential E_0 the reduction or oxidation on the electrode surface begins and a current I starts flowing. While the reaction continues, the concentration of the active species on the electrode surface decreases, the flux towards the electrode and therefore the current, increases, as well as the travel distance of the active species towards the electrode. Hence, the thickness of the diffusion layer is time depended and is described by $\delta_n = \sqrt{\pi D t}$. At the maximum value of the current peak, smaller amounts of reactants approach the electrode and the oxida-

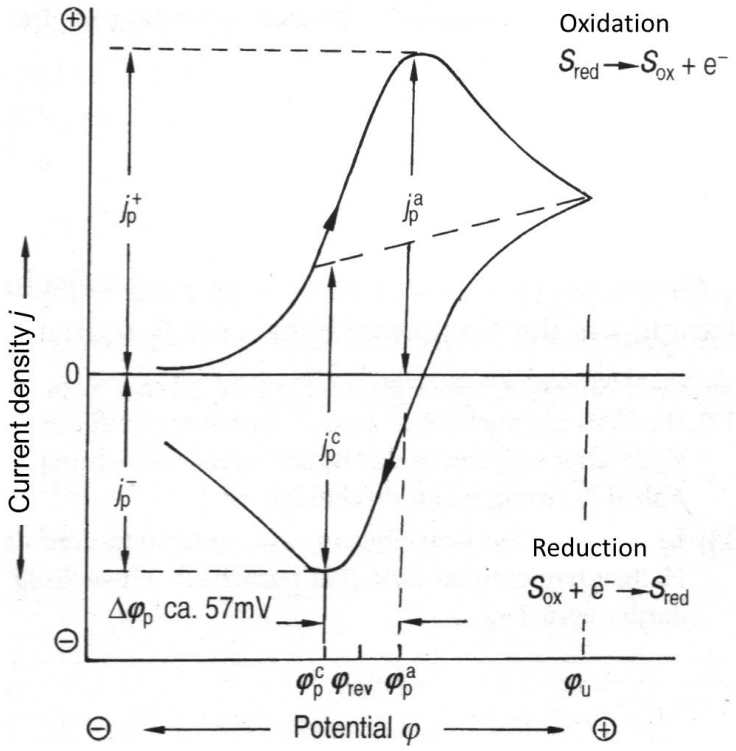

Figure 2.2: Cyclic voltammogramm of a reversible redox reaction; illustrating cathodic peak current j_p^c, anodic peak current j_p^a, cathodic peak potential φ_p^c, anodic peak potential φ_p^a, and reversibility potential $\varphi_{rev} = \frac{1}{2}\left(\varphi_p^a + \varphi_p^c\right)$ from Hamann, Hamnet, and Vielstich [35].

tion/reduction reaction depletes. The peak current j can be calculated by

$$j = nFD\frac{dc}{dx} \qquad \text{F: Faraday constant.} \tag{2.5}$$

Analysis of peak positions (potential), peak hight (current and total charge passed) and peak shifts as a function of scan rate determine limitations of charge transfer and reversibility of reactions. For a full reversible surface reaction the following requirements must be fulfilled:

- j is proportional to $v^{\frac{1}{2}}$, v: scan rate,
- quotient of anodic j_p^a and cathodic current density j_p^c should be $\frac{j_p^a}{j_p^c} \approx 1$,
- existence of uninhibited charge transfer reactions.

There are different ways to determine the value of the current peak density j_p, as it can be seen in Figure 2.2 from Hamann, Hamnet, and Vielstich [35]. If the current of the anodic branch starts at the zero line, the reached maximum value is the true peak density. Otherwise a new baseline has to be drawn from the starting point of the oxidation/reduction

branch to the inflection point of the counter reaction (an example is given for the reduction branch in Figure 2.2). To determine the presence of inhibited or uninhibited charge transfer reactions, CVs at different scan rates have to be performed. If the anodic peak shifts towards higher potentials with increasing scan rates the reaction is inhibited and a prior reaction has to finish first. This prior reaction influences the main reaction characteristics and a full reversible might not be constituted. If the reaction is fully reversible (conditions are listed above), diffusion coefficients D can be calculated by using the Randles-Sevcik equation:

$$j_p = 2.69 \cdot 10^5 n^{\frac{3}{2}} A c_{red}^0 D_{red}^{\frac{1}{2}} v^{\frac{1}{2}}. \tag{2.6}$$

2.1.4 EIS

EIS enables the separation of reactions and processes within a cell if temporally resolved. Therefore, this technique can be used to split-up surface and charge transfer reactions. For EIS studies, the applied current (PEIS) or potential (GEIS) is amplitude-modulated over a range of frequencies. The transfer function relating the stimulus to the resulting signal can be fitted using equivalent circuits, which describe electrode properties. EIS is used to investigate reactions by separation of processes with different time constants and to determine the internal resistance and charge transfer resistance, and additionally apparent diffusion coefficients can be extracted from the low-frequency Warburg branch.[31, 36, 37, 38, 39, 40, 41, 42]

EIS is conducted by applying an oscillation current (galvano-EIS, GEIS) or potential (potentio-EIS, PEIS) to a system and recording the phase and amplitude response. The potential or current stimulus should be low enough to keep the system within a quasi-stable state and a quasi-linear part of the voltage curve, but high enough for adequate signal-to-noise discrimination. The potential profile of the electrode can be used as an indication. For example, within the plateaus of the voltage profile, even a small potential stimulus induces an SoC change. The resulting impedance $Z(i\omega)$ can be calculated as shown in Equation 2.7.

$$Z(i\omega) = \frac{U \cdot e^{i\omega t}}{I \cdot e^{i(\omega t + \varphi)}} = Z_{real} - iZ_{imaginary} \tag{2.7}$$

The range of frequencies used for battery testing is between a few micro hertz up to a several kilohertz. Due to the different reaction rates the response of the system can be divided into different sections, as illustrated in Figure 2.3 from [43].

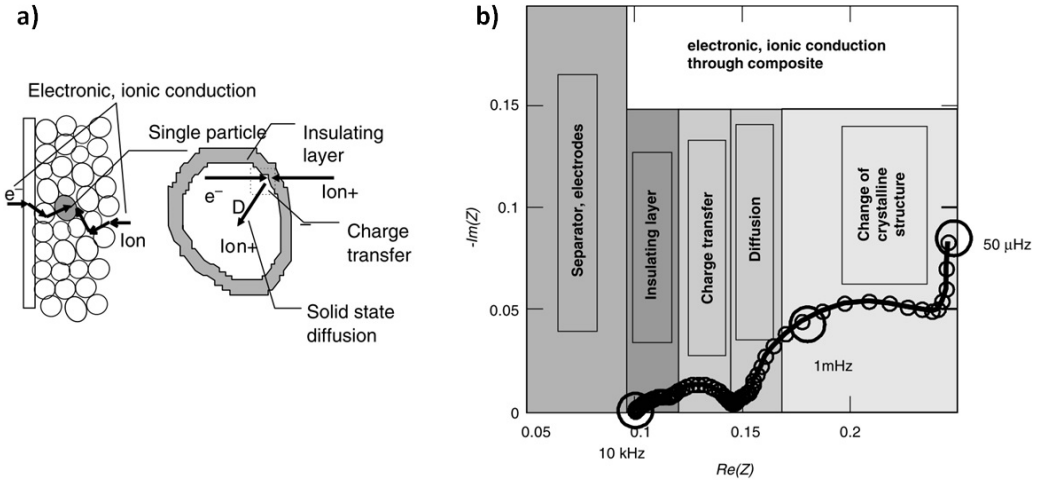

Figure 2.3: a) Schematic drawing of kinetic processes in lithium-ion batteries; b) Modelled impedance spectrum of an intercalation material by Barsoukov and Macdonald [43].

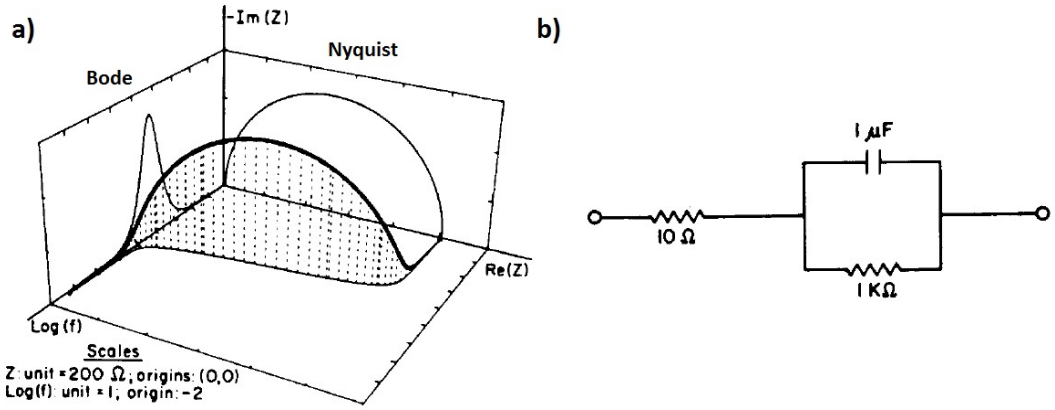

Figure 2.4: 3D representation of the EIS spectra. The left projection is a Bode diagram, whereas the right projection a Nyquist plot. The insert represents the Randles equivalent circuit for fitting [44].

In general, the generated data is presented in so-called Bode or Nyquist plots (shown in Figure 2.4). A Bode format is displayed by plotting the real part of the impedance versus the logarithm of the excitation frequency. A Nyquist format is generated by plotting the negative imaginary part of the impedance versus its positive real part. Figure 2.4 a from Macdonald, Schoonman, and Lehnen [44] shows a 3D plot combining both formats. Figure 2.3 b displays the corresponding equivalent circuit based on one RC parallel element in series with one resistor. The RC element is associated with the semi-circle in the Nyquist plot and represents an inter-phase within the battery. Displaying the data as a Nyquist plot helps to identify interfaces of the system as it is simple to identify semi circled shaped features within the graph. Hence, both axes of the plot should have the same scale to

distinguish the features more easily. For analysis, equivalent circuits are fit to the data to estimate capacitance, resistance and diffusion parameters. The analysis of the EIS data is challenging since, there is no standard model, that fits the internal battery processes over the full state-of-charge range. Furthermore, the morphology of electrodes is changing during cycling and consequently the model has to be adjusted.

EIS can also be used to calculate diffusion coefficients. The mathematical theory is given by Haran, Popov, and White [45]. The determination of the diffusion coefficients, D, for spherical particles with radius R is based on the slope of the Warburg element of each impedance spectra $\frac{d(Im)}{d(Re)}$:

$$\frac{d\,(Im)}{d\,(Re)} = \frac{T_4\left[-T_3 + (S_3S_5 + S_4S_7 - S_1S_6 + S_2S_8)\,\Psi\right] - 2T_3\,(S_4S_3 + S_2S_1)\,\Psi}{T_4\left[-T_5 + (S_3S_6 + S_4S_8 - S_1S_5 + S_2S_7)\,\Psi\right] - 2T_5\,(S_4S_3 + S_2S_1)\,\Psi} \tag{2.8}$$

where

$$T_3 = (S_4S_5 + S_2S_6) \qquad T_4 = \left(S_4^2 + S_2^2\right) \qquad T_3 = (S_4S_6 + S_2S_5)$$

$$S_1 = S_5S_6 \qquad S_2 = 2\Psi - S_5 \qquad S_3 = 2\coth(\Psi)\cot(\Psi)\,(1 - \Psi S_6) - 2\Psi S_5 + S_8$$

$$S_4 = 2\Psi\coth(\Psi)\cot(\Psi) - S_6 \qquad S_5 = \coth(\Psi) - \cot(\Psi)$$

$$S_6 = \coth(\Psi) + \cot(\Psi) \qquad S_7 = 2 - S_1 \qquad S_8 = \cot(\Psi)^2 + \coth(\Psi)^2$$

and

$$\Psi = \sqrt{\frac{\omega R^2}{2D}}.$$

These calculations can be used as an approximation for investigating the diffusion coefficients of composite electrodes. A more accurate model has to consider different particle sizes and material characteristics of binder and conductive additives.

Apparent diffusion coefficients are determined from experimental either via fitting to an equivalent circuit or, as mentioned above, on calculations based on the slope of the Warburg element. The potential or current stimulus should be low enough to keep the system within a quasi-stable state and a quasi-linear part of the voltage curve, but high enough for adequate signal-to-noise discrimination. The potential profile of the electrode can be used as an indication. For example, within the plateaus of the voltage profile, even a small potential stimulus induces an SoC change. Liu et al. state the equation to determine

the diffusion coefficient $\tilde{D}_{EIS}$ as

$$\tilde{D}_{EIS} = \frac{R^2T^2}{2S^2n^4F^4c^2\sigma^2} \tag{2.9}$$

with

$$Z_{RE} = R_\Omega + R_{CT} + \sigma\omega^{-\frac{1}{2}}..$$

Whereas R is the gas constant (J mol^{-1} K^{-1}), T the absolute temperature (K, ambient temperature), n the number of electrons exchanged (1), F the Faraday constant (A s mol^{-1}), and c the concentration of sodium-ions within the electrode (mol cm^{-3}). The real impedance (Z_{RE}) is the sum of the ohmic resistance or series resistance (R_Ω), the charge transfer resistance (R_{CT}) and the electrolyte resistance ($\sigma\omega^{-\frac{1}{2}}$); where σ is the Warburg coefficient, and ω is the radial frequency. As the Warburg coefficient σ can be obtained from the slope of the graph showing R_{RE} versus $\omega^{-\frac{1}{2}}$ [46], IR contributions are neglected.

2.1.5 Electrochemical Potential Spectroscopy

Electrochemical Potential Spectroscopy (EPS) is a voltage-step technique based on the potentiostatic intermittent titration technique (PITT), skipping the OCV steps.[46, 47, 48, 49] In both techniques, a repeated small step increase (or decrease) in voltage is applied, and the current transient monitored (chronoamperometry). The difference between PITT and EPS is that OCV is not reached between each pulse in EPS, but the time between each potential step is limited by the current. The minimum current value is chosen close to the thermodynamic equilibrium to insure the IR contributions' insignificance (e.g., 0.01 C). The diffusion-limited current is proportional to $t^{\frac{-1}{2}}$, and the apparent diffusion coefficient can be calculated using the Cottrell equation.[33]

The Cottrell equation describes the decay of the current $i(t)$ for diffusion-controlled redox reactions via

$$i(t) = \frac{nFSD_{EPS}^{\frac{1}{2}}c_{Na}^*}{\pi^{\frac{1}{2}}t^{\frac{1}{2}}}. \tag{2.10}$$

$c_{Na}^* = c_S - c_0$ describes the concentration difference (mol cm^{-3}) between the concentration c_0 in the electrode corresponding to equilibrium voltage and c_S at the electrode-electrolyte interface when a voltage step is applied at $t = 0$. n is the number of electrons transferred per mol of material (1), F is Faraday constant (A s mol^{-1}), and S is the electrode surface area . The diffusion coefficients D_{EPS} can be determined graphically. For short time approxima-

tion ($t \ll L^2 D^{-1}$), the chemical diffusion coefficient can be determined from the slope of the linear plot of I versus $t^{\frac{-1}{2}}$ by

$$i(t) = nFSc^*_{Na}\sqrt{\frac{D_{EPS}}{\pi t}}. \tag{2.11}$$

The slope of each current decay is proportional to $D^{\frac{1}{2}}_{EPS}$ provided that the concentration difference c^*_{Na} is known. For a long time approximation $\left(t \gg L^2 D^{-1}\right)$, D_{EPS} can be evaluated from a linear plot of $ln(I)$ versus t without the knowledge of c^*_{Na} by

$$i(t) = \frac{nFSc^*_{Na}D_{EPS}}{L} e^{-\frac{\pi^2 D_{EPS} t}{4L^2}}. \tag{2.12}$$

Assuming a diffusion length L of 4.5 μm (radius of spherical HC particle) and an apparent diffusion coefficient between 10^{-10} to 10^{-16} [50, 51, 52], the experimental parameters in this work meet the condition for short time approximation.

2.2 Physical characterisation techniques

There is a wide range of physical characterisation techniques available for the study of battery components. Within this work Scanning Electron Microscopy (SEM) is used to determine surface changes and the chemical composition of composite electrodes. X-ray computed tomography (CT) is used to visualise the 3D network of composite electrodes and to estimate porosity and tortuosity values. As SEM is a well known technique, this chapter gives only a brief introduction into SEM and focusses more on 3D X-ray CT.

2.2.1 SEM, FIB and EDX spectroscopy

The SEM is a well established technique. Depending of the energy and interaction of the primary electron beam with the sample, several modes of detection are possible. Most common are the detection of secondary electrons (SE, inelastic scattering) and backscattered electrons (BSE, elastic scattering). Further, Auger electrons, X-rays and photons can be detected to provide chemical analysis. An illustration about generation of different kind of SEM radiation is given in Figure 2.5 from Nijmegen [53].

The magnification and details of information depend on conductivity of detected particles, sample and lenses of the system. In general SEM is a surface observing technique as the depth of penetration varies between 10 nm to 2 μm. The lower the primary electron energy, the better the spatial resolution and less depth of penetration. Good systems can achieve a spatial resolution of smaller than 1 nm using energies below 30 kV.[54]

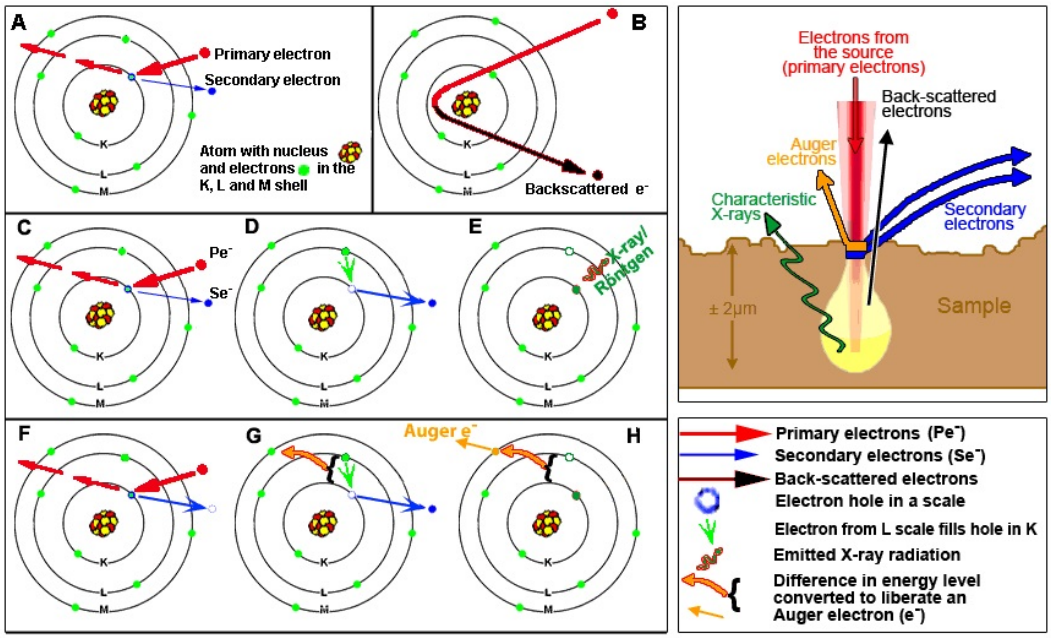

Figure 2.5: Illustration of different kinds of electrons; left: principle of generation. right: Schematic drawing of detection area by [53].

Optical analysis and material compositions can be investigated applying energy dispersive X-ray (EDX) or a focussed ion beam (FIB) techniques to the sample. X-rays are generated by inelastic scattering of primary electrons with the electron shell. The generated empty spots on low electron shells are filled from higher energy shell levels and the difference in energy is released by X-ray radiation. The energy of these X-rays is specific and can be attributed to certain elements. However, detection of hydrogen, helium, lithium and beryllium is not possible, as their energy spectra are within the energy peak of the primary electrons. FIB can be used for material depositioning or ablation. In combination with a secondary ion mass spectroscopy (SIMS), FIB enables also material analysis. During this process, single layers of material are removed and analysed by a mass spectrometer.[55]

2.2.2 X-ray CT

X-ray CT is based on the attenuation characteristics of the material. These characteristics are described by the Beer-Lambert law (Equation (2.13)) stating the probability $P(x)$ to find a particle at depth x in an material with an given attenuation length λ.

$$P(x) = \exp^{-\frac{x}{\lambda}} \tag{2.13}$$

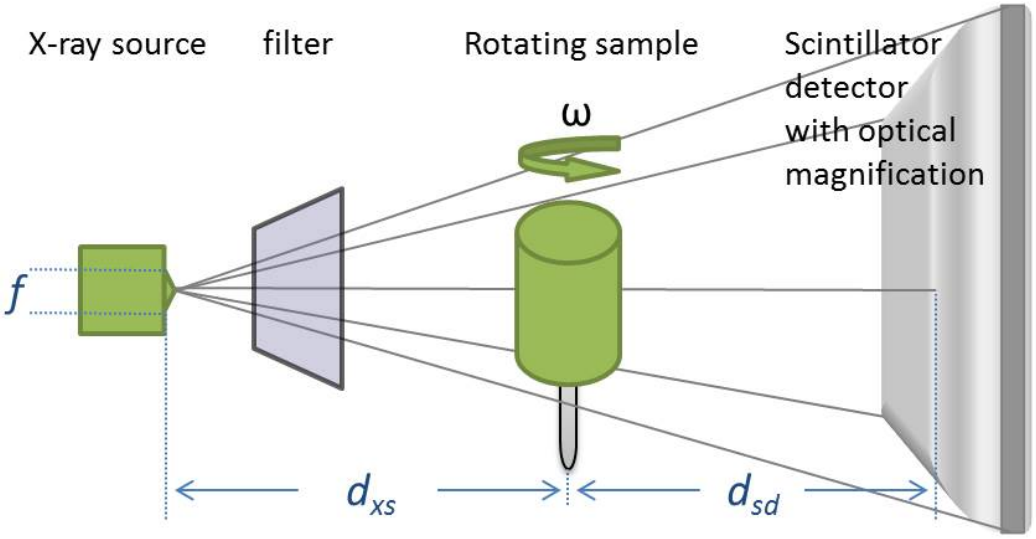

Figure 2.6: Schematic drawing of the working principle for X-ray CT operation.

Further, the intensity I of the radiation can be calculated based on initial intensity I_0 and mass attenuation coefficient μ by

$$I = I_0 \exp^{-\int_0^t \mu dt} \text{ with } \mu = \left(\frac{\mu}{\rho}\right)\rho, \tag{2.14}$$

where ρ is the density of the material. The quotient $\frac{\mu}{\rho}$ can be approximated by $Z^4 \cdot E^{-3}$ (Z: atomic number, E: photon energy).[56]

2.2.2.1 Working principle and parameters

The working principle of 3D X-ray CT is similar to 2D X-ray projections. A sample is placed between an X-ray source and a detector to image a radiograph. The sample is then rotated by an certain angle n or with an angular speed ω and multiple radiographs are created[1]. These steps are repeated until the sample returns to its initial position (Figure 2.6). This way an image stack containing $m = \frac{360°}{n}$ or $m = \frac{360°}{\omega}$ pictures is generated. Computer software programmes are used to calculate a 3D image based on the information of the image stack by mathematical reconstruction.

The resolution of the system depends on the focal spot size of the source f, the distance between the X-ray source and the specimen d_{xs} as well as the specimen and the detector d_{sd}, the detector pixel size p_d and the number of pixels n. Based on the theorem of intersecting lines, highest resolutions can be achieved for small d_{xs} and large d_{sd} settings ($d_{sd} \ll d_{xs}$).

[1] By rotating the sample instead of moving detector and source around the specimen compacter apparatus can be build.

Optical lenses between the specimen and the detector can be used to enhance the magnification. Therefore, the resulting geometric magnification M can be calculated by

$$M = \frac{d_{xs} + d_{sd}}{d_{xs}} + \text{optical.} \tag{2.15}$$

The magnification factor is needed to calculate the specimen pixel size p_s and the resulting field of view (FOV). These calculations are slightly different when a Zeiss Xradia Versa 520 is used as a high resolution detector is implemented. The specimen pixel size can then be calculated by

$$\text{in general:} \quad p_s = \frac{p_d}{M} \qquad \text{Zeiss:} \quad p_s = \frac{\sqrt{p_d^2 + b}}{M}, \tag{2.16}$$

$$FOV = n \cdot p_s \tag{2.17}$$

where b is the blurring size given by $b = (M-1)f$. It has to be considered, that some sources expand in diameter when used with a high current. Further, the voxel size is related to the pixel size as a voxel is a 3D pixel. In theory every voxel represents a feature of the sample. But not every voxel may be a real feature as there might be a 'bad pixel' resulting from detector errors or a bad signal-to-noise ratio. Hence, the smallest obtainable spatial resolution is about 2.5 to 3 times of voxel size.

To obtain useful data, at least 5000 counts are needed and a transmission of 20 to 30 %. The number of counts can be increased by extending the exposure time. The transmission can be adjusted by applying a filter to remove low energy electrons. Another way to increase the number of counts is 'binning'. Binning describes the consolidation of pixels/voxels. So a binning of two is reducing the pixel size by a factor of 4. This reduces the resolution, but also the measurement time. Hence, these parameters are set when a lower resolution can be tolerated.

The working principle of nano-scale instruments are similar to the one explained above. In case of the Zeiss Ultra XRM, additional post-transmission optics are implemented to improve the resolution. Instead of a polychromatic cone beam a filtered mono-energetic quasi-parallel beam (4.5 kV) is implemented.[57, 58]

2.2.2.2 Reconstruction

There are two different kinds of reconstruction algorithms: direct and iterative. The filtered-back projection (FBP) is a technique based on a direct algorithm, whereas the algebraic

reconstruction technique (ART) and the statistical image reconstruction technique (SIRT) rely on an iterative principle.[59]

Direct methods are faster and need less storage, but as straight monochromatic X-rays are assumed instead of polychromatic ones, further image processing is necessary. Additionally, when a polychromatic X-ray beam is used, low energy electrons are absorbed by matter. Hence, the beam becomes gradually harder and results in non-uniform intensity signals. Beam hardening can be compensated by either pre-filtering of low energy electrons, manual correction of the measurements based on material assumptions or by incorporating a polychromatic model. Zeiss developed three techniques to compensate this effect: source filters (filter of low energy electrons), software corrections, and secondary referencing.

Besides beam hardening, there are more artefacts, which might influence the data analysis. Figure 2.7 gives some examples of the most common effects [56]. The list below explains their visual appearance within the data.

Limited projections appear, when a limited number of projects N_j is used. The optimum can be calculated by $N_j = \frac{\pi}{2} P_n$ with P_n are the number of pixels.

Rotation speed artefacts show a sharp image in the centre and blurred details on rotation edges. These artefacts appear, when using 'on-the-fly-scans' and can be avoided by 'step scans'.

Beam hardening, as described above, can be either avoided by using a monochromatic source, filtering low energy electrons or compensated by mathematical calculations.

Streak artefacts appear with specimen having straight boundaries or sharp edges.

Misalignment of centre of rotation leads to a radial deformation of features. Circles appear oval instead of round shapes.

Specimen movement may result in a data set that is not possible to reconstruct. If the movements are small, features appear blurred.

Ring artefacts are a result of faulty detector pixels (weak or no response). These effects can be avoided or compensated by calibration of the detector or image processing.

Zinger's are straight black lines due to an interaction of X-rays with the detector.

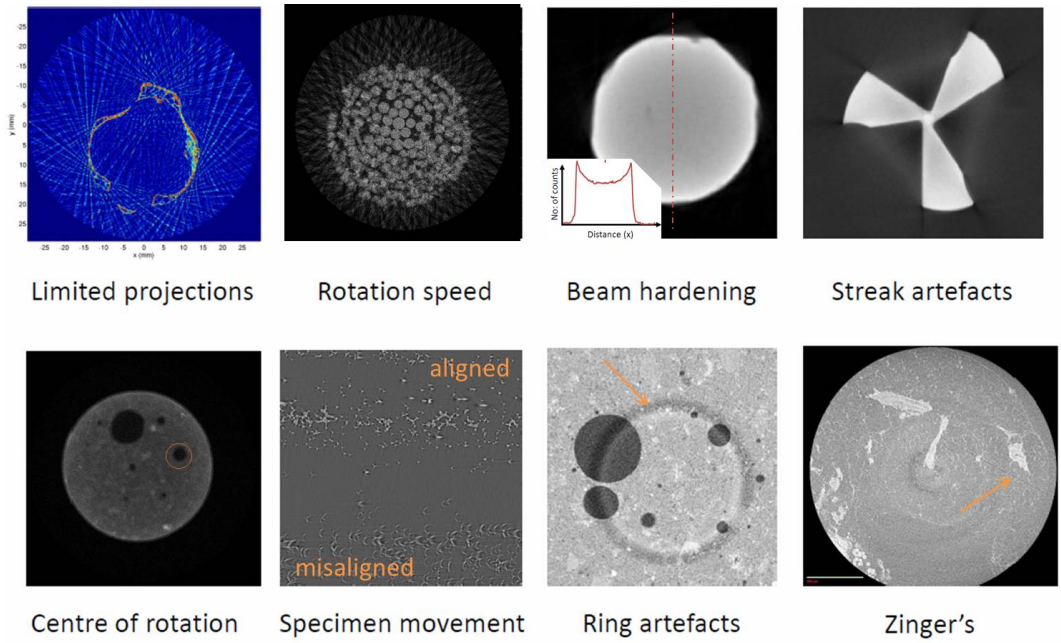

Figure 2.7: X-ray CT artefact overview summarised by Lowe et al. [56].

Most artefacts can be removed by image processing. But in general, image processing of CT data has to be done with great care, as the techniques applied might also remove or change true features.

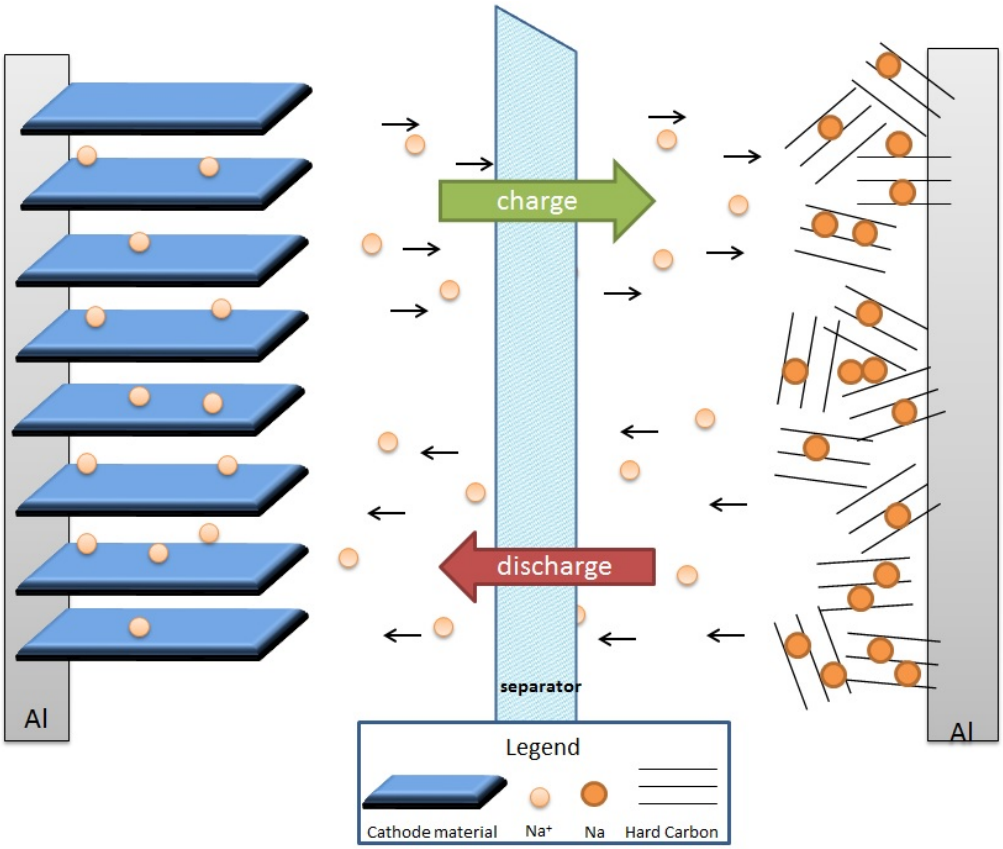

Figure 2.8: Illustration of charge and discharge of a sodium-ion battery.

2.3 Batteries: functional principle

The most important equations to describe the processes within a battery are the **Nernst equation** and the **Butler-Volmer equation**. The Nernst equation is given by

$$\varphi_0 = \varphi_{00} + \frac{RT}{nF} \sum lna_i. \tag{2.18}$$

φ_{00} is identical to Gibbs energy (ΔG, $U_1 = \Delta G_0 = \varphi_{00}$) (first and second law of thermodynamics), a_i is the chemical activity for the reduced or oxidized species. The equilibrium potentialφ_0 is the free energy at a second potential (ΔG, $U_2 = \Delta G = \varphi_0$). The Nernst equation describes the equilibrium between a chemical (second term) and electrical potential difference (first term). Hence, the potential at which the equilibrium between chemical and electrical potential is given can be calculated by the Nernst equation depending on the concentration of the species. As those are independent of time only the nominal voltage, not the OCV, can be determined.

The difference between OCV and nominal voltage is the so-called overpotential. Those

are processes depending on the current density within the battery and are either related to reactions (diffusion, charge transfer, concentration) or resistance (Ohmic). Therefore the sum of the overpotentials can be described as $\eta = E - E_{eq}$ with $E = \varphi_0$ the electrode potential and $E_{eq} = \varphi_{00}$ the equilibrium potential. The current resulting from a deviation of the E_{eq} is described by the Butler-Volmer equation:

$$j = j_0 \left[exp\left(\frac{\alpha nF}{RT}\eta_D\right) - exp\left(-\frac{(1-\alpha)nF}{RT}\eta_D\right)\right]. \tag{2.19}$$

whereas j is the current density, j_0 the exchange current density and α is th charge transfer coefficient, describing the ratio of the anodic and cathodic charge transfer coefficient.

In general the working principle of sodium-ion batteries is identical to lithium-ion and differs only by the kind of the carrier ion (sodium instead of lithium). In general the energy storage in a battery takes place within the electrodes. At charging/discharging a reduction/oxidation of the electrode material takes place with ions moving through the battery (working electrode → electrolyte → separator → counter electrode) and a red-ox equivalent of electrons over the external circuit to power the connected electrical load, as illustrated in Figure 2.8. When discharging, the active material within the anode is oxidised and gives electrons to the external circuit; whereas the active material within the cathode is reduced by accepting electrons from the external circuit. As a consequence sodium ions are removed from the anode and diffuse within the cathode active material to maintain the electro-neutrality. A rechargeable battery is called a 'secondary battery' or 'accumulator', if the described process is reversible. Lithium, sodium or any other alkali metal accumulators are based on the 'rocking chair' principle with lithium, sodium or alkali metal ions acting as carrier ions. On the cathode side materials such as layered oxides, phosphates or metal oxides are used in sodium and lithium-ion batteries. For sodium-ion battery anodes the most common and advanced material is HC[1]. But anodes containing HC blended with tin or antimony are increasingly discussed in the literature. Specifically, the designation of anode and cathode in accumulators depends on the electrochemical reaction taking place while discharged. The electrode with the lower electropotential in the galvanic series is the anode which is oxidised within the latter, the one which is reduced is named the 'cathode'.

The reduction/oxidation of the cathode active material leads to a change in oxidation numbers. An example is given in Equation 2.20 stating the full reaction and oxidation

[1] HC is disordered carbon and further introduced in Chapter 2.5.

numbers (superscripted in blue) for a LFP battery.

$$Fe^{+3}P^{+5}O_4{}^{-2} + Li^{+1}C_6{}^{-0.17} \rightleftharpoons Li^{+1}Fe^{+2}P^{+5}O_4{}^{-2} + C^0 \tag{2.20}$$

A charged $LiFePO_4$/graphite battery contains delithiated $FePO_4$ on the cathode side and LiC_6 on the anode side. During discharge the oxidation number for iron changes from +3 in $FePO_4$ to +2 in $LiFePO_4$. This is important as in most cases a change of the oxidation number involves a change of the electron configuration, which influences the lattice structure and induces mechanical stress to the system.

2.4 Electrode properties

Important characteristics for electrode and battery evaluation are the first cycle loss (FCL), Coulombic efficiencies (CE), direct current internal resistance (DCIR), the voltage profile versus SoC and ageing behaviour (state of health, SoH) and the corresponding polarization/overpotential. All those characteristics can be measured in half-cell experiments for anode and cathode, respectively. However, it is important to highlight, that the sum of the effects occurring on anode and cathode differ from the results gained in a full-cell set-up. Further, those characteristics depend on processing and material properties itself. There is a wide range of different electrode materials available. They differ in characteristics such as energy storage reaction, theoretical capacity, price, volume expansion, potential window, crystal structure and particle size. Within this chapter electrode reactions for intercalation, alloying, and conversion are explained, potential degradation effects on electrodes are discussed and process steps of electrode manufacturing are introduced. Furthermore, the material used within this thesis is elucidated in Chapter 2.5 *Anode material - HC*.

2.4.1 Electrode reactions: Intercalation, alloying, and conversion

As mentioned earlier, there are different kinds of electrode reactions: intercalation, alloying and conversion materials. Figure 2.9 illustrates the average potential of different kinds of cathode and anode materials versus their experimental (intercalation types) and theoretical (conversion-types) capacities.[60] The values given for conversion-type materials are theoretical as these electrodes are still under development. The following paragraphs state chemical reactions, crystal structures, advantages and disadvantages of each electrode reaction. All given chemical reactions are based on sodium-ion batteries, but are also true for lithium or any other alkali metal.

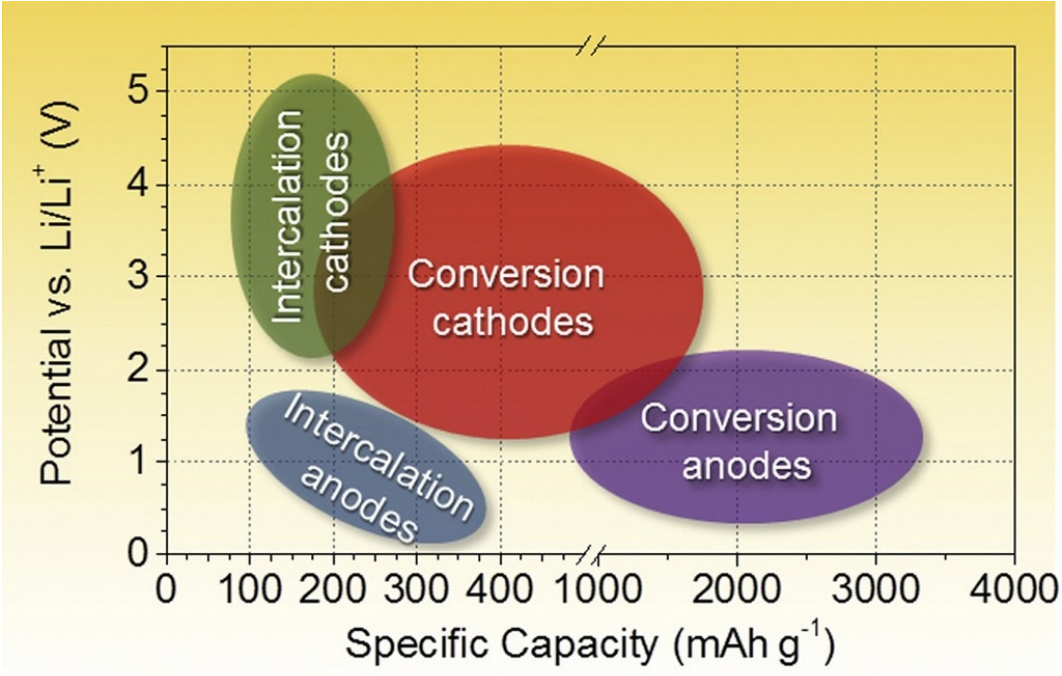

Figure 2.9: Overview of the average discharge potentials and specific capacities for all types of lithium-ion electrodes [60].

Intercalation/deintercalation describes the insertion of an exchange ion into a crystal structure. The exchange ion is inserted between layers, planes or tunnels within a topotactic reaction, which describes a structural change in a crystalline solid. Within this reaction, 0.5 to 1 electrons (equivalent to 0.5 to 1 lithium or sodium-ions) take part. The general chemical reaction can be expressed by:

$$A + xN \rightleftharpoons AN_x \tag{2.21}$$

with A representing the exchange alkali ion and N an active element or compound. Examples are graphite (C_6), titanium dioxide (TiO_2) or vanadium pentoxide (V_2O_5).[31, 61] The range of usable capacities for different intercalation materials are shown in Figure 2.10 (left) and lays between 100 to 230 mAh·g^{-1}.[60] The operating potential stretches from 2 up to 5 V. The process is highly reversible and shows fast kinetics depending on crystal structure, surface reactions and ionic diffusion coefficients. The crystal structure is important as it indicates stability and ionic conductivity of the material. Figure 2.10 (right) shows three different crystal structures for intercalation materials: lithium cobalt oxide as an example for a layered oxide, lithium manganese oxide as an example for a spinel structure and $LiFePO_4$ as an example for an olivine structure.[62] The fastest kinetics are stated for the two dimensional layered oxide structure as ions can easily move between the layers.

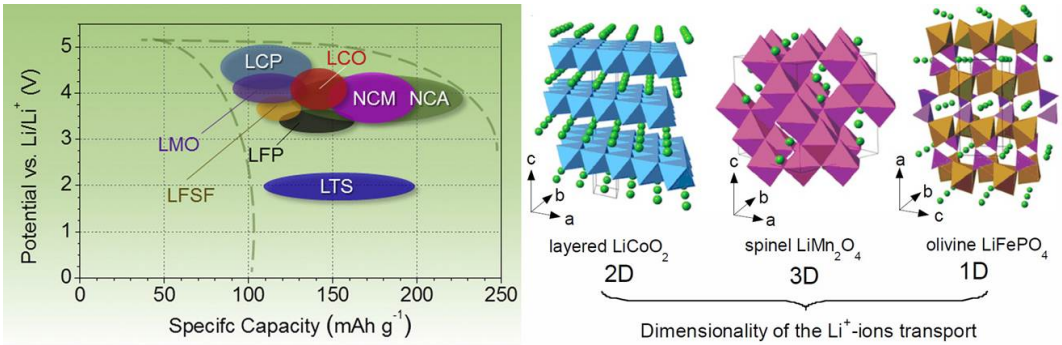

Figure 2.10: Overview of the average discharge potentials and specific capacities for all types of electrodes [62].

Table 2.1: Electrochemical characteristics of the three classes of insertion compounds, adapted from [62].

	Compound	Specific capacity ($mAh \cdot g^{-1}$)[1]	Average potential (V vs. Li^0/Li^+)	Specific energy ($mWh \cdot g^{-1}$)[2]
Layered oxide	$LiCoO_2$	272 (140)	4.2	588
	$LiNi_{\frac{1}{3}}Mn_{\frac{1}{3}}Co_{\frac{1}{3}}O_2$	272 (200)	4.0	800
Spinel	$LiMn_2O_4$	148 (120)	4.1	492
	$LiMn_{\frac{3}{2}}Ni_{\frac{1}{2}}O_4$	148 (120)	4.7	696
Olivine	$LiFePO_4$	170 (160)	3.45	552
	$LiFe_{\frac{1}{2}}Mn_{\frac{1}{2}}PO_4$	170 (160)	3.4/4.1	544

Within the spinel structure movement across the layers is possible, but pathways are longer due to a higher tortuosity. The lowest moving kinetics are within olive structures. Due to their 1D structure, ions are only able to move within channels. A comparison of electrochemical parameters such as specific capacity, the average potential and specific energy for different intercalation materials is listed in Table 2.1 (adapted from [62]). Due to their high specific capacities, layered oxides are more suitable for high energy applications. However, as volume expansions are better compensated by spinel and olivine crystal structures, these materials are more suitable for high power and long life applications, respectively.

Alloying/dealloying is a solid or solid-state solution of two solvents, mostly inter-metallic compounds. Materials should have similar atomic radii, same crystal structure, similar

[1] Value in parenthesis indicates the practical specific capacity of electrode.
[2] Calculation is based on the practical specific capacity of electrode.

electro-negatives, and valency (Hume-Rothery rules) to form an alloy. The chemical equation is given by:

$$A + xM \rightleftharpoons A_xM, \tag{2.22}$$

whereby A and a metal M forming an alloy AM by exchanging $x > 1$ electrons. Alloy electrodes promise capacities of up to 3500 $\mathrm{mAh}\cdot g^{-1}$, when used within their full potential range. The best developed alloy anode to-date is a silicon-carbon compound.[63] But electrodes containing e.g. tin (Sn) and antimony (Sb) are also of interest (Figure 2.11, right [60]). The main challenge when using alloy forming materials is the compensation of the huge volume expansion. Due to the fact that these materials are able to store more than one exchange ion per atom leads to volume expansions > 300 %, paired with nano-particle agglomeration and enormous mechanical stress. Therefore, a buffer matrix for alloying electrodes needs to be developed.[64]

Conversion reactions form new materials during charging and discharging processes, by breaking and recombining chemical bonds.

$$M_aX_b + yA \rightarrow aM + A_ybX \tag{2.23}$$

Whereby M is a transition metal with more than two valence metal ions, for example. Mn^{3+}, Fe^{3+}, Fe^{2+}, Co^{2+}, Ni^{2+} and X an non-metallic element, either a pnictogen (for example N, P), a chalcogen (for example. O, S) or a halogen (for example F, Cl).[65, 66] Figure 2.11 shows a range of potential conversion cathodes (left) and anodes (right).[60] These materials show in general higher specific capacities for cathodes than intercalation or alloying materials. However, cycle life and stability is still a problem.

In summary, intercalation materials are the best developed materials to date. They are more stable than conversion or alloy-types. Hence, they are more likely to compensate volume expansions caused by lithium or sodium-ion insertion due to their lower densities. As a drawback they also show lower capacities.

2.4.2 Degradation mechanisms

There are various degradation mechanisms within the electrodes. One of the main issues leading to capacity losses and decrease in battery performance can be linked to surface layer formation. The formed layers are non-conductive, passivated films on electrode surfaces. They are called the Solid Electrolyte Interphase (SEI) when formed on anodes and often re-

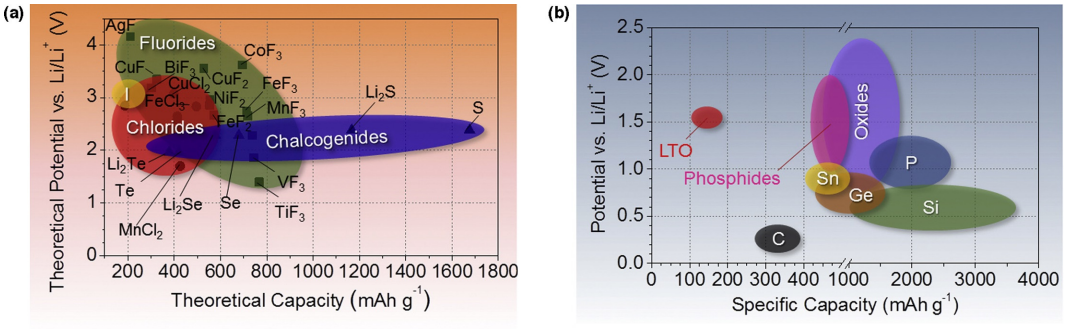

Figure 2.11: Approximate range of average discharge potentials and specific capacity of some of the most common alloying and conversion-type (a) cathodes (theoretical) and (b) anodes (experimental) for lithium-ion batteries.[60]

ferred to Cathode Electrolyte Interphase (CEI) for positive electrodes. The mechanisms are different for every material and are still under investigation. Although, it is common understanding that these surface layers are formed by decomposition products of the electrolyte solvent and conducting salts.[67, 68, 69] But a stable surface layer also slows down further side reactions and protects the active material surface against solvent ion intercalation[1]. Nevertheless, charging and discharging processes induce volume expansion and cause mechanical stress. Current research focusses on particle embedding frameworks to solve this issue (Figure 2.12 [70]). However, most composite electrodes do not have a flexible binder framework or matrix to compensate these effects. This leads to a 'breathing' movement of the particles and causes particle cracking and delamination. As a consequence the actual surface is increasing and additional SEI are formed.[71, 72]

Alongside uncontrolled SEI formation, particle cracking can lead to higher ohmic resistance, if single particles lose electronic contact to the current collector. Moreover, without contact to the current collector, these particles can no longer be charged and discharged. Furthermore, loose particles might move through the battery and block separator pores. This leads to an inhomogeneous current distribution and a local increase of the current density, as mentioned in Chapter 3.3. Hence, the voltage exceeds the safe potential window and a local overcharging/overdischarging of the materials occurs. Overcharging on cathode side leads to electrolyte decompensation and dissolution of transition metal into the electrolyte. Overdischarging of anodes leads to lithium and sodium plating and dendrite growth, respectively.[74, 75]

There a many different processes causing degradation of the electrode materials and

[1]The SEI hinders the intercalation of the complete counter ion solvation shell. While moving through the SEI layer the counter ion removes its solvent shell, which reduces the mechanical stress for the electrode

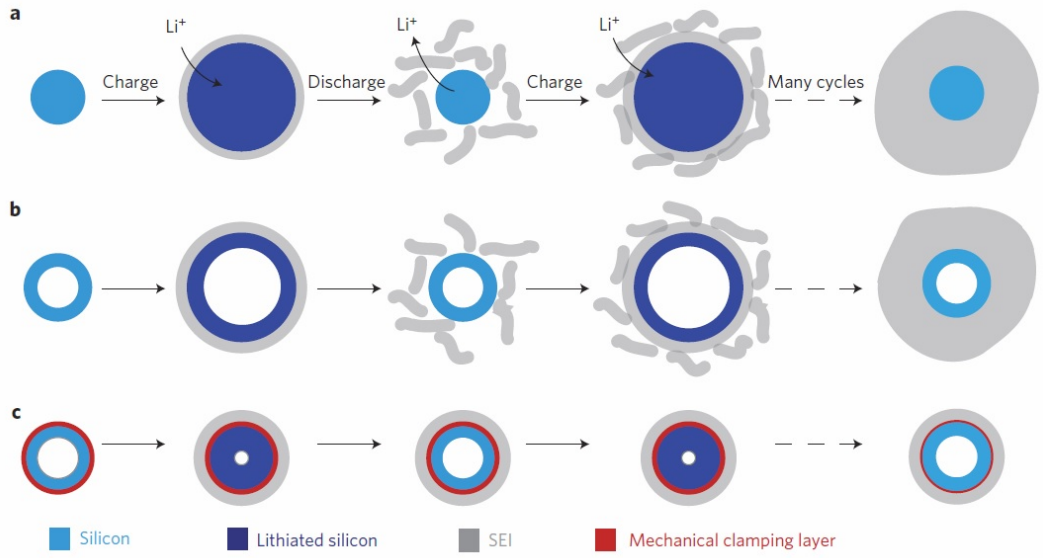

Figure 2.12: Schematic of SEI formation on silicon surfaces; Influence of silicon morphology onto SEI formation and stability a) full particle; b) hollow sphere; c) hollow sphere with artificial SEI.[70]

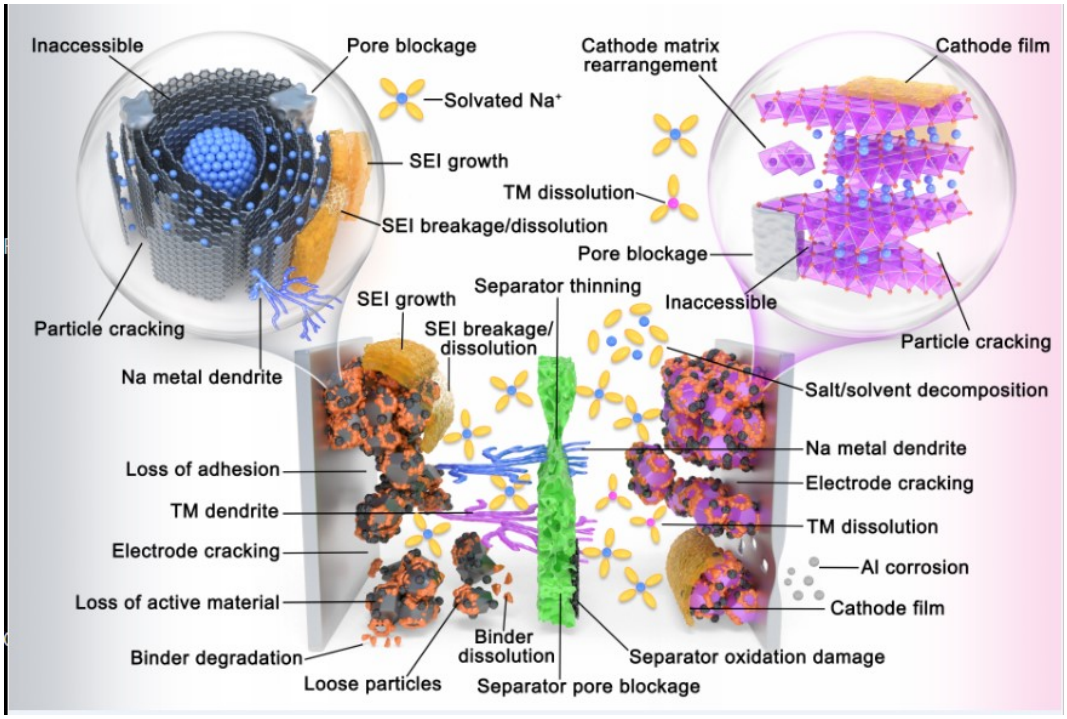

Figure 2.13: Degradation mechanisms in Na-ion cells; cell components from left to right: aluminium current collector, HC anode, organic carbonate electrolyte with sodium salt, polyolefin separator, organic carbonate electrolyte with sodium salt, sodium layered oxide cathode, aluminium current collector.[73]

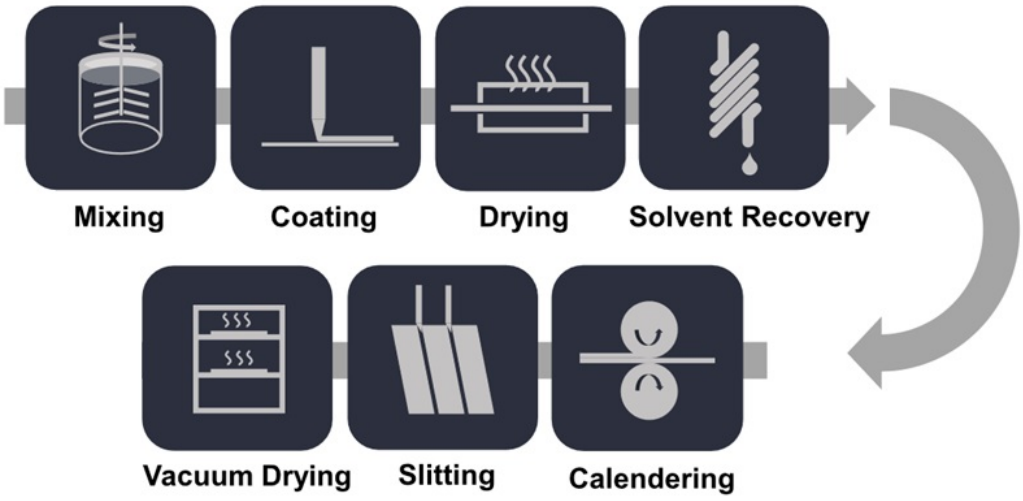

Figure 2.14: Illustration of main process steps for electrode manufacturing by Liu et al. [76].

hence reducing the battery performance. A good visual summery is given by Weaving et al. [73] as shown in Figure 2.13. The pictures summarises the different ageing and degradation mechanisms occurring in Na-ion systems, assuming a HC anode, organic carbonate electrolyte, polyolefin separator and metal oxide cathode.

2.4.3 Processing

Electrode manufacturing is a multi-step process and depends on a large number of parameters. The following fabrication steps give a short summary of the main tasks, which are: mixing, dispersing, coating, drying, and calendering. They are illustrated in Figure 2.14. These steps might differ due to processing routine, ingredients and active materials. Besides, in battery manufacturing some process steps (coating, drying, calendering) are combined to so called reel-to-reel coating machines. In addition some equipment enables in-line double side coating.

1. (Pre-)Mixing

   Depending on the number of ingredients and kind of active material: a dry mix of all ingredients might be necessary for a homogeneous mixture. As an alternative, a premix/pre-dispersion of some ingredients is required to ensure good solubility. Also, most carbon-nano fibres or polyvinylidene fluoride (PVdF) binders are pre-dispersed in a suitable solvent for better performing electrodes. Important parameters include ratio of ingredients and mixing time. The duration is crucial as it needs a sufficient time to obtain a homogeneous mixture, but long time mixing might result in particle

sizes changes or demixing.

2. Dispersing

   Most techniques use solvents to prepare slurries for the coating[1]. Common solvents are water and N-methyl-2-pyrrolidone (NMP). Water is used for water-soluble binder systems such as alginate, carboxylmethyl cellulose (CMC) or styrol butadien rubber (SBR). These systems are already available for commercial available anodes for lithium-ion batteries.[27, 79, 80] Often, inks containing cathode materials or HC are based on NMP solvents or the less harmful alternative N-etylpyrrolidone (NEP). The produced inks should have a high material content and viscosity. This is important to achieve thick coatings comprising high loadings of active material. For ink preparation high shear equipment comprising a propeller stirrer or planetary mixing are used. High shear forces are required to break apart agglomerates to obtain a smooth and homogeneous. Important parameters include the type of mixing equipment, viscosity of the ink and mixing time.

3. Coating

   A standard coating technique is the doctor blade method. Within this process the slurry is poured onto the current collector foil. A blade with a defined gap to the current collector removes any excess material while being pushed across the current collector foil (see Figure 2.14 from [81], step coating). Important parameters influencing the characteristics of the draw down are the blade gap, feed rate, and current collector tension.

4. Drying

   Drying on laboratory scale differs from industry-scale massively. On laboratory-scale heating plates, infra-red lights or vacuum ovens are used for drying. This process can take up to 1.5 hours depending on thickness and solid content of the ink. On industry-scale the drying step is implemented within the reel-to-reel process. Most reel-to-reel coating machines contain more than four heating elements or zones, placed above and underneath the coating to ramp the coating in several zones to different temperatures. As a result the coating will dry within 5 to 15 minutes depending on roller speed,

[1] A new technique of dry coating was presented to the battery community in 2016 and might be commercialised within the upcoming years. The technique is based on patents from Zhong et al. [77] and Duong, Feigenbaum, and Hong [78].

thickness and solid content of the ink. The important parameters within this step are the roller speed, temperature, and current collector tension.

5. Calendering

   Calendering is a compaction process for electrodes, where the electrodes are fed between two stainless steel rollers to achieve a certain thickness and hence densification. The process can be enhanced by heated rollers (hot roller press) choosing a temperature similar to the softening temperature of the binder used. Besides, the calendering step is important to increase cohesion and adhesion of the materials and the current collector. This process has a substantial impact on the pore structure and therefore the electrochemical performance of the electrodes. Adjustment of the porosity influences electrolyte wetting characteristics and also charge transfer reactions during cycling. A thickness reduction increases volumetric density which is important for portable and automotive applications. Important parameters include the line pressure, temperature, and residual moisture of solvents within the coating.

2.5 Anode material: HC for sodium-ion batteries

Graphite cannot be used in sodium-ion batteries containing carbonated electrolyte, as sodium does not reversible intercalate into graphite. So the most common anode material in sodium-ion batteries is HC. HC is a non-graphitic carbon that cannot be graphetised even at temperatures as high as 3000 °C.[82] Its distance between single graphene sheets is larger than within graphite. The synthesis of HC is a solid-state pyrolysis and is similar to soft carbons and differs by the maximum temperature only. Common used precursor materials are pitch and charcoal, but also renewable resources such as coconut shells, cotton, banana peels, and glucose are used.[29, 83, 84, 85, 86] The main difference between graphite and HC is their hybridisation. Whereas graphite has sp^2 bonds, HC has a mixed sp^2 and sp^3 hybridisation, which leads to cross-linking between the layers and a lack of long range ordering in the c direction of graphite, as seen in Figure 2.15.[87] As a result, the HC particles' 3-D electronic conductivity improves the electronic transport properties compared to graphite.[88] Furthermore, cross-linking reduces the density of the material. The density of HC is around 1.5 $g{\cdot}cm^{-3}$, which is slightly lower than the density of graphite of around 2.1 $g{\cdot}cm^{-3}$.

Sodium intercalation into HC was first described by Stevens and Dahn [83]. Within

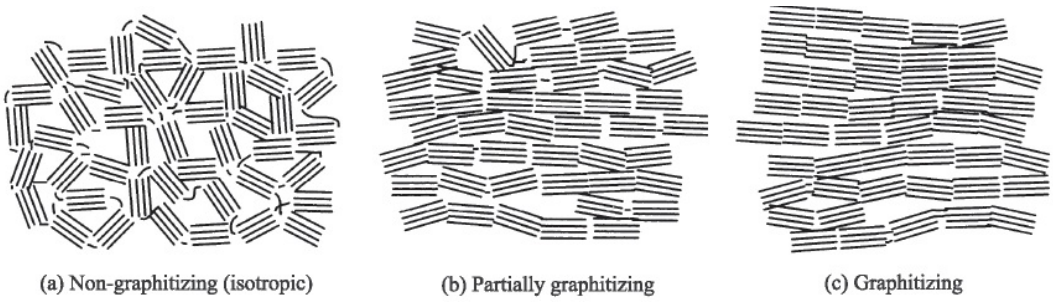

Figure 2.15: Franklin models for isotropic and graphitising carbons; a) non-graphitised carbon, HC; b) partially graphitised; c) graphitised, graphite by Mochida, Yoon, and Qiao [87].

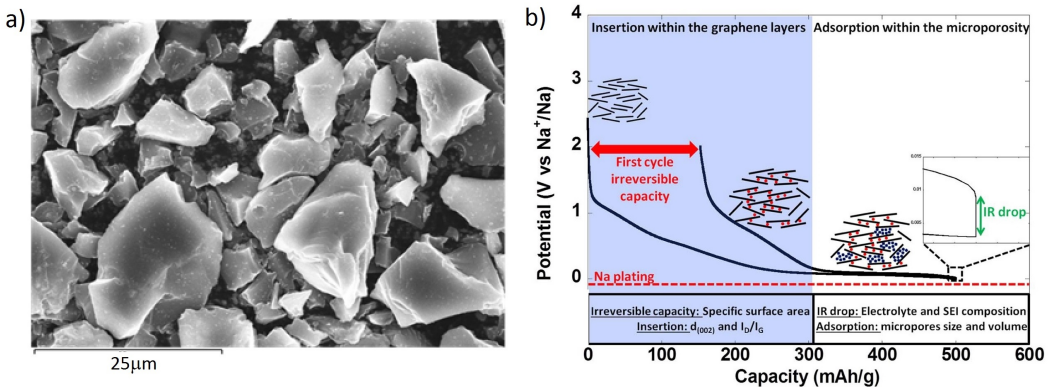

Figure 2.16: HC characteristics: a) SEM picture of a commercial HC material; b) Typical potential versus capacity profile for HC when tested against sodium metal counter electrodes. The different steps of the mechanism are also labelled and depicted [89].

the following years, synthesis routes and material characteristics were improved. Nowadays most carbons show similar capacities of around 300 to 350 $\mathrm{mAh{\cdot}g^{-1}}$ for room-temperature sodium-ion batteries. The observed FCL depends on the particle size of the different materials and electrode formulation and varies between 15 and 25 %. As SEI formation and its stability influence the cell performance massively, parameters such as particle size and surface area are crucial. The left picture in Figure 2.16 shows an SEM image of the commercial HC used within this thesis. The average particle size for this material is stated as 9 μm, but particles up to 20 μm can be found. The right picture in Figure 2.16 from Irisarri, Ponrouch, and Palacin [89] shows the usable capacity of a HC electrode versus sodium metal. The high discharge capacity of around 500 $\mathrm{mAh{\cdot}g^{-1}}$ might be caused by a large surface area[1] of 70 $\mathrm{m^2{\cdot}g^{-1}}$. Currently HC is the anode of choice for sodium-ion batteries, therefore improvements in the observed charge rate is required for many of the potential applications

[1]Commercial products are used to conduct the experiments within this thesis. These products state values around 3 to 8 $\mathrm{m^2{\cdot}g^{-1}}$.

on the horizon for sodium-ion batteries such as power tools, e-mobility (e-bikes, electric vehicles) and stationary energy storage.[13, 19, 90, 91] During cycling, and especially during the initial formation cycles, an electronically insulating SEI forms on the anode surface, this can increase internal resistance and cause a subsequent drop in cell performance.[92, 93, 94, 95] Xia and Dahn [95] show that the inter-phase for sodiated HC is more related toward the electrolyte compared to lithiated HC/electrolyte. Hence, the SEI in sodium-ion batteries is less stable than in lithium-ion batteries. The growth of the SEI decreases the porosity of the composite electrode as the SEI grows into the available pore space. Hence, possible electrolyte reservoirs vanish, and pathways for sodium-ion diffusion are elongated or removed altogether.

Chapter 3

Literature review

This chapter gives an introduction about the economic potential of the world wide battery marked as well as summarises and discusses prior research on electrode and material characterisation for lithium and sodium-ion batteries. Based on composite electrode characteristics and market needs bench-marks will be set, which are required for the sodium-ion technology to meet commercialisation targets. These bench-marks are based on state-of-the-art characteristics, e.g. performance and costs of commercially available lithium and sodium-ion batteries. Additionally, characterisation methods used to investigate material and hallf-cell performance are introduced. Section 3.1 *Comparison of lithium to sodium-ion batteries - costs and commercialisation* gives a general overview about the battery market and points out the advantages and disadvantages of both technologies. Electrode materials used in either lithium-ion or sodium-ion batteries are introduced in Section 3.2 *Electrode materials and reactions*. Cell designs used for material testing and commercial applications are summarised and discussed, subsequently. Finally, Chapters 3.5 *Electrochemical characterisation* and 3.6 *Physical characterisation* state suitable methods to investigate chemical and physical electrode properties and their utilisation in literature is discussed. The conclusion of the literature review summarises obstacles and objectives for the upcoming research to accomplish the bench-marks set by the lithium-ion technology.

3.1 Comparison of lithium to sodium-ion batteries: costs and commercialisation

The battery market is fast growing with a turnover of US$ 80 billion in 2018 with an overall share of lithium-ion batteries of approximately 30 % (data based on pack-level). The average growth rate was about 5 % over the last 15 years and an increase for the upcom-

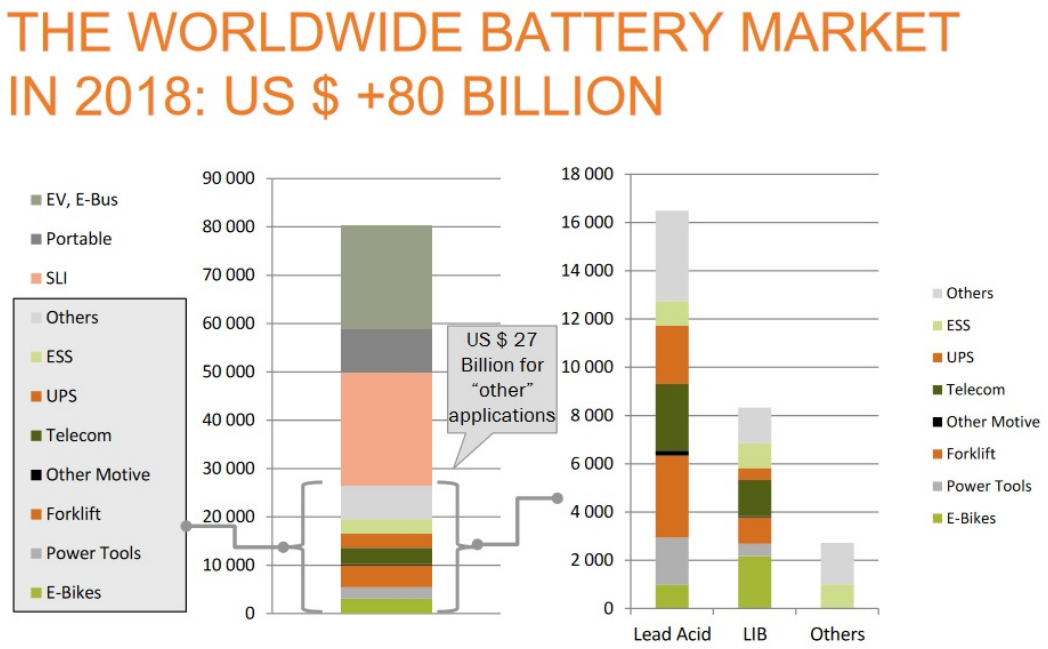

Figure 3.1: Analysis of the world wide battery market in 2018 by Pillot [96].
SLI: Start light and ignition batteries for cars, truck, motor boat etc.

ing years is expected.[96] Figure 3.1 shows the share of several applications to the battery market in 2018. The key applications for lithium-ion batteries are portable devices, power tools, and e-bikes. Furthermore, their percentage in applications for ESS (Energy Storage Systems) and other stationary systems is growing. With the increasing demand of portable devices, house or grid energy storage systems and electric vehicles, battery costs have become more important for many applications. Considering this, sodium-ion technology is an attractive alternative as sodium is much more abundant than lithium. Sodium can be extracted from seawater, whereas most of the lithium resources are located in China or South America. Furthermore, the manufacturing of sodium-ion batteries can be implemented as a drop-in technology into the existing infrastructure of lithium-ion battery production. Table 3.1 states the average costs of the most common electrode and current collector materials. A comparison of the cathode raw material costs shows a benefit for sodium-ion batteries as the precursor material sodium carbonate is about an order of magnitude cheaper than lithium carbonate. In the case of anode material costs, HC (sodium technology) is slightly more expensive than graphite (lithium technology)[1]. But the difference in price may change, as research projects are aiming to develop new blended electrodes containing silicon, tin or antimony for energy storage, to increase volumetric and gravimetric capacities. Nevertheless,

[1] HC needs to be used since sodium does not reversible intercalate into graphite.

Table 3.1: Prices of electrode and current collector materials for lithium and sodium-ion batteries.

Material	Application	Price in 100 US$/mt	Reference
Lithium carbonate	Cathode	6	[97]
Sodium carbonate (soda ash)	Cathode	< 0.2	[97]
Graphite	Lithium anode	7-13	[98]
HC	Sodium anode	25	[98]
Silicon	Anode	300	[97]
Tin	Anode	1500	[97]
Antimony	Anode	750	[97]
Aluminium	Current collector	2	[97]
Copper	Current collector	610	[97]

HC offers an environmental advantage as it can be easily produced from coconut shells, rice or other biomass.[29, 89, 99, 100] Additionally, in sodium-ion batteries aluminium can be used as an anode current collector, because in contrast to lithium, sodium does not form an alloy with aluminium at low potentials. Hence, the utilisation of aluminium reduces costs and improves safety as a freshly built sodium-ion battery can be shorted externally without the hazard of exothermic reaction and consequent fires or explosions.[101]

The main disadvantage of sodium-ion batteries is the theoretically lower energy and power density compared to lithium-ion technology. These calculations are based on the ionic radius[1] and the standard electrode potential (vs. SHE)[2]. Nevertheless, under operating conditions, theoretical capacities cannot be achieved for both technologies. Further efforts in sodium-ion battery development have to be made to improve these characteristics. Besides, capacities and cycling performance of batteries need to be improved to lower life-time costs. This can be done either by inventing new materials with higher capacities for high power applications comparable to lithium cobalt oxide (LCO) or by improving the cycle stability of existing materials to be able to compete with LFP batteries (see also Chapter 3.2). Bearing in mind the lower theoretical gravimetric capacity of sodium-ion batteries, focussing on a development of a low-cost and long-life battery seems to be a sensible approach. These low cost, high energy batteries can be used for house or grid scale energy storage systems where costs and life-time are essential, and volumetric/gravimetric capacities are secondary considerations. Current commercial solutions for home energy storage systems are e.g. the Tesla Powerwall, SonnenCore and LG Chem.[102, 103, 104] All these

[1] Ionic radii: 182 pm for lithium, 227 pm for sodium

[2] SHE: −3.04 V for lithium, −2.7 V for sodium

Table 3.2: Summary of characteristics and budget costing for a home energy storage system sold by Sonnen, Tesla, and LG Resu.

	SonnenCore eco	Tesla Powerwall 2.0	LG Chem
Chemistry	LFP	NMC	NMC
Usable energy	10 kWh	13.5 kWh	9.3 kWh
Power Output cont (peak)	4.5 (8.6) kW	up to 7 kW	5 (7) kW
Life time	10 000 cycles	unlimited	6 000
or throughput	58 MWh	37.8 MWh	22.4 MWh
Warranty	10 years	10 years	10 years
Depth of Discharge	100 %	100 %	90 %
Price system	9 500 US $	8 500 US $	7 000 US $
Price Converter	included	included	.
Installation costs	n.a.	2 000 US $	
Costs per kWh/throughput	0.16 US$	0.22 US$	0.31 US$

solutions are based on lithium-ion technology and a comparison including an approximation of costs is given in Table 3.2. The products state a warranty of 10 years and a cycle life of greater than 6 000 cycles. The calculated costs of the Sonnenbatterie system per lifetime throughput are around 0.16 US$, the Tesla is 50 % more expensive (0.22 US$), whereas the storage system from LG Chem is around 0.31 US$. The company called Aquion Energy (closed in 2017) offered a system based on sodium salt water batteries (Manganese oxide versus titanium phosphate (in 5 M $NaClO_4$). The costs of their system was at around 0.23 US$.[105]

The current key players in the sodium battery market include Faradion Ltd, AGM Batteries Ltd (amte power), NGK Insulators Ltd, TIAMAT SAS, HiNa Battery Technology Co. Ltd, Altris AB, and Natron Energy Inc. Except NGK Insulators Ltd, who offer a energy storage system on the high-temperature sodium/sulphur technology (NAS) [106], all other companies offer either active materials or assembled cells based on the room-temperature sodium-ion technology. As an example, the company Faradion Ltd. is a start-up company focussing on commercialising sodium-ion batteries. They claim a cost benefit of up to 30 % on cell level and state power densities similar to LFP.[107] With a cost reduction of 30 % in mind, sodium-ion batteries need to hit 3 500 cycles to compete with currently available lithium-ion products on the market.

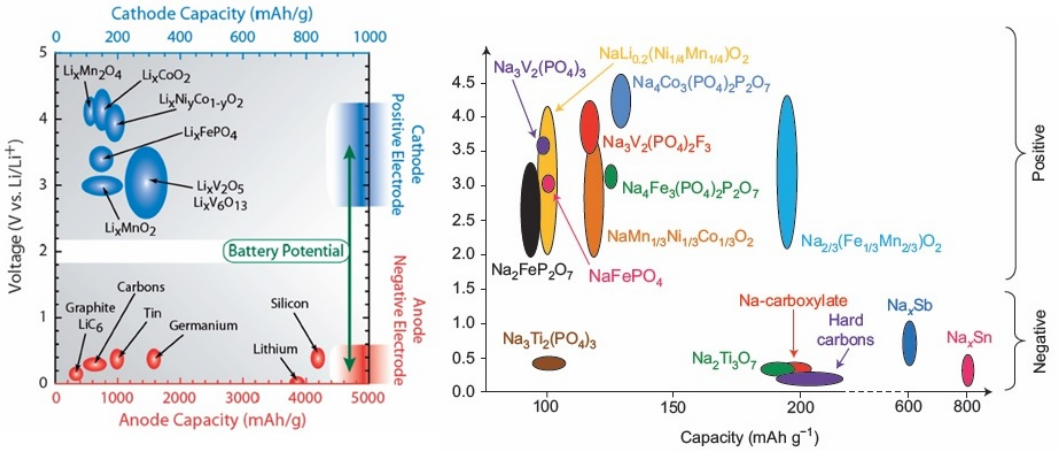

Figure 3.2: Illustration of capacity and electrochemical reduction potential of reported positive and negative electrode materials with plausible application in lithium-ion cells (left,[108]) and sodium-ion cells (right,[109]).

3.2 Electrode materials and reactions

Electrodes for sodium-ion and lithium-ion batteries are based on similar materials. In most cases layered oxides, phosphates or metal oxides are used on the cathode side. Common materials for anodes are different kinds of carbons or titanates.[108, 109] Many reviews have been published stating recent materials and developments in lithium and sodium ion research.[13, 16, 60, 89, 110, 111] But recent developments on blended or pure metal electrodes comprising e.g. lithium, sodium, tin, antimony or silicon, show promising results. These advanced electrodes operate at slightly higher potentials and show high capacity fade rates. But, if cycle stability and life can be improved, a huge boost in capacity can be achieved. Figure 3.2 illustrates the operating potential and capacities for several materials used in lithium-ion and sodium-ion batteries. Batteries can be built out of any combination of lithium-ion or sodium-ion materials. The battery voltage is the difference between the two potentials of the selected anode and cathode.

It can be seen that lithium-ion and sodium-ion batteries operate within the same voltage window, but lithium-ion batteries reveal the higher capacities, for both, anode and cathode materials. In 2014 Sharp Laboratories of Europe Ltd (SLE) invented a new cathode material suitable for sodium-ion batteries, showing capacities of 150 mAh·g^{-1}. A further development of this material led to an improved material with promising capacities of up to 190 mAh·g^{-1}.[112] These maximum capacities are similar to the ones stated for $LiFePO_4$ (Figure 3.2, [108, 109]) and makes SLE's material suitable for low power applications. Recent developments show cathode materials with similar or slightly higher capacities, altough

full cell testing has not reported with these materials, yet.[113, 114, 115]

Depending on the kind of material, different charging and discharging processes are happening. In the literature, often generic expressions like lithiation/delithation and sodiation/desodiation are used, respectively, to implicate processes such as intercalation/deintercalation, alloying/dealloying or conversion. Intercalation materials show a more stable cycle life than conversion and alloying materials, but due to their limited storage of exchange ions they offer lower capacities.[31, 60, 61, 63, 64, 65]

This Ph. D. project focusses on the characterisation and processing of HC composite electrodes (intercalation anode). Within Chapter 2.4 a detailed description of the different processes (intercalation, alloying, conversion) and a more detailed introduction into the materials used in this project, including synthesis routes, parameters and their material properties are given.

3.3 Importance and safety of the experimental set-up

A well-conceived experimental set-up is mandatory to generate reliable data. It also guarantees a safe testing environment and a minimisation of hazards. At cell level, good alignment of electrodes, a separator in good condition and balanced electrodes are essential.[1] A misalignment of anode and cathode or unbalanced electrodes lead to inhomogeneous current distribution, which results in lower capacities or dendrite formation.[2][116, 117, 118, 119] Dendrite formation has to be avoided as dendrites can cause internal short circuits, electrolyte evaporation and fires. Internal short circuits influence the results of cell characterisation as short circuits lead to a continuous small discharge current. Hence, charging capacities might appear higher, discharging capacities lower and therefore lead to an incorrect coloumbic efficiency. For example, Samsung investigated a misalignment of electrodes as one cause for the fire evolution within their Galaxy Note 7.[120] To prevent dendrite formation, the capacities of anodes are chosen to be slightly higher than the ones for cathodes.

Laboratory scale cells are often tested within half-cell configurations, this implies the working electrode is tested versus sodium or lithium metal, respectively.[84, 121, 122] But electrochemical testing has to be evaluated carefully, when done in a standard 2-electrode arrangement as stripping and plating of metallic sodium and lithium contributes to the overall cell polarisation.[123] Some research groups work on additives to suppress dendrite for-

[1] Electrodes are called balanced, when the capacities of anode and cathode are alike.

[2] Dendrites are metallic depositions on the anode surface.

mation. Besides, homogeneous lithium plating reduces the cell volume and enhances safety as internal short circuits are avoided. Ongoing research on dendrite formation is mainly focussed on lithium-ion metal or lithium air batteries as these battery types incorporate a solid or liquid lithium metal anode.[124, 125, 126]

To monitor the working and counter electrode potentials separately a 3-electrode arrangement comprising a reference electrode can be used. Different approaches of 3-electrode set-ups are discussed in Chapter 3.4. It is important that these mainly in-house made cell set-ups are gas tight to avoid any humidity entering the cell environment as metallic sodium and lithium react exothermically when in contact with water. Hence, lithium and sodium-ion batteries have to be built in an inert/dry atmosphere to reduce the water content to a minimum (< 15 ppm). Additionally hydrofluoric acid (HF) can be formed when conducting salts such as $LiPF_6$ or $NaPF_6$ are used. Besides health and safety risks, HF generation reduces the overall battery capacity as it reacts with transition metals used in the cathode materials and corrodes the aluminium current collector.[127, 128]

Other safety aspects are incorporated within cell assembling and battery manufacturing. Some cell manufactures use a triple layered separator. These separators comprising a safety layer, which melts down at higher temperatures (approx. 130 °C, [129]) and should avoid or stop thermal runaway as initiated by an internal short circuits. During a thermal runaway the cell temperature increases. After reaching an on-set temperature, the heat generation will be self-supplied and the battery cell will melt down.[130, 131] The use of a shut-down separator prevents any further ionic and electric exchange and causes a stop of the electrochemical reaction. One of the disadvantage of these separators is their sensitivity to heat within the manufacturing process. As a consequence, tab welding and sealing of pouch bags has to be done with caution to avoid separator melting. Also, partial melting of the separator leads to an inhomogeneous current distribution resulting in dendrite formation, as stated above.[75, 132] Besides, these separators are thicker than other double layered separators and therefore increase the internal resistance of the cell, which leads to power losses in the battery performance. Therefore, electrodes, balancing, separator and housing should be chosen depending on the purpose of testing. A range of different cell designs are introduced in the following section, discussing their advantages and disadvantages.

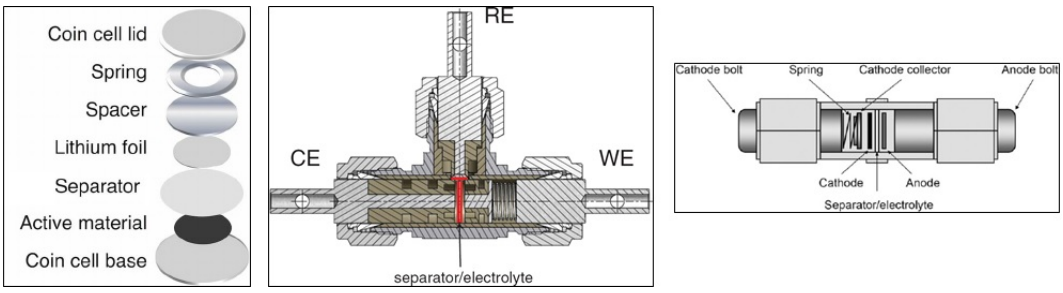

Figure 3.3: Assembling of different cell set-ups as used for research and development on laboratory-scale by [117, 121, 133].

3.4 Comparison of cell designs for material testing and commercial applications

The focus of cell characterisation on a laboratory-scale is on initial material testing (e.g. capacity and performance) whereas commercial battery tests are focussing on cycle life and rate stability. Furthermore, commercial cells have either a high volumetric or gravimetric energy density and have to be suitable for high power or high energy applications. Therefore, cell designs differ from each other as the cell or battery set-up has to match the application or testing purpose. Cell designs on laboratory scale need to be fast and easily assembled/disassembled, low-cost and gas-tight. Size and volume of the housing do not matter as gravimetric and volumetric densities are only important on an electrode level. The most common set-ups are disposable coin cells or reusable 'Swagelok cells'. Three different cell designs used for material testing are shown in Figure 3.3. For scale-up approaches and long term testing often small pouch bag cells with capacities up to 0.5 Ah are used as this set-up is closer to a commercial set-up. Most common are single layered pouch bags (SLP) consisting of a single electrode stack (anode, separator, cathode).

Coin cells (left picture in Figure 3.3) are low cost, and fast and easy to build. But in comparison to 2-electrode Swagelok cells (picture on the right) they are more difficult to disassemble if post-mortem analysis is necessary. In contrast, Swagelok cells are easy to disassemble and reusable. Being actually made for gas pipelines, they are gas tight, when assembled correctly. Swagelok housings are either made out of stainless steel, using insulating insets to avoid internal short circuits, or made from polyvinyl alcohol (PVA) or polyether ether ketone (PEEK). The cell design can be modified to a 3-electrode set-up by using a Swagelok Tee-union as the body part (Figure 3.3, middle). Via the third entrance a reference electrode enables the monitoring of the cathode and anode potential separately

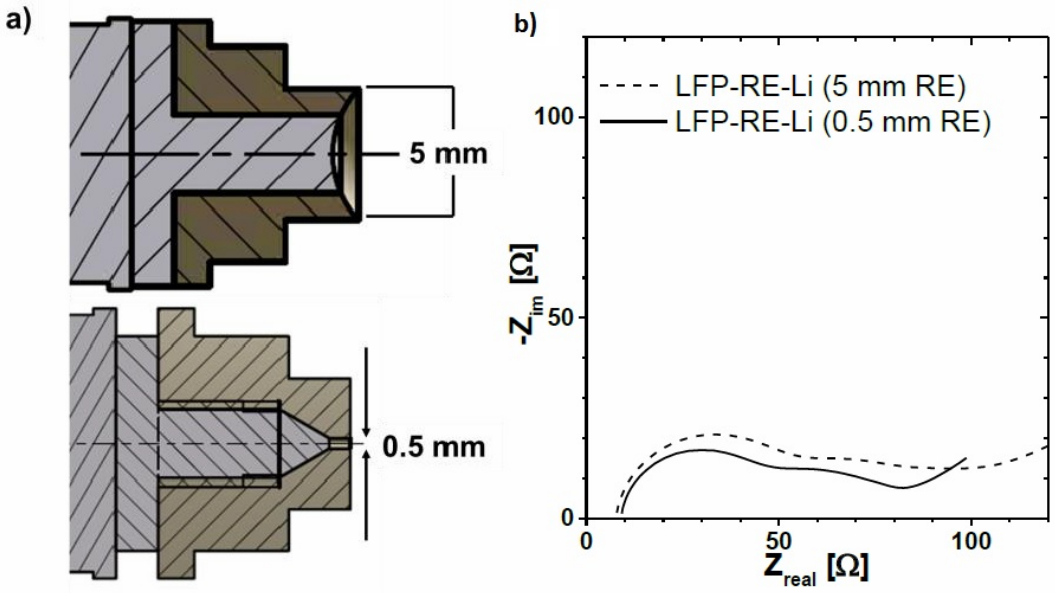

Figure 3.4: Optimisation of the reference electrode diameter by Klink [134]. a) Standard 5 mm reference electrode as used in 3-electrode Swagelok arrangement and an alternative 0.5 mm micro reference; b) Influence of the reference diameter on data collected by EIS.

from each other. This is important to allocate cell effects to individual electrodes.

Although material characterisation is done by so-called half-cell testing, the metal counter electrode influences the properties of the test cell as mentioned earlier. The reference material used should be stable within the voltage range, show low polarisation and be inert to electrolyte reactions. In most cases lithium is used as a reference material for lithium-ion battery testing and sodium for sodium-ion cells. The advantage of this 3-electrode Swagelok set-up is the rather small variation compared to a standard 2-electrode arrangement as the cell remains the same and the reference electrode is attached to the side of the stack. As a drawback, a large amount of reference material is needed. This causes side effects as surface layers occur on lithium and sodium when in contact with electrolyte. An investigation of different reference designs was done by Klink [134] and is shown in the top drawing in Figure 3.4 a. A reduction of the amount of reference material used results in a lower overall resistance as seen in Figure 3.4b. Nevertheless, both data sets show the same features, although the shape of the data set collected by using a 0.5 mm reference is more distinct. However, the reference electrode has to be aligned centrally towards the cell stack to ensure the shortest possible distance between counter and reference electrode, as well as between working and reference electrode. This can be more difficult with an diameter of 0.5 mm.

As alternative to these in-house solutions, commercial systems can be purchased. For example MTI Corporation (US) or EL-Cell (Germany) provide test housings. EL-Cell offers solutions for special experimental cell set-ups such as optical test cells, cells for gas analysis and reference electrode cell set-ups. The amount of reference material, which is used in their 3-electrode set-up is reduced to a minimum, but a thick separator (thickness around 1 mm) is needed to adjust the position of the reference correctly, which results in higher ohmic resistances. This makes this set-up less suitable for impedance or long term testing.

The research community is aware of the importance of accurate repeatable cell testing. The added value of monitoring working and counter electrode potential is expressed by Barker [49] and Abraham et al. [135]. Further, the issues resulting from geometry, position and size of the reference electrode are discussed by Klink et al. [116], Gómez-Cámer and Novák [136] and Dees, Jansen, and Abraham [137]. An influence of cell geometry and reference size on the monitoring of cell characteristics is shown in these publications. As an outcome, a small reference electrode close to the cell stack is suggested. The most recent developments integrate ring-shaped reference electrodes into test cells. A ring-shaped reference electrode has the benefit of a more homogeneous potential distribution. A commercial solution of an implemented ring-shaped reference electrode was introduced by EL-Cell recently. The modified cell set-up may lead to more accurate results, if assembled correctly.[138] As a small drawback a variation of the reference material cannot be done, as the reference component is already set-up and has to be disposed after single use. Although the industrial cell set-up differs from laboratory-scale cell testing, reference electrodes are also used in commercial cell designs to investigate the influence of ageing and scale-up.[139, 140] Within this thesis 3-electrode Swagelok cells are used. Their cell set-up and assembling is described in Chapter 4.1.

Cell designs for commercial applications have either stacked (pouch bag, coin cell) or wound (cylindrical, prismatic) electrodes. Pictures and schematic drawings of a range of commercially available lithium-ion batteries are shown in Figure 3.5. Cylindrical cells have good gravimetric and volumetric energy densities due to a minimum of packaging material, but they need to have a rupture diaphragm to release pressure in case of a cell failure due to the risk of a potential explosion.[130] This is not necessary for pouch bag cells as higher inner pressure ruptures the laminated foil more easily than a tin can of a cylindrical cell. Cylindrical, prismatic and pouch bag cells are used for secondary battery applications, such

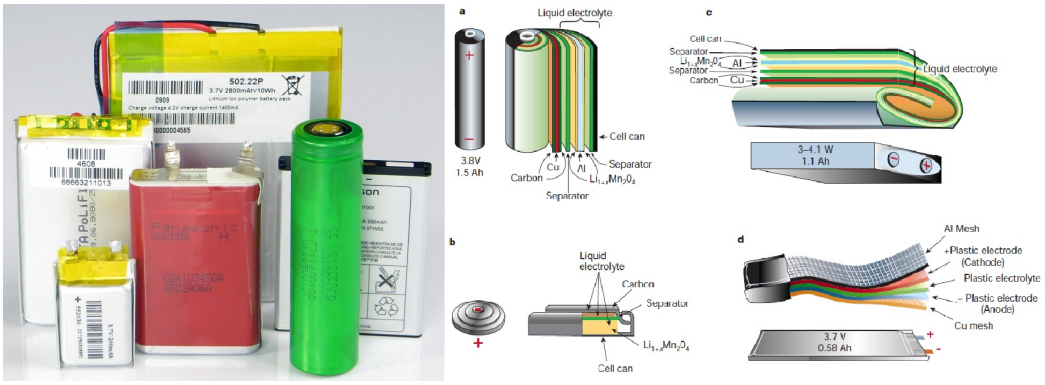

Figure 3.5: Left: photo of different kinds of lithium-ion battery shapes fabricated by different manufacturers.[141] Right: Schematic drawing of four different kinds of lithium-ion battery shapes. a: cylindrical; b: coin cell; c: prismatic; and d: plastic lithium-ion (PLiON).[119]

as laptops and smart phones. The coin cell design is used for primary batteries and low current applications only. Coin cells consist of a thick layer of active material (Figure 3.5), which results in poor electronic and ionic conductivity. Hence only low currents can be used to discharge the cell. New developments demonstrate batteries with extraordinary shapes. For example companies like Ascent Batteries (US) and Custom Cells (Germany) offer ring or Tee-shaped lithium-ion batteries.[142, 143]

In summary, a reliable cell set-up is mandatory for accurate and reproducible data. To ensure this, settings and parameters for electrochemical testing methods have to be carefully considered. The following section introduces the main testing methods and their application in the literature.

3.5 Electrochemical characterisation

Battery testing can be done in several different ways and there are no standard procedures yet. Therefore, comparison of published data is difficult.

The following subsections give a short overview about the implementation of the most common used techniques in the literature, their merits and limitations as well as the importance of parameter settings. Further, advantages and disadvantages of each testing method and its eligibility for material characterisation and industrial application are stated. A theoretical view about methods and analysis can be found in Section 2.1.

3.5.1 OCV

The OCV describes the voltage of an electrochemical cell, when disconnected from any circuit. It is important to realise the difference between OCV and the equilibrium potential.

Whereas the equilibrium potential is stable due to balanced kinetics of the forward and backward reactions, during OCV some reactions might be preferential. The contributions of these reactions are small, but accumulate over time and result in a self-discharge of the battery, thus influencing their shelf life. For rapid investigation of these slow processes, OCV measurements are often carried out at elevated temperature as this accelerates these processes (**Arrhenius equation**).

Most publications based on OCV data and measurements are stating new models to predict state-of-charge (SoC) and state-of-health (SoH) of batteries. To measure the true OCV potential, all diffusion reactions induced by charging or discharging steps have to come to a standstill. Therefore, this measurement is quite a time-consuming method. Many publications show low rate cycling curves instead of true OCV data (e.g. cycling at a C-rate[1] of C/40 [144]). Another approach is a calculation of the average voltage of charge and discharge recorded at a low C-rate.[145] In most cases the charging or discharging process at low C-rates is interrupted by several steps of OCV measurements for relaxation. The duration of these steps differs from around 30 minutes to up to 24 hours.[94, 146, 147] Furthermore, the relaxation time depends on materials and SoC. At the end of the OCV step, the potential should be stable; but the self-discharge of cells has to be considered. Whereas commercial cells have a rather low self-discharge rate of 2 to 3 % per month, cells on laboratory scale might discharge faster depending on the design used. Weng, Sun, and Peng [145] and Lavigne et al. [146], and Zhang et al. [94] used OCV data of commercial cells to develop models to estimate SoC and SoH of cycled cells. However, the deviations in parameter settings make it difficult to compare the published data to each other. But this kind of research helps enormously to improve the prediction of battery life. Nevertheless, the values stated in the literature are based on commercial full cells, and therefore these results are not material related and no linking towards inner processes is possible.

The results from Matsui et al. [147] and Schmidt et al. [144] are based on laboratory test cells. Matsui et al. used a coin cell set-up testing $LiFePO_4$ versus metallic lithium. Their OCV measurements show a change in diffusion behaviour depending on the SoC of the battery. As the tests are performed in a 2-electrode arrangement, the results are influenced by counter electrode contributions and might differ from the actual material potential.

[1] A C-rate names the charging or discharging current defined by the time, which is needed to fully charge or discharge a cell, independent of its capacity. A rate of 1 C corresponds to a full charge or discharge within 1 hour, 2 C within 30 minutes, etc.. The calculation of C-rate is often based on the theoretical capacity of the active material and therefore a charge at 1 C might take longer than 1 hour.

Schmidt et al. rebuilt dissasembled commercial batteries in a 3-electrode cell set-up to investigate the OCV behaviour of different materials. Based on this data, an OCV of blended electrodes can be calculated. Additionally, their simulation helps to conclude the composition of unknown cathode blends by knowing the OCV potential only. Again, these papers focus on material characterisation and do not link their results to electrode characteristics or morphology.

3.5.2 Galvanostatic and potentiostatic testing methods

Different charging and discharging profiles are used to determine the characteristics of materials or full cells. Discharging profiles from different current rates, for example, give an indication about transport and conductivity characteristics within the battery. Most papers introducing a new battery material or stating improved battery performance show these kind of rate tests. Figure 3.6 shows discharge curves at four different C-rates for a lithium-ion battery. It can be seen that the extractable capacity is reduced by around 15 % at higher C-rates. Rate tests give an idea about existing processes. To investigate these in more detail, additional tests are necessary. For example, characteristics such as diffusion coefficients are important as they give information about the transport limitations within electrodes. Suthar et al. [149] and Smekens et al. [150] investigate the correlation of porosity and usable capacity. Their mathematical models are based on Newman's diffusion model for lithium-ion electrodes and include electronic and ionic diffusion within the electrolyte and the solid phase [151, 152]. Whereas the approach by Suthar et al. is mathematical only, Smekens et al. validate their model using composite electrodes with different densities and correlate density to usable capacity at different C-rates. Nevertheless, this approach is based on non-aged cells only and the influence of the SoH is not considered. Furthermore, they link the reduced capacities to the properties of the electrodes, but do not bridge these results to material characteristics such as low conductivity of active materials or surface layer formation. Besides, the given capacity values are average values based on charge and discharge. To investigate diffusion coefficients depending on the SoC, the most common techniques are GITT, PITT and EIS. These techniques are discussed within the following sections.

3.5.3 GITT, PITT and EPS

Intermittent Titration Techniques, such as PITT and GITT, and EPS are powerful techniques to investigate material and cell behaviour related to the SoC of electrodes and batteries, respectively. These techniques can be used to calculate diffusion coefficients pointing out

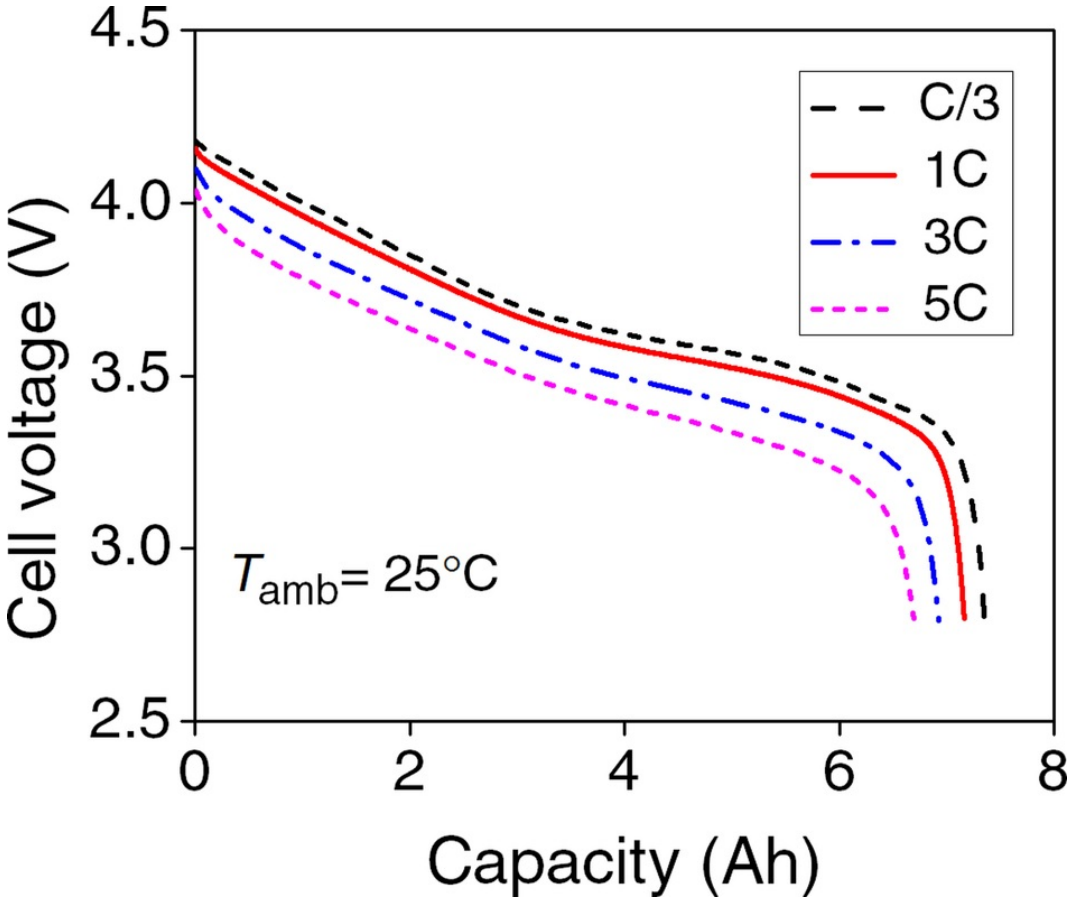

Figure 3.6: Example for different lithium-ion cell discharge curves $LiNi_{0.5}Co_{0.2}Mn_{0.3}O_2$ versus graphite at various C-rates at room temperature (published in Wang et al. [148]).

limitations of inner processes and kinetics as mentioned in Chapter 2.1.2. Furthermore, the generated data provides information about 1-, 2- or 3-dimensional ion movement, when calculated on material level and crystal structure only. A full understanding of SoC and SoH related diffusion coefficients can help to stabilise reaction processes and change the way of charging and discharging procedures.

Most papers present diffusion coefficients for a single charge and/or discharge to show changes of material properties within lithiation or sodiation, respectively, or stating an average value only. However, it has to be considered that the calculated diffusion coefficients are apparent diffusion coefficients as they are influenced by battery characteristics, such as electrode additives, electrolyte, and porosity. These apparent diffusion coefficients depend on electrode characteristics and changes due to continuous cycling are likely. Therefore, the published characteristics are only a snapshot in cycle life of the battery.[29, 153] The described experiments by Li et al. [29] and Zheng et al. [153] are based on a standard

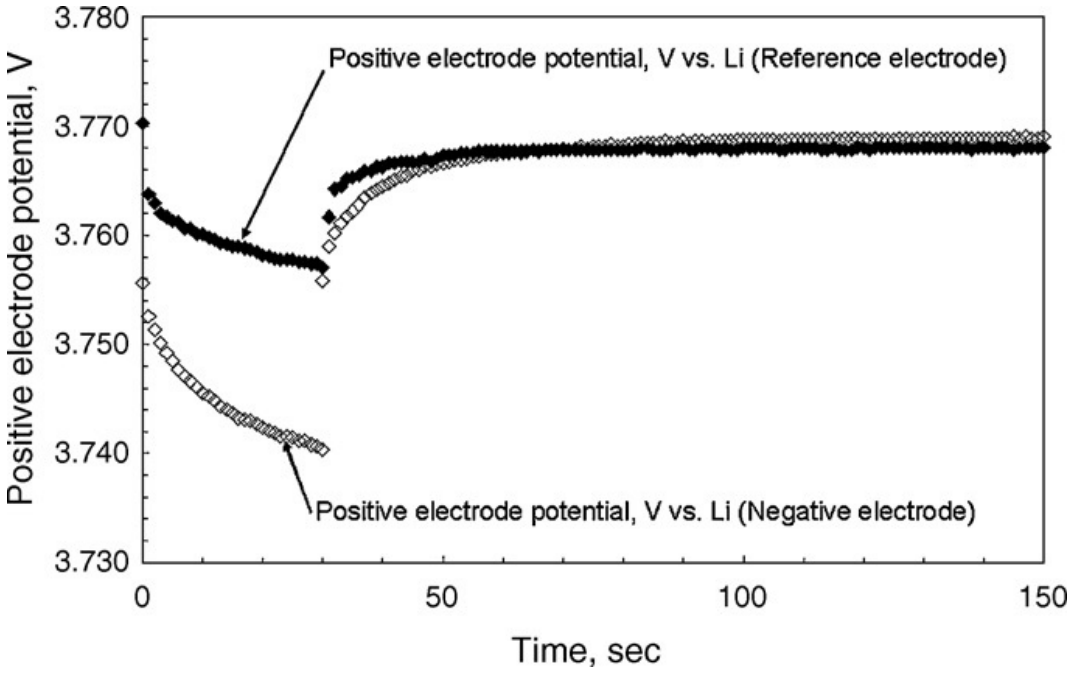

Figure 3.7: Typical GITT voltage trace of the working vs. counter electrode and working vs. reference electrode. A 30 s constant current discharge pulse is applied to the cell, followed by a long relaxation period [30].

2-electrode coin cell set-up and therefore the data is influenced by counter electrode contributions. The importance of a 3-electrode set-up for accurate data generation is given by Dees et al. [30] and was mentioned earlier. Dees et al. [30] perform GITT measurements to validate a model for lithium-ion diffusion in porous electrodes. Their experiments show clearly deviation between the working electrode potential measured via the reference electrode compared and the cell potential while using lithium metal as counter and reference electrode (see Figure 3.7). Furthermore, parameter settings are crucial to generate reliable data. To reach steady-state during OCV steps, the choice of the correct length of the charging/discharging and OCV step is important. By the end of the OCV step, the potential has to be in steady-state to assure a correct starting point for the following current/potential step. The duration of the current step is important as it has to be long enough to not only reverse polarity of the electrochemical double-layer, but also have some true charging/discharging processes happening.[33] For these reasons, comparison of results with published values has to be done with caution, as current density and OCV duration might differ between publications. However, to accredit these effects to any physical effect or morphology change, electrochemical testing needs to be done on modified electrodes and linked to physical characterisation as done by Bommier et al. [92] on HC anodes for sodium-ion batteries. Their

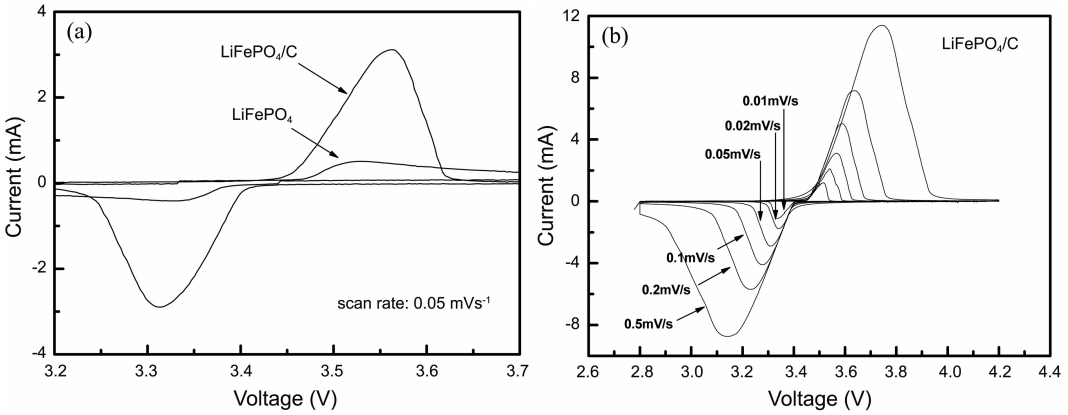

Figure 3.8: Cyclic voltamogramms of a) bare $LiFePO_4$ and $LiFePO_4$/C at a scan rate of 0.05 $mV \cdot s^{-1}$ and b) the $LiFePO_4$/C with various scan rates [155].

results indicate a main contribution of electrolyte and metallic sodium on the decreasing effects of apparent diffusion coefficients. However, their experiments seem to be performed in a 2-electrode arrangement, so changes within the diffusive profile cannot be linked to material or electrode properties. Therefore, a combination of electrochemical and physical investigation to assign these effects to changes in physical properties such as porosity or adhesion is necessary. This approach cannot be found in literature at present and will be part of this Ph. D. project.

3.5.4 CV

CV is one of the main electrochemical techniques to analyse chemical reactions and is widely used to investigate reduction and oxidation processes and phase transitions within the material. Furthermore, the reversibility and stability of these reactions can be determined. In case of reversible reactions, diffusion coefficients can be calculated.

Franger, Bourbon, and Le Cras [154] and Park et al. [155] show CV studies on LFP. Both publications show reversible processes, which enables diffusion coefficient calculations. Furthermore, Park et al. evaluate the difference of bare $LiFePO_4$ and carbon coated $LiFePO_4$/C. Their experiments illustrate the improved kinetics of carbon coated $LiFePO_4$/C as seen in Figure 3.8 a. Their diffusion coefficient calculation is based on the semi-reversible processes shown in Figure 3.8 b. Besides, CV is a common technique to investigate surface layer and SEI formation. Besides stability studies, influences of additives and scan rates on surface layers have been determined by Wang et al. [67] and Wu and Bennett [156].

A good summarising article comparing the elctrochemistry of lithium and sodium ion technology is given by De La Llave et al. [157]. In Figure 3.9 a comparison of lithium-ion

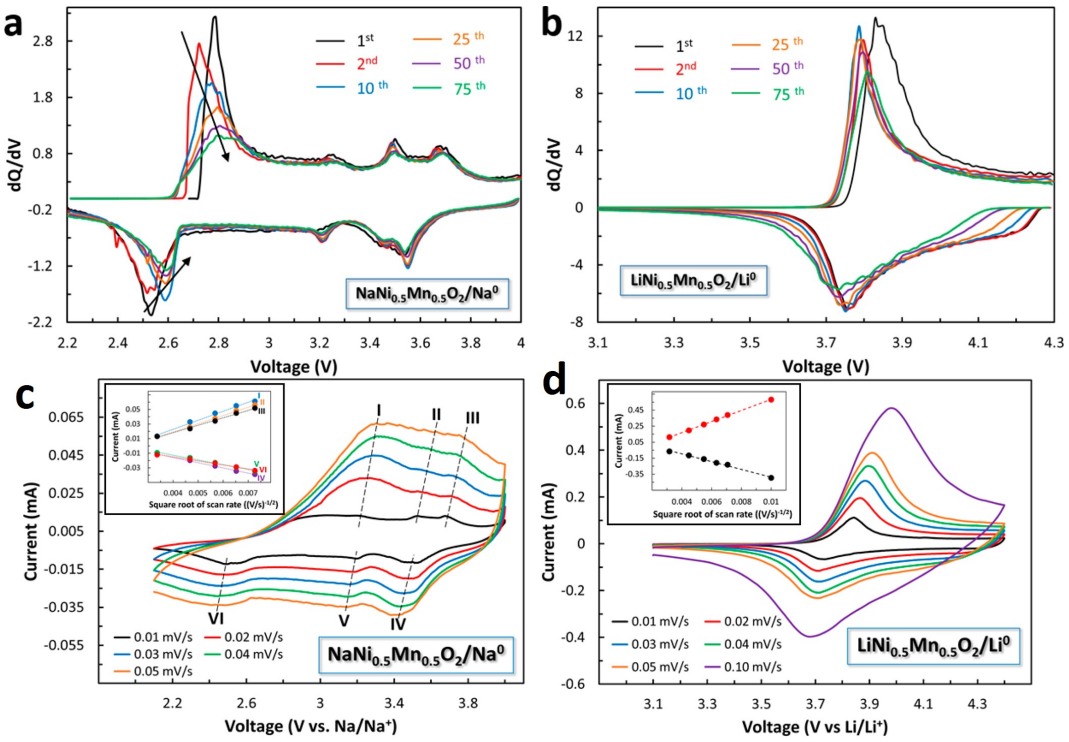

Figure 3.9: Comparison of electrochemical performance of cathodes in half cells. $\frac{dQ}{dV} vs. E$ (voltage profile derivatives) at 0.1 C for sodium and lithium-ion materials . Cyclic voltammogram for a a) sodium-ion cathodes compared to b) a lithium-ion cathode; cyclic voltammograms at different scan rates c) for a sodium-ion cathode; d) for a lithium-ion cathode; Inset: maximum peak currents versus the square root of the scan rate. Diffusion coefficients calculated from the slope of the linear curves thus obtained [157].

and sodium-ion kinetics using potentiostatic and CV techniques is shown.[157] The upper graphs show the voltage profile derivatives at different states of ageing, whereas the graphs c and d display CV curves at different scan rates for a lithium and a sodium-ion cathode material, respectively. To be able to calculate diffusion coefficients from CV data, red-ox reactions have to be reversible. Detailed information about how to prove the fulfilment of requirements for reversibility or semi-reversibility are given in Section 2.1.3. De La Llave et al. [157] point out faster kinetics for lithium-ion batteries and irreversible fast degradation processes for sodium-ion batteries. The graphs show an obvious irreversible red-ox reaction at around 2.7 V for sodium-ion batteries 3.9 (a). Hence, De La Llave et al. calculate diffusion coefficients based on following red-ox reactions shown in Figure 3.9 c and d. Due to the low resolution of current and voltages axes the quotient of anodic and cathodic current density cannot be determined and therefore, an evidence of full reversibility cannot be given by the pictured cyclic voltamogramms.

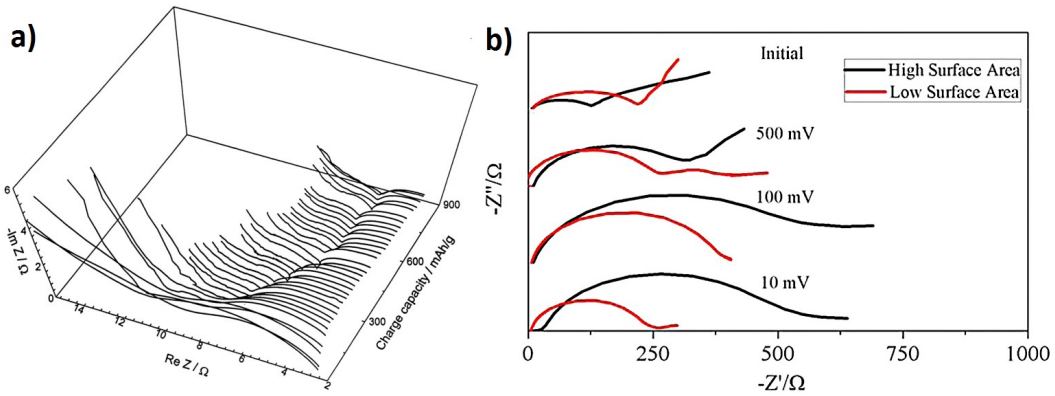

Figure 3.10: Nyquist plots for a) graphite at different degrees of lithium intercalation levels for initial cycling at 25 °C; b) comparison of high (1410 m^2 g^{-1}) and low (24 m^2 g^{-1}) surface area carbon materials at various stages during the first discharge.[163]

3.5.5 EIS

Within the last 20 years a lot of work was done to set-up a suitable model to describe the processes in lithium-ion electrodes. The group of John Newman pioneered within this area and publications by Doyle and Newman laid the foundation for subsequent work.[151, 152] An improved version of the equivalent circuit based on these models was published by Meyers et al. by adding an additional interface to the model to simulate surface layer formation.[158] Based on this model, density functional theory (DFT) can be used to study composition of surface layers and their electrochemical and mechanical properties.[159, 160, 161, 162] However, generation of reliable data is difficult. Besides the influence of different grades of porosity, electrode properties change within cycling and therefore affect the electrochemical properties as well. Among others, Wang, Appleby, and Little [39] investigated the resistance of the SEI under different temperature conditions on graphite electrodes for lithium-ion batteries. The dependency of the impedance on the SoC can be seen in Figure 3.10 a. 2-electrode half-cell studies on HC for sodium-ion batteries show the same effect. Bommier et al. [163] showed a change of impedance within the first cycle. Furthermore, they investigated the contribution of the surface area towards SEI formation and its negative effects on kinetics (Figure 3.10 b). Bommier et al. linked EIS generated data to electrode features. But long-term EIS measurements on continued cycled electrodes have yet to be explored. These kind of experiments might help to find out which ageing effect are influencing the inner resistance of the cell with time. The gained knowledge can help to create better equivalent circuit models to optimise processing and cycling parameters of lithium and sodium-ion batteries.

3.6 Physical characterisation

There is a wide range of possible physical characterisation techniques for electrodes. These methods can be used with different experimental set-ups and parameters to maximise the outcome of the investigation. Due to the large number of possible methods, this chapter concentrates on widely used techniques only, such as:

- Microscopy, e.g. Atomic Force Microscopy (AFM), Electrochemical AFM (EC-AFM), SEM also in combination with EDX.
- 3D X-ray CT.
- Porosity measurements using e.g. BET or mercury porosimetry.
- Spectroscopy, such as Raman, X-ray diffraction (XRD), X-ray photoelectron spectroscopy (XPS), Nuclear Magnetic Resonance (NMR) spectroscopy, and high energy synchrotron spectroscopy[1].

Techniques such as SEM, AFM, Raman spectroscopy, and XRD are fast and easily accessible techniques commonly applied in publications. Other techniques have high acquisition costs or restricted access, e.g. using high energy synchrotron X-rays. Whereas electrochemical measurements are done in a sealed cell set-up, physical characterisation can be invasive and/or non-invasive, and measurements can be done ex-situ, in-situ, or in-operando. This differentiation is important as a lot of electrode samples are moisture or air sensitive, so invasive or ex-situ experiments can change electrode properties while observing, which leads to misinterpretation. Therefore, special handling or transfer chambers need to be developed to perform these experiments, which introduces additional experimental complexity.

3.6.1 Microscopy

Most microscopes can be set-up for ex-situ, in-situ or in-operando experiments, depending on material properties, sample and equipment. AFM is a widely applied technique to observe surface features such as morphology and roughness. The operation can also be non-invasive, when run in non-contact mode. Breitung et al. [164] developed an EC-AFM within an argon filled glove-box to investigate SEI formation on lithium-ion anodes comprising silicon. AFM measurements by Becker et al. [165] showed a correlation of the anode potential to hight changes of silicon nano pillars. High resolution transmission electron

[1] Common techniques are for example: X-ray absorption near edge structure (XANES), X-ray emission spectroscopy (XES), X-ray fluorescence (XRF) and so on.

microscopy ((HR)TEM) is mainly used to observe volume changes due to lithium alloy formation or dendrite growth [166, 167]; whereas surface changes or inter-phases introduced by cycling or ageing are often observed by SEM.[168, 169] For in-situ SEM investigation, an ionic liquid has to be used to avoid fast evaporation of the electrolyte due to a vacuum atmosphere within the microscope chamber. Material analysis can also be done in combination with EDX. As an invasive method, focused ion beam and SEM in combination with Time-of-flight Secondary Ion Mass Spectroscopy (FIB-SEM ToF-SIMS) can be used to determine the chemical composition of surface layers and SEI.[55] Within this thesis all SEM experiments are performed ex-situ.

3.6.2 Porosity measurements

Measuring the porosity of electrodes is a challenge as electrodes consist of a highly porous network structure that spans different length scales. The structure may have a broad pore distribution as well as macro and micro-pores within the electrode itself. Some materials even have nano-pores due to agglomeration or surface texture. BET calculations (invented by Brauner, Emmett, and Teller) or mercury porosimetry can be used to measure the surface area. If the volume of the electrode is known, the porosity can be calculated. Both techniques are ex-situ and invasive methods. BET are performed by measuring the surface area using gas physiosorption.[170] Via application of different gases and pressures, a pore distribution can be evaluated as well. For porosimetry, a non-wetting liquid (mercury) is used for intrusion into pores of the tested material. Using mercury for lithium or sodium-ion electrodes is rather difficult as mercury reacts with the aluminium current collector by forming amalgam alongside gas evolution.[171] Removing the current collector beforehand will change the total surface of the electrode. Therefore, mercury porosimetry is a valuable method to compare different electrode formulation and their influence on the porosity, but does not give any absolute values. Furthermore, both techniques record accessible pores only. A different approach is the estimation of porosity by using morphology data gained by high energy synchrotron X-ray or CT (see techniques below).[172]

3.6.3 Spectroscopy

Spectroscopy describes the interaction between matter and radiation and can be used to assay materials or investigate changes in lattice structure or oxidation state. With various kinds of radiation sources available, different measurement set-ups can be arranged. Common radiation sources are laser, X-ray or magnetic radiation, introducing interactions of

the sample material with photons, electrons or an electromagnetic field, respectively. The choice of radiation depends on the physical characteristics of the sample material.

For example, Raman spectroscopy is a non-invasive technique and its functional principle is based on Raman scattering, where photons stimulate molecules by inelastic collision and to a virtual state. The resulting vibrations of the chemical bonds can be linked to a certain material.[173, 174] This technique is suitable for materials which allow a change of their polarisability, when being on a vibrational level. Often, infra-red spectroscopy (IR) might be an alternative, if the resulting Raman signal is too weak.[175]

In contrast, NMR is based on absorption and re-emittion of electromagnetic radiation. Depending on frequency and strength of the alternating magnetic field, nuclei absorb radiation and re-emit the energy, when their electromagnetic moment shifts back into initial state. Therefore, NMR is only suitable for paramagnetic materials. As isotopes such as ^{6}Li, ^{17}O, ^{23}Na, ^{29}Si, and others can be determined, an investigation of lithium and sodium-ion battery materials by NMR spectroscopy is possible.[61, 176]

Another method to investigate structural changes of active materials is XRD. Interference data is generated along the crystal lattice of the tested material by low or high energy electron diffraction. The effect is based on the Bragg equation

$$n\lambda = 2d\sin\theta, \tag{3.1}$$

where λ is the wavelength of the electron, d spacing between crystal layers and θ the angle of diffraction. The resulting interference peaks are unique and can be assigned to distinct materials and crystal structures. Diffraction patterns are often used to investigate the structural changes induced by air-sensitivity or cycling.[177] Furthermore, XRD techniques help to investigate structure changes and their reversibility during cycling, as done by Talaie et al. [178]. Figure 3.11 shows the results of an in-operando XRD measurement (left) and the related phase changes during cycling (right). This data helps to identify irreversible changes and indicates factors for mechanical stress, which lead to cracking and accelerated ageing effects. Neutron diffraction is based on the same principle. In contrast to X-rays, fast neutrons interact with nuclei, rather than the electron cloud of the tested material. Therefore, the resolution of neutron diffraction is much higher than XRD. To determine the elemental composition of the surface XPS can be used.

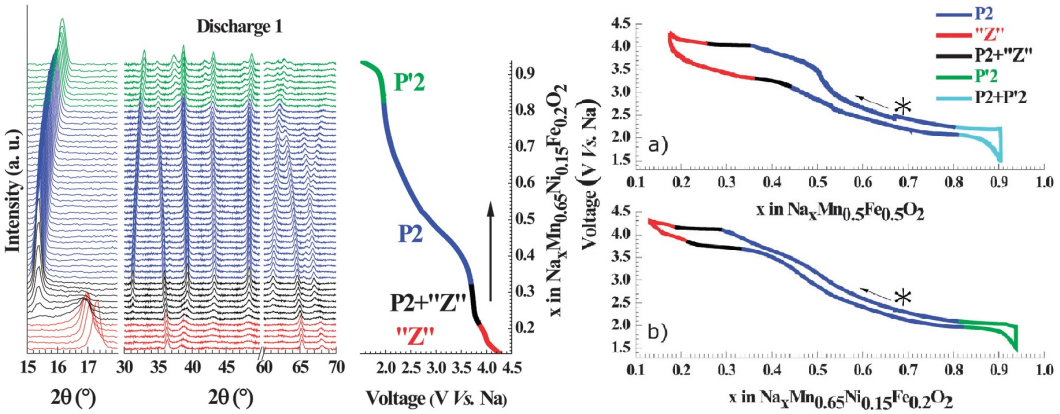

Figure 3.11: Left: Operando XRD data recorded during galvanostatic cycling at a rate of C/20 along with illustration of sodium content vs. voltage of the cell for the first discharge. Right: Phase evolution within two sodium-ion materials as a function of the sodium content during first cycle. The sign * shows the starting point of cycling.[178]

3.7 Summary and Conclusion

To compete with or replace lithium-ion batteries, a new battery technology has to provide either higher capacity or a cost benefit over its life-time. As lithium is the lightest metal on earth, has a high electrode potential and is an established technology, new technologies with higher theoretical capacities are unlikely to reach commercialisation in the near future. But considering costs, abundance and the restricted access of lithium, sodium-ion batteries might be an alternative. The best way for sodium-ion batteries to enter the market might be home or grid energy storage systems, as costs are the main factor for these applications. A comparison with commercially available systems show costings of approx. 0.10 to 0.15 US$ per kWh and cycle (as stated in Section 3.1), which are required for sodium-ion batteries to enter the market successfully. One approach to achieve this is by electrode optimisation, or more precisely by reduction of ageing processes and side reactions, respectively (Section 3.2). This prolongs the life time and usable capacity of sodium-ion batteries and will decrease the costs per kWh and per cycle. Currently, electrode optimisation is mainly based on experience and done by trial and error. And although the utilisation of electrochemical testing is well-established within the research and development community, unfortunately, these techniques are mainly used for material characterisation and less to investigate full electrode characteristics. But an understanding of material characteristics and their changes within charging/discharging and ageing is important to process composite electrodes, which compensate or minimise degradation effects. A limited number of approaches have been summarised within this review, but this field of research is still at an early stage. The gener-

ation of reliable and reproducible data is essential to investigate these correlating processes and characteristics.

Also the choice of the testing equipment is essential. Investigation of material and composite electrode effects have to be done in a 3-electrode cell set-up in order to achieve electrode-specific information. The cell set-up can be changed to e.g. smaller pouch bag cells for long term testing as they minimise effects caused by cut edges due to a higher surface area (Section 3.4, [149, 150, 163]). Furthermore, background knowledge of the techniques used is crucial to apply correct parameter settings to gain reliable and repeatable results.

Chapter 4

Methodology

This chapter summarises the experimental part of this work. Within the following sections the preparation of electrodes and their assembling in Swagelok cells, coin cells and pouch bags are described. Further, the used equipment is introduced and parameter settings for electrochemical and physical characterisation are given.

4.1 Preparation of HC anodes for sodium-ion batteries

The HC processed is a commercially available material. The commercial material was chosen to avoid any differences in material properties caused by the use of different in-house synthesised batches. Unless stated otherwise the electrodes tested comprise a commercial HC material (D_{50} particle size distribution: 9 μm), PVdF (Kynar, HSV900), and carbon black (CB, TimCal, C45) in a 90:5:5 wt. % ratio. PVdF was pre-dispersed in NMP (anhydrous, Sigma Aldrich) and used to formulate an ink aiming for a solid content of approx. 42 %. For mixing a planetary centrifugal mixer (Thinky, ARE-310) was used, adding in liquid ingredients first and then adding solid materials such as HC powder on top. The ingredients were mixed for ten minutes at 2000 rpm and subsequently for two minutes at 2200 rpm for degassing. The ink was left to cool down to room temperature and was then coated onto a carbon-coated aluminium current collector using the doctor blade method (MSK-AFA-L800BH, MTI). The blade gap was set to 250 μm. The electrodes were pre-dried using an infra-red lamp and then placed into a vacuum oven at 120°C for at least 90 minutes to remove any NMP residues. All electrodes were calendered to a porosity of approximately 35 % by placing the electrode between two metal shims before feeding through the heated rollers of a calender machine (MTI Corporation, MSK-HRP-01, temperature: 90°C). The electrode was stored in a vacuum oven at 80°C until needed and then cut into electrodes. For porosity calculation, and active surface area of the electrode, the average density of

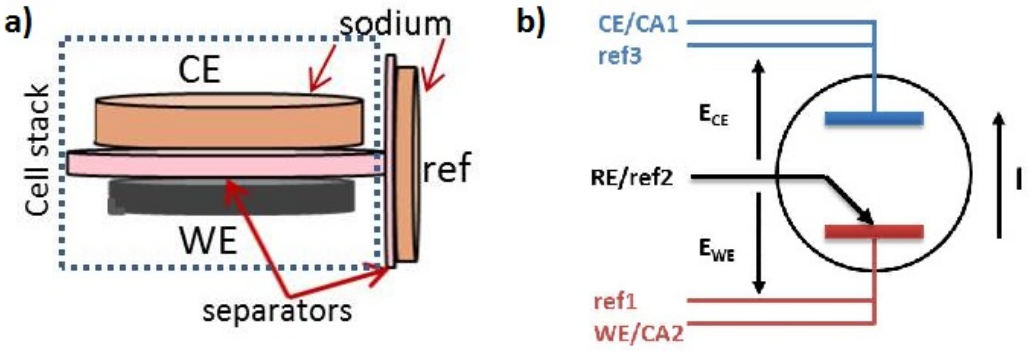

Figure 4.1: a) drawing of a standard cell stack with attached reference electrode; b) electrical connection and wiring of a 3-electrode test cell.

the composite electrode materials and the volume of the dry coating (electrode surface × thickness) were considered. Electrode thickness was measured with a micrometer gauge.

4.2 Cell set-up, assembling and optimisation

To gain reproducible and reliable data sets a well elaborated and tested experimental set-up is crucial. The following subsections give an description of the different optimisation steps for testing set-ups such as cell design, choice of electrolyte and laboratory conditions.

4.2.1 Assembling of different cell set-ups

Electrode discs were cut from the prepared electrode sheets and transferred into a glove box (argon atmosphere). For cell building, a 3-electrode cell set-up was used utilizing a Tee-union compression fitting (see Figure 3.3 in Section 3.4, test cells purchased from University of Muenster, Germany). A schematic drawing including wiring of the 3-electrode cell set-up is shown in Figure 4.1. An oil-free sodium ingot (Goodfellow) was flattened to approximately 0.5 mm thickness before 10 mm sodium discs were punched out as counter electrodes. An acceptor attachment of the 3-electrode cell was filled with sodium for reference electrode connection. A combination of one GF/A Whatman and one 20 μm PP separator (2020, Celgard) were used in the cell stack and were placed perpendicular to the cell stack for electronic insulation of the reference electrode. A total of 130 μL of a premade electrolyte containing 1 M $NaPF_6$ in a 1:1 (v) mix of EC and DEC (Kishida Chemical Co. Ltd) was used as an electrolyte to wet both separator stacks.

All cell components are shown and labelled in Figure 4.2 a. For assembly, a long steel plunger (i), with mounted round (B), and cone shaped plastic ferrule (A), was inserted into the Swagelok Tee-union and aligned to the middle of the Swagelok chamber (see bottom left

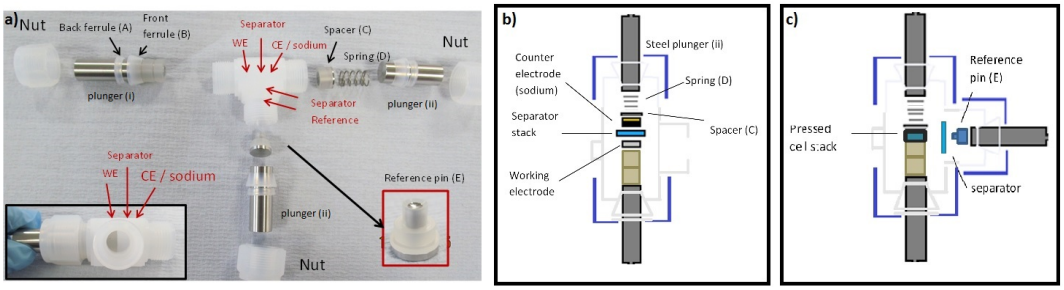

Figure 4.2: Assembly of a 3-electrode Swagelok cell. a) Picture of all cell parts; schematic drawing of b) a cell stack assemby; c) reference attachment.

inset in Figure 4.2 a). The nut was screwed hand tight on the cap end and turned by another quarter using a spanner to ensure an air tight seal. The WE (anode or cathode material) was then loaded facing up into the main chamber and covered by a separator stack consisting of two glass fibre separators[1] (Sigma, GF/A, thickness 0.26 mm)s. 100 μl electrolyte were filled in to wet the cell stack[2]. Additionally 30 μl electrolyte were added to wet the reference separator. Then the CE or sodium metal electrode was placed on top facing towards the cell stack (see Figure 4.2 b). Finally, a spacer (C) and a spring (D) were inserted. The cell stack was pressed and closed by a second plunger including ferrules and nut (ii). To connect the reference, a separator was attached to the cell stack and wetted with electrolyte. The sodium filled reference pin (E) and a third metal plunger (also type ii) with ferrules were inserted, tightened, and closed using a nut (see Figure 4.2 c).

Type 2032 coin cells were built using standard stainless steel housings, 13 mm cathode discs, 14 mm anode discs, glass fibre separators and a sufficient amount of electrolyte to wet electrodes and separator. Cells were crimped using a MTI Hydraulic Crimper MSK-110 and a crimping pressure of approx. 65 $kg{\cdot}cm^{-2}$.

Pouch bags were assembled using 30×30 mm single side coated anodes, 28×28 mm single side coated cathodes and a PP separator. Anodes were chosen to be larger than cathodes to ensure a homogeneous current density on cathode side and to avoid any sodium plating on the anode edges. The cathode was placed into a separator pouch and the anode was aligned. To hold the anode in place a small amount of Kapton tape was used to secure of the position within the cell stack. The cell stack was placed in a laminated aluminium foil pouch and filled with 400 μl electrolyte. The cell was left to soak for at least an hour

[1] As the separator affects cell performance, different separator set-ups might be necessary for high energy or high power performance test

[2] The amount of electrolyte depends on electrode and separator thickness.

before being sealed using a vacuum sealer. The balance of full cells was aimed at 5 % anode excess based on first theoretical charge capacity.

4.2.2 Influence of cell design on stability of long-term OCV

Long-term OCV measurements were performed to investigate material characteristics and cell set-up reliability. Long-term stability of the cell set-up and the material itself is important to ensure accurate data analysis. Also, material characteristics have to be determined first, to link changes in composite electrode properties to substitutions made. Tests were carried out in charged and discharged states for standard HC anodes. Half and full cells were built comprising a HC anode, sodium metal and a sodium-ion intercalation cathode, respectively. Furthermore, experiments at elevated temperatures were conducted for accelerated testing. To investigate the influence of the cell design in more detail, 2- and 3-electrode Swagelok cell data was compared to results gained by using coin cell and pouch bag designs. The cells were assembled as described in Chapter 4.2 using 1 M $NaPF_6$ ethylene carbonate (EC) and diethylene carbonate (DEC) electrolyte (ratio 1 : 1 (v)) as electrolyte (premixed electrolyte provided by Kishida Chemicals).To ensure equal conditions for all cells, three formation cycles were performed at room temperature before the cells were set on OCV. Figure 4.3 summarises the results of the conducted long term OCV experiments.

Figure 4.3 a shows a comparison of full and half cell data, rested at room and accelerated temperature in a 3-electrode arrangement. The HC electrodes were cycled versus a sodium metal CE (half cell configuration) and a sodium intercalation cathode material (full cell configuration), respectively. Different CE were chosen to investigate the influence of the sodium metal CE onto the HC WE potential. The shown HC profiles were measured versus the sodium metal reference electrode to minimise counter electrode contributions. In general, HC electrodes are fully desodiated when freshly assembled. As there is no current flow to favour either a forward or backward reaction, an equilibrium on the electrode-electrolyte inter-phase is established (Bulter-Volmer: α=0.5) resulting in a stable potential. Hence, the straight green line of the un-cycled HC electrode can be seen as a base line as no reactions were induced.

The other displayed profiles were recorded on cells being cycled and desodiated up to 1.5 V in full and half cells configuration, before being left at OCV at either RT or accelerated temperature of 60°C. All profiles show a potential increase up to approx 2.6 V to the discharged HC state. The blue and black profiles are both related to full cell data, but

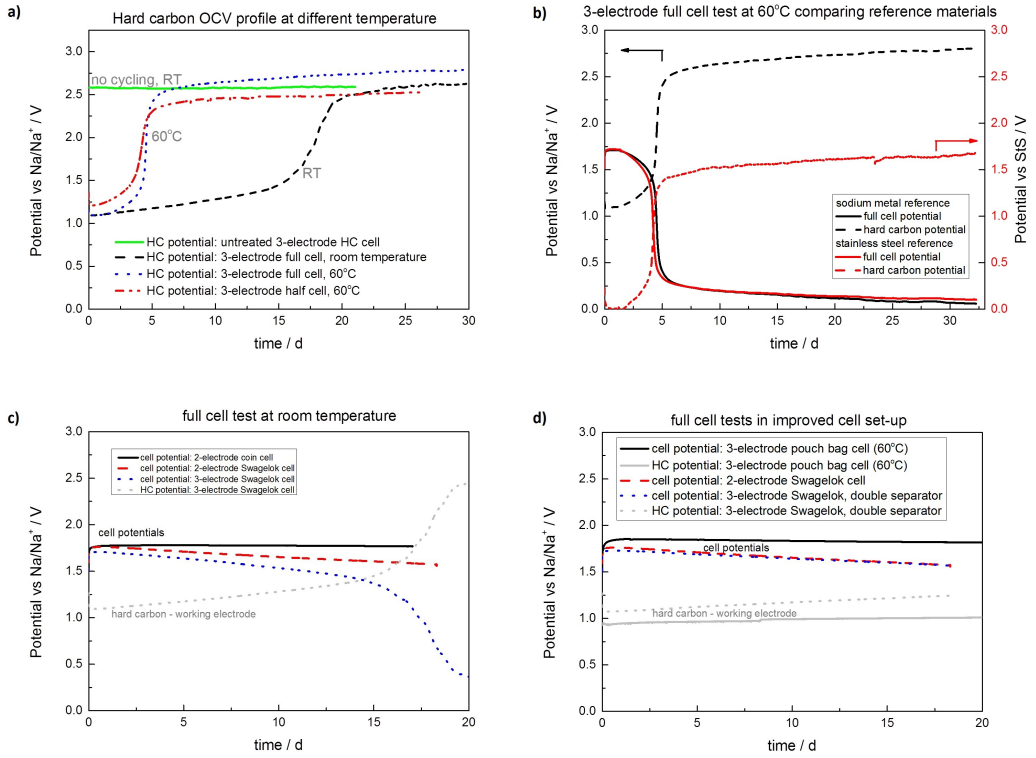

Figure 4.3: OCV profiles of full cells and HC electrodes; a) OCV profiles observed at RT and at 60°C compared to an untreated HC electrode; b) OCV profiles measured versus two different reference materials: stainless steel and sodium metal; c) OCV profile of full cells and HC electrodes in different cell designs; d) OCV profile of full cells and HC electrodes using improved cell designs.

differ in environmental temperature. It can be seen, that the voltage change is speeded-up at accelerated temperature. As the same effect appears in half cells (red line), this effect cannot be caused by the sodium metal CE.

The observed potential increase may be caused by dissolution of sodium from the HC electrode into the electrolyte or by internal short-circuits. Further, the slightly higher desodiation potential of the blue profile might be induced by a potential drift of an unstable reference potential or by oxidation of the HC at higher voltages resulting in a change of the OCV.

These hypotheses were investigated by replacing the sodium metal reference electrode with a stainless steel reference. The experiment was performed at accelerated temperature to shorten measurement time. Figure 4.3 b shows the comparison of these two different reference materials. Again, both profiles were measured versus the reference electrode; the data based on a sodium metal reference is shown in black and the potential is stated on the

left y-axis. The data gained by using a stainless steel is shown in red and numbers are given on the right y-axis. The self-discharging effect of the displayed cells is identical, as seen in the shape of the full cell potential (straight lines). The difference between the HC profiles is caused by the different standard potential of stainless steel differs from sodium. The potential of sodium versus the standard hydrogen electrode (SHE) is -2.71 V versus SHE. The reference pin is made of passivated stainless steel, type 316. The standard potential versus sodium was not investigated. However, the HC potential measured versus the stainless steel reference seem shifted by 1.2 V towards the sodium reference. As shape and trend of the profiles are identical a similar reference behaviour can be assumed. This implies no influence of the (sodium metal) reference electrode to the OCV behaviour.

To provide evidence for this hypothesis, 2-electrode full-cells were assembled devoid of any sodium metal or reference set-up. Therefore, a 2-electrode coin cell and a 2-electrode Swagelok configuration were chosen. Figure 4.3 c compares the data gained by these two different full-cell set-ups (coin cell - straight black, Swagelok - dashed red) to previously in Figure 4.3 b shown 3-electrode full-cell data (dotted). The data of the 3-electrode full-cell is split up into two profiles. The full cell profile is shown in blue, the HC CE profile is shown in grey. The graph shows a stable coin cell potential whereas the potentials of both Swagelok cell configurations decrease slightly. However, the potential decrease for the 2-electrode Swagelok cell is less pronounced compared to the 3-electrode one.

The differences between these two 2-electrode set-ups (Swagelok vs coin cell) are the amount of dead volume within the housing, clamping pressure, and air and light tightness. The differences between 2- and 3-electrode Swagelok set-up are the absence of a reference electrode within the 2-electrode configuration and the amount of dead volume within the housings. Further, misplacing or piercing the reference separator during assembling or cycling causes leakage currents or internal short-circuits. This indicates cell design issues rather than effects caused by the presence of metallic sodium.

To investigate the differences between 2- and 3-electrode Swagelok cells and to test the hypothesis of leakage currents via the reference, a pouch bag cell containing a reference electrode was designed. Also, the 3-electrode Swagelok set-up was improved by replacing the thin PP separator by a double glass fibre separator. Figure 4.3 d shows the voltage profiles of the HC working electrodes (grey) and cell potentials of the tested cells. The performance of the 3-electrode Swagelok cell with double glass fibre separator is identical

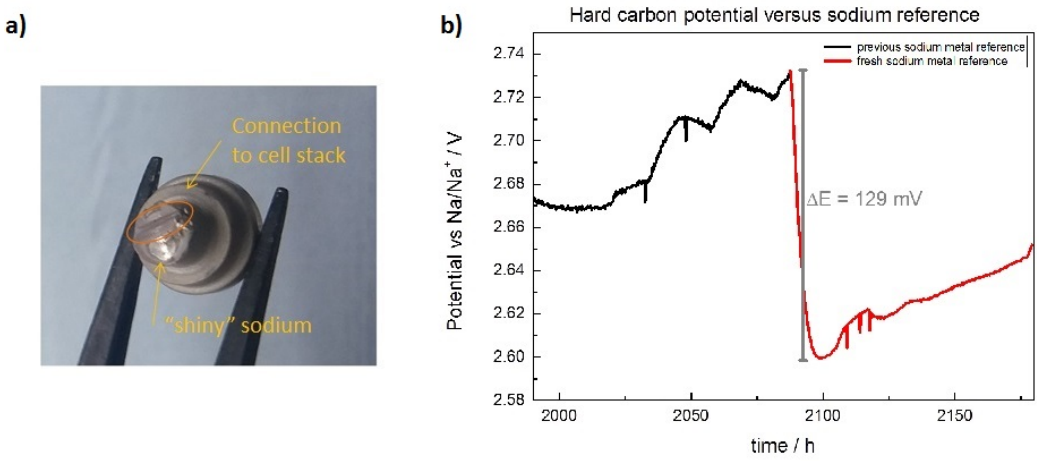

Figure 4.4: Picture of an used sodium metal reference showing darker sodium metal around the imprint of the cell stack connection and shiny parts of metallic sodium where no reference currents were present.

to the 2-electrode Swagelok configureation. This supports the hypothesis based on leakage currents and short-circuits via the reference electrode. However, HC and full-cell profiles seem to be less stable in a Swagelok cell set-up compared to a 3-electrode pouch bag (graph d, black) or a 2-electrode coin cell (graph c, black). As mentioned earlier, variations between these different designs are: dead volume, clamping pressure, light and air tightness, and the use of different cell stack separators. The effect cannot be caused by dead volume, as pouch bags have a larger dead volume than Swagelok cells. Also, all cells were stored in closed cabinets, so translucency cannot cause these differences in behaviour either. Within the cell stack of pouch bags, a thin polypropylene separator is used, whereas the coin cell set-up and Swagelok design is based on glass fibre separators. However, separators cannot be the issue as the conducted pouch bag tests and coin cell test look similar. More difficult is the determination of air tightness and clamping pressure of the cell. As Swagelok parts are made for gas pipes and the assembling was followed instructions given by Swagelok, air tightness is assumed. To obtain certainty, further experiments have to be performed, varying the clamping pressure in Swagelok, coin or pouch bag cells to determine any differences in OCV behaviour and self-discharge, respectively. An insufficient clamping pressure might lead to gas trapping between separators and electrodes and an inhomogeneous current density, which results in local overcharging/overdischarging and benefits side reactions.

Besides the difference in OCV behaviour, the maximum OCV potential reaches different values, as mentioned above and seen in Figure 4.3 a. To investigate these differences the

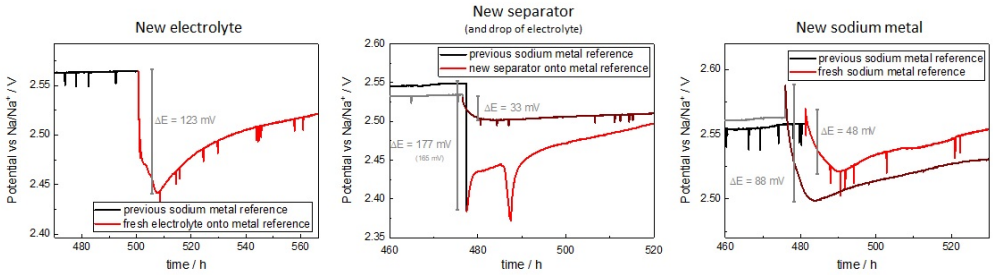

Figure 4.5: HC potential versus sodium reference before and after (a) addition of new electrolyte, (b) replacement of reference separator, and (c) new sodium metal reference.

sodium metal reference acceptor and separator of a test cell were renewed. The new separator was wet with 30 μl of fresh electrolyte to ensure ionic connection to the reference. Then the cell was reassembled and put back on test. Figure 4.4 a shows a picture of the removed sodium metal reference. A clear imprint of the cell stack can be seen on the sodium surface. Also, the surface of the sodium metal within this region appears darker and matt. The area of the sodium metal, which was compressed to the plunger and had no contact to the cell stack, still appears to be shiny. Figure 4.4 b shows the OCV profile of the test cell before and after replacing the sodium metal reference and a voltage drop of around 130 mV can be determined. The voltage drop might be caused by the sodium replacement or by the addition of fresh electrolyte. To investigate the influence of fresh electrolyte, further experiments were done.

Figure 4.5 shows the HC versus sodium metal reference potential before and after partial replacements of the reference components during long term OCV measurements. The highest impact can be seen when fresh electrolyte is added to the cell or the separator is replaced. However, wetting of the new separator is needed for ionic conductivity during the replacement process. Therefore the effect seen in Figure 4.5 (b) might be induced by the extra electrolyte addition. Nonetheless, interestingly also the replacement of the sodium metal acceptor also influences the voltage profile. This indicates (in combination with the de-coloration of the sodium metal seen in Figure 4.4 (a)) a surface layer formation causing a polarisation on the sodium metal reference although no currents present. Consequently, the stability of sodium metal in electrolytes were tested (as described in the next section).

4.2.3 Reactivity of sodium metal to carbonates

To prove the stability of sodium within the electrolyte, fresh sodium ingots can be placed into different electrolytes and left within inert atmosphere for several days. Surface changes

can be investigated either by eye or using optical spectroscopy, if airless transfer is possible. These experiments were partly conducted and show a reaction with propylne carbonate (PC) containing electrolytes (Figure 4.6). A macroscopic change of the sodium surface was not seen, if an EC : DEC (1 : 1 (v)) electrolyte was used. Microscopic investigations were not possible due to the lack of airless transfer chambers.

The left picture in Figure 4.6 shows three vials containing sodium metal and different electrolytes. On the left 1 M $NaPF_6$ in 4 : 1 (v) PC:DEC electrolyte, in the middle sodium in 1 M $NaPF_6$ of 1 : 1 (v) EC:DEC electrolyte and on the right in 1 M $NaPF_6$ in 1 : 1 : 1 (v) of PC : EC : DEC. The sodium was stored within these vials for three weeks and the change of the electrolyte and sodium was documented in the middle and right pictures in Figure 4.6. The middle picture shows sodium in PC:EC:DEC electrolyte after three weeks; the electrolyte is still clear. The picture on the right shows the vial containing the 4:1 mix of PC : DEC electrolyte. The electrolyte was discoloured and the sodium metal showed a thick surface layer. The results of these experiments show no evidence that the

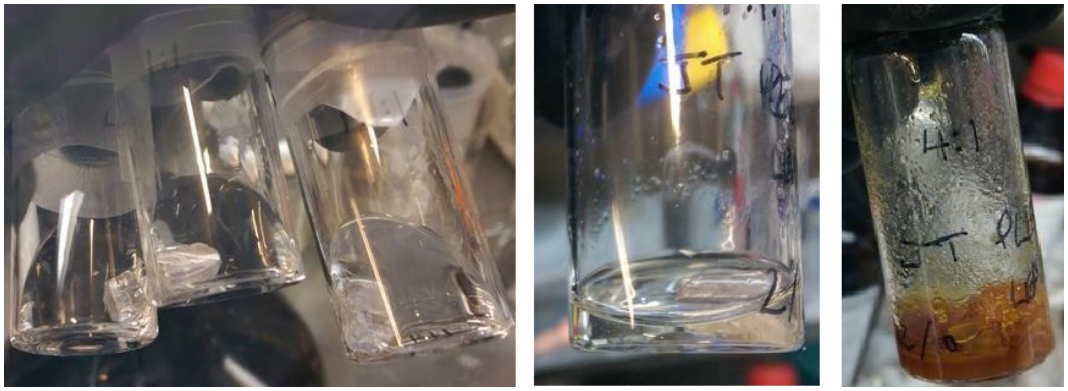

Figure 4.6: (a) Picture of sodium metal stored in three different electrolytes, initial state; (b) sodium in PC : EC : DEC after three weeks; (c) sodium in PC : DEC after three weeks.

presence of metallic sodium is influencing the full and half-cell OCV, but they reveal the importance of cell design in testing. Results gained by comparison of the HC profiles with different separator settings helped to understand the issues of cell design and to improve the cell set-up. The experiments show a reduction of self-discharge, if a thin PP separator is replaced by a glass fibre separator. In the literature, thin polypropylene (PP) separators are often used to ensure low ohmic resistance within a battery. But these thin separators cause higher self-discharge rates due to leakage currents, as shown in the results above. Therefore, electrochemical techniques, which are based on steady-state have to be done with caution to achieve reliable data.

4.2.4 Influence of the temperature on battery testing

Chemical reactions are accelerated at elevated temperatures (Arrhenius equation). Hence, it is important to state the temperature at which the electrochemical testing was conducted. The journal Joule just recently made this mandatory for battery based publication being submitted to the journal.[179] The influence of the temperature was already mentioned in Chapter 4.2.2 and shown in Figure 4.3. But also small increases in temperature also have an effect and can be observed in the collected data. Modulation in the IR drop or current densities as seen in Figure 5.3 and will be discussed in detail in Chapter 5.2 might be misleading.

Figure 4.7 shows the temperature profile for 90 days in the battery testing lab at Sharp Laboratories of Europe prior the installation of an air conditioning system. Day and night times as well as weekends can be distinguished clearly and the time stamp of the temperature amplitude coincides with the modulation of the potential in Figure 4.7. The impact

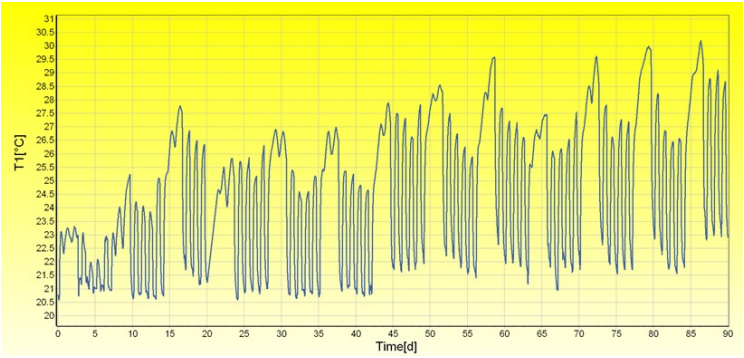

Figure 4.7: Temperature profile in battery testing lab over 90 days at Sharp Laboratories of Europe prior the installation of an air conditioning system.

can be minimised when temperature or climate chambers are used as a cell cycling environment. Likewise, a temperature-controlled laboratory with a set temperature would be sufficient. However, smaller research laboratories or universities might not have the equipment to do so. In that case stating the total testing time helps the reader to understand the published results.

4.3 Cell connection

When characterising electrodes it is important to collect true working electrode data. As mentioned earlier the contribution of the sodium metal counter electrode can be severe due to polarisation effects and surface layer formation induced by the electrolyte. The extent of

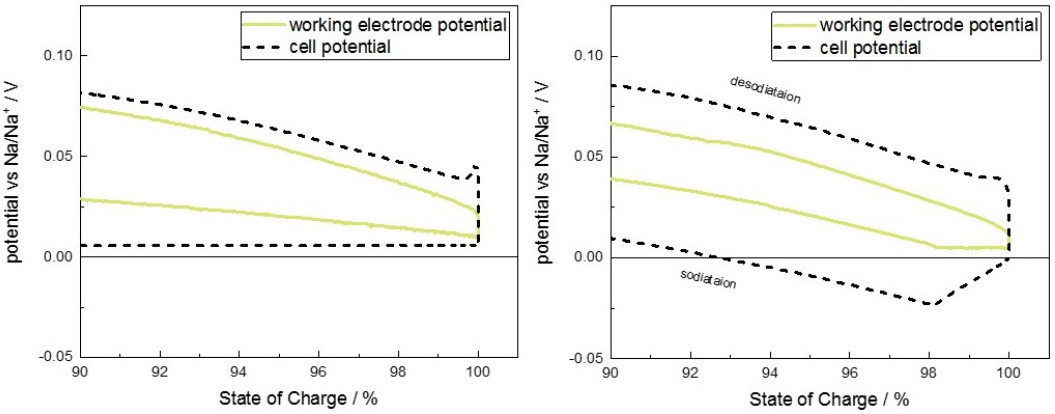

Figure 4.8: WE and cell profile of a HC composite electrode vs. Na metal in a 3-electrode arrangement. Current flow between WE and CE. Left: voltage control via cell potential; right: voltage control via WE.

the polarisation effects depend on the current applied and resulting current density, hence effects may vary during cycling with the increasing amount of sodium moss being formed. Using a three-electrode arrangement helps to decrease these kinds of side effects, when applying the current between working and counter electrode (CE) and using the potential measured between working electrode (WE) and reference electrode (RE). When programming test plans for cycling, the measured potential between WE and RE can be used as parameter for the cut-off voltage to ensure the access of the full cycling window. Figure 4.8 shows the difference in cycling when the cut-off potential is set between WE and CE (left) and WE and RE (right), respectively. In both cases a polarisation of the cell voltage (WE vs CE, dashed line) of around 20 mV can be seen at the beginning of desodiation. In both cases a constant current constant voltage (CCCV) sodiation is used. Nevertheless, using the set-up with a cut-off voltage parameter measured between WE and CE (left), the actual potential of the WE does not reach the suggested 5 mV needed for full sodiation.[89, 180] However, when using the measured potential between WE and RE as cut-off voltage condition, the overall cell voltage (potential WE and CE) becomes negative before the WE is fully sodiated due to the polarisation on the sodium metal CE. Based on these results an accurate set-up and same sodiation parameters are needed to ensure comparability between different electrodes and their physical characteristics e.g. microstructures and porosity.

4.3.1 Parameters for electrochemical characterisation

Within this thesis two different potentiostats were used to conduct electrochemical experiments. Standard charging and discharging tests as well as OCV and rate tests were done

using a BaSyTec potentiostat (CTS system, 1 μs time resolution, 0.05 μA current resolution, 0.3 mV voltage resolution). Experiments which required a higher data accuracy and resolution such as CV, GITT, and EIS were performed on a VMP3 potentiostat system (Bio-Logic). All three electrodes, CE, WE and RE, were monitored when a 3-electrode arrangement was used. All electrochemical measurements were conducted at room temperature.

4.3.1.1 Parameter settings for OCV, charge, discharge and rate test

For standard testing, a BaSyTec CTS potentiostat with reference monitoring was used and for rate testing asymmetrical cycling was conducted. A full formation cycle at 0.2 C (based on an assumed capacity of 330 mAh g^{-1}) was conducted before testing. During formation, the cell was discharged in constant current/constant voltage (CCCV) mode, with a cut-off voltage of 0.005 V and a current of 0.01 C (sodiation process). Charging was conducted using a constant current (CC) at 0.2 C up to 2.0 V (desodiation process). Some conditions were applied for subsequent cycling. For rate assessments, tests were performed by varying the desodiation current from the third cycle onwards from 0.2 C to 0.5 C, 1.0 C, 2.0 C, 5.0 C, and back to 0.2 C while keeping the same sodiation conditions (CCCV sodiation at 0.2 C with a cut-off voltage of 5 mV).

4.3.1.2 Parameter settings for CV

A VMP3 potentiostat (Bio-logics) was used for CV testing. The CV was conducted at different scan rates starting with initial three cycles at 50 $\mu V \cdot s^{-1}$, followed by three cycles at 25 $\mu V \cdot s^{-1}$, 10 $\mu V \cdot s^{-1}$, and again 50 $\mu V \cdot s^{-1}$. Anodes were tested between 0.005 and 1.5 V.

4.3.1.3 Parameter settings for GITT

The tests were conducted using a VMP3 potentiostat system (Bio-Logic). To perform the GITT measurements, a current equivalent to 0.2 C was applied for five minutes, followed by an open-circuit voltage (OCV) step with a termination condition based on a working electrode potential variation of $\Delta E_{WE} \leq 0.001\,mV \cdot s^{-1}$. The potential termination parameter is essential to ensure a quasi-equilibrium state of the electrode as ongoing diffusion processes and polarization affect the results.[123] Subsequent cycling was performed using identical parameters as for the formation cycle.

4.3.1.4 Parameter settings for EIS

The EIS measurements using a BioLogic VMP3 system were conducted at 16 evenly spread potential steps within sodiation and desodiation, respectively. Each potential step was fol-

lowed by a 150-minute OCV step to ensure full relaxation of the electrode to reach the equilibrium state before conducting the EIS measurement. For EIS a spectrum of 52 frequencies between 50 mHz and 1000 kHz were chosen, applying an amplitude of 2 mV and recording the average impedance based on three measurements per frequency. A low amplitude was chosen to minimize the contributions of SoC changes within the low plateau region. Subsequent cycling was performed using identical parameters as for the formation cycle.

4.3.1.5 Parameter settings for EPS

EPS using a BioLogic VMP3 system was conducted in 10 mV potential steps monitoring the current decay. Termination condition of each voltage step was a minimum current I_{min} of 0.01 C. A sufficient low cut-off current I_{min} is essential as it ensures a state close to the equilibrium and avoids any influence of polarization effects, as stated earlier. After triggering the termination condition, the working electrode potential was raised by another 10 mV relative to the previous starting value. Subsequent cycling was performed using identical parameters as for the formation cycle.

4.4 Sample preparations for SEM

For SEM and EDS imaging, an uncycled (identical batch as used for electrochemical characterization) and a cycled electrodes were used. The cells were charged to 1.75 V before being dismantled under inert atmosphere and transferred via an air-less transfer chamber or glove bag to the SEM. For detailed cross-section measurements an FEI Scios DualBeam system accessed at the Advanced Material Manufacturing Centre in Warwick was used. Batch testing was done using an Ion beam mill for electrode cutting and and SEM-EDX machine at EIL.

Often electrodes are washed using dimethylcarbonate (DMC) to remove any conducting salt residues. The here determined electrodes were scanned as cycled as the contact with DMC might also change the surface layer and might remove the SEI partly. For the SEM-FIB experiments at Warwick University an 1 μm thick layer of platinum was deposited on the surface to enable even material removal during FIB slicing. First, material in U-shape was removed to obtain a cuboid of material for conducting FIB slicing with an Auto Slice and View Software (Figure A.11). The dimensions of the cuboid were set to 32×30×15 μm for the uncycled and 28×29×15 μm for the cycled sample, respectively. Next, slices with

a thickness of 50 nm were removed using an ion beam current of 5 nA at an accelerating voltage of 30 kV. The resolution of the images taken was set to 1536×1024 pixels.

Chapter 5

The Performance of HC in a Sodium Ion Battery and Influence of the Sodium Metal in Observed Properties

This chapter lays the foundation for cell assembling and testing as conducted in this thesis. The investigation includes the electrochemical testing protocols for a HC sodium ion anode material, in respect of charge and discharge behaviour, ageing and discusses the use of a sodium metal counter electrode with respect to the material and cell stability during the electrochemical testing. Some of the results present in this Chapter were published in ECS transactions.[123]

5.1 Introduction

Typically, in a sodium ion cell, HC anodes are partnered with sodium containing transition metal oxides or polyanions.[112, 181] The HC anode offers specific capacities of 250 to 300 mAh g^{-1} with good cycle life, and there are many previous reports on the manufacture and testing of these HC materials.[20, 83, 89] To test the performance of HCs the electrochemical testing is often performed in a standard 2-electrode set-up, e.g. compression fitting ('Swagelok') cells, coin cells or similar using a sodium metal CE. We show that the performance of the HC is extremely sensitive to processing conditions and testing methods.[182] In particular, the electrochemical performance of the HC WE and a sodium metal CE with the use of 3-electrode cells are described and the influence that the sodium metal CE may have upon 2-electrode testing is discussed. Rate tests are utilised to investigate the specific properties of the HC in more detail and to eliminate any contribution from the CE. For some of the tests, two different electrolytes were chosen to compare their influence on

polarisation effects and in particular to investigate the influence of PC on metallic sodium. In literature, PC is stated as more unstable and responsible for enhanced side reactions on sodium [180] (see also Figure 4.6 in Chapter 4).

5.2 Electrochemical analysis

The electrode preparation and cell building are conducted as described in Chapter 4. Additionally to the 1 M $NaPF_6$ EC : DEC (1 : 1, wt.%) electrolyte, also 1 M $NaPF_6$ in PC : EC : DEC (1 : 1 : 1, wt.%) was used and the formation cycle was done at 0.1 C for lower polarisation effects. In this cell set-up, the voltage and current are controlled between WE and CE electrode, whereas the reference electrode is for monitoring only.

5.2.1 Charge and discharge behaviour

Figure 5.1 shows the first charge and discharge, sodiation and desodiation of the HC, respectively. A specific capacity of approx. 320 mAh g^{-1} is observed upon sodiation and 270 mAh g^{-1} upon desodiation at a 0.1 C-rate. The solid lines show the cell potential, which are typical charge and discharge curves versus gravimetric desodiation capacities of HC, as seen in standard 2-electrode set-ups and published in literature.[89, 91, 180] The WE potential (dashed) shows a slightly lower hysteresis compared to the cell potential. This mismatch of cell and WE potential is more pronounced during sodiation (inset in Figure 5.1 (a)). Figure 5.1 (b) shows the change of the sodium metal CE upon the same first cycle, as seen above. At the beginning of the HC sodiation (sodium stripping) the potential drops down immediately from around 0.4 V to 0.1 V and decreases slightly to 4 mV until the end of the HC sodiation. During the charging process (sodium plating) and during the first 5 mAh g^{-1} of passed capacity, the voltage is seen to immediately increase, but then fall just as quickly before stabilising at around –6 mV versus Na/Na^+. The sodiation limitation (CCCV to 5 mV and 0.01 C) is not reached by the HC, due to the polarisation effects of the CE.

5.2.2 Rate performance

Figures 5.2 (a) and (b) show the desodiation potentials of the cell, WE and CE at different C-rates, respectively. In Figure 5.2 (a) an increase in total polarisation as well as an increase in mismatch of cell and WE potential can be seen with higher C-rates. Whereas the polarisation for the cell potential increases by 300 mV compared to the potential at 0.1 C, the difference between 0.1 C and 5 C is slightly less for the WE (250 mV). Furthermore, the difference between cell and WE potential is around 50 mV during most parts of the sodia-

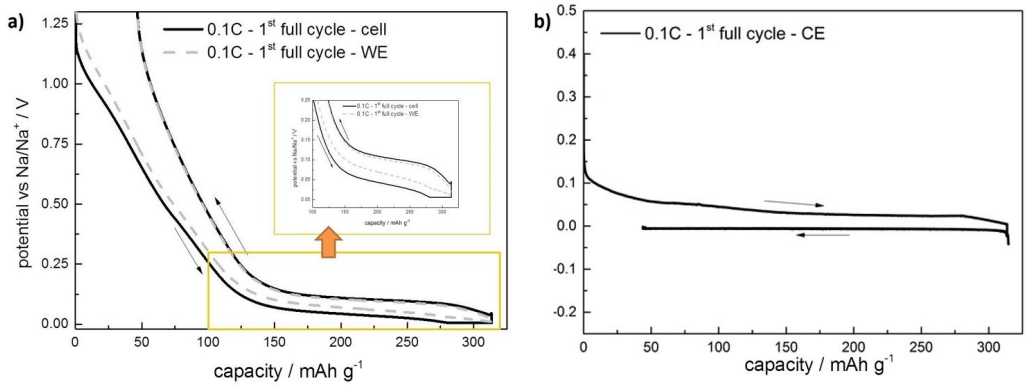

Figure 5.1: Voltage profile of a HC electrode versus sodium metal in a 3-electrode arrangement. (a) First full cycle at 0.1 C. Solid: cell potential, dashed: WE potential. The inset is a blow-up of the lower potential region. (b) Profile of the sodium metal CE for the first full cycle of HC

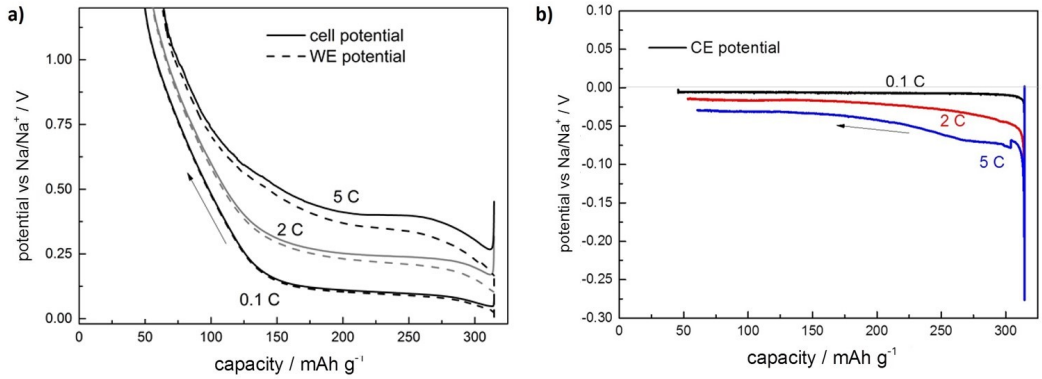

Figure 5.2: Voltage profile of a HC electrode vs. sodium metal in a 3-electrode arrangement at different C-rates. (a) Desodiation profiles of the cell (solid) and WE (dashed) potential for 0.1, 2 and 5 C. (b) Desodiation profiles of the sodium metal CE potential for 0.1, 2 and 5 C.

tion and more than 270 mV at the beginning of the 5 C desodiation (overshoot). Regarding the cell potential, all desodiation curves show overshoots at the beginning of the desodiation, whereas the WE potential appears to be smooth. Looking upon the behaviour of the CE potential at different C-rates, the similar effects can be observed (Figure 5.2 (b)). As the sodium plating profile for 0.1 C is rather smooth, the profile for 2 and 5 C starts with an immediately potential increase, which decreases rather fast and stabilises at around 80 mV and 100 mV after 150 mAh g^{-1}, respectively. The immediate increase of the potential is pronounced at higher C-rates and goes up to around 270 mV for 5 C.

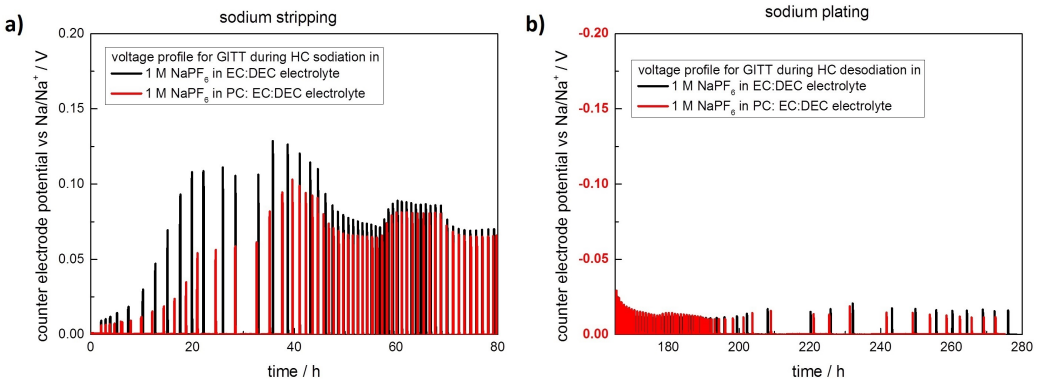

Figure 5.3: GITT voltage profile of sodium metal CE in two different electrolytes during a) stripping and b) plating; black: 1 M $NaPF_6$ in 1 : 1 EC : DEC, red: 1 M $NaPF_6$ in 1 : 1 : 1 EC : DEC : PC.

5.2.3 Influence of the electrolyte

GITT is used to characterise material and electrode properties, such as one-dimensional diffusion within electrodes and polarisation effects. The mathematical background and methods for analysis are given in Chapter 2.1.2. Here the collected data is analysed for changes in the IR resistance depending on the SoC of the electrode similar to DCIR (direct current internal resistance) testing. The experiments were performed in 3-electrode Swagelok cells as described in Chapter 4.

Figure 5.3 shows the polarisation of the sodium metal CE during (a) HC sodiation (sodium stripping) and (b) desodiation (sodium plating). The polarisiation spikes occur during the charging/discharging steps, when a current is flowing. The gaps between the spikes are related to OCV measurements after each charge/discharge pulse during GITT testing. Within the OCV steps the potential of the sodium CE measured versus the reference is close to 0 V (no sodium metal contribution to the potential as shown in Chapter 4.2.2). The polarisation values of the sodium metal increase to maximum values of around 0.125 V during the first 40 hours. Afterwards, the polarisation values oscillates around 0.075 V. The oscillating part of the profile shows a 'wavelength' of 24 hours and might be related to the daily temperature changes within the lab as the lab is not temperature-controlled (Figure 4.7). For desodiation (sodium plating) the polarisation values are much lower with values around $\frac{1}{3}$ of the sodiation value. For sodiation as well as for desodiation the effect is pronounced for the cell containing the EC:DEC electrolyte. This is different as expected as an addition of PC to a EC : DEC mixture should increase the overall viscosity and lower the

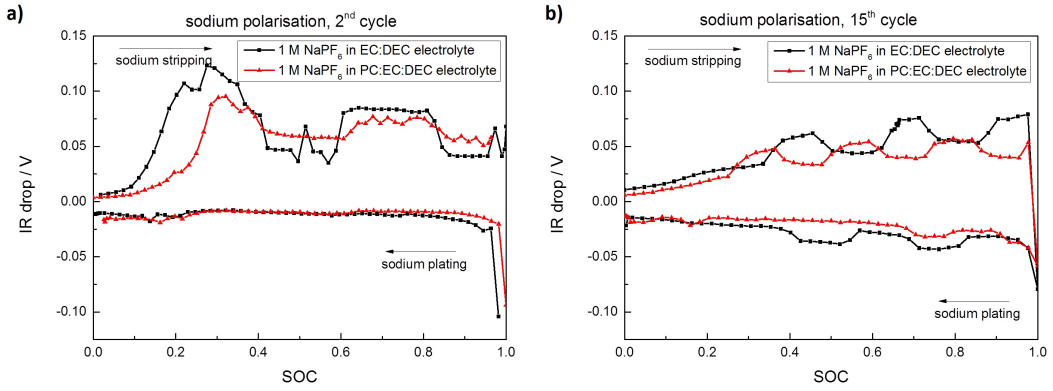

Figure 5.4: IR drop on sodium metal CE in two different electrolytes during stripping and plating; black: 1 M $NaPF_6$ in 1 : 1 EC : DEC, red: 1 M $NaPF_6$ in 1 : 1 : 1 EC : DEC : PC within the a) second and b) 15^{th} cycle.

ionic conductivity of the electrolyte. But sodium metal CE discs are hand rolled and might differ in thickness and surface roughness (= surface area), which will effect its response to the current applied.Figure 5.4 shows the calculated IR drop at the beginning of every GITT step based on the data above. The calculation is based on the potential difference of the first second of sodiation and desodiation, respectively. The graph shows the IR drop values plotted versus SoC of the HC WE. Similar to the previous illustration, an increase for both sodiation branches can be seen, changing into a waveform that oscillates slightly around an average value. For both electrolytes a maximum around 30 % SoC within the sodiation profile is observed.

Without further investigations credible conclusions are difficult. It is known, that sodium is stripped and plated during HC sodiation and desodiation. Hence, surface irregularities might lead to an inhomogeneous stripping and plating, respectively. An investigative approach would be to change the surface area and hence the current densities of the CE sodium metal disc; for example by using different shapes, diameters and surface patterns. If the effect is surface related, the peak should shift towards higher or lower SoC values, respectively. Another reason could be the ratio of sodium 'moss' and metallic sodium on CE side. Sodium moss might be easier to strip from the electrode than metallic sodium. The amount of sodium moss is growing via cycling and therefore the peak should shift towards higher SoC. These effects can also be observed using nano-scale imaging techniques such as neutron diffraction.

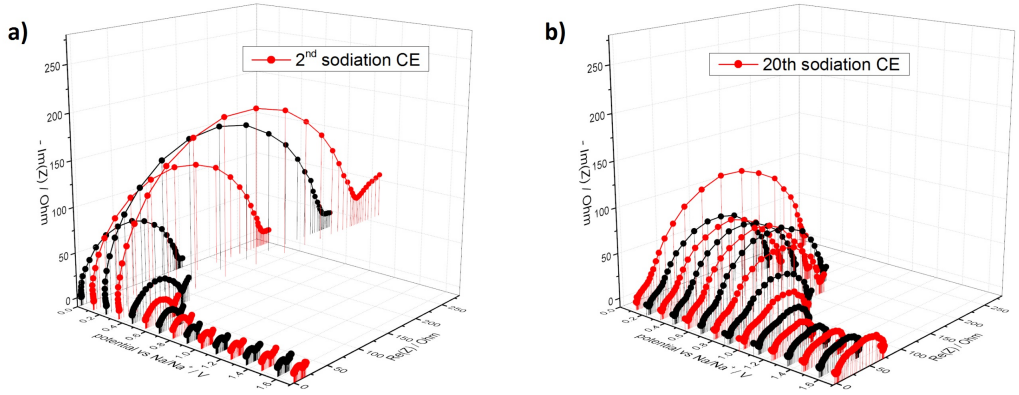

Figure 5.5: Impedance spectra of sodium metal CE for full sodiation in 1 M $NaPF_6$ in 1 : 1 EC : DEC electrolyte; a) 2nd HC WE sodiation, b) 20th sodiation.

5.2.4 Resistance changes observed upon cycling

EIS is used to split up cell processes based on different time constants. Therefore, electrode processes like surface reactions and bulk diffusion can be determined separately from each other. EIS was chosen to investigate the surface reactions on sodium metal CE as well its change in resistivity. Again, 3-electrode cells were built as described in Section 4.2 comprising a sodium metal CE and a HC WE. The cells were filled with EC : DEC electrolyte (ratio 1 : 1 (v)) comprising 1 M $NaPF_6$ and tested as described in Chapter 4.3.1.5.

Figure 5.5 shows all 15 EIS spectra for the second (a) and 20th HC WE sodiation (b) versus the cell voltage (CE versus WE). Although the overall impedance is increased for the 20th sodiation (stripping of sodium), both spectra show similar features. At the beginning of each sodiation at 1.7 V the impedance is low and stable until half way through the sodiation. In both graphs an increase until the end of sodiation can be observed. The increase of the impedance starts at slightly lower voltage (around 0.7 V) for the fresh cell and around 1.1 V for the cycled one. Further observations are the increasing number of inductance features seen for the cycled electrode, whereas the serial resistance is stable at all potentials but increases from around 1.5 Ω to around 8 Ω in the 20th sodiation. The impedance characteristics at low frequency are related to diffusion and pore geometry, hence also to electrode thickness.[43, 183] In each cycle sodium is stripped and plated from and onto the sodium metal causing a moss-like structure as described for lithium-ion batteries.[184, 185, 186, 187] Therefore, the features observed are likely related to surface changes on the sodium metal CE due to cycling; sodium stripping/plating and surface layer formation in conjunction with the electrolyte used.

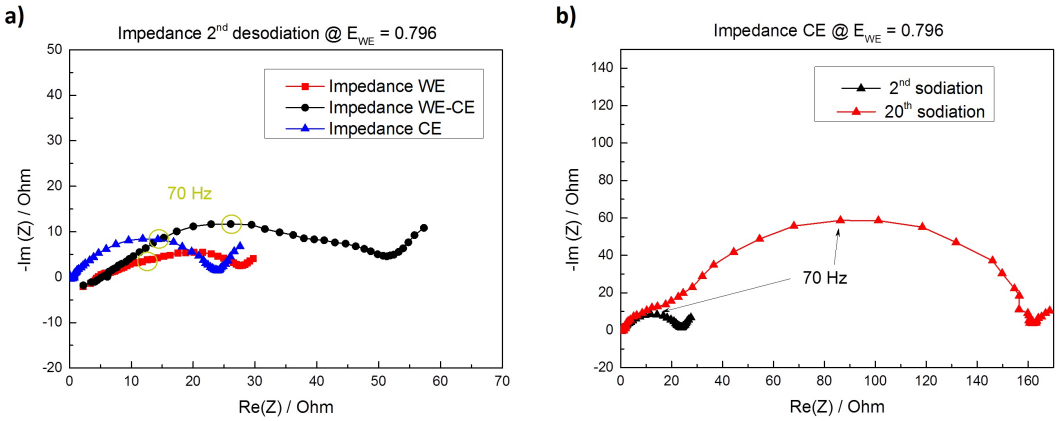

Figure 5.6: a) Difference of WE and CE impedance compared to full-cell data in 1 M $NaPF_6$ in 1 : 1 EC : DEC electrolyte for 2nd sodiation; b) impedance growth on sodium metal CE during sodiation in 1 M $NaPF_6$ in 1 : 1 EC : DEC electrolyte.

Figure 5.6 shows a selection of the recorded data. Figure (a) displays the EIS data for the WE, the CE and the full-cell. In comparison the impedance spectra for the sodium metal CE shows the lowest ohmic resistance. In general, the electrolyte contribution should be similar for each electrode and is stated by the intercept of EIS spectra with the x-axes on high frequencies (compare to Figure 2.3 in Section 2.1.4 [43]). The difference shown between the WE, CE and full-cell spectra might be due to a differences in contact resistance towards the metal plunger. In particular sodium metal is sticking better to the metal cell plungers than a current collector foil. The spectrum of the WE seems to comprise at least two semi-circles. In addition to the one semi-circle observed for the CE, the full-cell profile comprises at least three semi-circles. As mentioned above and noted in Chapter 2.1.4, the low frequency region also contains information about the porosity of the electrodes. Hence, the pore size distribution of the WE is likely to influence the shape of EIS spectra. In Figure 5.6 b two single EIS spectra of the sodium metal CE are compared. The spectra shown are recorded at the same HC WE potential for the second and 20th cycle. The fresh CE shows a total impedance of approx. 27 Ω at 50 mHz, whereas the impedance of the aged cell has increased to more than 160 Ω at 50 mHz. The EIS spectrum for the second sodiation shows two semi-circles, whereas the spectrum based on the data of the 20th comprises at least three semi circles. A further comparison of these spectra in more detail shows, that the semi circles within the high frequency range keeps it shape, whereas within the middle and low frequency region additional features occur along with an increase in values. Again, the appearance of additional semi circles might be caused by sodium moss formation as the

density and porosity of sodium moss differs from metal sodium.

5.3 Conclusion

Sodium metal counter electrodes have been studied using 3-electrode cells in order to elucidate the effect of the sodium counter electrode on the observed 2-electrode electrochemical results. Experiments show that with the application of a current, a polarisation of the sodium metal is observed; this polarisation increases with increasing current, in addition the polarisation is more pronounced upon stripping rather than plating. These results indicate that care must be taken when testing these materials in a 2-electrode configuration, and simply controlling the sodiation by voltage may result in partially sodiated HC materials. Understanding and minimising polarisation is important for electrode optimisation. Higher polarisation results in a higher average voltage and a lower overall capacity, which lowers the energy density of tested cells. However, rate tests are important for material and composite electrode tests. These test methods indicate, if a material or electrode fulfils the requirements for a high power or high energy application.[188, 189] The results show that WE data obtained by using a 2-electrode set-up with sodium metal as a CE differs from the actually true data of the WE and may lead to misinterpretation. The results of the rate tests performed in 3-electrode mode show a huge polarisation of sodium metal depending on state-of-charge and rate (Figures 5.1 and 5.2). Additionally, the rapid increase and sudden decrease in voltage seen at the beginning of the desodiation of the cell potential are related to the sodium metal CE (Figure 5.1 and 5.2). Furthermore, a contribution of the sodium metal to the overall polarisation of more than 15 % was seen at 5 C. As this effect is non-linear towards C-rates and state-of-charge, an off-set calculation cannot be made.

Further, similar effects are true for resistance measurements in 2-electrode half-cell configuration. The results show that an increase in full cell resistance cannot exclusively allocated to the working electrode. Besides, continuous cycling increases the impedance on the sodium metal CE (factor of 8 in 20 cycles). Hence, the analysis of results for ageing studies gained in a 2-electrode half-cell needs to be done with caution and in respect of any CE contribution.

To develop a full understanding of the sodium metal influence as a counter electrode in 2-electrode experiments, more work is required. Future work will investigate the influence of sodium ‘moss’, i.e. dendritic growth vs. bare sodium metal and the independent contribution towards the hysteresis. A difference being expected due to our observations

based on the ageing and cycling conditions of sodium metal. The reason for this behaviour cannot be explained yet and further experiments are necessary to investigate a relation towards the geometry or amount of sodium moss on the surface of the metallic sodium CE. For example, if the inflection point between sodium moss and sodium metal stripping can be determined and linked to an increase in impedance, EIS in-situ techniques can be used to investigate ageing effects on sodium and lithium metal electrodes. These results will help to understand the inner processes of lithium and sodium-ion batteries in more detail and furthermore, assist within the development of lithium air batteries.

These results point out the importance of a reliable test set-up to determine true electrode characteristics. Hence, all following electrochemical testing is performed in an 3-electrode test set-up, monitoring the WE and CE voltage via the reference. Furthermore, the presented results and methods will be used to investigate the sodiation and desodiation process of HC as well as the characteristics of aged or modified electrodes.

Chapter 6

Determining the apparent diffusion coefficients of HC using GITT, EIS and EPS

In this chapter, GITT, EPS, and EIS are used to determine sodium-ion diffusion characteristics within composite HC electrodes using a 3-electrode cell set-up. The techniques are used to calculate diffusion coefficients; comparisons are reported, and the characteristics of approach are discussed, including the relative advantages and limitations.[28, 47, 48, 51, 99, 190]

6.1 Introduction

To be able to design higher power, longer life and higher capacity electrodes for assigned applications, a complete picture of the electronic and ionic transport mechanisms within the electrode (positive and negative) and the electrolyte is required including an understanding of the ion diffusion and reaction mechanisms at the anode, regardless of the charge carrying ion, effective materials selection, and electrode design.[22] Although density-functional theory (DFT) calculations and numerous experiments show similar mobility of sodium-ions within electrolytes and electrodes compared to lithium-ions, their larger ion radius induces more mechanical stress in the active materials during sodiation.[191, 192, 193, 194, 195] Depending on the type of active materials, these processes may include intercalation, alloying, stripping and plating metals, and diffusion of carrier ions. The electrochemical reactions depend on material characteristics. As mentioned earlier, the exact sodiation mechanisms are still under investigation. Rest publication suggest a two-staged process: intercalation during the sloping region of the voltage profile and pore occupancy within the plateau stage.[176, 196, 197] However, the reaction rates and overpotentials are influenced by the electrode composition itself. An investigation of the ion diffusion as a function of

SoC and SoH is essential for effective electrode design and performance assessment.[89, 111] A full understanding of SoC related diffusion coefficients can help to stabilize reaction processes and change the charging and discharging procedures. Several different electrochemical techniques can be utilized to study these processes: GITT, EPS and EIS. These are all commonly used in battery research to investigate the properties of cathode and anode materials and calculate diffusion coefficients.[28, 29, 47, 49, 50, 51, 83, 89, 99, 190] It has been shown previously that the electrode composition impacts the observed electrochemical properties extracted using GITT and EIS techniques.[198, 199]

6.2 Electrochemical analysis

To conduct those measurements 3-electrode test cells were built and tested as described in Chapters 4.2 and 4.3.1. All electrochemical tests start with a formation cycle to assure good cycling properties. Hereby, characteristics such as initial capacities, FCL, and reference connections can be checked. An example of a formation cycle is shown in Figure 6.1. The graph displays the working electrode potential (dashed line, E_{WE} measured between WE and reference electrode) and the cell potential (straight line, cell, measured between the working and counter electrode). A mismatch between the E_{WE} and cell potential can be seen during sodiation caused by the polarization on the sodium metal counter electrode.[123] The HC electrode shows an initial sodiation capacity of approximately 330 mAh g^{-1} and a first cycle efficiency of approximately 85 % in consistence with the literature.[20, 83, 84, 89, 190, 200]

The parameters in the test set-up can also affect the accuracy of the measurements. For example, in GITT, too short relaxation times mean that OCV is not reached. Therefore, ΔE_S is smaller than it should be, which results in errors in the diffusion coefficient when the titration method (Equation 2.1.2) is used for calculation; using the Sand equation to fit the voltage transient overcomes this.[22] Similar limitations are valid for PITT experiments. As a solution, the Cotrell equation is used to fit the current transient at the end of the pulse, instead of using the titration technique to reach the OCV. Here, a third electrode or reference electrode is used to overcome some of these limitations and assumptions.[116, 123, 199] This means that the diffusion parameters can be elucidated which relate to the HC working electrode only, and the polarization of the counter electrode can be ignored. Also the calculated testing parameters are based on low current densities, so the pore sizes do not affect the diffusion properties. The pulse times are short enough to reduce the effect of

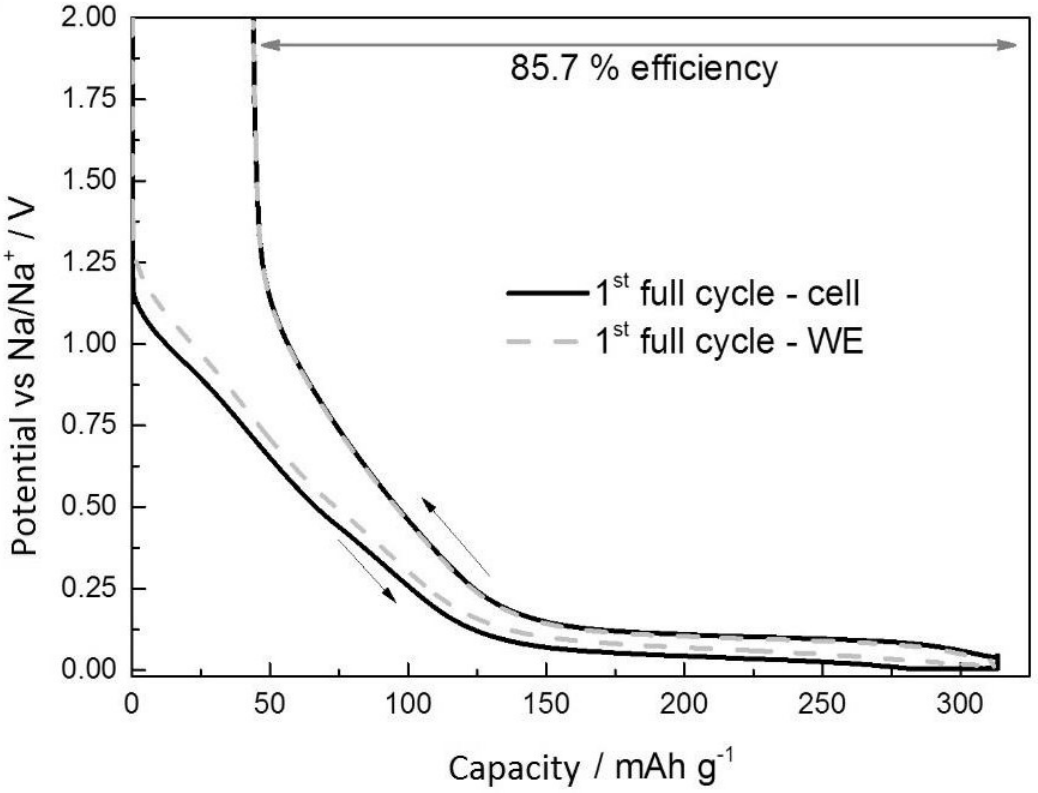

Figure 6.1: Full formation cycle of an HC half-cell showing the working electrode (WE) potential (HC vs Na metal reference) compared to full-cell potential (WE vs counter electrode, CE) and the first cycle efficiency.

any small particles being fully sodiated before the larger particles and long enough to make sure that steady-state for sodiation is reached, and the electric double layer's contribution is minimized.

Further, in the calculated diffusion coefficients discussed below, we have utilized a surface area S related to the active electrode area, based upon an electrode coat weight of $110\,\mathrm{g\,m^2}$, the porosity of 35 %, and an average HC particle of $9\,\mu$m (calculation based on spherical particles with a radius of $4.5\,\mu$m). When using the geometrical electrode area, as also stated in the literature, the diffusion coefficient would change by a factor of around $4{\times}10^4\,\mathrm{cm^2\,s^{-1}}$. This should be considered when comparing results to literature.

6.2.1 Apparent diffusion coefficient calculations based on GITT

The GITT measurements were performed in the second and 10$^{\text{th}}$ cycle to investigate the influence of cycling on the ionic mobility using a 3-electrode cell set-up. A full GITT cycle showing the sodiation and desodiation branch of an HC working and sodium metal

counter electrode is shown in Figure 6.2. The series of sodiation and desodiation steps, each followed by an OCV step can be observed in Figure (a) and (b), respectively. The length of the OCV steps varies depending on the SoC and potential of the WE as the limitation was set to $\Delta E_{WE} \leq 0.001\,\mathrm{mV\,s^{-1}}$. Figure 6.2 (c) and (d) however, shows the same data plotted versus the capacity. The polarization of the sodium metal counter electrode during sodiation and desodiation can be clearly observed. The polarization depends on the SoC of the electrode and is approx. double during sodiation compared to desodiation.

The apparent diffusion coefficients were calculated using Equation 2.3, with $\tau = 300\,\mathrm{s}$, $m_{AM} = 12.4\,\mathrm{mg}$, $V_M = 48\,\mathrm{cm^3\ mol^{-1}}$, $M_{AM} = 72\,\mathrm{g\ mol^{-1}}$, and $S = 49.8\,\mathrm{cm^{-2}}$. The diffusion length L of the sodium-ions depends on the composite electrode characteristics such as porosity and particle size of the active material. The diffusion length would range between 4.5 μm (= radius of the spherical particle, $D_{50} = 9\,\mu\mathrm{m}$) and approx. 100 μm (= thickness of the electrode coating in case of for dense electrodes). Assuming those numbers as a minimum and maximum diffusion length and an apparent diffusion coefficient between 10^{-9} and $10^{-13}\,\mathrm{cm^2\ s^{-1}}$, a time interval of 300 s fulfills the requirement $\left(\tau \gg \frac{L^2}{D}\right)$ as lined out in Chapter 2.1.2.[196, 199] The calculation for each GITT step was done within a voltage range between 1.2 V and 5 mV, and the results are shown versus the capacity in 6.2 (e) and (f).

The apparent diffusion coefficients' values vary by at least one order of magnitude for all four profiles. In the second sodiation, minimum values of around $5\times10^{-12}\,\mathrm{cm^2\ s^{-1}}$ and maximum values of around $1\times10^{-10}\,\mathrm{cm^2\ s^{-1}}$ are determined. The profile for the second desodiation is revered, and the values are lower compared to the sodiation (minimum around $3\times10^{-12}\,\mathrm{cm^2\ s^{-1}}$; maximum around $8\times10^{-11}\,\mathrm{cm^2\ s^{-1}}$). A general decrease in the diffusion coefficient is apparent for the cycled electrodes. The cycled electrodes' profiles appear noisier within a prolonged plateau region (minimum around 2×10^{-12}; maximum around $7\times10^{-11}\,\mathrm{cm^2\ s^{-1}}$) indicating a change of the initial parameters and resulting in maybe less accurate data collection. Hence for further examination smoothed data points are discussed.

All profiles of the apparent diffusion coefficient can be divided into four regions for sodiation and five regions for desodiation. For sodiation, the values are plateau-like for the first 100 mAh $\mathrm{g^{-1}}$ (region 1), followed by a decrease of one to two orders of magnitude (region 2) to a second plateau from around 150 to 250 mAh $\mathrm{g^{-1}}$ (region 3). For both sodiation cycles, the values increase slightly at the end of sodiation from 250 and 270 mAh $\mathrm{g^{-1}}$

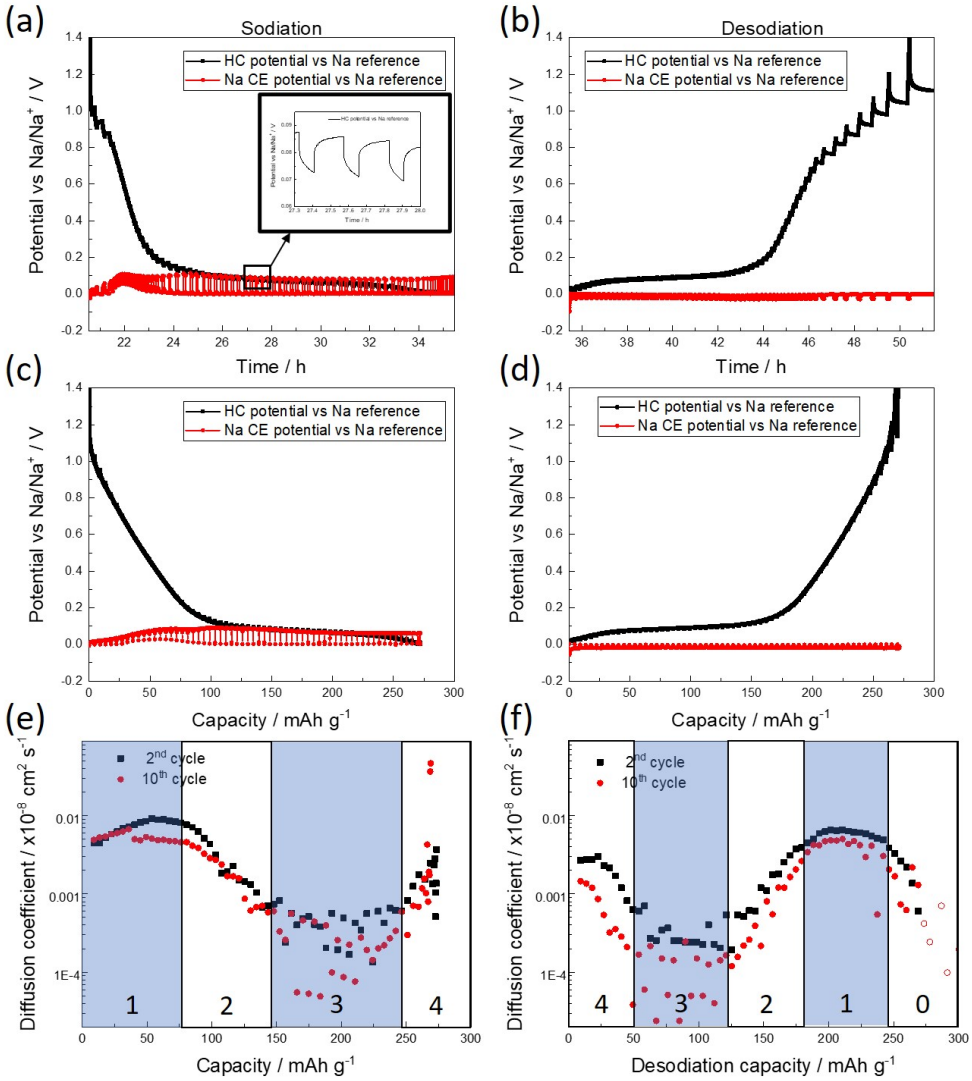

Figure 6.2: GITT profile of the sodiation (left) and desodiation (right) branch of the HC working and sodium metal counter electrode versus time. (a) and (b) show the potential curve versus testing time, (c) and (d) show the potential versus capacity. (e) and (f) show the corresponding apparent diffusion coefficients during sodiation (left) and desodiation (right) within the second (squared marker) and 10th cycle (circular marker) determined from 3-electrode GITT measurements. Coat weight of 13.5 mg.

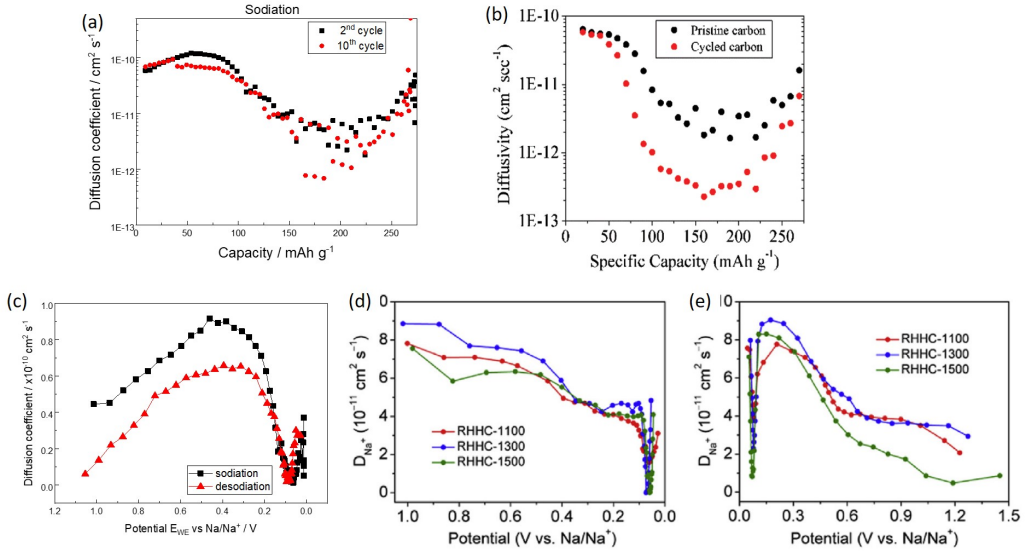

Figure 6.3: Comparison of the determined diffusion coefficients as seen in 6.2 (a) versus capacity, (c) versus potential; (b): pristine anode material and one that has undergone 350 cycles.[92] (d) sodiation and (e) desodiation of the second cycle of rice husk-derived hard carbons (RHHC) at different temperatures.[99]

onwards (region 4), respectively. The profile for the apparent diffusion coefficient values for the second desodiation is mirrored to that of the sodiation (region 4 to 1). An additional region (region 0) can be distinguished as the values drop at the end of desodiation by one order of magnitude (Figure 6.2 (f)). A similar performance can be seen for the 10^{th} sodiation for region 4 to 0.

Ionic mobility within battery materials is essential for the overall battery performance. Hence, apparent diffusion coefficients for HC electrodes based on GITT experiments have been reported in the literature before with maximum values between 10^{-11} to 10^{-8} cm^2 s^{-1}.[29, 50, 51, 92, 99, 201] The results differ based on the parameters and settings used; for example, testing in 2- versus 3-electrode arrangement and varying the length of the OCV step to achieve an equilibrium. Further, the parameter setting for S differs in publications, as often the geometrical surface, BET surface or numbers of approx. calculation based on porosity and particle size are used. Although the mentioned parameters influence the absolute values, the shape of the diffusion curve is similar as seen in Figure 6.3.

Figure 6.3 (a) and (b) is a comparison of the determined data within this PhD project (a) and data published by Bommier et al. [92] (b). Both graphs show the apparent diffusion coefficients during sodiation for a fresh and cycled electrode. The observed capacities, shape of the curve and the lower performance for the cycled electrode can be seen in both

graphs. The values observed for fresh cells in this PhD project are covering a slightly wider range (10^{-10} to 10^{-12} $cm^2\,s^{-1}$) versus the values observed by Bommier et al. [92] (6×10^{-10} to 2×10^{-12} $cm^2\,s^{-1}$). Figure 6.3 (c), (d) and (e) shows the diffusion coefficients versus the working electrode and cell potential, respectively. Subfigure (c) details the values as recorded in this work and seen in 6.2, whereas Subfigures (d) and (e) show the values as derived during sodiation and desodiation of the second cycle of rice husk-derived hard carbons (RHHC) at different temperatures.[99] All profiles follow the same trends: higher between values between 1.2 and 0.2 V, lowest values around 0.1 V, followed by a slight increase towards 0 V. Differences can be seen in the sodiation profile between 1.2 and 0.4 V. The trend for the diffusion values obtained in this work are increasing from 0.4 to around 0.9×10^{-10} $cm^2\,s^{-1}$, whereas the values shown by Wang et al. [99] are decreasing from around 0.8 down to 0.4×10^{-10} $cm^2\,s^{-1}$ within the same potential window.

Overall the three data sets seem very similar except the sodiation values of the RHHC (6.3 (d)). Therefore, it can be concluded, that graphs shown in Figure 6.2 are mainly in accordance with published data. The rather small mismatch of the data might be caused by differences within the cell-set-up and chose of parameter settings for the electrochemical testing. For a better comparison a summary is listed in Table 6.1. Besides the use of different precursors, the main differences are the cell set-up (2-electrode coin cells versus 3-electrode Swagelok) and the limitation parameter for the OCV step. Both settings are important to obtain reliable OCV data as stated in Chapter 4. The OCV limitations chosen by Wang et al. [99] (t = 1 h) might be too short to achieve an equilibrium for a true OCV value. Further, polarisation effects are very likely within the voltage sloping region of HC during desodiation. Hence the cut-off voltage might be triggered early, resulting in a reduced pulse time which needs to be considered in the calculations. No information about adjustments in calculation or polarisation effects can be found in their publication.

The mirrored profiles for sodiation and desodiation for GITT values as seen in Figure 6.2 indicate a reversible process for the second cycle. The variation of the apparent diffusion coefficients within each sodiation and desodiation cycle points out a strong dependence on the SoC. Further, a correlation of the apparent diffusion coefficients' low plateau region to HC's low voltage potential is prominent. The presented stepped voltage profile of the GITT curve (Figure 6.2) suggests different stages for ionic diffusion within the sodiation and desodiation process, which correspond to the diffusion coefficient changes. Plateau regions

Table 6.1: Differences in cell building and parameter settings for GITT testing as chosen in this PhD project, Bommier et al. [92], and Wang et al. [99].

	PhD project	Bommier et al.	Wang et al.
Precursor	petroleum pitch	Tencel-C fiber HC	rice husks
Interlayer spacing	0.38 nm[202]	0.366 nm	0.38 - 0.4 nm
Cell design	Swagelok	coin cell	coin cell
Reference electrode	yes	no	no
Electrolyte	1 M $NaPF_6$	1 M $NaPF_6$	1 M $NaClO_4$
	EC:DEC (1:1)	EC:DEC (1:1)	EC:DEC (1:1)
AM loading	1.5 mg cm^{-2}	7 mg cm^{-2}	1.0 - 1.5 mg cm^{-2}
Current	60 mA g^{-1}	10 mA g^{-1}	20 mA g^{-1}
Pulse length	300 s	1 h	0.5 h
Capacity per pulse	5 mAh g^{-1}	10 mAh g^{-1}	10 mAh g^{-1}
Limitation OCV	$\Delta U \leq 0.001$ V	4 h	1 h

might indicate semi-stable diffusion characteristics (region 1 and 3), whereas regions of fast decreasing or increasing values suggest changes in the diffusion characteristics (region 2, 4, and 0), and hence a change in the sodiation mechanism.

The voltage transient at low voltages is not linear at the end of the pulse, making the diffusion coefficient more difficult to calculate. The non-linearity indicates that the processes occurring in the material and electrode are non Fickian. Hence, the calculated values at low sodiation potentials are less conclusive. Besides, as the plating potential is reached, no or limited diffusion occurs in the active material. Additionally, this could indicate that the sodium metal 'pooling' in the HC at the low voltages is not limited by the intercalation but the formation of the nano-clusters of sodium and that at these low voltages sodium could plate onto the surface of the electrodes.[196, 203, 204]. Measurements of the diffusion coefficients at higher potentials were difficult to calculate due to the high polarization at those potentials, which triggered the cut-off voltage and stopped the charge pulse before τ = 300 s was reached. This polarisation is expected as the sodium concentration is very low in the HC at these voltages resulting in a lower overall electronic conductivity in the composite electrode.

6.2.2 Apparent diffusion coefficient calculations based on EIS

Identical to the GITT measurements, EIS was conducted in the second and tenth cycle using a 3-electrode cell set-up. Within each sodiation and desodiation cycle, 16 EIS spectra (equidistant voltage steps) were generated to cover the full range of SoC. Figure 6.4 shows the 16 EIS spectra for sodiation (left) and desodiation (right) in a voltage range be-

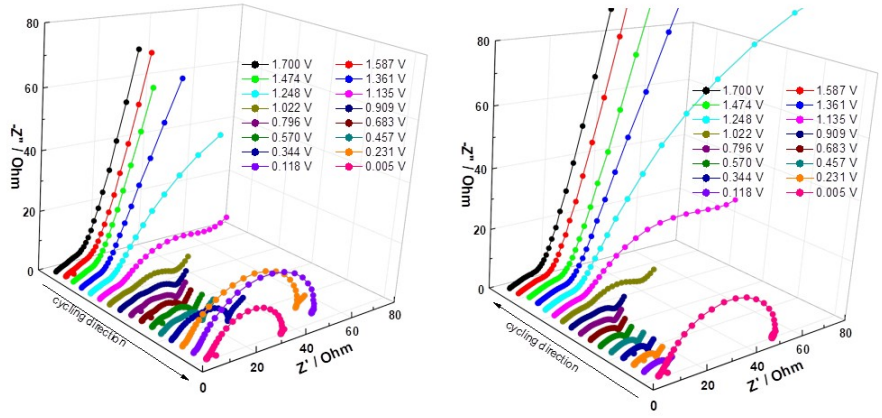

Figure 6.4: EIS spectra versus voltage for the full second sodiation (a) and desodiation (b) between 0.005 and 1.7 V. Data was recorded between WE and reference electrode in a 3-electrode set-up. Electrode coat weight: 13.8 mg.

tween 1.7 V and 5 mV. Differences in the shape of the Nyquist plots at various SoC indicate changes in resistance, capacitance, surface layer formation, and pore sizes changes.[38, 43, 84, 158, 205] Further, the low-frequency branch's appearance, which reflects solid-state diffusion impedance, changes with the SoC. During sodiation, the spectra below 0.231 V show inductance-like behaviour at low frequencies. This has been observed similarly for fuel cells and is related to mass transport of the reactive species.[206, 207] The observed induction phenomena are potentially related to the mass transport of the reactive species (Na^+) away from the electrode's surface. Similar features can be seen during desodiation for potentials lower than 0.01 V. Hence, the observation of the induction component in the Nyquist plot at 0.005, 0.118 and 0.231 V vs Na/Na^+ upon sodiation, is likely to the high concentration of solvated sodium ions at the surface of the electrode. Whereas upon desodiation, the sodium concentration at the surface is likely lower because of the faster diffusion in the liquid electrolyte compared to the solid. However, the appearance of this artefact makes the calculation of the diffusion coefficient difficult and may be misleading.

As an example, and to visualize the influence of ageing onto the electrode performance, Figure 6.5 show the EIS spectra at 0.457 V for the second cycle (a) and tenth cycle (b) displayed in Nyquist plot. The graphs show a higher overall impedance (R_{CT}: charge transfer) for the sodiation compared for desodiation (second cycle: 20 to 14 Ω; tenth cycle: 150 to 87 Ω) as well as an increase in impedance during cycling (sodiation: 20 to 150 Ω; desodiation: 14 to 87 Ω). The differences in sodiation, desodiation, and age of the electrodes can be seen in the angle and frequency-shift of the low-frequency region. Hence, Figure 6.5 (c) and

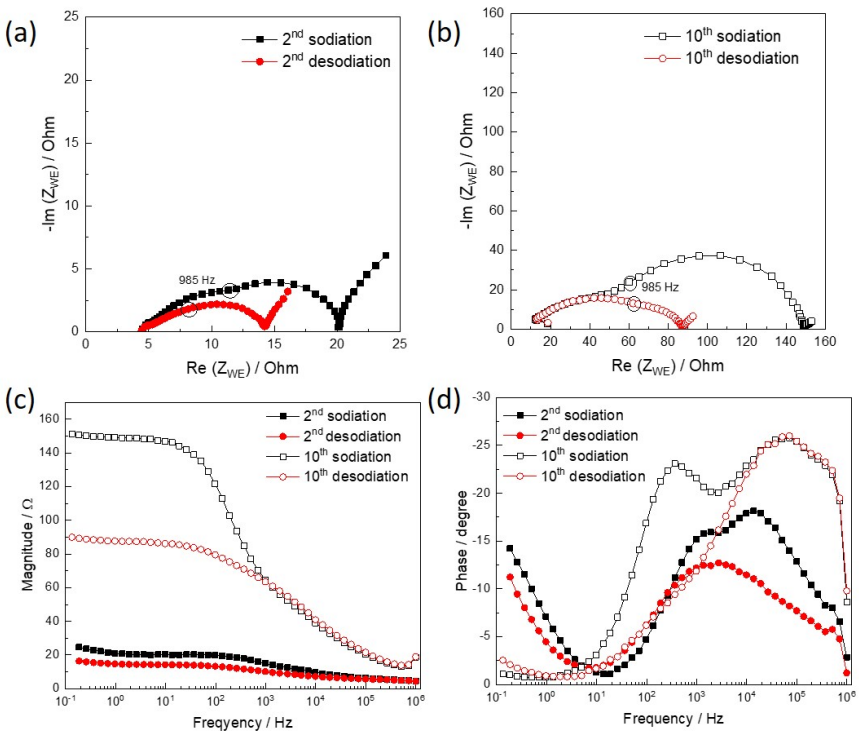

Figure 6.5: Impedance data of the second and tenth sodiation and desodiation at 0.457 V.

(d) shows the Bode plots based on the same data. The increase in the overall impedance is also seen in Figure 6.5 (c) highlighting the pronounced effect for lower frequencies. Also, the impedance profile of sodiation and desodiation diverge for frequencies above 1 kHz. Within the phase diagram in Figure 6.5 (d) two distinctive local minima and two local maxima can be determined for the sodiation curve, whereas the desodiation branch shows less distinct features.

Besides gaining information on serial resistance and charge transfer, diffusion characteristics can be determined from impedance data. To analyse the diffusion characteristics, the focus for the EIS measurements is on the low-frequency region, which relates to the diffusion in a solid. The apparent diffusion coefficients were calculated using Equation 2.9, with σ gained from the slope Z_{RE} versus $\omega^{-\frac{1}{2}}$ for low frequencies, as mentioned earlier (Figure 2). For more information graphs showing Z_{RE} versus $\omega^{-\frac{1}{2}}$ and the fitting results are listed in the Appendix (Table A.1 and Figure A.2 and A.3). Figure 6.6 shows the calculated diffusion coefficients versus the SoC of the composite electrode for sodiation (left) and desodiation (right). Within the sodiation and desodiation of the second cycle, the values of the apparent diffusion coefficients increase or decrease by four orders of magnitude in a

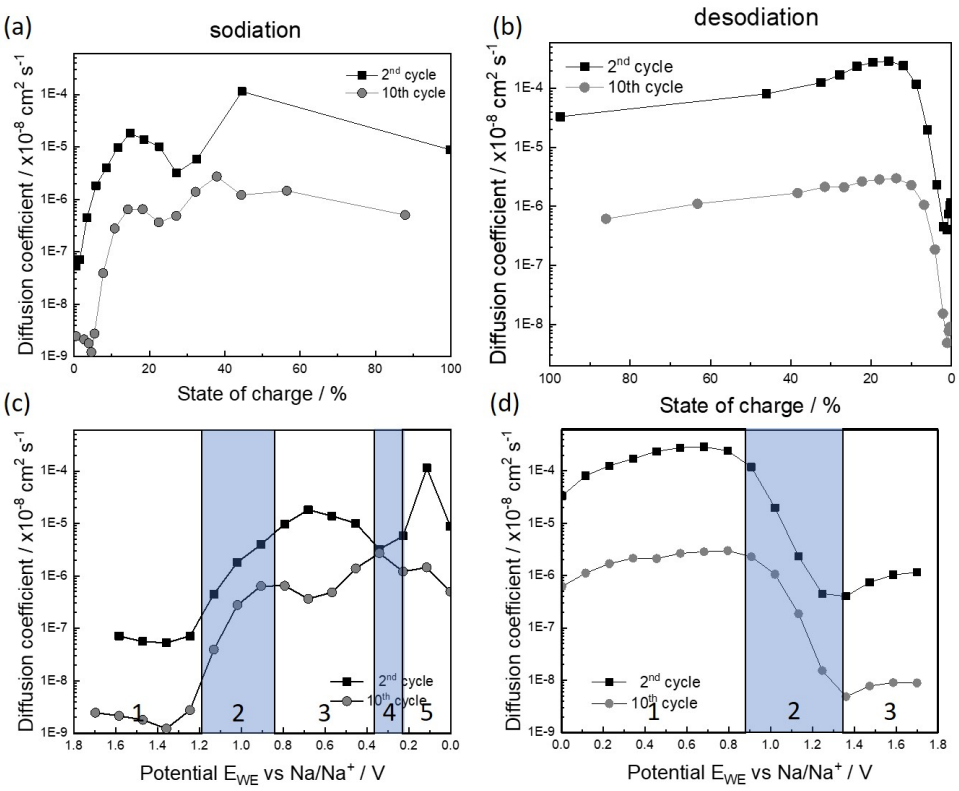

Figure 6.6: Apparent diffusion coefficients based on low-frequency impedance data for sodiation (left) and desodiation (right) of the 2nd cycle and cycled electrodes plotted versus the SoC and potential, respectively.

four- and five-step profile, respectively. Compared to the fresh cells, the maximum values for the cycled cells are reduced by one order of magnitude with the profiles of the apparent diffusion coefficients following the same trends.

There are a limited number of data points for the low voltage plateaux region, as the EIS measurement was taken at a particular voltage rather than a capacity. Besides, at these low voltages, the fitting of the slope was poor. The Warburg contribution was difficult to elucidate, and this led to difficulties in the calculation of the diffusion coefficients. However, the sodiation process shown in the left graph of Figure 6.6 can be divided into five regions, including three plateau regions and two sloping regions. Values start at a low-value plateau until approximately 5 % SoC (corresponding to 1.25 V) at around 6×10^{-16} cm^2 s^{-1} (Region 1), which is followed by an increase up to an SoC of 15 % (corresponding to 0.8 V, region 2). The diffusion remains constant in a plateau (region 3) and is about three orders of magnitude higher for the fresh (1×10^{-13} cm^2 s^{-1}), as well as for the cycled electrode (8×10^{-7} cm^2 s^{-1}) compared to the initial values. At 30 % SoC, the values show a 'blip' and start rising again

(region 4) to values similar to the third region (region 5).

The desodiation process in Figure 6.6 (right) can be divided into three regions, including two plateaus and one sloping region. The regions mirror the sodiation profile, but regions 3 to 5 of the desodiation process merge into one plateau region, missing the sloping region previously described as region 4 in the sodiation process. The diffusion coefficient values start at the same level as at the end of the sodiation and are stable for most of the entire desodiation process (down to 10 % SoC and 0.8 V, respectively). Within 10 to 5 % SoC (approximately 1.3 V), the values decrease by four orders of magnitude to 1×10^{-14} cm^2 s^{-1} (Region 2). Identical to the sodiation profile, a low plateau can be seen at the end of desodiation (Region 1).

Publications on apparent diffusion coefficients gained from EIS data are rare in the literature. EIS is mostly used to investigate the diffusion in cathode materials as the crystal structure changes during charge and discharge.[39, 42, 122, 155, 208, 209] For analysis, it has to be considered that the resolution within the low voltage region is quite low. Additionally, the data acquisition is not as accurate within the low voltage plateaus. Even a low voltage amplitude changes the SoC, and the requirement for the semi-stable condition is not fulfilled. Using GEIS would lead to more reliable results in the low voltage plateau. However, it would cause inaccuracy for the diffusion coefficient calculation as even a low applied current amplitude would lead to an SoC change at low frequencies, which are needed for the diffusion coefficient calculation. In this study, Potentiostatic EIS was chosen to gain more information in the sloping voltage region of the HC to compliment the information obtained through the GITT measurement.

6.2.3 Apparent diffusion coefficient calculations based on EPS

EPS measurements were again conducted in a 3-electrode cell set-up after an initial formation cycle. The EPS profile for the working electrode, the counter electrode (sodium metal), and the monitored cell current is plotted in Figure 6.7. The graphs show the profiles for sodiation (left) and desodiation (right). The working electrode potentials (upper graphs) show the staircase profile of the 10 mV voltage steps. The polarization of the counter electrode at each voltage steps can be seen in the middle graph. During sodiation of the HC working electrode, the counter electrode's polarisation is increasing towards lower potentials; during desodiation, the polarization is decreasing towards higher potentials. The polarization shows a maximum of around 8 mV within the low plateau region of the HC potential

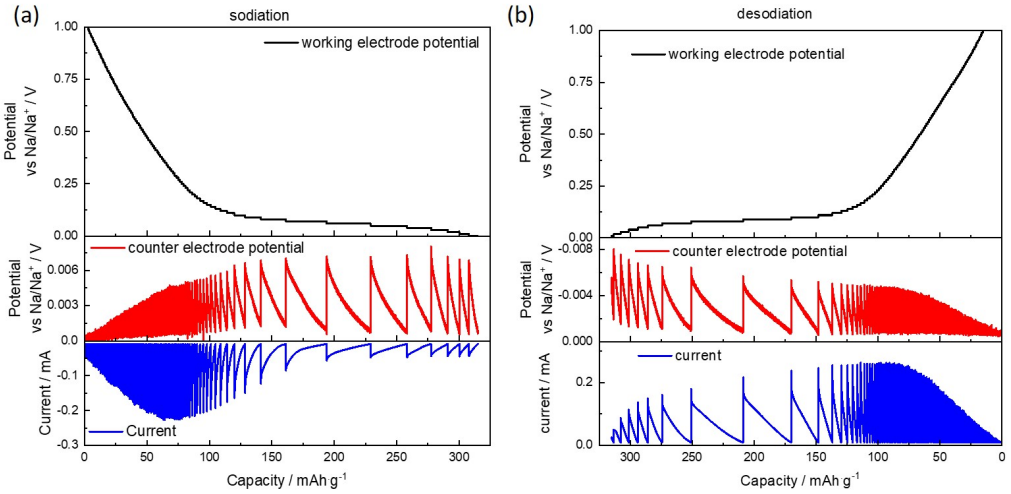

Figure 6.7: Working (HC), counter (Na metal) electrode potential and current profile of the EPS cycle for sodiation (left) and desodiation (right) of an HC composite electrode versus the gravimetric capacity (active material based). Coat weight 12.8 mg.

(middle graphs). The bottom graphs show the current profile monitored during sodiation and desodiation. Each voltage step is accompanied by an exponential current decay due to diffusion processes. As an additional remark, Figure 6.7 highlights the importance of a three-electrode set-up as the sodium counter electrode's potential varies between 6 mV and -8 mV at sodiation and desodiation, respectively. Calculations based on the cell voltage profile may lead to inaccuracies in the diffusion coefficient's calculated values.

Apparent diffusion coefficients were calculated following Equation (2.10) using a linear fit for the current $i(t)$ versus the time $t^{-\frac{1}{2}}$ with the slope of each current decay being proportional to D_{EPS}. The results are plotted in Figure 6.8. It displays the calculated apparent diffusion coefficients based on the EPS measurements for sodiation and desodiation versus the SoC. The values of the apparent diffusion coefficient change by three orders of magnitude during sodiation and desodiation. For sodiation, the values start at a high level (7×10^{-8} cm^2 s^{-1}) and decrease, undulating to around 0.03×10^{-8} cm^2 s^{-1} when 100 % SoC is reached. The first decrease to 0.2×10^{-8} cm^2 s^{-1} appears within the 0 to 3 % of SoC. This is followed by a rise of the values to around 0.8×10^{-8} cm^2 s^{-1} at 20 % SoC and a subsequent drop with its minimum at around 60 % SoC. The lowest values can be found between 50 and 80 % SoC (0.006×10^{-8} cm^2 s^{-1}). The desodiation profile is in reverse, showing slightly increased values between 100 and 20 % SoC.

The profile of the apparent diffusion coefficient appears similar for sodiation and des-

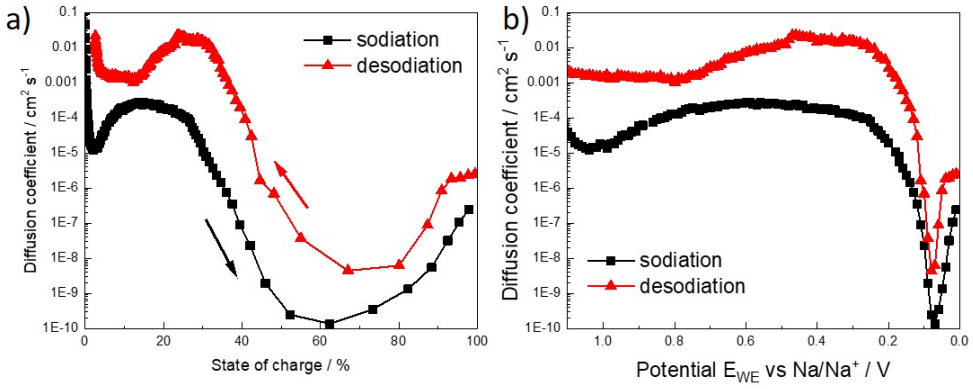

Figure 6.8: Apparent diffusion coefficients based on EPS data for sodiation (black square) and desodiation (red triangle) of the 2nd cycle plotted versus the SoC (a) and working electrode potential (b).

odiation, suggesting a reversible process. The changes in diffusion during the sodiation and desodiation process indicate at least a two-step process. Again, one step within the sloping region of the voltage profile and a second one within the plateau region, as described and discussed above.

Based on the test plan's set-up, the data points of the apparent diffusion coefficient are not equidistant when plotted versus the SoC (capacity). Since the measurements are taken in equidistant voltage steps, and the characteristic voltage profile of the HC consist of a sloping and a plateau region, the data density is much higher at low SoC (sloping) compared to higher SoC (plateau). This leads to a high resolution between approx. 0 to 30 % SoC, followed by just a few data points between 40 and 80 % SoC (plateau region).

6.2.4 Comparison and discussion of the results gained from GITT, EIS and EPS

For comparison of the results gained from GITT, EPS, and EIS all data are normalized to the maximum observed diffusion coefficient at 20 % SoC ("Δ Diffusion coefficient") during sodiation to elucidate the changes in the order of magnitude, which will be discussed later, and for a clearer comparison between sodiation and desodiation for each technique. The results are shown in Figure 6.9. The left column of plots shows the results for sodiation (black square) and desodiation (red triangle) versus the potential of the working electrode E_{WE}. The right graphs display the data versus the SoC of the working electrode to focus on the low potential region (0.2 to 0.05 V or 40 to 100 % SoC). Both illustrations were chosen as the graph versus the SoC is beneficial for GITT measurements which is based on capacity

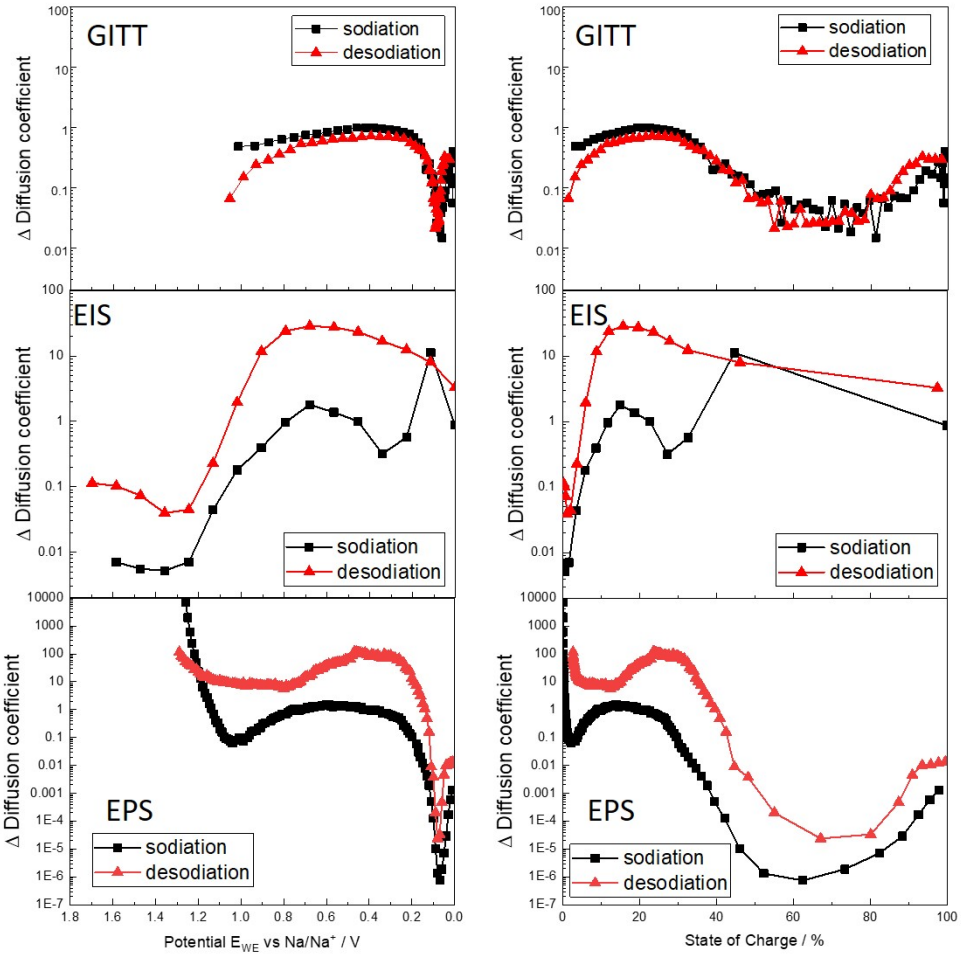

Figure 6.9: Comparison of GITT, EIS, and EPS data showing changes within the apparent diffusion coefficient based on their 20 % SoC sodiation value. Left: results plotted versus the potential of the working electrode. Right: results plotted versus the SoC of the working electrode.

intervals, whereas the EIS and EPS measurements were performed in voltage step intervals and benefit from a display versus the WE potential.

The apparent diffusion coefficients shown in Figure 6.9 indicate a reversible sodiation and desodiation for all three techniques. Whereas the shape of the sodiation and desodiation profiles of the apparent diffusion profiles based on GITT end EPS look very similar, showing a wavelike profile with a high plateau region between 0 and 35 % and a low plateau region between 45 and 80 % followed by an increase towards the end of sodiation, the EIS data follows more a two step sodiation/desodiation, showing to plateaus and an single sloping region 1.2 and 0.8 V.

The values gained from all three techniques decrease with ageing whereas the differ-

Table 6.2: Minimum and maximum values of the apparent diffusion coefficient for sodiation and desodiation, respectively. Values are based on the second cycle, as seen in Figure 6.2, 6.6, and 6.8.

	Diffusion coefficients of the 2nd cycle in $\times 10^{-8}$ cm^2 s^{-1}			
	Minimum		**Maximum**	
	Sodiation	Desodiation	Sodiation	Desodiation
GITT	0.000 4	0.000 2	0.01	0.008
EIS	0.000 000 1	0.000 001	0.000 2	0.001
EPS	0.01	0.4	1000	1000000

ences between fresh and cycled cycles are largest in the plateau region of the HC sodiation/desodiation profile (130 to 220 mAh g^{-1}, 35 to 85 % SoC). Previous publications show that the change in diffusion upon cycling and the increase in resistance are due to reduced pore networks within the electrode. The pores become blocked with SEI growth, limiting the transport of electrolyte and ions to the surface of the material.[22, 92, 199]

For detailed analysis, the minimum and maximum apparent diffusion coefficient for each technique are shown in Table 6.2. When comparing the range of the apparent diffusion coefficient values, it is noticeable that the values based on GITT measurements change within two orders of magnitude, whereas the values for EIS change by four and EPS by six orders of magnitude. This might be caused by many different parameters. A list of the parameters chosen for each technique is given in Table 6.3. The table states the accounted parameters needed for the evaluation of the apparent diffusion coefficients and highlights the key differences of the three techniques used. Those differences can be categorized in three groups: general settings, behaviour within the low voltage region, behaviour within the high voltage region.

General aspects: The important key parameters valid for the whole potential region are: experimental control, step limitation, IR contribution, parameter settings and test duration.

- In all methods, the derivation of the method is based upon *Fick's laws of diffusion*. Therefore, if the sodium ion transport mechanism deviates from the assumption that the sodium concentration changes, the calculations for diffusion coefficient will not hold true.

- The *step limitations* were chosen to be close to an equilibrium state. The time scales of the sodiation and desodiation steps reach from 1 to 17 minutes for GITT, fixed 150 minutes for EIS, and tens of seconds up to 4.5 hours for EPS. The corresponding

Table 6.3: List of parameters for evaluation of the apparent diffusion coefficient for the three techniques used: GITT, EIS, and EPS.

	GITT	**EIS**	**EPS**
Controlled via	Current	Potential	Potential
Based on	Fick's laws of diffusion		
Step limitation	$\Delta E_{WE} \leq 0.001\,\mathrm{mV\,s^{-1}}$	150 min OCV	$\mathrm{I} < 0.01\,\mathrm{C}$
constant	Surface Pulse time τ Molar mass Molar volume Active material mass	Surface Temperature	Surface Diffusion length Current
IR contribution	None	None	Yes, low
graphical analysis	ΔE_S ΔE_t	Warburg coefficient Concentration Current	Step time Δ Concentration
Test duration	51 hours	174 hours	69 hours

currents are 0 mA for GITT (OCV step), < 0.002 C for EIS and < 0.001 C for EPS. The variation in time lines and current ranges strongly depends on the SoC of the electrode and the technique used (see also following paragraphs).

- The *control of the techniques* is either done via the current (GITT) or the potential (EPS and EIS). When controlled via current, the polarisation effects trigger the step limitations faster. Therefore, the voltage range covered by the apparent diffusion coefficients differs slightly between the different techniques used.

- EIS is a time-intensive method, especially when focussed on the low frequency region for diffusion analysis. Despite the fact that EIS shows the lowest data's resolution (16 data points per sodiation) of all three techniques (GITT: 64 data points per sodiation, EPS: 138 data points for sodiation), the *testing time* is three time larger compared to GITT. The cell-set up chosen is very reliable, but test cells built on lab-scale, especially 3-electrode cells, might suffer from higher self-discharge or leakage currents via the reference electrode and ageing. This might lead to higher capacities during sodiation and lower capacities for desodiation and deficient concentration calculations. Hence, more data points would have extended the testing time even more, making it difficult to compare results due to described "side" effects.

- As the electrodes' porosities were set to 35 %, the *diffusion length* should be similar at

initial state. During sodiation, especially at low voltages, pathways might be blocked by localized sodium deposition which could increase the diffusion length, but also increases the internal resistance and impede the charge transfer (initial results for the serial resistance, SEI and charge transfer resistance for each of the 16 EIS spectra are listed in the Appendix A in Table A.2 and A.3). As the diffusion length is assumed to be constant, the influence of enlarged diffusion pathways are left out.

- For EIS calculations the temperature is taken into account. Although all experiments was conducted at ambient temperature, changes in temperature during night/day or workday/weekend may cause small variations.

- All test cells were built from the same printed electrode, and an identical cell design is used, electrode related parameters are unlikely to be the cause for the differences.

- In general, the GITT condition of $\Delta E_{WE} \leq 0.001\,\mathrm{mV\,s^{-1}}$ might be too soft. Hence an equilibrium is not reached, leading to too high values for ΔE_S, causing an overestimation of the apparent diffusion coefficient. In this case, it may be more appropriate to fit the SAND equation to the voltage transient, as then the variation in reaching OCV would not be taken into account.

Effects on low voltage level: So besides the factors discussed above, several potential testing artefacts are arising at different voltage levels for these methodologies. At the low voltage level these include:

- For GITT at the low voltages very low diffusion coefficients are observed. Towards the end of sodiation, where $\tau < 300\,\mathrm{s}$ as the limitation voltage is triggered, it is likely that no charge was transferred (only double layer formation). This would mean that ΔE_t would be too large, leading to underestimating the diffusion coefficient.

- EIS and EPS were both controlled by voltage rather than current. Therefore the calculation of the concentration of sodium in the solid is difficult at the low voltage plateau. However, the small changes in voltage in EPS measurements mitigate some inaccuracies, especially as a limitation current of 0.001 C is still linked to a sodiation/desodiation. However, only two points across the low voltage region for the EIS measurements will likely not reflect the complete change in the diffusion coefficient at the low voltage.

- Especially the EIS measurements seem to be affected by processes occurring at very low voltages. It is suggested that within the low voltage region, sodium metal deposits on the HC surface and metal sodium clusters form within the HC's pore space.[176, 196, 197, 201, 203] This would enhance the electronic conductivity of the HC and change the local sodium concentration (local potential ≠ electrode potential [74, 210]) and could cause induction effects. The Nyquist plots at low voltages shown in Figure 6.4 show the lack of a Warburg feature, but induction loops. Besides, as the Warburg feature is missing during desodiation, a faster sodium transport away from the surface upon desodiation through faster transport in the electrolyte would be expected. The data gained from simple equivalent circuit fitting (Figure A.4) shows a lower variation within the SEI and charge transfer resistance for desodiation than for sodiation, explaining the higher apparent diffusion coefficient values during desodiation.

- When conducting PEIS measurements within the plateau region of the HC sodiation/desodiation a small change in voltage induces a high current response reflected in inaccuracies in the impedance measurements. The high current response leads to charge/discharge of the working electrode, especially during low-frequency measurements. This means that the electrochemical system is not in a semi-equilibrium state. Hence, the interpretation of the calculated values within the plateau region of the HC voltage profile is difficult for EIS-based measurements.

Effects on high voltage level:

- EIS and EPS are controlled via voltage, leading to a better and controllable data resolution. However, as the limitation conditions are met quickly (tens of seconds), the charge contribution within the current profile used for fitting might be masked by double-layer formation. Further, the SEI formation might not be completed after the first formation cycle. This means holding the voltage at approx. 0.7 V will grow the SEI layer. This is also true for any other side reactions triggered by a certain voltage, which might be enhanced if the potential is held at the triggering voltage. In terms of the EPS experiment, the second cycle's differential capacity plot is shown in the Appendix (Figure A.5), showing no ongoing reactions within the HC potential's sloping region.

- The benefit of using a small voltage amplitude during the PEIS measurement to avoid

altering the SoC within the plateau region too much might be a disadvantage at high potentials. The change in potential (amplitude modulation) might be too small to cause a reliable current response. The data gained from the PEIS measurements performed in this study are based on the average value of three iterations per frequency to minimize the effect of inaccurate numbers.

- The pulse length for GITT measurements needs to meet the condition: $\tau \ll \frac{L^2}{D}$. Nevertheless, due to the steep sloping region, there is the potential to induce a big chance in the SoC. So the registration interval is poor. This effect is intensified because due to the low electronic conductivity, the IR contribution at high voltages is quite high. Still, the pulse length τ has to be chosen long enough to induce an actual charge into the material, which is on longer time scales than the ohmic polarization and double-layer forming and capacitance. However, with sufficient long OCV periods within the GITT measurements, the Ohmic resistance changes are considered and can be neglected in discussing the results. In addition, the influence of the sodium metal counter electrode can be neglected, and a 3-electrode arrangement is used. Nevertheless, sodium metal is also used as reference material and although there are only measurement currents present, sodium metal is known for surface layer formation within carbonated electrolytes.[114, 123]

Differences in the reported diffusion coefficients arise from both experimental set-ups and the assumptions made in the calculations. The original GITT experiment was related to discussion into a thin film rather than a porous electrode, and therefore the surface area used in the calculation was the electrode area - as the transport limitation was the flux of counter ions to the surface of the thin film. In terms of batteries which contain liquid electrolytes, electrodes consist of a porous network. Therefore, the diffusion should be calculated from the flux of counter ions to the active particles' surface. However, the effective surface area is difficult to calculate because of the carbon binder domain accurately, and the particles' embedded into the current collector. The surface area is a shared constant in calculating the diffusion coefficient from all methods and is related to the particle size. Single-particle size and spherical particle are assumed for evaluation, rather than a particle size distribution and differently shaped particles. Consequently, this will also affect the accuracy of the calculated diffusion parameters.

The analysed techniques have their advantages and disadvantages. On basis of the ratio

of data points per testing times, GITT and EPS are the techniques of choice. With a higher registration rate per testing time systematic errors are easier spotted and the data seems more reliable. Nonetheless, the EIS measurement itself bring much more information, if analysed in full. This part of work concentrates on diffusion only, but the acquired data will be used for further studies, for example to investigate the SEI information in more detail. Further, it is prominent that the shape of the diffusion coefficients gained via GITT and EPS look very similar. The choice of technique should be made in terms of the region of interest, as EPS has its strengths in sloping regions of the potential of the material determined, whereas GITT is beneficial for investigation of processes within the voltage plateau regions.

6.3 Conclusion and Outlook

HC composite electrodes have been studied in a 3-electrode cell set-up to examine sodium-ions' diffusion behaviour using the GITT, EIS, and EPS. All techniques were conducted using the same electrode and the importance of the correct cell set-up, as well as parameter settings, and analysis has been discussed, including the relative advantages and limitations.

The collective finding from all techniques conducted indicates a reversible sodiation/desodiation process. Moreover, all generated data shows a dependence of diffusion capability during on the SoC for sodiation and desodiation. The same general trend of sodium ion diffusion capability with SoC is derived from each technique showing higher values within the sloping region and lower values within the low voltage plateau. Between these stages, the apparent diffusion coefficient varies by orders of magnitude. Differences in minimum and maximum values are related to parameter settings and quasi-equilibrium state adherence.

The data gained by GITT befits from a high resolution in the flat potential regions but shows disadvantages in steep sloping regions, where features might get lost due to a dependence on capacity rather than voltage. EIS data shows better resolution within the sloping profile range but likely leads to inaccurate data when too high voltage amplitudes are used. Especially in regions showing a voltage plateau of the investigated electrode. Further, the EIS data for low potentials lacks a Warburg feature, possible due to sodium clusters forming within the HC and enhancing the electronic conductivity.[196, 197, 201, 203] EPS data becomes beneficial in regions of steep voltage profiles and high polarization but misses data density in voltage plateaus.

Each approach has different implications for practical implementation, and there are

trade-offs to be considered. For example, EIS has the advantage of being easily implemented into standard test plans and is not as time-consuming as GITT or EPS when used at a single voltage, but is not effective over the entire SoC range. Hence, these methods are not contradictory but complementary, and a combination of their use is recommended in order to gain a better overall picture of diffusion characteristics.

In this work apparent diffusion coefficient were determined using GITT, EPS, and EIS. All techniques are commonly used in literature, but a thorough analysis and comparison pointing out critical parameters and limitations has not been published to date. Many of the assumptions made cannot be proven by the work presented without further experimental work which could include adjusting the parameter settings for the techniques (for example pulse length, width of the frequency spectrum, cut-off parameters). Further, the electrode composition and microstructure should not be ignored as they will also impact the observed diffusion.[199] In particular, electrode porosities influence the ability to transport ions to the active material's surface for the reaction. This is partly taken into account when calculating the surface area of the material in the electrode film. However, the pores' size is not considered. If the pore size is not large enough, this could limit the transport of ions to the materials' surface, particularly at higher current densities.

The implementation of real surface data would benefit a deeper understanding of those techniques as well as determine the diffusion process on electrode level. This would not just involve the approx. 15 % volume expansion of the HC material during sodiation, but also surface layer formation, blocked pathways and the influence of other degradation processes occurring during cycling. This way, actual surface changes can be monitored and the diffusion coefficients can be calculated with S depending on SoC and SoH. The gained results can be used to optimise the electrode structure in terms of electronic and ionic mobility to enhance the rate capability and safety, since a more homogeneous current density avoids local overcharge or deep discharge which causes for example electrolyte decomposition and dendrite formation.

Chapter 7

Optimisation of HC composite electrodes by adjusting electrode porosity

In the previous chapter, GITT has been proven to be a reliable and easy accessible method to determine the apparent diffusion coefficients in HC composite electrodes, especially within the low voltage plateau region (Chapter 6). The correlation of inner resistance and SoC and SoH is known, but as the prior results indicate also a correlation of the ionic mobility on SoC and SoH, it is essential to ensure a balanced combination of ionic and electronic transport for a tailored electrode performance.

In this chapter, electrodes of the same print are calandered to different porosities prior testing. GITT is conducted to investigate diffusion within electrodes and to investigate polarisation effects and diffusion characteristics depending on the SoC and SoH. The results demonstrate the requirement for optimized electrode designs for targeted cell performances and shows the effect of porosity upon the interplay between electronic and ionic mobility and the SoH.

7.1 Introduction

Apparent diffusion coefficients detailing the HC material characteristics have been reported previously. However, electrode design and microstructural properties, such as porosity, and the effect upon cycling and performance have been mainly neglected. Hence, a comparison between materials is challenging as testing methods, and set-ups differ between the publications. The reported experiments vary in electrolytes used and electrode characteristics such as loadings, particle sizes, and particle shapes.[29, 32, 50, 92, 99, 201]

Here, the ionic mobility of Na^+ in HC composite electrodes is investigated. The electrodes are manufactured close to commercial standards with loadings around $110\,g\,m^{-2}$.

The porosity of the electrodes as coated are around 45 %. To gain reliable data, the porosity range for this study was chosen between just coated (all matched to 40 %) and highly densified (25 %). The electrodes were used to study the influence of the electrode microstructure and porosity on the resistivity, ionic mobility, and SoH using GITT. As the apparent diffusion coefficient takes the electrode composition, porosity, ionic, and electronic 3-D connectivity into consideration and these characteristics change with the SoC, SoH, and electrode manufacturing processes, differences in ionic mobility are expected. It is important to note that the calculated diffusion coefficients should be considered apparent diffusion coefficients of the electrode, as the phase-transition reaction, charge transfer, and ionic diffusion are taking place at the same time.[34]

7.2 Electrochemical analysis

Electrodes were manufactured comprising 90 % HC active material (commercial, D_{50}: 9 μm, 4-8 $m^2\ g^{-1}$, according to datasheet), 5 % binder (HSV900, Kynar), and 5 % CB (C45, TimCal) by weight as described in 4.1. After printing and drying the electrodes were densified to 20, 25, 30, 35 or 40 % porosity by calendering to designated thicknesses. For calendering, an electrode sheet was placed between two metal shims before feeding through the heated rollers of a calender machine (MTI Corporation, MSK-HRP-01, temperature: 90°*C*). For porosity calculation, the average density of the composite electrode materials and the volume of the dry coating (electrode surface × thickness) were considered.

For electrochemical cell testing cells in a three-electrode 'Swagelok' design (PFA-820-3, Swagelok) were used. 130 μL of a premade 1 M $NaPF_6$ in a 1 : 1 (v) mix of EC and DEC (Kimisha Chemicals) were added to electrodes and separator stacks during assembling (detailed information can be found in Chapter 4.2). All testing was conducted on a BaSyTec CTS potentiostat with reference monitoring.

7.2.1 Investigation of the ionic and electronic mobility in HC electrodes

DCIR measurements were conducted based on ISO 12405-1:2011 by monitoring the voltage profile during constant current GITT charge and discharge pulses.[211, 212, 213] For

calculation the following equations were used:

$$R_{\text{discharge},10s} = \left| \frac{U_{0s} - U_{10s}}{I_{\text{discharge}}} \right| \tag{7.1}$$

$$R_{\text{charge},10s} = \left| \frac{U_{0s} - U_{10s}}{I_{\text{charge}}} \right| \tag{7.2}$$

where U_{0s} is the voltage at the beginning of the charge and discharge pulse, U_{10s} is the voltage after 10 s of charge or discharge, and I_{charge} and $I_{\text{discharge}}$ are the applied charge and discharge current, respectively.

GITT has been performed on a HC composite electrode (35 % porosity, 90:5:5 active:binder:cb, 12.6 mg active mass, 110 mg cm^{-2}). The testing was conducted after formation to eliminate surface electrolyte interphase formation and any counter electrode artefacts. Calculations for the apparent diffusion coefficient are based on Equation 2.1.2, as stated in Chapter 2.1.2. To apply those equations the condition $U \propto t^{-\frac{1}{2}}$ must be met, which can be seen in Figure A.8.

The observed voltage profile and apparent diffusion coefficients as well as the DCIR are shown in 7.1. The voltage profiles in (a) and (b) show the GITT profile of the HC WE and the CE versus the sodium metal reference. The HC voltage profile consists of a sloping region between 1.0 V and 0.2 V versus Na/Na$^+$ and a plateau between 0.2 and 0.05 V versus Na/Na$^+$, as it has been shown previously. The variation within the CE profile during sodiation and desodiation has been discussed earlier (Chapter 5). However, the contribution of the CE to the overall cell performance is removed since a 3-electrode arrangement is used.[123]

Figure 7.1 (c) and (d) show the corresponding apparent diffusion coefficients and DCIR values for sodiation and desodiation versus capacity. The profiles can be divided into four steps for sodiation and five steps for desodiation. Within step I the values are nearly constant around 1×10^{-7} cm^2 s^{-1} at the beginning of the sodiation correlating to a voltage window of around 1.0 to around 0.2 V and capacity between 0 and 80 mAh g^{-1} (SoC: 0 and 25 %). Between 0.2 and 0.1 V, the values decrease by nearly two orders of magnitude (step II) and reach a second plateau at around 4×10^{-9} cm^2 s^{-1} (step III). The second plateau corresponds to capacities between 140 and 240 mAh g^{-1} (SoC: 35 to 70 %). Within the second sloping region, around 50 and 5 mV of the sodiation (step IV, capacity > 250 mAh g^{-1}, SoC of around 80 to 100 %), the values increase until the approximate starting values are reached.

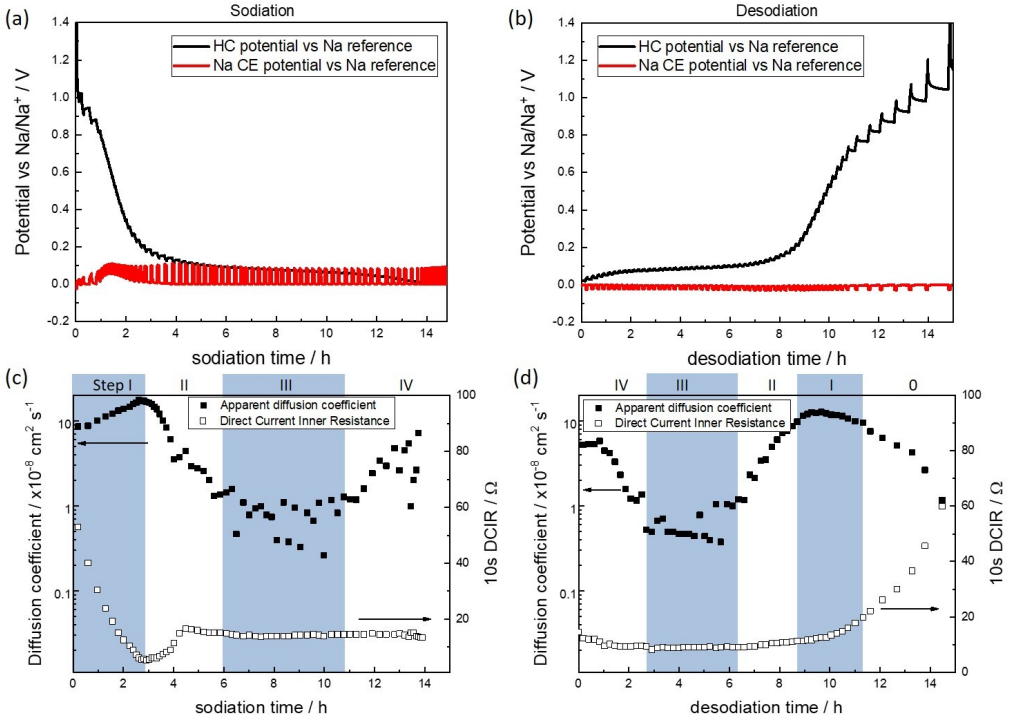

Figure 7.1: (a) and (b) GITT voltage profiles versus capacity of the second cycle for sodiation (a) and desodiation (b) displaying working electrode (WE) potential (black) and sodium metal counter electrode (CE) potential versus sodium metal reference electrode (red); (c) and (d) show the apparent diffusion coefficients (filled squares) and corresponding 10 s DCIR values (empty squares) calculated from the GITT data for sodiation (c) and desodiation (d) versus capacity of a HC WE of 35 % porosity and loading of approx. 110 mg cm^{-2}. For reasons of clarity and comprehensibility, the area of every other step of the is shaded. Steps are outlined in the text.

The DCIR values start at around 80 Ω for the sodiation. The values decrease by a tenth when the potential reaches 0.2 V (end of step I). Subsequently, the values are increasing again until halfway through step II and stabilize around 15 Ω for the remaining sodiation process of the HC. For desodiation, the DCIR profile is reversed. The values are stable around 15 Ω and increasing exponentially up to 80 Ω after a potential of 0.15 V is reached.

The changes in the apparent diffusion coefficient and DCIR profile during desodiation are reversed to the sodiation profile, indicating a reversible process. Both values change during sodiation and desodiation by at least one order of magnitude, which points out a strong dependence on the SoC of the electrode. The desodiation profile follows the sodiation profile in reverse, showing an additional step at the end of desodiation (step 0). Within this step (1.0 and 1.4 V) the apparent diffusion values are decreasing by approximately one order of magnitude.

DCIR shows a strong dependence on the SoC. During sodiation, sodium is increasingly intercalated, resulting in a reduction of the resistivity due to the growing electronic conductivity through the intercalated sodium. Likewise, the high polarization at high voltages during desodiation is caused by the small amount of sodium in the HC and the high concentration within the electrolyte resulting in low apparent diffusion coefficients. Although the cut-off voltage for all test cycles was set to 5 mV for sodiation and 1.7 V for desodiation, the values for the apparent diffusion coefficient and DCIR are challenging to track within the lower voltage window due to sodium plating on the HC surface and in the upper voltage window due to high polarization.

The sodiation profiles for the apparent diffusion coefficients are in accordance with previously published data.[29, 32, 50, 92, 197] The presented step profile of the GITT curve suggests different stages for ionic diffusion within the sodiation and desodiation process. Therefore, the differences in sodium-ion mobility (high versus low apparent diffusion coefficient) might be linked to different sodiation mechanisms. However, the calculation of the apparent diffusion coefficients is based on the relaxation processes to reach an equilibrium. Therefore, the slowest occurring process might dominate the apparent diffusion coefficient calculation. Based on this hypothesis, there are two regions of a semi-stable diffusion (step I and III) and three regions of decreasing and increasing diffusion ability (step II, IV, and 0), respectively. Processes in step 0 and IV are also accompanied by strong polarization effects caused by a low or high sodium content within the active material, respectively. The high polarization in step 0 causes an increase in resistance and facilitates plating in step IV.

Two step intercalation models were described in the literature before. The most-cited ones are published by Stevens and Dahn, and Bommier et al.[32, 83] Stevens and Dahn suggest a “falling card house” model with intercalation occurring within the sloping region, followed by the occupancy of the nanopores in the low voltage plateau. Bommier et al. propose the charge storage occurs by binding to the edges/defect sites in the sloping region, followed by intercalation between graphene sheets within the low voltage plateau and Na-atom absorption on the sp^2 configured pore surface at a very low potential below 0.05 V. The main differences between the two models are pointed out in Figure A.9 in Appendix A. The hypothesis of intercaltion during the sloping region and pore occupancy within the plateau region was also recently endorsed by Weaving et al using Raman spectroscopy.[196,

197]

Cycling affects the physical characteristics of the electrode, including surface layer formation and particle cracking, and therefore has an influence of the electrochemical properties of the electrode.[180] Particle cracking, for example, increases the surface area of the electrode and induces additional surface layer formation accompanied with an increase in internal resistance and polarisation resulting in lower capacities and electrolyte decomposition. Further the electrode porosity is reduced and pores acting as electrolyte reservoir vanish. Hence the ionic mobility decreases, too.

For a better understanding of the limiting factors of the battery performance, the test cell used to generate the data displayed in Figure 7.1, has been cycled as described in the Experimental Section with additional GITT measurements conducted in the 15th and 25th cycle. The results give insight into the changes of the ionic mobility in HC composite electrodes.

Figure 7.2 shows the profile of the calculated apparent diffusion coefficients of an HC composite electrode at 35 % porosity for the second cycle (as seen in Figure 7.1) compared to the 15th and 25th cycle. All graphs feature the step profile mentioned in the precious subsection. For sodiation, the graphs for the second, 15th and 25th cycle, starting at similar values and follow the trends of the second cycle up to approximately a capacity of 100 mAh g^{-1}, which coincides with the voltage profile inflection point of the sloping and plateau region. Afterwards, the profiles of the 15th and 25th cycle drop to lower apparent diffusion coefficients compared to the second cycle. The effect is pronounced for the 25th cycle showing a total decrease of one order of magnitude. For desodiation, the ion mobility in the 15th and 25th cycles is decreased by up to two orders of magnitude for the low plateau region (0 to 100 and 150 mAh g^{-1}, respectively) compared to the second cycle.

The DCIR values for sodiation and desodiation change with cycling (Figure 7.2 (c) and (d)). The values for the 15th and 25th cycle are increased throughout each full cycle. Again, the effect is pronounced for the 25th cycle at the beginning of sodiation and end of desodiation. Similar to the profile in Figure 7.1, the values start at 80 Ω and decrease with sodiation until the plateau region of the HC sodiation profile is reached (at around 100 mAh g^{-1}). The DCIR resistance quickly increases and remains remains constant at around 15 Ω for the second cycle and around 25 Ω for the cycled electrodes. The values for the apparent diffusion coefficient follows the curve of the DCIR: high apparent diffusion

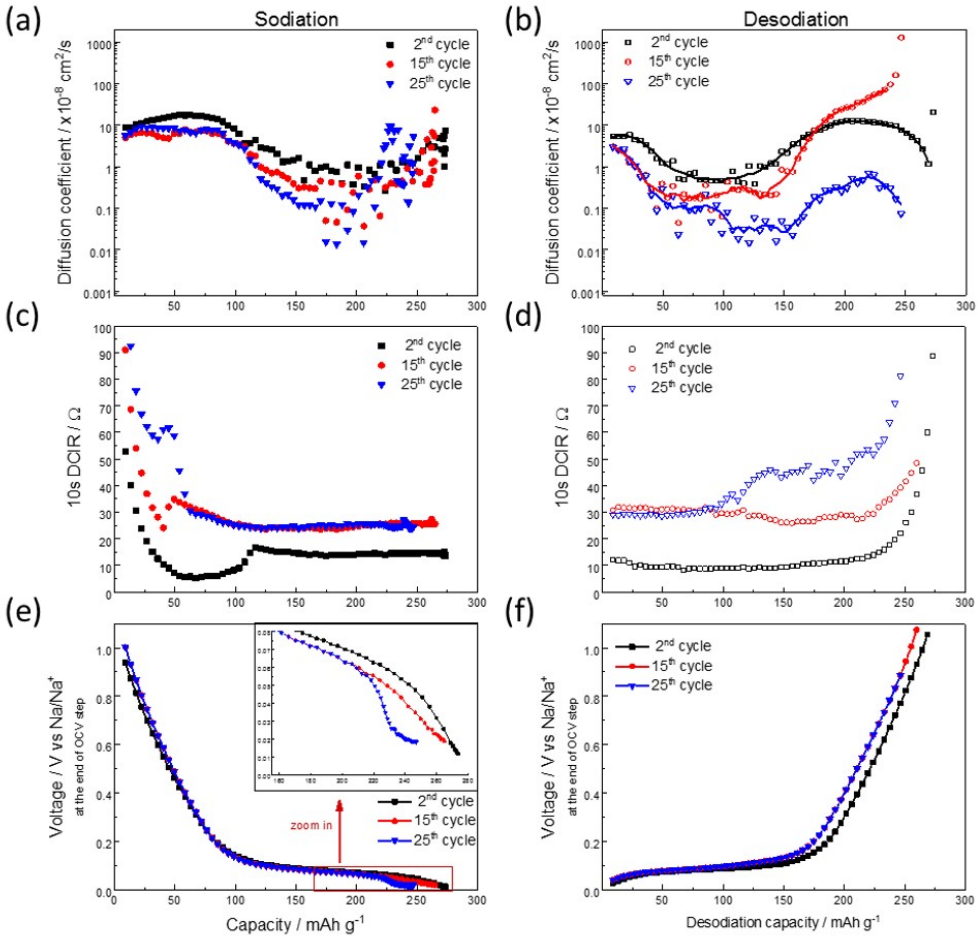

Figure 7.2: Apparent diffusion coefficients (a) and (b) and DCIR values (c) and (d) calculated for a HC electrode for the second (squares), 15th (circles) and 25th (triangles) cycle versus capacity for sodiation (a) and (c) and desodiation (b) and (d). Figure (e) and (f) show the corresponding voltage profiles for sodiation and desodiation. The capacity is plotted versus the voltage values at the end of each OCV step. Data is extracted from the GITT profiles recorded in a 3-electrode arrangement; current applied between working and counter electrode, working electrode potential recorded via reference electrode; sodiation at 0.2 C to 5 mV, desodiation at 0.2 C to 1.4 V; C-rate is based on 330 mAh g^{-1} for HC.

coefficient values for low DCIR. For the apparent diffusion coefficient the effect of cycling is more dominant within the plateau region of the HC voltage profile as the ionic mobility decreases by an order of magnitude from the second to the 25th cycle. For desodiation, the profiles of the 15th and 25th cycle are similar until 100 mAh g^{-1} of desodiation capacity. Whereas the profile of the 15th cycle runs in parallel to the profile of the second cycle, the values for the 25th cycle increase at 100 mAh g^{-1} up to 50 Ω and remain unstable. No distinct differences can be seen between the electrodes for both voltage profiles and the DCIR desodiation profile of the second cycle. The higher resistivity values at low SoC at the beginning of sodiation and end of desodiation might be linked to the low sodium content within the HC composite electrode. Whereas the sodiation shows two stages in the DCIR profile (0 to 100 mAh g^{-1} and > 100 mAh g^{-1}), the profile of the desodiation is smooth. This might be caused by the slow ionic transport within the voltage plateau of the HC. Hence, the intercalation and pooling process might be distinct during sodiation, both processes occur at the same time during desodiation.

The graphs highlight the impact of cycling on the ionic and electronic mobility and show that both, the ion and electron mobility, is impaired with cycling. The effect differs between sodiation and desodiation, and the influence additionally depends on the state of sodiation and desodiation. Whereas the apparent diffusion values within the sloping regions of the voltage profile seem to be unchanged, the ionic mobility within the voltage plateau region decreases depending on the cycling. An increase in cell resistance with cycling is known; hence, an increase in DCIR measurements was expected. However, the DCIR and voltage profile for the 25th desodiation (Figure 7.2 (d) and (f)) indicate dendrite formation on the HC electrode surface at around 100 mAh g^{-1}. This might explain the similar DCIR resistance to the 15th cycle during sodiation and at the beginning of the desodiation up to 100 mAh g^{-1}. During desodiation the sodium metal on the HC electrode surface might be stripped of ahead of the removal of the intercalated sodium. Post mortem analysis of the cycled electrodes showed sodium plating (Figure A.10 in A). Additionally, the presence of sodium depositions on the electrode surface might block the pores and prolong the diffusion pathways, but additionally might reduce the overall resistivity of the electrode due to the higher electronic conductivity of the sodium metal compared to the HC active material. Further the changes might be influenced by

- The *SEI* layer is known as being insulating and therefore, its formation and growing

in thickness results in resistivity growth. If grown unrestrained the resistance might increase with decreasing SoH, but should be independent of the SoC.

- At low *SoC* the DCIR is elevated and ion mobility is increased due to the low sodium concentration within the HC composite electrode. The higher the occupation of the HC with sodium, the lower the ion mobility, but also decreased DCIR due to the higher amount of metallic like sodium within the electrode.

An increase in resistivity decreases the rate capability or obstructs the electronic transport between particles and causes inaccessibility of single particles and therefore results in capacity fade. It is important to note, that although the DCIR values are mainly stable between the 15th and 25th sodiation, the overall capacity per sodiation and desodiation is decreased. Hence, the capacity losses cannot be attributed to polarization and resistivity growth only. Possible explanations might be a loss of accessible active material (loose particles) through blocked channels or pores (sodium plating), which also impairs the ionic transport from the 15th to the 25th cycle as observed in the apparent diffusion coefficient analysis.

7.2.2 Influence of porosity on ionic and electronic mobility

Composite electrodes (90 % HC, 5 % binder, 5 % CB) with a range of different electrode porosities (25, 30, 35, and 40 %) have been manufactured and cycled to determine the influence of porosity on the ionic and electronic transport. Electrochemical properties have been tested in the second and 15th cycle to identify and assign limiting factors to porosity characteristics. Figure 7.3 displays the DCIR versus the capacity of the tested electrodes and the correlated voltage profiles. Figure 3 (a) and (b) show the results for sodiation and desodiation of the second cycle, respectively, with the insets displaying the HC WE voltage at the end of each OCV step. All electrodes show a similar performance to the one described in Figure 7.1 and 7.2 (35 % porosity). A local maximum at around 100 mAh g^{-1} (inflection point of voltage profile (inset)) is followed by stable values of around 10 to 15 Ω. The composite electrode of 25 % porosity shows the best performance within the sloping region of the sodiation profile, followed by the electrodes of 35, 30 and 40 % porosity. Within the plateau region (above 100 mAh g^{-1}) the lowest values can be seen for the electrode of 40 % porosity, followed by 35, 25 and 30 % porosity. The profile displaying the resistivity of the cycled electrodes is nosier, particularly for the desodiation branch. The DCIR values within the 15th cycle (Figure 7.3 (c) and (d)) show the same features for all displayed electrodes but

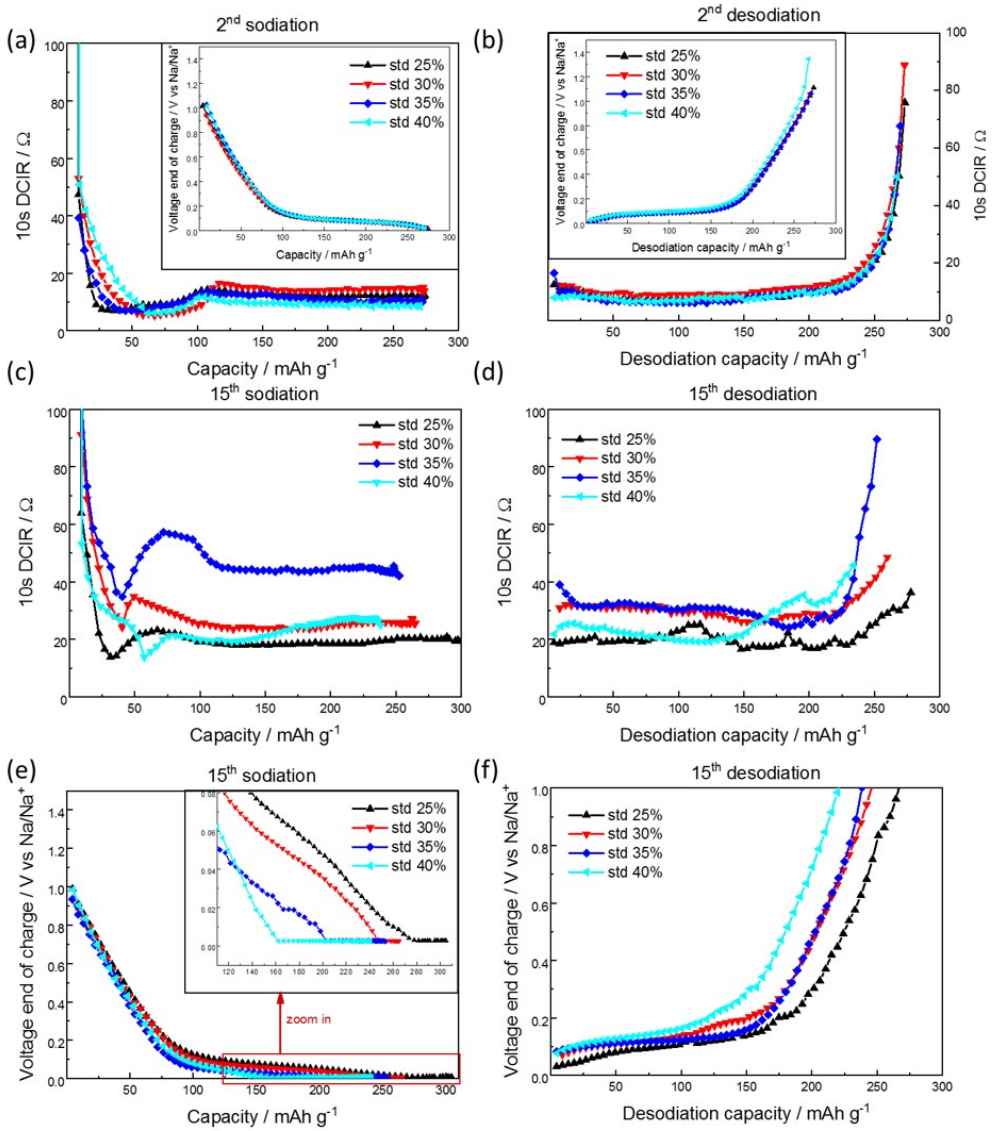

Figure 7.3: Comparison of DCIR resistance measured for HC composite electrodes having different porosities for the second and 15th cycles versus the state-of-charge; Figure (a) and (b) show DCIR versus capacity for the second cycle sodiation and desodiation, respectively. Figure (c) and (d) show DCIR versus capacity for the 15th cycle sodiation and desodiation, respectively. Figure (e) and (f) and the insets in (a) and (b) show the voltage profiles for sodiation and desodiation based on the OCV after each current step, extracted from the GITT profiles; sodiation at 0.2 C to 5 mV, desodiation at 0.2 C to 1.4 V; C-rate is based on 300 mAh g^{-1} for HC.

differ in the shape of the characteristics. Electrodes with a lower porosity show higher overall capacities. The capacity losses seem to occur within the low voltage plateau, whereas the performance of all electrodes within the sloping region is similar. No direct observable link can be determined between porosities and resistivity values. The resistivity is increased with higher porosity (25, 30, and 35 % porosity), except for the electrode of 40 % porosity. Its resistivity values are on a similar level compared to the 25 % porosity electrode. The local maximum, as seen in the second sodiation, is increased for all electrodes and also shifted to lower capacities. The change to constant resistance to lower capacities for the cycled electrodes indicates an earlier inflection point within the HC voltage profile. This can be seen in Figure 7.3 (e).

The sodiation mechanisms within the sloping and plateau region differ from each other (sloping region: intercalation between the graphene sheets; plateau region: pore occupancy [185, 196, 197]). These observations lead to the following suggestions:

- The shift of the inflection point within the voltage profile can be used to allocate occuring losses towards the sodiation steps.
- Due to higher polarisation and cycling sodium plating occurs and might block pathways for intercaltion and deintercalation between the graphene sheets (sloping region). With ongoing sodiation sodium could be stripped and then intercalated into the electrode (chemically intercalation) similar to the process seen for lithium in graphite.[214, 215, 216]
- The internal resistance is lower in less porous electrodes (as expected). As the porosity increases the surface increases – as does the SEI quantity – hence during cycling the DCIR is increased with porosity. The change in 35 % to 40 % is interesting, as there might be a trade off between ionic vs electronic conductivity.

Figure 7.4 shows the corresponding calculated apparent diffusion coefficients of HC electrodes at 25, 30, 35, and 40 % porosity for the second and 15th cycle. Again, all electrodes show the previously described step-like profile for sodiation and desodiation. The results gained from the second cycle are plotted in Figure 7.4 (a) and (b). No significant differences can be pointed out between the tested electrodes compared to the previously shown data of the 30 % porosity electrode (red pointing-down triangle, also Figure 7.1 and 7.2). The highest apparent diffusion coefficients at the end of the sodiation (capacity > 200 mAh g^{-1}) are

seen for a porosity of 40 %. The data sets of the other tested electrodes are overlapping for the second cycle. The profiles of the apparent diffusion coefficients retain the step-like profile for the 15th cycle for all porosities (Figure 7.4 (c) and (d)). Within the first 80 mAh g^{-1}, the electrodes show a similar performance. Afterwards, the values diverge towards the second plateau region. Here, the width and minimum value of the plateau seem to depend on the porosity of the electrode. The electrode with 25 % porosity shows the best ionic conductivity (around 1×10^{-8} cm^2 s^{-1}); the worst performance is seen by electrodes of 35 and 40 % porosity (approximately one order of magnitude lower at 1×10^{-9} cm^2 s^{-1}). An increase in diffusion coefficient values can be determined when the constant-voltage step is reached.

The differences within the desodiation branches are less distinct than within the sodiation branch without clear trends pointing out a dependency on electrode porosity (Figure 7.4 (d)). Within the early desodiation process of the 15th cycle (first 100 mAh g^{-1}), the highest apparent diffusion coefficients can be seen for a 35 % porosity electrode, but do not increase as much as for the electrodes of 25, 30, and 40 % porosity at the end of desodiation.

The results show that both, resistivity and ionic mobility, are depending on the state of sodiation/desodiation and cycling. When the electrode porosity is changed, cycled electrodes show altered characteristics; here the higher apparent diffusion coefficients within the low voltage plateau can be linked to lower electrode porosities. The data shows that cycling of the electrodes increases the resistance and reduces the diffusion ability to different extents across the sodiation and desodiation processes. It has been shown that the amount of SEI formation depends on the BET specific surface area of the HC material.[99, 217, 218] The growing insulating SEI affects the electrochemical properties and physical characteristics of cycled electrodes. Hence, the overall increase in resistivity, as seen for all cycled electrodes, is expected. However, at the end of sodiation, the values for the cycled electrodes seem to converge (Figure 7.2 (d)). Assuming an unrestrained growth of the SEI during cycling into the available pore space, all void space (pores) will be filled. Thenceforward, hypothesizing that the surface layer grows on the "geometrical" surface only which is identical for all electrodes, results in a similar resistivity increase independent from the original porosity.

Further, it has been found that pressing and calendering of electrodes enhances the contact between the secondary particles, binder and electronic conductive and therefore increases the adhesion and cohesion between particles and the current collector.[3, 219, 220,

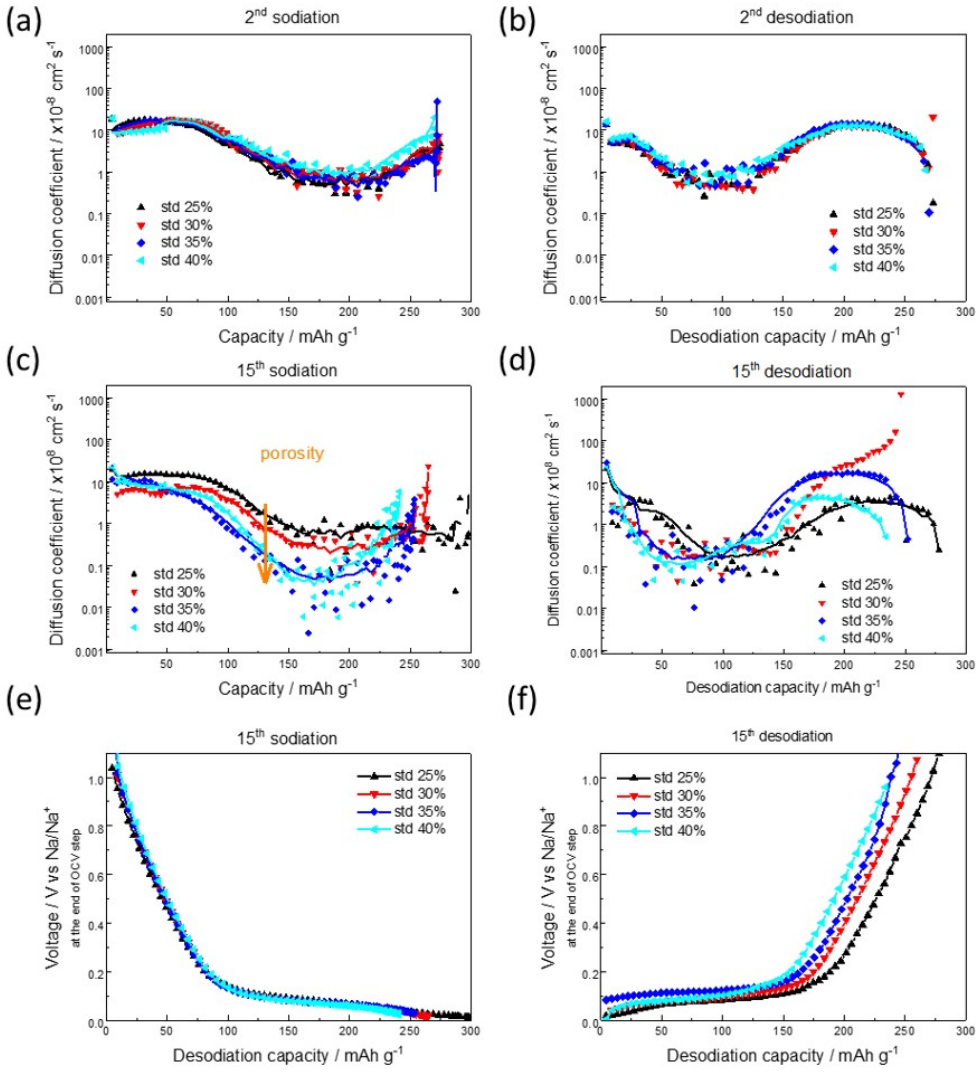

Figure 7.4: Apparent diffusion coefficients versus capacity for HC electrode at different porosities for the second and 15th cycle. (a) and (b) show sodiation and desodiation for the second cycle, respectively; (c) and (d) show sodiation and desodiation for the 15th cycle, respectively. (e) and (f) are replots of Figure 7.3 (e) and (f).

221, 222, 223] Therefore, the result of the lowest resistivity shown for the most densified electrode (25 % porosity) is as expected. Interestingly, the worst performance within the second cycle is not seen for the highest porosity, but the ones of 30 % porosity. High porosities are accompanied by a larger surface area, which increases the electrode-electrolyte interphase and shortens the distance for solid-state diffusion to the current collector. Hence, the higher porosity might compensate for reduced electronic connectivity of the electrode components in uncycled electrodes . In terms of the apparent diffusion coefficients, a higher porosity might indicate a better electrolyte wetting accompanied by better ionic conductivity and shorter diffusion distances for ions within the solid electrode material. Hence, the slightly higher apparent diffusion coefficient values for the high porosity electrode within the second sodiation.

A strong influence of porosity on the ionic diffusion is seen during sodiation on cycled electrodes. Whereas the changes of the apparent diffusion coefficient profile within the first 100 mAh g^{-1} (sloping region of the voltage profile) are marginal, the effect is most pronounced in the low plateau region during the sodiation process where the values diverge by one order of magnitude, comparing the 25 and 40 % porosity. The ionic diffusion might be slowed down by the earlier discussed ongoing SEI formation on the HC electrolyte interface. The electronically insulating characteristics of the SEI are well-known.[70, 224] However, assuming a reduced ionic conductivity (liquid electrolyte versus solid SEI), in addition to the electronic insulating characteristics of the SEI, would lead to an overall reduction of the apparent diffusion coefficient. Hence, the ion mobility might be reduced by the ongoing growing SEI, as diffusion within the liquid electrolyte is partly replaced by solid-state diffusion through an increasingly thicker surface layer for intercalation and deintercalation. Therefore, the same effect applies to the apparent diffusion coefficient as for the resistivity. Conducted experiments using Focused Ion Beam SEM (FIB) to generate cross-sections of the electrodes show a surface layer growth into the pore space of the composite electrodes (Figure 7.5).

In regards to the desodiation, the poorer performance might be caused by partial sodium plating at low potentials during sodiation (Figure A.10). It is highly likely that the plated sodium blocks the deintercalation paths and therefore enhance the electron and ionic migration length within the solid electrode material, increasing the resistivity and interfering with the apparent diffusion coefficient. Cycled electrodes with a lower porosity

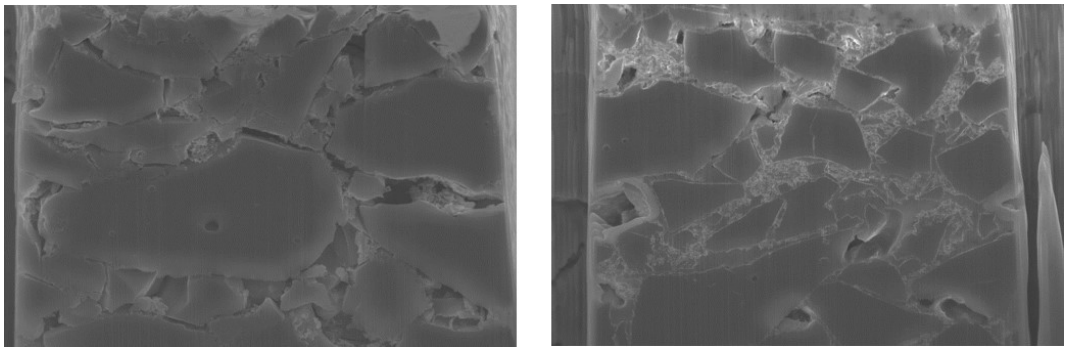

Figure 7.5: Crossection images of FIB cut (15×20 μm) of two electrodes of 30 % porosity. Left: uncycled; right: cycled.

deliver the best durability based on mass transport effects, although other factors, such as electrical interconnection influence the overall optimal performance.

7.3 Conclusion

Different sodiation mechanisms have been postulated for HC, and discussions are still ongoing. The results show at least a two-step process, separated into the voltage sloping region, low voltage plateau region, and towards the end of sodiation. The different stages are associated with different apparent diffusion coefficients, and therefore, it is highly likely that at least two different sodiation processes are involved. The results shown in this work cannot be used to investigate processes on the material level but add more information to the picture.

Here, for the first time, GITT was used to determine the ionic and electronic mobility in respect of the overall porosity of composite electrodes. The results demonstrate that GITT can be utilized to determine the resistivity and the apparent diffusion coefficients for HC composite electrodes. Furthermore, the apparent diffusion coefficients and DCIR show a strong dependence on SoC and SoH, as well as on the overall porosity of the electrodes.

Regarding the DCIR the main observations are:

- Changes are most dominant within the low plateau region of the HC voltage profile.
- In all sodiation graphs, the DCIR profile starts at high, but decreasing resistivity values before levelling on low values within the low voltage plateau region.
- In all desodiation graphs the resistivity values remain low until the last 20-30 mAh g^{-1} indicating that the desodiation process linked to the sodiation process at the lower voltage plateau occurs during all desodiation steps.

- Within the profile of the cycled electrodes, the changes in DCIR values within the sloping region indicate additional processes to intercalation.
- Based on the observation of sodium deposition on the electrode surface after cycling, DCIR measurement might be used to observe the plating mechanism.

The results indicate, that the different areas of DCIR values can be linked to the sloping and low plateau voltage profile of the HC composite electrode. Hence, DCIR measurements might be able to be used to indicate changes in the sodiation mechanism. Additionally, the change in DCIR during SOC could indicate plating in real time for sodium ion batteries. If confirmed, a fast and reliable DCIR measurement can be used to grade batteries and prevent fatal defects.

The main observations regarding the apparent diffusion coefficient are:

- The diffusion process in uncycled electrodes seems to be reversible for sodiation and desodiation.
- The ionic mobility decreases with cycling. The effect is distinct in the low plateau voltage region and pronounced for desodiation.
- Although different electrode porosities show no effect on the ionic mobility in the second cycle, a trend based on porosity can be seen for the cycled electrodes. The results show a stronger depletion of ionic movement with increasing porosity for the sodiation branch.
- For desodiation the effect seems reverse: the apparent diffusion coefficients decrease with decreasing porosity.

For sodiation, the results show a clear correlation of porosity and ionic mobility. Electrodes with lower porosity show a better ionic mobility retention upon cycling. The data gained from FIB experiments on cycled and uncylced electrodes show, that a surface layer growth within the pores of the electrode causing electrolyte depletion and hence lowering the overall ionic conductivity of the electrode. Considering an unrestricted surface layer formation, electrodes with a higher porosity provide more space for enhanced growth resulting in an increased thickness and therefore reduced ionic mobility.

The effects on desodiation are different, and might be influenced by sodium plating upon the previous sodiation cycle. Further, the results show that, as true for all electrodes,

there is a trade-off between electronic and ionic conductivities. Hence, it is important to maintain the ionic conductivity within the composite electrode. Subsequently, the approach of producing a highly electronic conductive electrode and neglecting the improvement of ionic pathways in composite electrode might not be fully rewarding. The adaptation in, e.g., fast charging and discharging methods can be made to consider the behaviour of resistivity and ionic conductivity depending on the SoC. This will maximize battery performance while reducing the ageing and side-effect, which are caused by high polarization. Hence, based on these results consecutively conducted experiments with electrodes comprising different ratios of electronic and ionic conductive additives were tested for capacity retention, rate capability, as well as for ionic and electronic conductivity (Chapter 8).

Chapter 8

Optimisation of HC electrodes by implementation of an ionic conductive additive

To enable fast charging of sodium ion batteries and eliminate metallic dendrite growth on the electrodes an improvement in electrode design is required. In this Chapter, the benefit of a mixed composite electrode containing ionic and electronic conducting additives for a sodium-ion battery negative electrode is shown. HC electrodes with 5 % additive containing different proportions of zeolite and carbon black are coated. The performance of the electrodes is elucidated through electrochemical and physical characterization methods; fast sodiation, EIS, GITT and SEM. The addition of zeolite improves the sodium-ion transport diffusivity within the composite electrode by an order of magnitude at low voltages and high states of charge. EIS shows significantly lower series and surface electrolyte interface (SEI) resistances in the zeolite containing electrode after cycling. The capacity retention at higher rates is improved and a significant reduction of sodium dendrite growth was observed after cycling. SEM images confirm that porosity is still present in the zeolite containing electrode samples, enabling a pore network for sodium ion transport. These results emphasize the importance and limitations of ionic transport within HC electrodes, and the required optimisation between electronic and ionic conductivity for sodium ion transport in these electrodes. The findings of this Chapter were published in "Batteries & Supercaps".[199]

8.1 Introduction

The spheric ionic conductive additive (NanoH-ZSM-5 P91, ACS Materials) is made of SiO_2 and Al_2O_3 in a molar ratio of 1:91.[225] A cage size of 5 Å was chosen to channel sodium

ions efficiently (van der Waals radius: 227 ppm). Zeolite-like materials have been used in lithium-ion batteries before as a solid electrolyte [226, 227] or to capture moisture [228, 229]. Some patents state the use of metal composites (metal oxide and metal-carbon alloyed), such as Zeolite, within the electrode slurry for lithium-ion batteries.[198] Here, composite electrodes were manufactured, adding a commercially available solid ionic conducting additive to the electrode slurry to retain ionic pathways and maintain the ionic conductivity of the electrode compound. The authors are not aware of any publications of an approach using zeolite within the electrode slurry to enhance or maintain the ionic conductivity within the dried composite electrode structure for sodium-ion batteries to date.

This chapter compares the modified zeolite containing composite electrodes to standard electrodes to evaluate the influence of the additive within the electrode structure onto the electrode performance. Hence, GITT and desodiation tests up to 5 C (based on a capacity of 330 mAh g^{-1}) are conducted to determine ionic diffusion and rate performance of the electrodes. Besides the enhanced ionic conductivity, faster ion transport might be beneficial to reduce dendrite formation at high sodiation rates. The dendritic growth at high sodiation rates is a safety concern as the metallic dendrites cause internal short circuits accompanied by exothermal reactions and gas evaluation of the electrolyte.[230, 231, 232, 233, 234, 235, 236]

8.2 Results and discussion

Three composite electrodes have been characterized and compared regarding their sodium-ion diffusibility in the fresh and cycled state, rate performance, and physical characteristics such as pore space and surface formation. For electrochemical characterization, GITT and rate testing have been conducted. Post mortem analysis was determined using SEM and EDS.

8.2.1 Electrochemical characterization

Three electrodes were made as described in Chapter 4.1 with varying compositions of electronic and ionic conductivity additive, zeolite. The Standard Electrode contains 90 % HC, 5 % binder, and 4 % CB and is identical to the electrodes determined in the previous chapters. Two sets of electrodes were made, replacing a part of the CB with a solid ionic conductor (Nano-ZSM5 P91, ACS Material®). Electrode A contains 90 % HC, 5 % binder, 4 % CB, and 1 % ionic conductor. Electrode B contains 90 % HC, 5 % binder, 1 % CB, and 4 %

ionic conductor. All electrodes were calandered to a porosity of 35 %, whereas the electrode thickness was measured with a micrometer gauge. Details are given in Table A.4 and A.5 in Appendix A. The 3-electrode cell were assembled following the routine outlined in Chapter 4.2, the conducted test protocols for formation, GITT, EIS, and rate tests are detailed in Chapter 4.3.1.

Inks as being used for electrode preparations were made and coated using Mylar foil as substrate rather than a current collector foil. This enables us to neglect any contribution of the current collector and determine coating conductivity values only. A four-point probe (linear array, Jandel cylindrical four point probe with HM21 hand held meter) was used to measure the in-plane conductivity of the coating. To take the measurements a current was passed between the outer two probes, and the voltage difference was measured between the two inner probes. The probe was placed on different areas of the electrode sheet following a pattern from top to bottom and left to right, and an average value was written down. The pattern was kept identical for all electrodes.

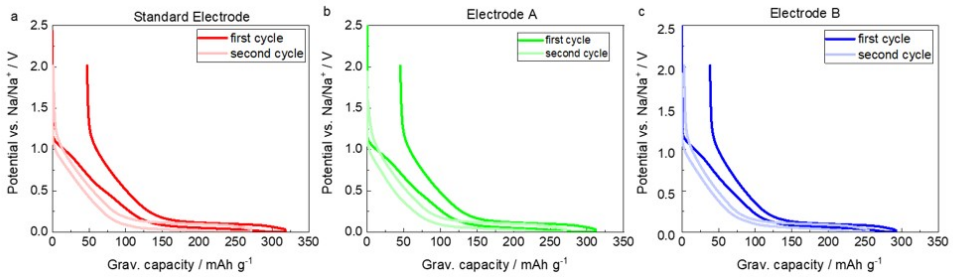

Figure 8.1: First and Second cycle of HC electrodes vs Na/Na^+ for (a) Standard electrode (b) Electrode A with 4 % CB and 1 % Ze, and (c) Electrode B with 1 % CB and 4 % Ze.

The physical and electrochemical characteristics of the electrodes are summarised in Table 8.1, and the first two cycles at 10 mA g^{-1} shown in Figure 8.1. The specific capacity and FCL was similar for the Standard Electrode and Electrode A (1 % zeolite additive), whereas the specific capacity and FCL were slightly lower for Electrode B (4 % zeolite additive). The addition of zeolite leads to an increase in the electrical sheet resistance of the electrode, (Table A.6 in Appendix A). Further electrochemical testing parameters can be found in the Experimental section.

8.2.1.1 Apparent diffusion coefficients and resistance

GITT was performed to determine the apparent diffusion coefficients of sodium-ions within the electrode structure.[21, 28, 30, 40, 51, 153, 237] The resulting apparent diffusion coef-

Table 8.1: Summary of working electrode properties as used for the electrochemical testing listing composition (A:Active (A), B: binder, C: carbon black, Ze: Zeolite), porosity, electrode loading, and active material (AM) loading in gram per square meter (GSM)

	A:B:C:Ze	**Electrode porosity** (%)	**Electrode** loading (GSM)	**AM** loading (GSM)	**FCL** (%)	**Specific Capacity** (mAh g^{-1})
Std Electrode	90:5:5:0	35	129	116	14.8(2)	272(2)
Electrode A	90:5:4:1	35	134	120	14.5(1)	271(4)
Electrode B	90:5:1:4	35	122	110	13.0(2)	254(1)

ficients were calculated using the equation

$$\tilde{D} = \frac{4}{\pi\tau}\left(\frac{m_{AM}\cdot V_M}{M_{AM}\cdot S}\right)^2\left(\frac{\Delta E_S}{\Delta E_t}\right)^2, \qquad \left(\tau \gg \frac{L^2}{\tilde{D}}\right) \tag{8.1}$$

as introduced by Weppner and Huggins (see Nomenclature for more information).[40] ΔE_S and ΔE_t were obtained graphically, S was calculated from the electrode thickness, porosity and particle size (Table A.5).

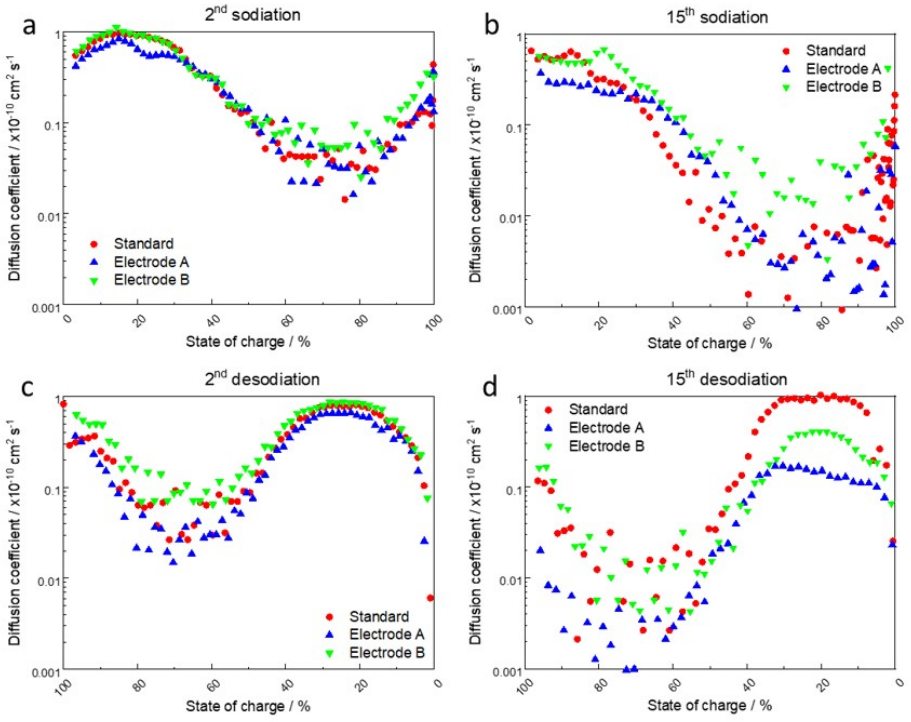

Figure 8.2: Apparent diffusion coefficients versus the state of sodiation and desodiation, of one set of three different electrodes: Standard Electrode (5CB, red circle), Electrode A (1Ze:4CB, blue triangle), and Electrode B (4Ze:1CB, green triangle). (a) Profile during the second sodiation; (b) profile during the second desodiation; (c) profile during 15th sodiation; (d) profile during 15th desodiation.

Figure 8.2 shows the results of the diffusion behavior for the second and 15th cycle for one set of electrodes. The graphs display the effects of cycling upon the apparent diffusion coefficient. Figure 8.2 (a) and (b) show the values based on the second cycle sodiation and desodiation, respectively. All electrodes show a similar behaviour following a wavelike profile; with a peak until around 100 mAh g^{-1} (approximately 20 % SoC) with a maximum of 1×10^{-10} cm^2 s^{-1} followed by a trough until approximately 200 mAh g^{-1} (approximately 70 % SoC) with a minimum of 1×10^{-12} cm^2 s^{-1}. The profile for desodiation features a similar trend in reverse, with smaller differences at the end of desodiation in terms of the length of the maximum plateau (175 mAh g^{-1} onwards). Figure 8.2 (c) and (d) display the apparent diffusion coefficients versus capacity based on the 15th cycle. The characteristic wavelike profile, as observed for the second cycle, is maintained for this 15th cycle data for all electrodes during both sodiation and desodiation. However, the absolute values of the apparent diffusion coefficient values of all electrodes are decreased compared to those of the second cycle. There are several key trends in this data:

- The diffusion coefficient between 0-50 % SOC is several orders of magnitude higher than the 50-100 % SOC.
- Samples which contain zeolite additive show higher apparent diffusion coefficients between 50-100 % SOC than those without.
- The apparent diffusion coefficients for sodiation and desodiation are very similar for the 2nd cycle, but not for the 15th cycle.
- The diffusion coefficients for sodiation on the 15th cycle are slightly lower than that of the desodiation and between 50-100 % SOC are higher with the zeolite additive than without.
- The desodiation shows significantly higher effective diffusion coefficients for the Standard Electrode than that containing zeolite additives.

These results indicate that the zeolite additive has a positive effect upon the low plateau sodiation, which is close to 0 V vs Na/Na$^+$, but has a negative effect upon desodiation at the low states of charge 50-0 %. Table 2 lists the maximum and minimum apparent diffusion coefficient values for the 2nd and 15th sodiation and desodiation.

Table 8.2: Average values for the maximum (max) and minimum (min) of apparent diffusion coefficients for the 2nd and 15th sodiation and desodiation $\times 10^{-10}$ cm^2 s^{-1}. Std Electrode: 5 % CB, Electrode A: 4 %CB : 1 %Ze, Electrode B: 1 %CB : 4 %Ze.

	2nd Cycle Apparent Diffusion Coefficient $\times 10^{-10}$ cm^2 s^{-1}				15th Cycle Apparent Diffusion Coefficient $\times 10^{-10}$ cm^2 s^{-1}			
	Sodiation		Desodiation		Sodiation		Desodiation	
SoC (%)	15	70	25	70	15	70	25	70
Std. Electrode	1	0.028	0.81	0.033	0.58	0.0012	1	0.005
Electrode A	0.83	0.028	0.65	0.015	0.26	0.0019	0.15	0.0015
Electrode B	0.96	0.052	0.86	0.067	0.47	0.0145	0.4	0.0072

Apparent diffusion coefficients of the sodium-ions within HC-based on GITT have been published in the literature.[29, 32, 51, 84, 89, 92, 99] However, most of the published data is generated on uncycled electrodes and does not take cycling and the composite electrode features such as porosity and composition into account.[25, 150, 238] The pores within the electrode function as a reservoir of the highly ionic conductive electrolyte. Hence, the porosity, and the growth of the SEI layer influences the ionic mobility at macroscale.

In this study the porosities of the as-made electrodes are kept identical. Consequently, the change in the electrode performance observed here is due to the additive, and its effect upon the change in the porosity during cycling. The EIS results are shown in Figure 8.3. These show the difference in the resistances of the three electrodes in the first and second cycle, and after cycling. In all cases Electrode B shows a greater resistance initially. The resistance at 0.005 V vs Na/Na$^+$ and 1.0 V vs Na/Na$^+$ all increase with cycling, however the Standard Electrode shows significant more resistance after cycling at 0 V vs Na/Na$^+$ compared to Electrode A and Electrode B. At 1.0 V vs Na/Na$^+$ the resistance of the Standard and Electrode A was very similar in the first and second discharge, after cycling the resistance of the Standard electrode was again significantly greater than either Electrode A or Electrode B. The series resistance of the cells also changed with cycling, and these are shown in the Appendix in Tables A.7 and A.8. The series resistance of the Standard Electrode and Electrode A both increase more than Electrode B. The results of the GITT measurements indicate that the addition of an ionic conductivity additive effects the sodiation of the HC at the low voltage region, between 50-100 % SoC. From the EIS results we can observe that in the low voltage region, the total charge transfer resistance after cycling of the Standard Electrode increases more than the electrodes with ionic additive; in the high voltage region

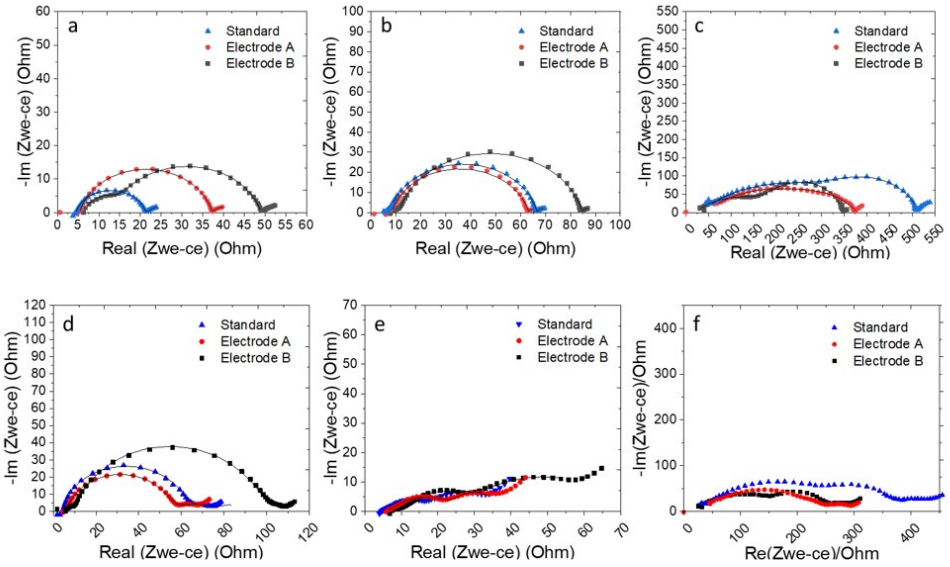

Figure 8.3: EIS for HC composite electrodes; blue triangle (Standard), red circles (Electrode A), black squares (Electrode B) and the equivalent circuit fitts (black line) at 0.005 V vs Na/Na^+ for (a) first discharge, (b) second discharge and (c) after 10 cycles. At 1.0 V vs Na/Na^+ for (d) first discharge, (e) second discharge and (f) after cycling.

the same is also true. The EIS at 0.005 V vs Na/Na^+ for the Standard and Electrode B was fitted using an equivalent circuit model (Table A.1). As observed from Figure 8.3 f after cycling the resistance from the SEI decreases with increasing zeolite content.

8.2.1.2 Rate testing

Rate testing at different rates is conducted to understand the polarisation and capacity retention of electrodes containing ionic (zeolite) and electronic (CB) conductive additives. C rate is based upon rated capacity of 300 mAh g^{-1}. Figure 8.4(a) shows the voltage profile for a standard HC electrode at three different C-rates, ranging from 0.1 (30 mA g^{-1}) to 5.0 C (1500 mA g^{-1}), measured in a 3-electrode cell. A 3-electrode electrochemical set-up (see Experimental) was used to ascertain the true polarisation increase on the working electrode rather than the combined working and counter.[30, 123, 239] The increase in rate causes an increase in polarisation on the working electrode, and therefore the average voltage upon desodiation increases. Hence, the cut off voltage is triggered earlier, and the capacity obtained decreases. This issue is addressed with the use of a three-electrode setup as used here.

The rate tests with increasing desodiation rates were conducted after formation (two symmetrical cycles at 0.2 C). After each desodiation, the HC WE was fully sodiated by applying a CCCV sodiation at 0.2 C. The desodiation or charging of the HC (in a half cell)

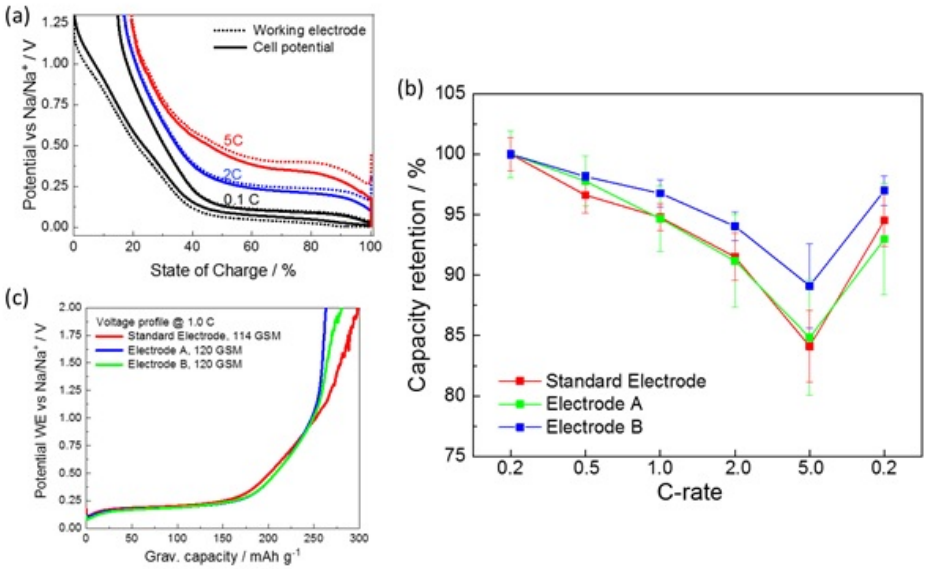

Figure 8.4: Performance graphs of rate testing. (a) Profile of sodiation and desodiation profiles at different C-rates for cell (straight) and the working electrode (dotted) potential at 0.1, 2, and 5 C versus SoC for a Standard Electrode; (b) Capacity retention for fast desodiation at different C-rates. Capacities are based on three test cells and measured via CCCV sodiation (5 mV, 0.01 C) at 0.2 C after each fast desodiation; (c) desodiation voltage profiles at 1 C for a selection of three different composite electrodes versus capacity.

at 1 C is shown in Figure 8.4 (c), the higher voltage cut-offs are included here to show the noisy signal at the higher voltages. This noise is typically observed when sodium dendrites are formed and touch to form an instantaneous short circuit the heat produced subsequently destroys or melts the dendrite.[32, 83, 201] This phenomena is termed a 'soft short' [208, 240, 241, 242, 243, 244] and is accompanied by large coulombic inefficiencies between the charge and discharge capacities. The graph shows that with zeolite in the electrode, less noise is observed. The electrode which contains 1 % nano zeolite, shows less noise than the 4 % nano zeolite, indicating that there is still a trade-off between electronic and ionic conductivity requirements in the electrode which require further optimisation. When these conductivities are optimised correctly this leads to less sodium plating. In order to evaluate the actual level of desodiation at these increasing rates, a low rate (0.2 C) CCCV discharge (or sodiation) was performed, with a 5 mV and 0.01 C cut-off, the % capacity observed is shown in Figure 8.4 (b).

The observed initial capacities and FCL are shown in the the Appendix (Figure A.12) and are similar to the data stated in the literature.[89] To account for ageing effects, which are observed during cycling, the low C-rate of 0.2 C is repeated at the end of the fast charging

tests to provide a comparative capacity. Compared to the third cycle at 0.2 C, the highest losses (around 8 %) can be seen for Electrode B. The losses for the Standard Electrode are around 6 %. In contrast, Electrode A has a total capacity loss of 4 %.

A comparison of three voltage profiles of the second and eight sodiation is given in Figure 8.5. The addition of the ionic conductivity additive is accompanied by an increase in polarization, which can be seen in Figure 8.5 (a). The average voltage within the plateau region is shifted to lower potentials, triggering the constant-voltage step at lower capacities (in-set). After the rate test, the voltage profile for all three cells has changed (Figure 8.5 (b)). Capacity losses are noticeable within the low plateau region, resulting in a ratio change of sloping versus plateau voltage region. Moreover, the polarization within the voltage plateau region increases compared to the second sodiation. The effect is most pronounced for the Standard Electrode and shows a similar profile for Electrode A and Electrode. B. Polarization increases with cycling due to increases in internal resistance. A lower polarization enhances obtainable capacities, especially at higher rates.

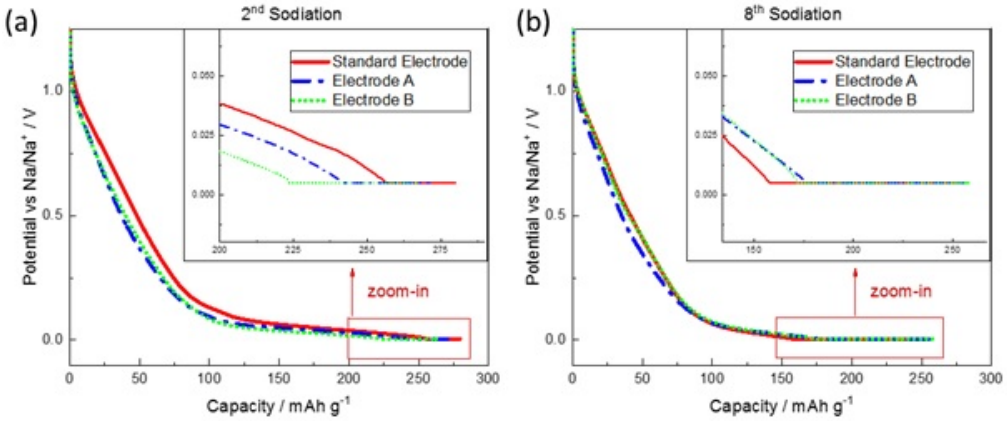

Figure 8.5: Sodiation profiles of the second (a) and eighth (b) sodiation for the Standard Electrode, Electrode A, and Electrode B.

The discharging capacities decrease with increasing discharge current for all tested electrodes. Also, a distinct decrease in capacity can be seen for the Standard Electrode when the rate is changed from 2 C to 5 C.

Table 8.3 lists the average desodiation capacities, as displayed in Figure 8.5 (c). The observed desodiation capacities at different rates of the Standard Electrode and Electrode A are similar, whereas the cells of Electrode B show a lower desodiation capacity. This is due to the increase in electrical sheet resistance (Table A.6). A significant increase in electrical sheet resistance is observed when the ionic conductivity additive content is increased, or

Cycle C-rate	Standard (5 %CB)		Electrode A (4 %CB:1 %Ze)		Electrode B (1 %CB:4 %Ze)	
	Capacity mAh g^{-1}	percentage %	Capacity mAh g^{-1}	percentage %	Capacity mAh g^{-1}	percentage %
1st / 0.2	303(3)	111	313(1)	116	301(8)	117
2nd / 0.2	273(2)	100	270(2)	100	258(5)	100
3rd / 0.2	271(4)	99	266.8(9)	99	255(5)	99
4th / 0.5	262(4)	96	261.8(9)	97	250(5)	97
5th / 1.0	257(3)	94	258.(3)	96	242(7)	94
6th / 2.0	248(5)	91	250(3)	93	233(10)	90
7th / 5.0	228(8)	83	237(9)	88	217(7)	84
8th / 0.2	256(6)	94	258(3)	96	237(11)	92

Table 8.3: Average desodiation capacities based on three cells per set. Values are given in gravimetric capacities based on the HC content. Percentage values are based on the second cycle capacities.

CB content is decreased. Also, DCIR measurements conducted during GITT measurements show an increase in resistance for Electrode B compared to the Standard Electrode (Figure A.13). Electrode A shows the best capacity retention for all currents above 1 C as well as after the rate test, when examined at 0.2 C in both absolute and percentage values. The Standard Electrode and Electrode B show similar performance (excluding the FCL), including a higher dependency on the current rate and higher overall losses (from the second to the eighth cycle).

8.2.2 Physical characterisation

The cycled electrodes were dismantled, and the physical and morphological changes investigated. Therefore, cycled electrodes are compared with fresh, as-made, electrodes. Photographs of two cycled electrodes (Standard Electrode and Electrode B) after cell dismantling can be found in the Appendix (Figure A.22). Sodium metal depositions are identified on both electrodes, showing higher amounts of deposition on the Standard Electrode than on Electrode B. In Figure 8.6 SEM surface images of uncycled and cycled electrodes show a porous structure of large HC particles (D_{50} particle size distribution as given by technical datasheet: 9 μm) and electrode additives. The uncycled Standard Electrode (Figure 8.6 (a)) shows large HC particles embedded in a matrix of binder and CB where the edges and interspaces of the HC particles can be seen to have a higher concentration of covering with CB.

Figure 8.6 (b) shows an uncycled electrode B with 4 % zeolite, the small cubic addi-

tives are the zeolite which are dispersed throughout the electrode along with the CB (small spherical particles). Most of the ionic conductivity additive "nests" in combination with the CB in the interspaces of the HC particles. In these uncycled electrodes the edges of the HC particles appear sharp, and the additives (binder, CB, ionic conductivity additive) can be distinguished from the HC particle. In contrast, after cycling a film covers the HC particles embedding the CB into its matrix (Figure A.23). Features appear less distinct, and HC particles less sharp.

The cross sectional images of the Standard electrode and Electrode A are shown in Figure 8.6 (c and d). Where possible, the samples were transferred under inert conditions; however, contamination of the zeolite electrode samples and exposure to air limited any further analysis of Electrode B. The porosity of both electrodes are low, and an insulating layer which charged under the SEM, can be observed upon the surface of the HC. In the Standard Electrode, there appears to be no small porosity between the HC particles, this will cause problems for sodium ion transport between the particles, as there is no pore interconnectivity for the electrolyte transport. In the sample which contains the zeolite additive, an insulating surface covering is still apparent on the HC, however the growth of the interface appears less than in the Standard Electrode, and small pores are observed. Further studies were performed upon the Standard Electrode in order to understand the reduction in apparent diffusion coefficient and the increase in resistance after cycling.

8.3 Conclusion

In this work, the effect of electrode formulations is investigated by partly substituting the electronic conductive additive CB with the ionic conductivity additive zeolite. A negative electrode with weight 115(±5) GSM and 35 % porosity was investigated where the electronically conductive CB was partly substituted with the ionically conducting zeolite. The ratio of additive to active material and binder content was kept constant (90:5:5, active:binder:additive). Electrochemical techniques; galvanostatic cycling, fast sodiation, EIS and GITT were used to determine the ionic conductivity, resistance, rate performance, and capacity retention of the composite electrodes. The physical characteristics such as porosity changes during cycling were investigated using electron microscope imaging. The electrode composites which contain zeolite:carbon compositions (4:1) show improved rate performance (90 % at 5 C) and cycling stability where less sodium plating is observed. The effective diffusion coefficients extracted from the 15^{th} cycle shows an order of magnitude in-

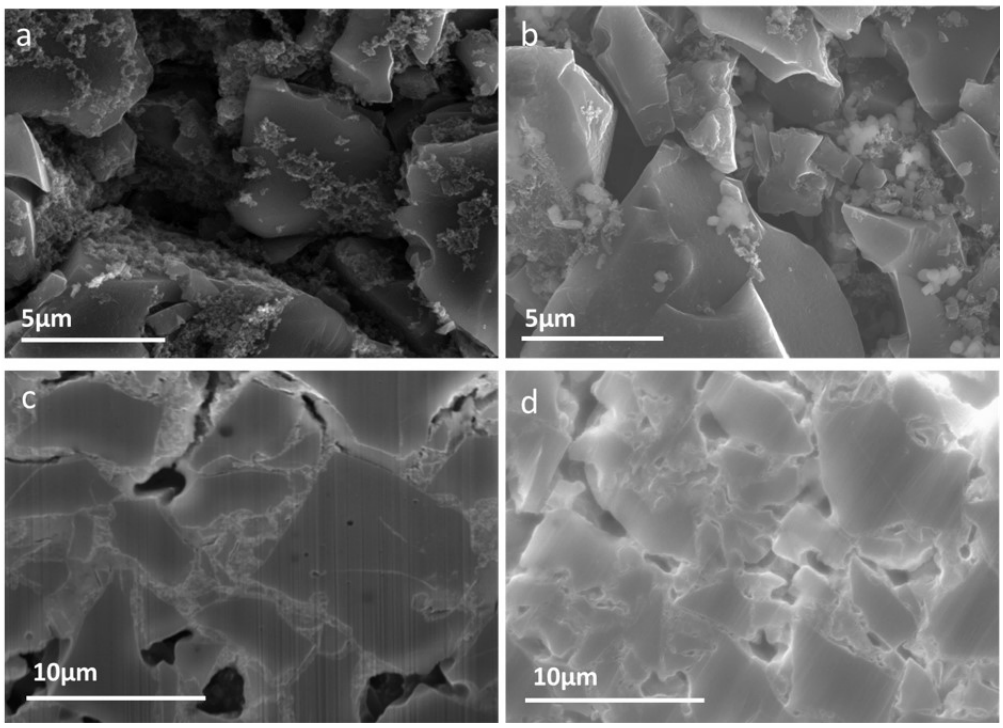

Figure 8.6: SEM images of an uncycled (a) Standard Electrode and (b) Electrode B (4 % Ze), and cross-sectional analysis of cycled electrodes (c) Standard Electrode (d) Electrode B detailed imaging of the particle network at 20 k (lower row).

crease upon the lower voltage plateaux (15 % SOC) from 1.5×10^{-12} cm^2 s^{-1} (4:1) compared to 1.2×10^{-13} cm^2 s^{-1} (0:5) during sodiation. Upon desodiation at higher states of charge (70 % SOC) within the sloping voltage region, the ionic conductivity is not the limiting factor and the effective diffusion appears decreased (0.4×10^{-10} cm^2 s^{-1} (4:1) 1×10^{-10} cm^2 s^{-1} (0:5)). This shows that changes in the ionic and electronic conductivity pathways during cycling is an important consideration when designing electrode micro-structures. The physical characterization of the electrodes indicate that an interphase layer grows into the pores of the electrode micro-structure during cycling, this correspondingly results in a reduction in electronic transport and an increase in Ohmic resistance and polarization. The growth of this interphase affects the porosity, 3-D electrode electronic and ionic conductivity due to the incorporation of the conductive carbon into the interphase reducing electronic transport properties. This also reduces sodium-ion transport pathways through vanishing electrolyte channels. The addition of a nano-zeolite additive in the electrode reduces the SEI on the HC and helps keep open the sodium ion transport pathways. The ohmic resistance and the SEI resistance is reduced in these electrodes after cycling. Moreover, the zeolite additive helps to reduce sodium plating on the carbon surface at higher rates and upon cycling. This mixed

ionic and electronic conductive approach for sodium-ion HC electrodes enhances rate and improves aging characteristics, which may enable faster charging of sodium-ion batteries.

Chapter 9

Conclusions and Outlook

The aim of this PhD project is to link physical electrode properties to electrochemical performance. Initial testing set the focus on the investigation of the ionic mobility contribution towards the overall cell performance. Thorough studying of test cell set-up and analysing the parameter dependence of the electrochemical methods prior to changing electrode characteristics provided the basis for a comprehensive study on HC composite electrodes for sodium ion batteries. Within this project characteristics of standard HC electrodes, containing 90 % active material, 5 % binder and 5 % carbon black, were gradually changed and investigated. The data sets indicate an issue in depletion of ionic pathways within the electrode structure, hence the Standard Electrodes were modified by adding an ionic conductor to act as an electrolyte reservoir. A full characterisation and comparison of the Standard Electrode and two modificated composite electrodes was conducted. The results show an improvement in cycle stability, rate performance and potential gain in safety when a mix of ionic and electronic conductive additives is used.

Conclusions

Sodium-ion batteries are one of the most promising alternatives to lithium-ion batteries. Besides, their potential benefit in cost-reduction, most materials needed for sodium-ion batteries more abundant and less-restrictive in access . Moreover, sodium-ion batteries can be handled as a drop-in technology using the established infrastructure. However, HC, the material of choice on the anode side, lacks in performance compared to graphite in lithium-ion batteries. To compete with the established technology, sodium-ion batteries need to be suitable for high-power and high-energy applications, which is paralleled by a good capacity retention and good rate capability. To conquer the requirements of good rate capability, in this work, HC electrodes were investigated regarding their ionic conductivity.

As a start, different testing set-ups were tested for reliable and reproducible data generation. In Chapter 5 the effects of the housing used, electrolytes utilized and wiring connections set-up were evaluated. The results show that the contribution of the sodium metal counter electrode in half-cell testing is massive. Hence, a 3-electrode set-up is crucial to gain reliable results.

In Chapter 6 three electrochemical testing have been compared to evaluate the apparent diffusion coefficient: GITT, EIS, and EPS. Therefore, a set of identical electrodes was used to conduct each measurement. For the first time, the strengths and weaknesses of those methods regarding the apparent diffusion coefficient are shown. The chapter includes a thorough list of parameters and settings influencing the gained results. It has been pointed out that those techniques have to be used in with caution and the comparability with values stated in literature are not always comparable. Considering all information, GITT was chosen to be the best method to conduct the following experiments.

Unmodified HC electrodes were investigated in Chapter 7. The utilisation of GITT for analysis of the apparent diffusion coefficient gave also insight into the electronic conductive behaviour upon cycling and electrode porosity. The results clearly show a trade-off between ionic and electronic conductivity. Additionally, the gained results indicate a slightly different desodiation mechanism than for sodiation; but further work is required to examine these findings in detail. Besides, the conducted DCIR analysis of the GITT data might enable the user to detect sodium plating on the HC surface. Hereby, defective batteries can be spotted and removed prior fatal malfunction.

The collective information of the previous chapters led to the hypothesis of electrolyte depletion within cycled electrodes. To prove this theory, HC composite electrodes were modified and tested in Chapter 8. The results show that changes in the ionic and electronic conductivity pathways during cycling is an important consideration when designing electrode microstructures. The physical characterization of the electrodes indicate that an interphase layer grows into the pores of the electrode microstructure during cycling, this correspondingly results in a reduction in electronic transport and an increase in Ohmic resistance and polarization. The addition of a nano-zeolite additive in the electrode reduces the SEI on the HC and helps keep open the sodium ion transport pathways. Moreover, the zeolite additive helps to reduce sodium plating on the carbon surface at higher rates and upon cycling. This mixed ionic and electronic conductive approach for sodium-ion

HC electrodes enhances rate and improves ageing characteristics, which may enable faster charging of sodium-ion batteries.

Several mechanisms for sodium ion incorporation have been proposed and the process is still under discussion.[20, 32, 50, 83, 89, 196, 201, 203] Four different models are suggested: "Intercalation-filling" model, "Absorption-intercalation" model, "Absorption-filling" model, and "Three-stage" model. A good overview describing the different models in detail is given by Xie et al. [90] and Chen et al. [245]. Two models are pointed out here. Stevens and Dahn introduced the "Intercalation-filling" model of sodium ions into HC in 2000.[83, 246] The model describes a two-stage process with sodium-ion insertion between parallel or nearly parallel layers within the sloping potential profile and an eventual interaction of sodium with turbostratic nanodomains (TN). This process is followed by filling the pore space within the low potential "plateau region". Other researchers verified the model in the following years.[176, 196, 247] Bommier et al. describe an alternative view stating three different processes ("three-stage" model). The charge storage occurs in the sloping region by binding to the edges/defect sites (e.g., carbenes, vacancies, and dangling bonds on the edges of TN) of the HC. Secondly, within the plateau region, charge occurs due to intercalation of Na^+ between graphene sheets, followed by Na-atom absorption on the sp2 configured pore surface at very low potential below 0.05 V.[32] They validate their findings with electrochemical characterization, Raman and XRD data based on HC synthesized at different temperatures. By varying the synthesis parameters, domain dimensions of the TN along the axial axis and ab planes are controlled, thus modifying the physical characteristics of the material. This proposed mechanism of Na clustering within carbon materials has also been endorsed experimentally and agrees with DFT calculations.[203, 248, 249]

All GITT data presented in this work for sodiation show a three main areas of diffusion. High diffusion values within the HC high potential region, diffusion values of at least two orders of magnitude reduced within the plateau region, and a slightly increase towards the end of the sodiation. The experiments conducted on cycled electrodes with different porosities showed the most significant differences within the plateau region and barely any changes within the sloping profile. These effects were pronounced in electrodes manufactured with higher porosities. The SEM-FIB images of cycled electrodes elucidate the SEI growth into the pores, indicating blocked and reduced pore space. The ionic mobility of Na^+ in HC composite electrodes was investigated using electrochemical methods

only. Hence claims regarding the occuring sodiation processes are speculative. But based on the observations of Chapter 6, 7, and 8, the findings might endorse the "intercalation-filling" model. The effect seen towards the end of the sodiation could be caused by plating of sodium metal on the electrode surface. Physical characterisation techniques, especially in-situ, such as CT, TEM, and Operando 23Na NMR conducted on the manufactured and cycled HC composite electrode will help to investigate those effects further.

Outlook

Within this work, many interesting findings and effects were discovered. Unfortunately, most of those could not be investigated further as it would be to time intense or would have been distractive.

However, regarding the understanding of the sodium metal influence as a counter electrode in 2-electrode experiments, more work is required. Future research might focus on the investigation of sodium 'moss', i.e. dendritic growth vs. bare sodium metal. Also the relation towards the geometry or amount of sodium moss that is generated based on on the surface of the metallic sodium CE or current density used will be beneficial for half-cell testing. For example, if the inflection point between sodium moss and sodium metal stripping can be determined and linked to an increase in impedance, EIS in-situ techniques can be used to investigate ageing effects on sodium and lithium metal electrodes. These results will help to understand the inner processes of lithium and sodium-ion batteries in more detail and furthermore, assist within the development of lithium air batteries.

Regarding the comparison of electrochemical testing methods the influence of real surface data would be of peculiar interest. Real surface data would benefit a deeper understanding of those techniques as well as determine the diffusion process on electrode level. This would not just involve the approx. 15 % volume expansion of the HC material during sodiation, but also surface layer formation, blocked pathways and the influence of other degradation processes occurring during cycling. This way, actual surface changes can be monitored and the diffusion coefficients can be calculated with S depending on SoC and SoH. The gained results can be used to optimise the electrode structure in terms of electronic and ionic mobility to enhance the rate capability and safety, since a more homogeneous current density avoids local overcharge or deep discharge which causes for example electrolyte decomposition and dendrite formation.

Appendix A

Appendices

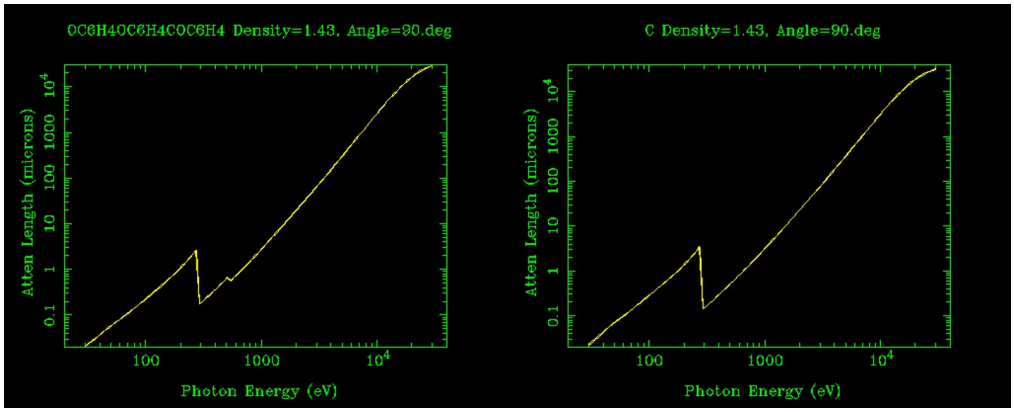

Figure A.1: Profile of the attenuation length of PEEK and carbon between 30 eV and 30 keV.

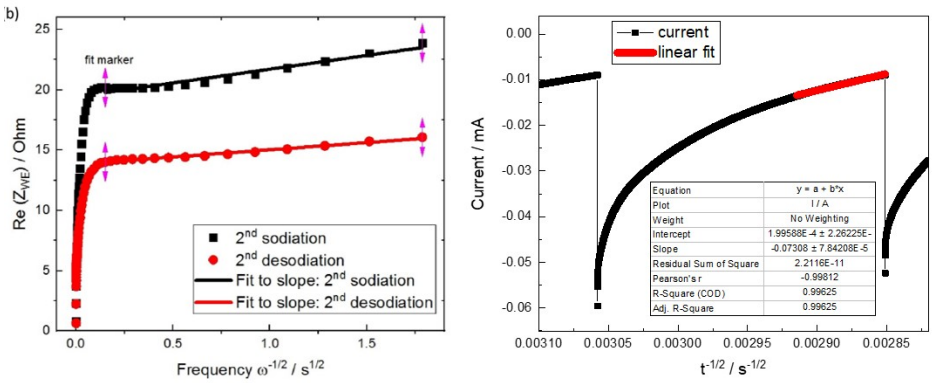

Figure A.2: Left: Example for the linear fitting of low-frequency EIS data using a data generated at a potential of 0.457 V. Right: Example fit for calculating the diffusion coefficients from EPS data.

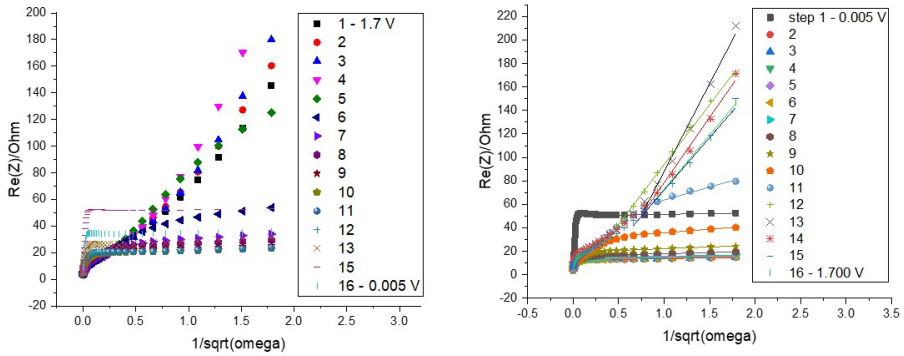

Figure A.3: Graphs of EIS data for warburg fitting.

Table A.1: Analysis data of the slope fitting for σ evaluation

	sodiation			**desodiation**		
Voltage	slope	error	Adj. R-Square	slope	error	Adj. R-Square
1.7	82.72	3.49	0.98	89.39	3.51	0.99
1.587	93.07	4.07	0.98	92.32	4.03	0.99
1.474	104.54	5.91	0.97	111.43	5.59	0.99
1.361	144.53	7.27	0.98	149.32	7.31	0.99
1.248	72.13	2.49	0.99	102.06	1.55	1.00
1.135	14.23	1.25	0.95	21.99	1.81	0.97
1.022	5.25	0.25	0.98	6.01	0.34	0.98
0.909	3.29	0.11	0.99	2.86	0.11	0.99
0.796	2.34	0.04	1.00	1.83	0.02	1.00
0.683	1.87	0.05	0.99	1.49	0.02	1.00
0.57	1.99	0.10	0.98	1.34	0.04	0.99
0.457	2.48	0.12	0.97	1.27	0.05	0.99
0.344	3.97	0.08	1.00	1.49	0.02	1.00
0.231	2.54	0.08	0.99	1.41	0.05	0.99
0.118	0.84	0.06	0.95	1.31	0.04	0.99
0.005	1.00	0.05	0.97	1.28	0.11	0.94

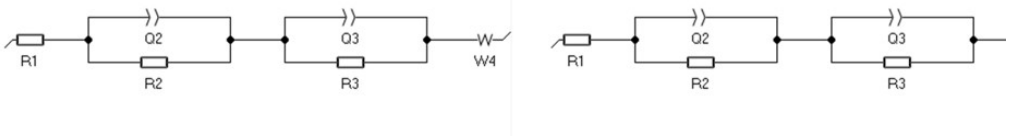

Figure A.4: Equivalent circuits for EIS data fit, with (left) and without (right) Warburg feature. R_1 = R_s (serial resistance), Q_2 = CPE_1, R_2 = R_{SEI}, Q_3=CPE_2, R_3 = R_{CT}, W_4= Warburg.

Table A.2: Fitting parameters for equivalent circuit of the second cycle during sodiation.

V vs Na/Na^+	R_s	R_{SEI}	CPE_1	R_{CT}	CPE_2	warburg
1.700 V	2.33	1.98	-2.17E-04	12.79	5.24E-05	0.86
1.587 V	1.80	3.46	-1.10E-05	8.57	1.52E-04	0.94
1.474 V	1.73	3.28	-1.30E-05	8.64	2.12E-04	1.20
1.361 V	1.64	3.22	-1.48E-05	9.29	3.00E-04	1.30
1.248 V	1.88	2.72	-2.42E-05	9.09	5.02E-04	1.33
1.135 V	1.74	2.64	-2.95E-05	10.08	8.03E-04	1.46
1.022 V	1.69	8.47	-1.66E-04	17.57	5.86E-04	1.67
0.909 V	2.00	141.98	-6.64E-05	153.08	7.33E-05	1.95
0.796 V	1.68	537.78	-4.95E-05	553.79	5.11E-05	2.81
0.683 V	1.81	2216.96	-3.61E-05	2244.25	3.65E-05	4.73
0.570 V	1.72	326.01	-6.23E-04	395.96	7.00E-04	11.47
0.457 V	1.64	499.41	-1.19E-03	888.91	1.38E-03	39.55
0.344 V	1.32	5772.40	-4.92E-04	10355.78	5.21E-04	43.04
0.231 V	1.80	16038.12	-3.16E-04	66731.79	3.02E-04	43.23
0.118 V	3.82	30678.16	-3.14E-04	113213.44	3.74E-04	41.55
0.005 V	3.97	119729.60	-1.47E-04	6620053.27	1.39E-04	42.34

Table A.3: Fitting parameters for equivalent circuit of the second cycle during desodiation.

V vs Na/Na^+	R_s	R_{SEI}	CPE_1	R_{CT}	CPE_2	warburg
0.005 V	3.53	29.29	0.012	229.20	0.003	-
0.118 V	4.18	11 155	0.004	18.36	0.007	-
0.231 V	3.41	22.67	0.012	177.00	0.004	-
0.344 V	3.36	480.20	0.005	14.69	0.009	-
0.457 V	3.52	189.90	0.008	9.40	0.005	-
0.570 V	3.42	12.39	0.008	25.86	0.001	7.759
0.683 V	3.86	5.48	0.002	20.98	0.010	3.322
0.796 V	3.69	35.19	0.011	0.00	0.421	-2.057
0.909 V	4.63	0.07	0.003	18.00	0.004	2.123
1.022 V	4.71	18.48	0.003	21.33	0.328	1.394
1.135 V	4.48	184.90	0.056	20.68	0.002	12.300
1.248 V	4.53	5.37	0.002	9.52	0.003	2.807
1.361 V	5.69	4964.00	0.006	14.01	0.002	-
1.474 V	5.08	2206.00	0.005	21.90	0.005	-
1.587 V	4.66	2261.00	0.004	19.75	0.006	-
1.700 V	2.67	16.78	0.003	n.a.	0.004	-

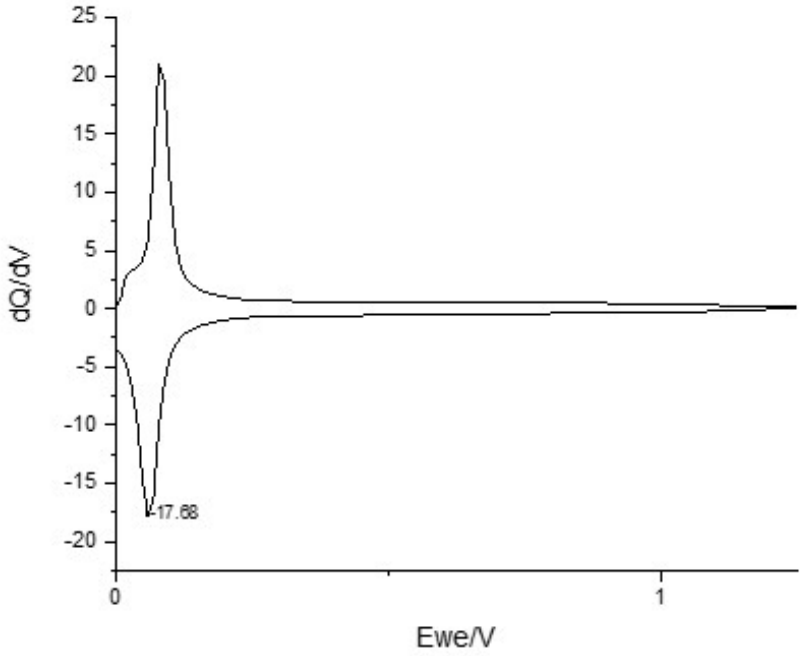

Figure A.5: Differential capacity plot for the 2nd cycle of the EPS measurement.

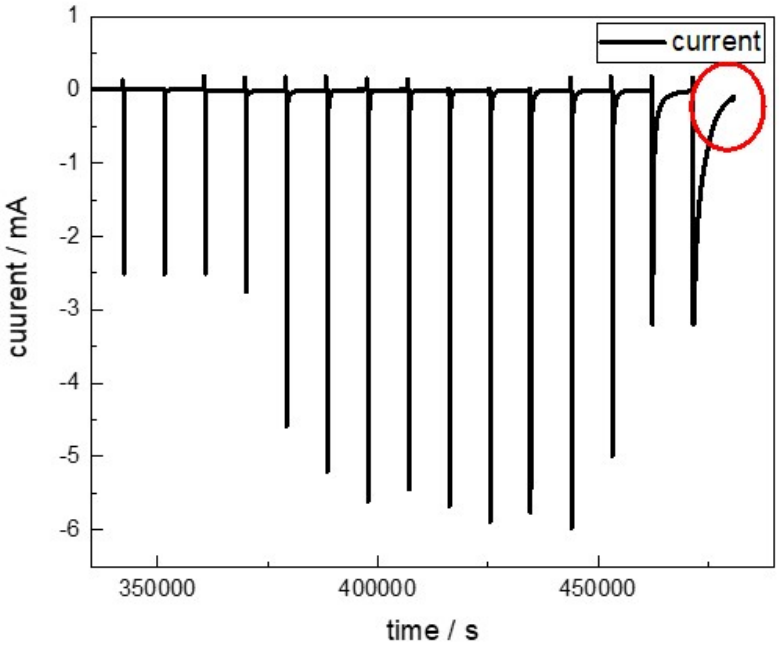

Figure A.6: Current profile during the voltage steps between EIS measurements at desodiation.

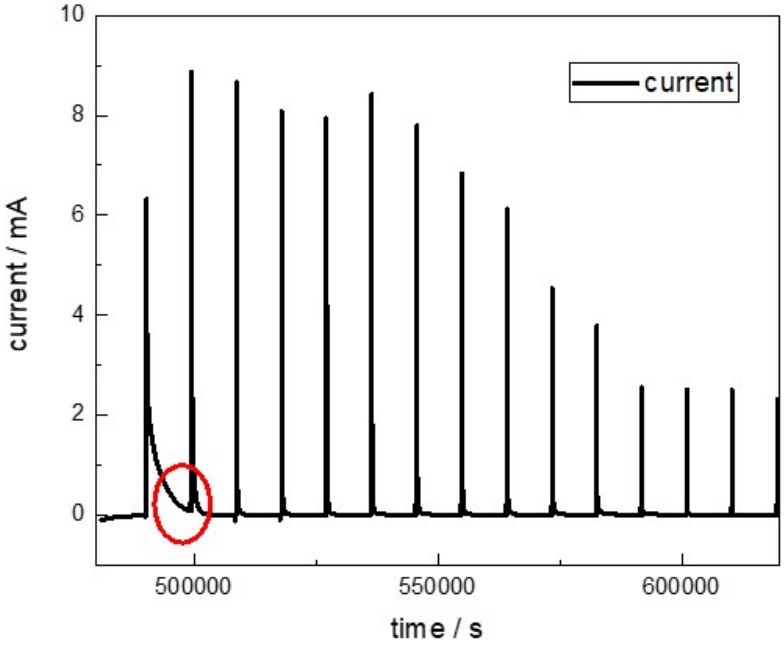

Figure A.7: Current profile during the voltage steps between EIS measurements at desodiation.

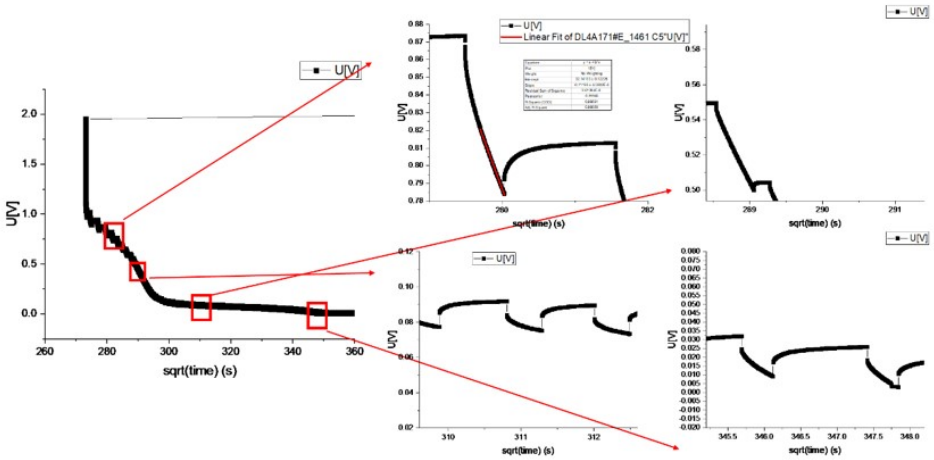

Figure A.8: Voltage profile of GITT measurement versus square-root of time. Left: whole sodiation and desodiation; Right: zoom in on two desodiation and relaxation steps.

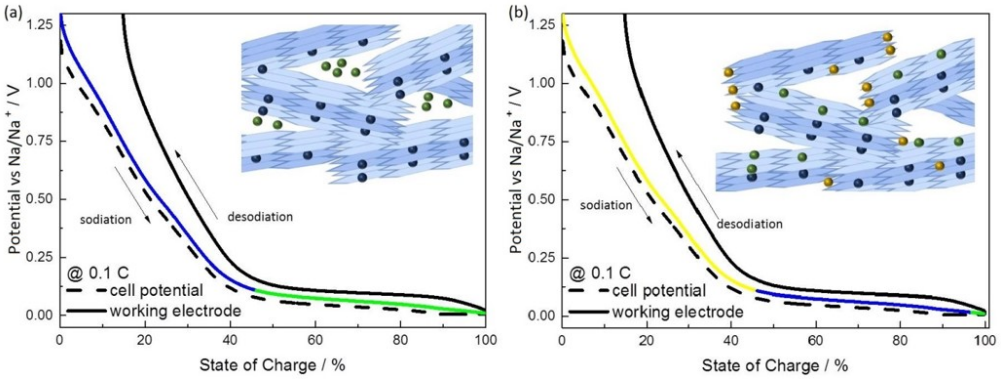

Figure A.9: Comparison of two proposed intercalation models. Figure (a) illustrates the 'falling card house' model, as suggested by Stevens and Dahn [83]. Figure (b) the model as proposed by Bommier et al. [32] They show an illustration of the sodium storage mechanism on and within the HC structure (inset), and the sodiation/desodiation potential versus SoC of the electrode profile with different colours representing the different sodium locations.

Figure A.10: Left: Photographs of cycled electrodes after disassembling showing sodium plating on the electrode surface. Electrode diameter 12 mm. Right: SEM image of the cycled electrode surface.

Table A.4: Summary of porosity and volume fraction calculations 1.

HC content [%]	Binder content [%]	CB content [%]	Ze content [%]	Sheet resistance [Ω/□]
Electrode Composition	mass %	Vol	Vol %	Density gcm^{-3}
HC (D_{50} - 9 μm)	90	60.81	91.58	1.48
PVdF	5	2.81	4.23	1.78
Ze	4	2.24	3.37	1.785
CB C65	1	0.54	0.81	1.86
Average Composition	100	66.4	100	1.506
Electrode Density				0.983

Table A.5: Summary of porosity and volume fraction calculations 2.

Electrode Property	Measurement	units
Coat weight (electrode)	130	g m^{-2}
Thickness	133	μm
Active Electrode Area	1.131	cm^2
Electrode Porosity	35.1	%
Active Volume Fraction	59.44	%
Molar Volume	48.65	cm^3 mol^{-1}
Assumed Formula Weight	72	g cm^{-3}
Active Surface Area	52.73	cm^2

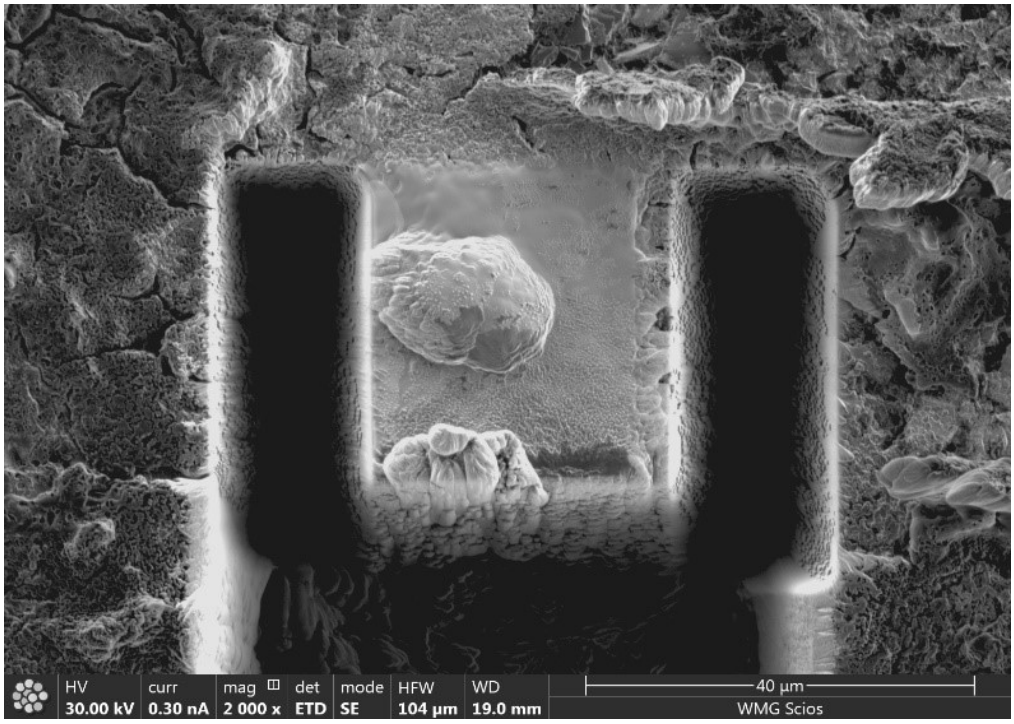

Figure A.11: Image of the electrode block prepared for FIB slicing of a cycled Standard Electrode. Size approx. 27×30×15 μm with platinum deposition on top to obtain a smooth surface.

Table A.6: The sheet resistance of electrode coatings coated on mylar foil. Electrode coatings with a solid content of 35.5 % ± 0.4 % and a blade gap of 100 μm. Sheet resistance was measured via four-point probe measurements. The table shows the minimum and maximum values across the coating.

HC content [%]	Binder content [%]	CB content [%]	Ze content [%]	Sheet resistance [Ω/□]
87.5	5	7.5	0.0	39 to 65
90.0	5	5.0	0.0	50
93.0	5	2.0	0.0	60 to 75
85.0	5	5.0	5.0	40 to 60
85.0	5	2.5	7.5	60 to 130
85.0	5	0.0	10.0	120 to 180
90.0	5	0.0	5.0	60 to 120
90.0	5	2.5	2.5	38 to 43

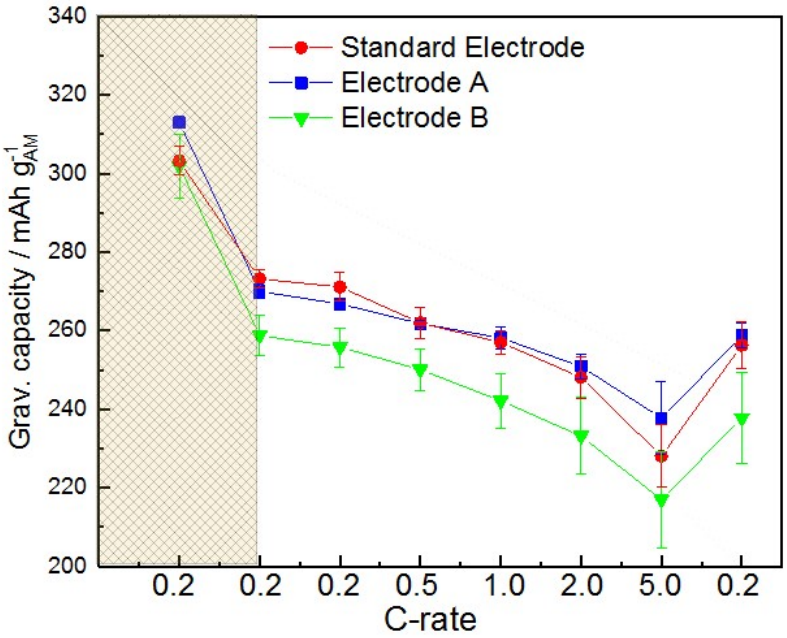

Figure A.12: Average gravimetric capacities based on active material content for a set of three electrodes each: Standard Electrode (circle), Electrode A (square), and Electrode B (triangle). Capacities are shown versus the previously conducted desodiation at accelerated C-rates. The shadowed area indicates the first cycle losses.

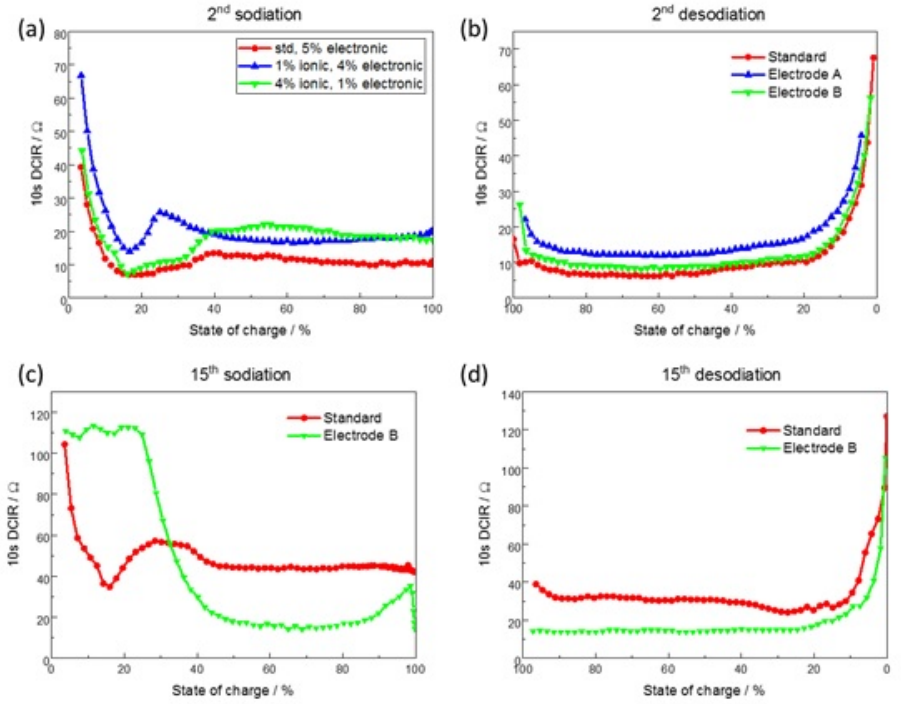

Figure A.13: Results of the DCIR measurements conducted during GITT measurements for the Standard Electrode (red circles), electrode A (blue triangle), and electrode B (green pointing down triangle) for the second (a and b) and 15th sodiation/desodiation (c and d), respectively.

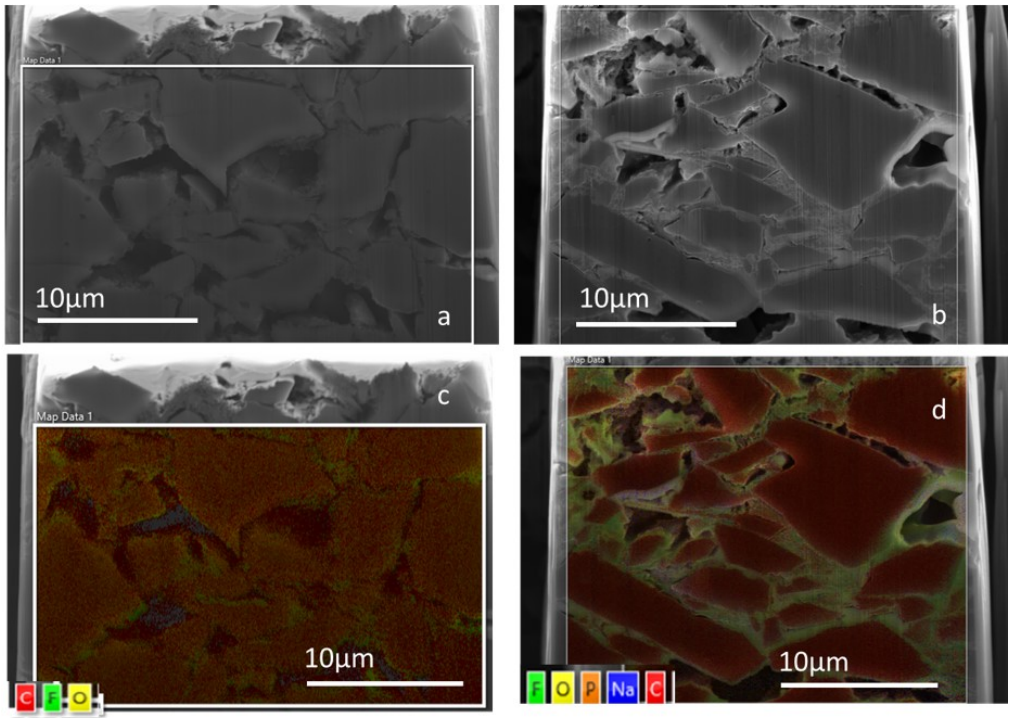

Figure A.14: Cross-section micrographs of FIB cuts (15 × 25 μm) and EDS data of a Standard Electrode of 30 % porosity. (a) uncycled, (b) after 47 cycles.

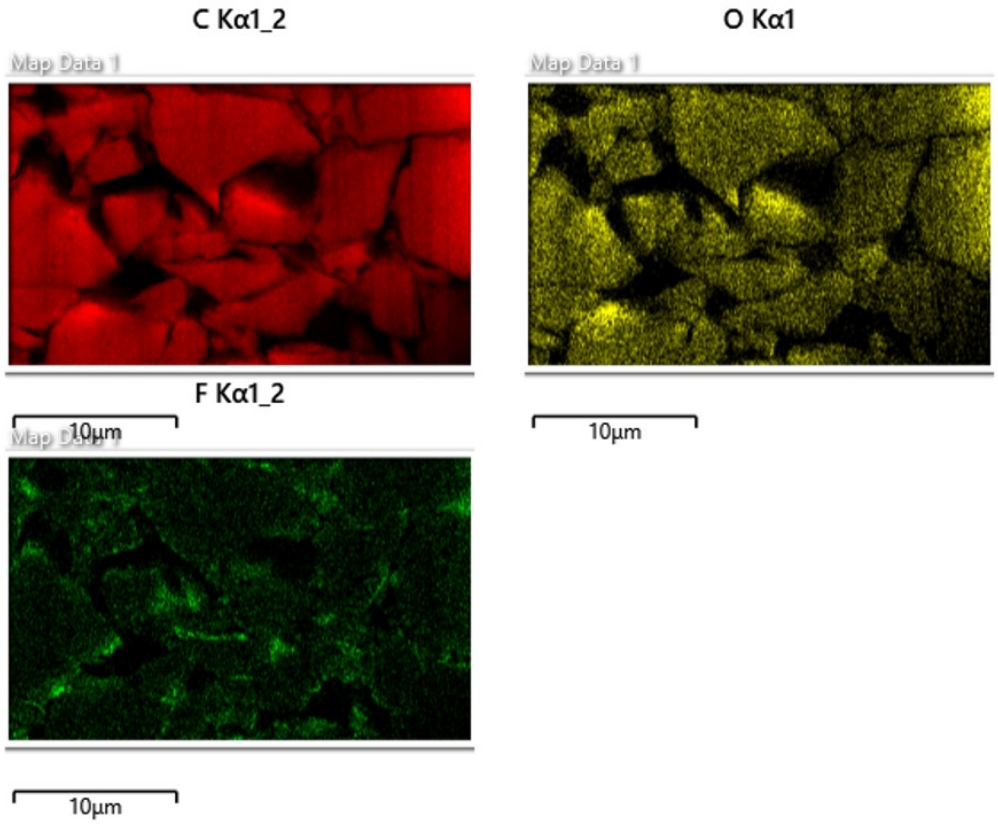

Figure A.15: Detailed EDS images by the element of the uncycled standard HC electrode, showing carbon(red), oxygen (yellow) and fluorine (green).

Table A.7: Series resistance of the electrode coatings at 0.005 V and 1.0 V vs Na/Na^+

V vs Na/Na^+	Cycle No.	standard	A	B
0.005	1st cycle	4.459	5.399	5.637
	2nd cycle	8.262	7.488	11.28
	Cycling	29.84	41.83	18.62
1	1st cycle	4.733	4.524	2.804
	2nd cycle	4.144	6.318	6.879
	Cycling	29.47	33.4	21.1

Table A.8: Series resistance of the electrode coatings at 0.005 V and 1.0 V vs Na/Na^+

	Standard	Electrode B
R_s	29 (3)	18 (2)
R_{SEI}	351 (26)	136 (18)
R_{CT}	138 (20)	192 (20)

Table A.9: Results of the map sum spectrum for a Standard Electrode in the uncycled and cycled state. Data in wt%.

	Carbon	Sodium	Oxygen	Fluorine	Phosphorous	Chlorine	Other
Uncycled	95.2	n. a.	n. a.	n. a.	n. a.	1.1	3.7
Cycled	67.1	16.2	10.8	3.7	1.7	0.5	0.0

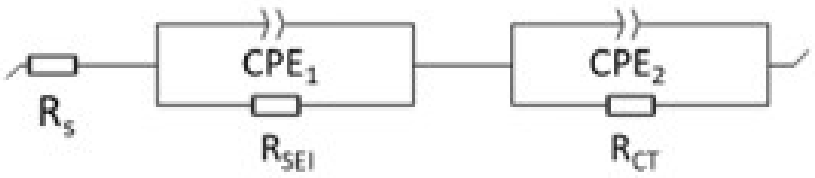

Figure A.16: Equivalent Circuit as used to fit EIS data.

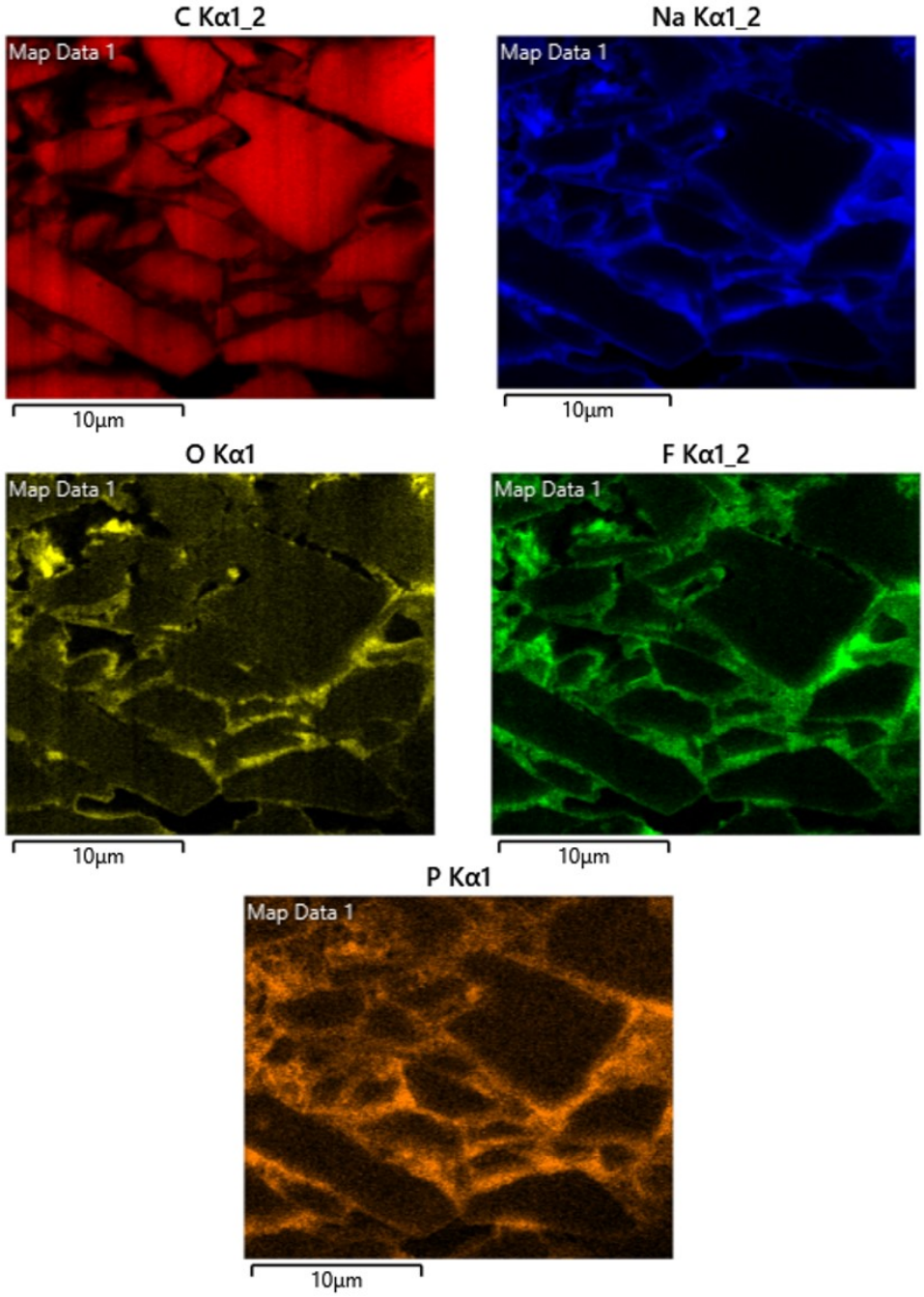

Figure A.17: Detailed EDS images by the element of the cycled standard HC electrode showing carbon(red), oxygen (yellow), fluorine (green), sodium (blue), and phosphorous (orange).

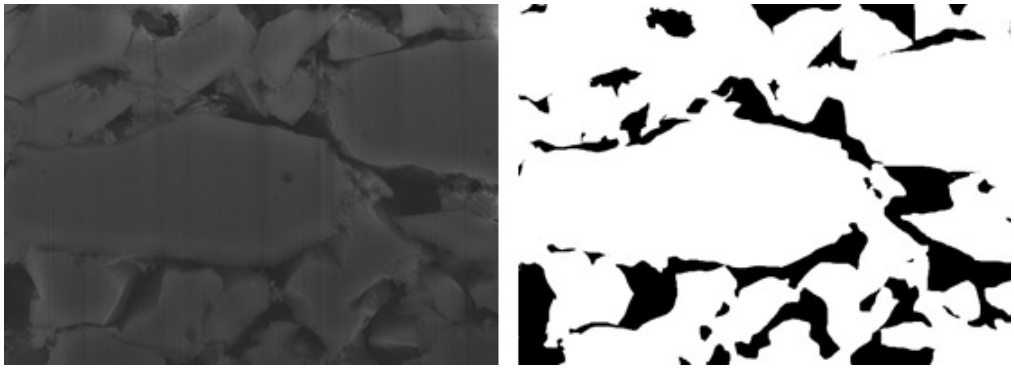

Figure A.18: SEM micrograph (left) and generated binary picture using GIMP (right) of a crosssection of an uncycled electrode.

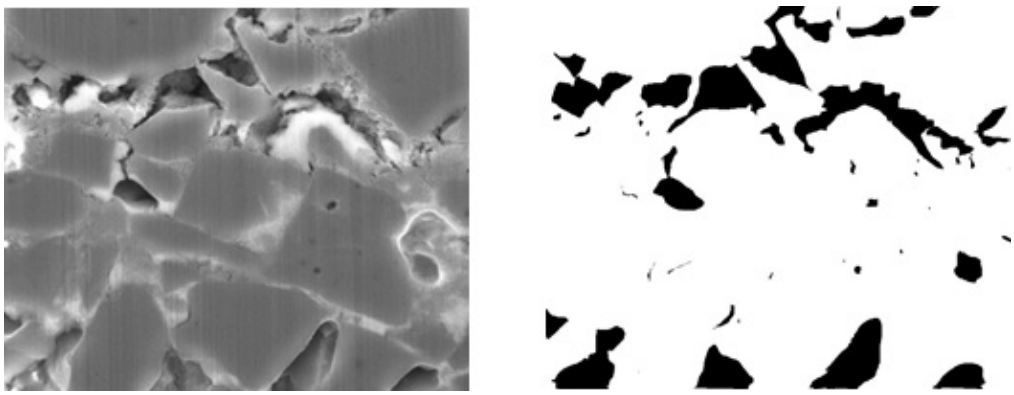

Figure A.19: SEM micrograph (left) and generated binary picture using GIMP (right) of a crosssection of a cycled electrode.

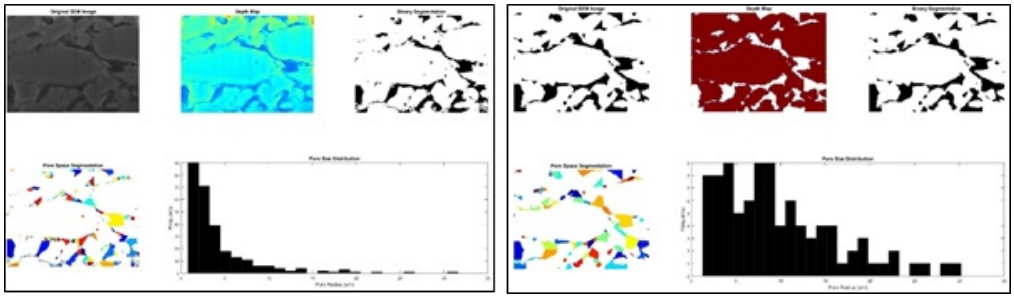

Figure A.20: Results of the Matlab App SEM Image Processing for an SEM micrograph (left) and previously generated binary picture (right) of a crosssection of an uncycled electrode. The calculated porosities are 14.7 and 19.2 %, respectively.

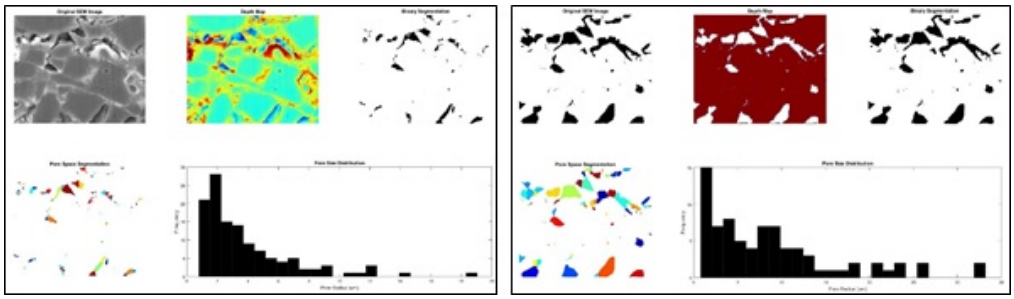

Figure A.21: Results of the Matlab App SEM Image Processing for an SEM micrograph (left) and previously generated binary picture (right) of a crosssection of a cycled electrode. The calculated porosities are 4.1 and 13.8 %, respectively.

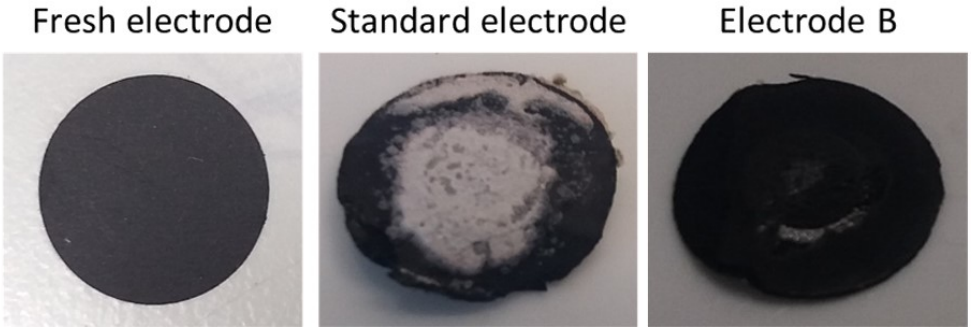

Figure A.22: Photographs of an uncycled and two cycled electrodes (126 cycles, 2 V cell voltage at dismantling) of the test cells showing silver-coloured sodium plating on the electrode surface. Electrode diameter 12 mm; Standard Electrode: 26 % porosity; Electrode B: 30 % porosity.

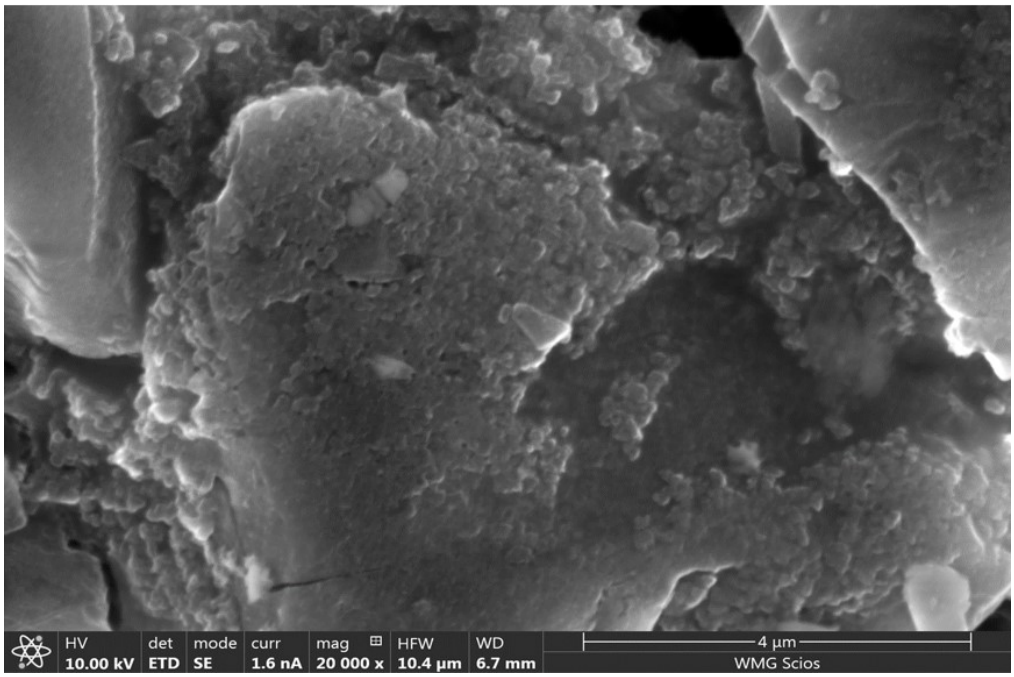

Figure A.23: SEM micrograph of a cycled electrode.

Appendix B

Conference Contributions and Publications

The conference contributions and publications since start of the Ph. D. are listed in chronological order.

Talk: The Influence of Sodium Metal in Sodium Ion Half-Cell Testing Shown in HC Anodes

D. Ledwoch, P. Adamson, P. Shearing, D. J. L. Brett, and E. Kendrick, Early Career Researcher Conference, Abingdon, 5^{th} – 6^{th} of April, 2016.

Talk (invited): New directions in electrode design for electrochemical energy storage

D. Ledwoch, Alumni Science Evening of the Royal Commission of the Exhibition of 1851, London, 6^{th} of February, 2018.

Talk (invited): Influence of Ionic Mobility in HC Composite Electrodes in Sodium-Ion Batteries

D. Ledwoch, K. Smith, P. Shearing, D. J. L. Brett, and E. Kendrick, MRS Spring Meeting, Phoenix, 18^{th} of April, 2018.

Talk (invited): New directions in electrode design for electrochemical energy storage (Best talk award)

D. Ledwoch, Johnson Matthey Academic Conference, Coventry, 30^{th} of May, 2019.

Patent: High energy density metal ion cathode

PCT/JP2016/004711, E. Kendrick, D. Ledwoch, Sharp Cooperation Ltd.,
Priority: 30/10/2017, Filing: 26/10/2016, Publication: 04/05/2017.

Patent: Composite electrode including microporous ionically conducting material, composite slurry, and methods of manufacturing same.

US Application US20180287134, D. Ledwoch, E. Kendrick, P. Adamson, Sharp Co-operation Ltd.,

Priority: 31/03/2017, Filing: 31/03/2018, Publication: 04/10/2018.

First author paper: HC Composite Electrodes for Sodium-Ion Batteries with Nano-Zeolite and Carbon Black Additives

D. Ledwoch, J. Robinson, D. Gastol, K. Smith, P. R. Shearing, D. J. L. Brett, E. Kendrick, Batteries & Supercaps 4 (1), 163-172, 2020.

Other: Elucidating the sodiation mechanism in HC by operando raman spectroscopy

J. Weaving, A. Lim, J. Millichamp, T. Neville, D. Ledwoch, E. Kendrick, P. McMillan, P. Shearing, C. Howard, D. J. L. Brett, ACS Appl. Energy Mater 3, 7474-7484, 2020.

Other: Sodium-ion Batteries: Aging, Degradation, Failure Mechanism and Safety

J. Weaving, J. Robinson, D. Ledwoch, G. He, E. Kendrick, P. Shearing, D.J.L. Brett, in Sodium-Ion Batteries: Materials, Characterization, and Technology. WILEY-VCH Verlag GmbH & Co. KGaA, 2021.

Conference Paper: The Performance of HC in a Sodium Ion Battery and Influence of the Sodium Metal in Observed Properties

D. Ledwoch, D. J. L. Brett, E. Kendrick, ECS Transactions 72 (33), 17-22, 2016.

Conference Paper: Investigation of the sodiation and desodiation of HC by electrochemical testing and X-ray computed tomography

D. Ledwoch, D. J. L. Brett, P. R. Shearing, E. Kendrick, ECS Transactions, 75 (52), 81 - 90, 2017.

Conference Paper: Novel High Energy Density Sodium Layered Oxide Cathode Materials: From Material to Cells

K. Smith, J. Treacher, D. Ledwoch, P. Adamson, E. Kendrick, ECS Transactions, 75 (22), 13 - 24, 2017.

Poster: Development of a Nickelate Layered Oxide and HC Sodium Ion Battery

D. Ledwoch, R. Gruar, P. Adamson, K. Smith, J. Treatcher, and E. Kendrick, UK-Korea Symposium on Lithium and Sodium Batteries, London, 18^{th} – 19^{th} of January, 2016.

Poster: The Performance of HC in a Sodium Ion Battery and Influence of the Sodium Metal in Observed Properties

D. Ledwoch, D. J. L. Brett, E. Kendrick, 229^{th} Meeting of the Electrochemical Society, San Diego (US), 29^{th} of May – 3^{rd} of June, 2016.

Poster: Investigation of the sodiation and desodiation of HC by electrochemical testing and X-ray computed tomography

D. Ledwoch, D. J. L. Brett, P. R. Shearing, E. Kendrick, 230^{th} Meeting of the Electrochemical Society, Honolulu (US), 2^{nd} – 7^{rd} of October 2016.

Poster and flash presentation: Investigation of the sodiation and desodiation of HC by electrochemical testing and X-ray computed tomography

D. Ledwoch, D. J. L. Brett, P. R. Shearing, E. Kendrick, Royal Society of Chemistry, London, 16^{th} of November, 2016.

Poster and Three Minute Presentation: Investigation of the sodiation and desodiation of HC by electrochemical testing and X-ray computed tomography

D. Ledwoch, D. J. L. Brett, P. R. Shearing, E. Kendrick, 2^{nd} year poster presentation, London, 12^{th} of December, 2016.

Poster: The Influence of Cell Design on Testing HC Composite Electrodes in Sodium Ion Batteries

D. Ledwoch, K. Smith, P. Shearing, D. J. L. Brett, E. Kendrick, The International Battery Materials Association, Annual Conference, Jeju, Korea, 2^{nd} of March, 2018.

Poster: The Influence of Porosity and Ionic Conductive Additives on the Apparent Diffusion Coefficient in HC Electrodes in Sodium Ion Batteries

D. Ledwoch, P. R. Shearing, D. J. L. Brett, E. Kendrick, International Meeting of Lithium Ion Batteries, Kyoto, Japan, 10^{th} of June 2018.

References

[1] D. Farnsworth, J. Shipley, J. Lazar, and N. Seidman. *Beneficial Electrification Ensuring Electrification in the Public Interest*. Tech. rep. June. Montpelier: VT: Regulatory Assistance Project, 2018.

[2] U.S. EIA. *Annual Energy Outlook 2019 with projections to 2050*. Tech. rep. 8. Washington: U.S. Department of Energy, 2019, pp. 1–64.

[3] C. Meyer, H. Bockholt, W. Haselrieder, and A. Kwade. "Characterization of the calendering process for compaction of electrodes for lithium-ion batteries". In: *Journal of Materials Processing Technology* 249.April (Nov. 2017), pp. 172–178.

[4] R.C. Stempel. *The future is electric*. 2005.

[5] M. Hilfer and L. Guerra. *Boeing Autonomous Passenger Air Vehicle Completes First Flight*. `https://boeing.mediaroom.com/`. Accessed: 2019-08-30. 2019.

[6] S. Lekach. *The future of flight*. 2002.

[7] L. Cailloce. *A Battery Revolution in Motion*. `https://news.cnrs.fr/articles/a-battery-revolution-in-motion`. Accessed: 2019-08-29. 2015.

[8] A. Fabiani Appavou, B. Brown, D. Epp, B. Gibb, et al. *Renewbles in Cities - 2019 Global Status Report*. Tech. rep. Paris: REN21, 2019, p. 336.

[9] Climate Reality. *Follow the Leader: How 11 Countries Are Shifting to Renewable Energy*. `https://www.climaterealityproject.org/blog/`. 2016.

[10] P. B. Jones, J. Bosco, J. Howat, and J. W. Van Alst. *The Future of Transportation Electrification: Utility, Industry and Consumer Perspectives*. Tech. rep. Lawrence Berkeley National Laboratory Report, 2018.

[11] Edison Electric Institute. *Transportation Electrification - Utility Fleets Leading the Charge*. Tech. rep. December. Washington: Edison Electric Institute, 2014, p. 74.

[12] U.S. Geological Survey. *Mineral Commodity Summaries*. Tech. rep. U.S. Department of the Interior, 2018.

[13] S. Roberts and E. Kendrick. "The re-emergence of sodium ion batteries: testing, processing, and manufacturability". In: *Nanotechnology, Science and Applications* Volume 11 (June 2018), pp. 23–33.

[14] K. Smith, J. Treacher, D. Ledwoch, P. Adamson, and E. Kendrick. "Novel High Energy Density Sodium Layered Oxide Cathode Materials: from Material to Cells". In: *ECS Transactions* 75.22 (2017), pp. 13–24.

[15] K. Kubota, M. Dahbi, T. Hosaka, S. Kumakura, and S. Komaba. "Towards K-Ion and Na-Ion Batteries as "Beyond Li-Ion"". In: *Chemical Record* 18.4 (Apr. 2018), pp. 459–479.

[16] A. M. Skundin, T. L. Kulova, and A. B. Yaroslavtsev. "Sodium-Ion Batteries (a Review)". In: *Russian Journal of Electrochemistry* 54.2 (2018), pp. 113–152.

[17] SAS TIAMAT. *TIAMAT*. `http://www.tiamat-energy.com/en/{#}apropos`. 2019-08-30. 2019.

[18] HiNa Battery Technology Co. *Company Profile*. `http://www.hinabattery.com/en/index.php?catid=7`. Accessed: 2019-08-30. 2019.

[19] B. Jache, J. O. Binder, T. Abe, and P. Adelhelm. "A comparative study on the impact of different glymes and their derivatives as electrolyte solvents for graphite co-intercalation electrodes in lithium-ion and sodium-ion batteries". In: *Physical Chemistry Chemical Physics* 18.21 (2016), pp. 14299–14316.

[20] S. Komaba, W. Murata, T. Ishikawa, N. Yabuuchi, et al. "Electrochemical Na insertion and solid electrolyte interphase for hard-carbon electrodes and application to Na-ion batteries". In: *Advanced Functional Materials* 21.20 (2011), pp. 3859–3867.

[21] D. Ledwoch, D. J. L. Brett, P. R. Shearing, and E. Kendrick. "Investigation of the Sodiation and Desodiation of Hard Carbon By Electrochemical Testing and X-Ray Computed Tomography". In: *ECS Transactions* 33.72 (2017), pp. 81–90.

[22] C.-H. Chen, F. Brosa Planella, K. O'Regan, D. Gastol, W. D. Widanage, and E. Kendrick. "Development of Experimental Techniques for Parameterization of Multi-scale Lithium-ion Battery Models". In: *Journal of The Electrochemical Society* 167.8 (2020), p. 080534.

[23] Jasper Jolly. *UK carmakers have three years to source local electric car batteries*. `https://www.theguardian.com/politics/2021/jan/03/`. Accessed: 31/01/2021. 2021.

[24] Q. Xu, T. S. Zhao, and C. Zhang. "Performance of a vanadium redox flow battery with and without flow fields". In: *Electrochim. Acta* 142 (2014), pp. 61–67.

[25] G. Lenze, H. Bockholt, C. Schilcher, L. Froböse, D. Jansen, U. Krewer, and A. Kwade. "Impacts of Variations in Manufacturing Parameters on Performance of Lithium-Ion-Batteries". In: *Journal of The Electrochemical Society* 165.2 (2018), A314–A322.

[26] R. von Hagen, A. Lepcha, X. Song, W. Tyrra, and S. Mathur. "Influence of electrode design on the electrochemical performance of Li3V2(PO4)3/C nanocomposite cathode in lithium ion batteries". In: *Nano Energy* 2.2 (2013), pp. 304–313.

[27] W. Loevenich, L. Komsiyska, E.-M. Hammer, and D. Ledwoch. *Use of conductive polymers in battery electrodes, WO2014079581A1*. 2014.

[28] W. Weppner and Robert A. Huggins. "Determination of the Kinetic Parameters of Mixed-Conducting Electrodes and Application to the System Li3Sb". In: *Journal of The Electrochemical Society* 124.10 (1977), pp. 1569–1578.

[29] Y. Li, Y. S. Hu, M. M. Titirici, L. Chen, and X. Huang. "Hard Carbon Microtubes Made from Renewable Cotton as High-Performance Anode Material for Sodium-Ion Batteries". In: *Adv. Energy Mater.* (2016), pp. 1–9.

[30] D. W. Dees, S. Kawauchi, D. P. Abraham, and J. Prakash. "Analysis of the Galvanostatic Intermittent Titration Technique (GITT) as applied to a lithium-ion porous electrode". In: *J. Power Sources* 189.1 (2009), pp. 263–268.

[31] M. V. Reddy, G. V. Subba Rao, and B. V. R. Chowdari. "Metal Oxides and Oxysalts as Anode Materials for Li Ion Batteries". In: *ACS Chem. Rev.* 113.7 (2013), pp. 5364–5457.

[32] C. Bommier, T. W. Surta, M. Dolgos, and X. Ji. "New Mechanistic Insights on Na-Ion Storage in Nongraphitizable Carbon". In: *Nano Letters* 15.9 (2015), pp. 5888–5892.

[33] C. J. Wen, B. A. Boukamp, R. A. Huggins, and W. Weppner. "Thermodynamic and Mass Transport Properties of "LiAl"". In: *J. Electrochem. Soc.* 126.12 (1979), p. 2258.

[34] Y. Zhu and C. Wang. "Galvanostatic intermittent titration technique for phase-transformation electrodes". In: *J. Phys. Chem. C* 114.6 (2010), pp. 2830–2841.

[35] C. H. Hamann, A. Hamnet, and W. Vielstich. *Electrochemistry*. 2nd. Weinheim: WILEY-VCH Verlag GmbH & Co. KGaA, 2007, p. 550.

[36] E. Barsoukov. "Kinetics of lithium intercalation into carbon anodes: in-situ impedance investigation of thickness and potential dependence". In: *Solid State Ionics* 116.3-4 (1999), pp. 249–261.

[37] C. J. Wen. "Chemical Diffusion in Lithium Alloys". PhD thesis. Stanford University, 1980.

[38] Q.-C. Zhuang, X.-Y. Qiu, S.-D. Xu, Y.-H. Qiang, S.-G. Su, and S.-G. Sun. "Diagnosis of Electrochemical Impedance Spectroscopy in Lithium-Ion Batteries". In: *Lithium Ion Batteries - New Developments*. Ed. by Ilias Belharouak. InTech, 2012. Chap. 8, pp. 189–226.

[39] C. Wang, A. J. Appleby, and F. E. Little. "Electrochemical impedance study of initial lithium ion intercalation into graphite powders". In: *Electrochim. Acta* 46.12 (2001), pp. 1793–1813.

[40] M. D. Levi, G. Salitra, B. Markovsky, H. Teller, D. Aurbach, U. Heider, and L. Heider. "Solid-State Electrochemical Kinetics of Li-Ion Intercalation into $Li_{1-x}CoO_2$: Simultaneous Application of Electroanalytical Techniques SSCV, PITT, and EIS". In: *Journal of The Electrochemical Society* 146.4 (1999), p. 1279.

[41] M. D. Levi and D. Aurbach. "Diffusion Coefficients of Lithium Ions during Intercalation into Graphite Derived from the Simultaneous Measurements and Modeling of Electrochemical Impedance and Potentiostatic Intermittent Titration Characteristics of Thin Graphite Electrodes". In: *The Journal of Physical Chemistry B* 101.23 (1997), pp. 4641–4647.

[42] H. Liu, C. Li, H. P. Zhang, L. J. Fu, Y. P. Wu, and H. Q. Wu. "Kinetic study on LiFePO4/C nanocomposites synthesized by solid state technique". In: *Journal of Power Sources* 159 (2006), pp. 717–720.

[43] E. Barsoukov and J. R. Macdonald. *Impedance Spectroscopy Theory, Experiment, and Applications*. Second. John Wiley & Sons, 2005.

[44] J. R. Macdonald, J. Schoonman, and A. P. Lehnen. "Three dimensional perspective plotting and fitting of immittance data". In: *Solid State Ionics* 5 (1981), pp. 137–140.

[45] B. S. Haran, B. N. Popov, and R. E. White. "Determination of the hydrogen diffusion coefficient in metal hydrides by impedance spectroscopy". In: *J. Power Sources* 75.1 (1998), pp. 56–63.

[46] A. J. Bard and L. R. Faulkner. *Electrochemical Methods*. Second. John Wiley & Sons, 2001.

[47] A. H. Thompson. "Electrochemical Potential Spectroscopy: A New Electrochemical Measurement". In: *J. Electrochem. Soc.* 126.4 (1979), p. 608.

[48] J. Barker, D. Baldwin, D. C. Bott, and S. J. Porter. "Electrochemical Voltage Spectroscopy; Dopant Diffusion in Durham Polyacetylene". In: *Synth. Met.* 28 (1989), pp. D127–D134.

[49] J. Barker. "Three Electrode Electrochemical Voltage Spectroscopy (TEVS): evaluation of a model lithium ion system". In: *Electrochim. Acta* 40.11 (1995), pp. 1603–1608.

[50] K. Wang, Y. Jin, S. Sun, Y. Huang, et al. "Low-Cost and High-Performance Hard Carbon Anode Materials for Sodium-Ion Batteries". In: *ACS Omega* 2.4 (2017), pp. 1687–1695.

[51] X. Li, X. Zeng, T. Ren, J. Zhao, Z. Zhu, S. Sun, and Y. Zhang. "The transport properties of sodium-ion in the low potential platform region of oatmeal-derived hard carbon for sodium-ion batteries". In: *Journal of Alloys and Compounds* (May 2019), pp. 229–238.

[52] R. Li, J. Huang, Z. Xu, H. Qi, et al. "Controlling the Thickness of Disordered Turbostratic Nanodomains in Hard Carbon with Enhanced Sodium Storage Performance". In: *Energy Technology* 6.6 (2018), pp. 1080–1087.

[53] Radboud University Nijmegen. *Image formation and element analysis with a SEM-EDS system*. `http://www.vcbio.science.ru.nl/en/fesem/eds/`. Accessed: 2017-02-21. 2011.

[54] *Hitachi Launches World's highest resolution FE-SEM*. `http:nanotech-now.com/news.cgi?Story_id=42612`. Accessed: 2017-02-21. 2011.

[55] T. Sui, B. Song, J. Dluhos, L. Lu, and A. M. Korsunsky. "Nanoscale chemical mapping of Li-ion battery cathode material by FIB-SEM and TOF-SIMS multi-modal microscopy". In: *Nano Energy* 17 (2015), pp. 254–260.

[56] T. Lowe, R. Bradley, C. Egan, J. Carr, and S. Coburn. *Course notes: Introduction to X-ray Computed Tomography (CT) theory*. 2015.

[57] Carl Zeiss X-Ray Microscopy, Inc. *Zeiss Xradia 520 Versa - Advanced Training*. 2013.

[58] P. R. Shearing, D. S. Eastwood, R. S. Bradley, J. Gelb, et al. "Exploring electrochemical devices using X-ray microscopy: 3D micro-structure of batteries and fuel cells". In: *Microsc.* 1.2 (2013), pp. 19–22.

[59] N. Rezvani. "Reconstruction Algorithms in Computerized Tomography". In: *Canadian Applied and Industrial Mathematics Society*. London, Ontario, 2009.

[60] N. Nitta, F. Wu, J. T. Lee, and G. Yushin. "Li-ion battery materials: Present and future". In: *Materials Today* 18.5 (2015), pp. 252–264.

[61] C. P. Grey and N. Duprè. "NMR studies of cathode materials for lithium-ion rechargeable batteries". In: *Chem. Rev.* 104.10 (2004), pp. 4493–4512.

[62] C. M. Julien, A. Mauger, K. Zaghib, and H. Groult. "Comparative Issues of Cathode Materials for Li-Ion Batteries". In: *Inorganics* 2 (2014), pp. 132–154.

[63] I. H. Son, J. Hwan Park, S. Kwon, S. Park, et al. "Silicon carbide-free graphene growth on silicon for lithium-ion battery with high volumetric energy density." In: *Nature Commun.* 6 (2015), p. 7393.

[64] J. Wang, F. Fan, Y. Liu, K. L. Jungjohann, et al. "Structural Evolution and Pulverization of Tin Nanoparticles during Lithiation-Delithiation Cycling". In: *J. Electrochem. Soc.* 161.11 (2014), F3019–F3024.

[65] F. Wu and G. Yushin. “Conversion Cathodes for Rechargeable Lithium and Lithium-Ion Batteries”. In: *Energy Environ. Sci.* (2016), pp. 1–54.

[66] M. R. Palacín. “Recent advances in rechargeable battery materials: a chemist’s perspective”. In: *Chem. Soc. Rev.* 38.9 (2009), pp. 2565–2575.

[67] F.-M. Wang, M.-H. Yu, Y.-J. Hsiao, B.-J. Tsai Y.and Hwang, Y.-Y. Wang, and C.-C. Wan. “Aging Effects to Solid Electrolyte Interface (SEI) Membrane Formation and the Performance Analysis of Lithium Ion Batteries”. In: *Int. J. Mol. Sci.* 6 (2011), pp. 1014–1026.

[68] M. Nie. “Anode Solid Electrolyte Interphase (Sei) of Lithium Ion Battery Characterized By Microscopy and Spectroscopy”. PhD thesis. Univerity of Rhode Island, 2014.

[69] S. J. An, J. Li, C. Daniel, D. Mohanty, S. Nagpure, and D. L. Wood. “The state of understanding of the lithium-ion-battery graphite solid electrolyte interphase (SEI) and its relationship to formation cycling”. In: *Carbon* 105 (2016), pp. 52–76.

[70] H. Wu, G. Chan, J. W. Choi, I. Ryu, et al. “Stable cycling of double-walled silicon nanotube battery anodes through solid–electrolyte interphase control”. In: *Nature Nanotechnology* 7.5 (2012), pp. 310–315.

[71] Y. Li, K. Yan, H.-W. Lee, Z. Lu, N. Liu, and Y. Cui. “Growth of conformal graphene cages on micrometre-sized silicon particles as stable battery anodes”. In: *Nature Energy* 1.2 (2016), p. 15029.

[72] Y. Jin, S. Li, A. Kushima, X. Zheng, et al. “Self-healing SEI enables full-cell cycling of a silicon-majority anode with a coulombic efficiency exceeding 99.9%”. In: *Energy Environ. Sci.* (2017), pp. 580–592.

[73] J. Weaving, J. Robinson, D. Ledwoch, G. He, E. Kendrick, P. R. Shearing, and D. Brett. “Sodium-ion Batteries: Aging, Degradation, Failure Mechanism and Safety”. In: *Sodium-Ion Batteries: Materials, Characterization, and Technology*. Ed. by Maria-Magdalena Titirici, Philipp Adelhelm, and Yong-Sheng Hu. WILEY-VCH Verlag GmbH & Co. KGaA, 2021.

[74] M. Meyer, L. Komsiyska, B. Lenz, and C. Agert. “Study of the local SOC distribution in a lithium-ion battery by physical and electrochemical modeling and simulation”. In: *Appl. Math. Modelling* 37.4 (2013), pp. 2016–2027.

[75] J. Cannarella and C. B. Arnold. “The Effects of Defects on Localized Plating in Lithium-Ion Batteries”. In: *J. Electrochem. Soc.* 162.7 (2015), A1365–A1373.

[76] Y. Liu, R. Zhang, J. Wang, and Y. Wang. “Current and future lithium-ion battery manufacturing”. In: *iScience* 24.4 (2021), p. 102332.

[77] L. Zhong, X. Xi, P. Mitchell, and B. Zou. *Dry particle based energy storage device product, US7791861 B2*. 2010.

[78] H. M. Duong, H. Feigenbaum, and J. Hong. *Dry energy storage device electrode and methods of making the same, US20150303481 A1*. 2015.

[79] F. M. Courtel, S. Niketic, D. Duguay, Y. Abu-Lebdeh, and I. J. Davidson. “Water-soluble binders for MCMB carbon anodes for lithium-ion batteries”. In: *J. Power Sources* 196.4 (2011), pp. 2128–2134.

[80] D. Shao, H. Zhong, and L. Zhang. “Water-Soluble Conductive Composite Binder Containing PEDOT: PSS as Conduction Promoting Agent for Si Anode of Lithium-Ion Batteries”. In: *Chem. Electro. Chem.* 1.10 (2014), pp. 1679–1687.

[81] B. Westphal. “Ermittlung des Einflusses von Prozess- und Stoffparametern auf die Formulierung von Elektrodensuspensionen und deren Verarbeitung zu Elektroden für Lithium-Ionen-Batterien”. Diploma thesis. TU Braunschweig, 2010.

[82] X. Dou, I. Hasa, D. Saurel, C. Vaalma, et al. “Hard carbons for sodium-ion batteries: Structure, analysis, sustainability, and electrochemistry”. In: *Materials Today* 23.March (2019), pp. 87–104.

[83] D. A. Stevens and J. R. Dahn. “High Capacity Anode Materials for Rechargeable Sodium-Ion Batteries”. In: *J. Electrochem. Soc.* 147.4 (2000), p. 1271.

[84] R. Väli, A. Jänes, T. Thomberg, and E. Lust. “D-Glucose Derived Nanospheric Hard Carbon Electrodes for Room-Temperature Sodium-Ion Batteries”. In: *J. Electrochem. Soc.* 163.8 (2016), A1619–A1626.

[85] Z. Guo, C. Wang, M. Chen, and M. Li. “Hard carbon derived from coal tar pitch for use as the anode material in lithium ion batteries”. In: *Int. J. Electrochem. Sci.* 8.2 (2013), pp. 2702–2709.

[86] E. M. Lotfabad, J. Ding, K. Cui, A. Kohandehghan, W. P. Kalisvaart, M. Hazelton, and D. Mitlin. "High-Density Sodium and Lithium Ion Battery Anodes from Banana Peels". In: *ACS Nano* 8.7 (2014), pp. 7115–7129.

[87] I. Mochida, S. H. Yoon, and W. Qiao. "Catalysts in syntheses of carbon and carbon precursors". In: *J. Braz. Chem. Soc.* 17.6 (2006), pp. 1059–1073.

[88] H. O. Pierson. *Handbook of Carbon, Graphite, Diamond and Fullerenes*. First. Noyes Publications, 1993, p. 417.

[89] E. Irisarri, A. Ponrouch, and M. R. Palacin. "Review—Hard Carbon Negative Electrode Materials for Sodium-Ion Batteries". In: *J. Electrochem. Soc.* 162.14 (2015), A2476–A2482.

[90] F. Xie, Z. Xu, Z. Guo, and M. M. Titirici. "Hard carbons for sodium-ion batteries and beyond". In: *Progress in Energy* 2.4 (Sept. 2020), p. 042002.

[91] M. M. Titirici, H. Alptekin, H. Au, A. C.S. Jensen, et al. "Sodium storage mechanism investigations through structural changes in hard carbons". In: *ACS Applied Energy Materials* 3.10 (2020), pp. 9918–9927.

[92] C. Bommier, D. Leonard, Z. Jian, W. F. Stickle, P. A. Greaney, and X. Ji. "New Paradigms on the Nature of Solid Electrolyte Interphase Formation and Capacity Fading of Hard Carbon Anodes in Na-Ion Batteries". In: *Adv. Mater. Interfaces* 3.19 (2016).

[93] R. Mogensen, D. Brandell, and R. Younesi. "Solubility of the Solid Electrolyte Interphase (SEI) in Sodium Ion Batteries". In: *ACS Energy Letters* 1.6 (2016), pp. 1173–1178.

[94] C. Zhang, J. Jiang, L. Zhang, S. Liu, L. Wang, and P. Loh. "A Generalized SOC-OCV Model for Lithium-Ion Batteries and the SOC Estimation for LNMCO Battery". In: *Energies* 9.900 (2016).

[95] X. Xia and J. R. Dahn. "Study of the Reactivity of Na/Hard Carbon with Different Solvents and Electrolytes". In: *J. Electrochem. Soc.* 159.5 (2012), A515.

[96] C. Pillot. *The Rechargeable Battery Market and Main Trends 2018-2030*. Tech. rep. Avicenne energy, 2019, p. 43.

[97] U. G. Survey. *USGS Mineral Commodity Summaries 2016*. https://minerals.usgs.gov/minerals/pubs/mcs/2016/mcs2016.pdf. Acessed: 2017-01-13. 2016.

[98] C. Pillot. *Lithium ion battery raw material Supply & demand 2016-2025*. Tech. rep. Avicenne energy, 2017, p. 43.

[99] Q. Wang, X. Zhu, Y. Liu, Y. Fang, X. Zhou, and J. Bao. "Rice husk-derived hard carbons as high-performance anode materials for sodium-ion batteries". In: *Carbon* 127 (2018), pp. 658–666.

[100] J. Górka, C. Vix-Guterl, and C. Matei Ghimbeu. "Recent Progress in Design of Biomass-Derived Hard Carbons for Sodium Ion Batteries". In: *C* 2.4 (2016), p. 24.

[101] J. Barker and C. J. Wright. *Storage and/or transportation of sodium-ion cells, WO2016027082A1*. 2016.

[102] *Tesla - Powerwall 2*. https://www.tesla.com/powerwall. Accessed: 2018-11-27. 2016.

[103] *sonnen support UK*. https://sonnenservice.wordpress.com/2018/01/10/battery-chemistry/. Accessed: 2021-06-13. 2018.

[104] *Tesla - Powerwall 2*. https://www.tesla.com/powerwall. Accessed: 2018-11-27. 2016.

[105] *Aquion Energy*. http://aquionenergy.com/. Accessed: 2018-11-27. 2016.

[106] *NGK Insulators - NAS Batteries*. https://www.ngk-insulators.com/en/product/nas.html. Accessed: 2021-06-20. 2021.

[107] *Faradion Ltd.* http://www.faradion.co.uk/. Accessed: 2018-11-27. 2016.

[108] B. J. Landi, M. J. Ganter, C. D. Cress, R. DiLeo, and R. P. Raffaelle. "Carbon nanotubes for lithium ion batteries". In: *Energy Environ. Sci.* 2.6 (2009), p. 638.

[109] D. Larcher and J.-M. Tarascon. "Towards greener and more sustainable batteries for electrical energy storage." In: *Nature chemistry* 7.1 (2015), pp. 19–29.

[110] M. H. Han, E. Gonzalo, G. Singh, and T. Rojo. "A comprehensive review of sodium layered oxides: Powerful cathodes for Na-ion batteries". In: *Energy and Environmental Science* 8.1 (2015), pp. 81–102.

[111] R. Ramachandran, S. M. Chen, and G. P. Gnana Kumar. “Recent developments in electrode materials for oxygen reduction reaction”. In: *International Journal of Electrochemical Science* 10.10 (2015), pp. 8581–8606.

[112] E. Kendrick, R. Gruar, M. Nishijima, H. Mizuhata, T. Otani, I. Asako, and Y. Kamimura. *Tin-containing compounds, WO2015177568A1*. 2014.

[113] M. Law, V. Ramar, and P. Balaya. “Na2MnSiO4as an attractive high capacity cathode material for sodium-ion battery”. In: *Journal of Power Sources* 359 (2017), pp. 277–284.

[114] L. Gao, J. Chen, Y. Liu, Y. Yamauchi, Z. Huang, and X. Kong. “Revealing the chemistry of an anode-passivating electrolyte salt for high rate and stable sodium metal batteries”. In: *Journal of Materials Chemistry A* 6.25 (2018), pp. 12012–12017.

[115] A. Sarkar, S. Sarkar, and S. Mitra. “Exceptionally high sodium-ion battery cathode capacity based on doped ammonium vanadium oxide and a full cell SIB prototype study”. In: *Journal of Materials Chemistry A* 5.47 (2017), pp. 24929–24941.

[116] S. Klink, E. Madej, E. Ventosa, A. Lindner, W. Schuhmann, and F. La Mantia. “The importance of cell geometry for electrochemical impedance spectroscopy in three-electrode lithium ion battery test cells”. In: *Electrochem. Commun.* 22.1 (2012), pp. 120–123.

[117] N. A. Cañas, K. Hirose, B. Pascucci, N. Wagner, K. A. Friedrich, and R. Hiesgen. “Investigations of lithium-sulfur batteries using electrochemical impedance spectroscopy”. In: *Electrochim. Acta* 97.June 2013 (2013), pp. 42–51.

[118] R. Bhattacharyya, B. Key, H. Chen, A. S. Best, A. F. Hollenkamp, and C. P. Grey. “In situ NMR observation of the formation of metallic lithium microstructures in lithium batteries.” In: *Nat. Mater.* 9.6 (2010), pp. 504–510.

[119] J.-M. Tarascon and M. Armand. “Issues and challenges facing rechargeable lithium batteries.” In: *Nature* 414.6861 (2001), pp. 359–67.

[120] *Samsung Newsroom*. `https://news.samsung.com/global/infographic-galaxy-note7-what-we-discovered`. Accessed: 2017-02-07. 2017.

[121] C. R. Birkl, E. McTurk, M. R. Roberts, P. G. Bruce, and D. A. Howey. "A Parametric Open Circuit Voltage Model for Lithium Ion Batteries". In: *J. Electrochem. Soc.* 162.12 (2015), A2271–A2280.

[122] S. H. Yu, C. K. Park, H. Jang, C. B. Shin, and W. I. Cho. "Prediction of lithium diffusion coefficient and rate performance by using the discharge curves of LiFePO4 materials". In: *Bull. Korean Chem. Soc.* 32.3 (2011), pp. 852–856.

[123] D. Ledwoch, D. J. L. Brett, and E. Kendrick. "The Performance of Hard Carbon in a Sodium Ion Battery and Influence of the Sodium Metal in Observed Properties". In: *ECS Transactions* 72.33 (2016), pp. 17–22.

[124] S.-O. Tung, S. Ho, M. Yang, R. Zhang, and N. A. Kotov. "A dendrite-suppressing composite ion conductor from aramid nanofibres." In: *Nat. Commun.* 6 (2015), p. 6152.

[125] R. Miao, J. Yang, Z. Xu, J. Wang, Y. Nuli, and L. Sun. "A new ether-based electrolyte for dendrite-free lithium-metal based rechargeable batteries." In: *Sci. Rep.* 6 (2016), p. 21771.

[126] D. Wang, W. Zhang, W. Zheng, X. Cui, T. Rojo, and Q. Zhang. "Towards High-Safe Lithium Metal Anodes: Suppressing Lithium Dendrites via Tuning Surface Energy". In: *Adv. Sci.* (2016).

[127] S. F. Lux, I. T. Lucas, E. Pollak, S. Passerini, M. Winter, and R. Kostecki. "The mechanism of HF formation in LiPF6 based organic carbonate electrolytes". In: *Electrochem. Commun.* 14.1 (2012), pp. 47–50.

[128] J. Wu, N. Membreno, W.-Y. Yu, J. D. Wiggins-Camacho, D. W. Flaherty, C. B. Mullins, and K. J. Stevenson. "Influence of Hydrofluoric Acid Formation on Lithium Ion Insertion in Nanostructured V_2O_5". In: *J. Phys. Chem. C* 116 (2012), 21208-21215.

[129] Celgard. *Product Information 2325 Separators*. `http://www.ldcgm.com/Celgard/CELGARD-2400.pdf`. 2016.

[130] C. Mikolajczak, M. Kahn, K. White, and R. T. Long. *Lithium-Ion Batteries Hazard and Use Assessment*. Tech. rep. July. The Fire Protection Research Foundation, 2011, p. 112.

[131] D. P. Finegan, M. Scheel, J. B. Robinson, B. Tjaden, et al. “In-operando high-speed tomography of lithium-ion batteries during thermal runaway”. In: *Nat. Commun.* 6 (2015), p. 6924.

[132] P. Bohn, G. Liebig, L. Komsiyska, and G. Wittstock. “Temperature propagation in prismatic lithium-ion-cells after short term thermal stress”. In: *J. Power Sources* 313 (2016), pp. 30–36.

[133] M. Ender, A. Weber, and E. Ivers-Tiffée. “Analysis of Three-Electrode Setups for AC-Impedance Measurements on Lithium-Ion Cells by FEM simulations”. In: *J. Electrochem. Soc.* 159.2 (2012), pp. 128–136.

[134] S. Klink. “in-Depth Analysis of Irreversible Processes in Lithium Ion Batteries”. PhD thesis. Ruhr-Universitaet Bochum, 2013.

[135] D. P. Abraham, S. D. Poppen, A. N. Jansen, J. Liu, and D. W. Dees. “Application of a lithium-tin reference electrode to determine electrode contributions to impedance rise in high-power lithium-ion cells”. In: *Electrochim. Acta* 49.26 (2004), pp. 4763–4775.

[136] J. L. Gómez-Cámer and P. Novák. “Electrochemical impedance spectroscopy: Understanding the role of the reference electrode”. In: *Electrochem. Commun.* 34 (2013), pp. 208–210.

[137] D. W. Dees, A. N. Jansen, and D. P. Abraham. “Theoretical examination of reference electrodes for lithium-ion cells”. In: *J. Power Sources* 174.2 (2007), pp. 1001–1006.

[138] EL Cell electrochemical testing equipment. *Discover the PAT series*. `https://el-cell.com/products/discover-the-pat-series`. Accessed: 2017-01-20. 2016.

[139] E. McTurk, C. R. Birkl, M. R. Roberts, D. A. Howey, and P. G. Bruce. “Minimally Invasive Insertion of Reference Electrodes into Commercial Lithium-Ion Pouch Cells”. In: *ECS Electrochem. Lett.* 4.12 (2015), A145–A147.

[140] J. R. Belt, D. M. Bernardi, and V. Utgikar. “Development and Use of a Lithium-Metal Reference Electrode in Aging Studies of Lithium-Ion Batteries”. In: *J. Electrochem. Soc.* 161.6 (2014), A1116–A1126.

[141] Richtek Technology. *Designing Applications with Li-ion Batteries*. `http://www.richtek.com/battery-management/en/designing-liion.html`. Accessed: 2017-01-19. 2014.

[142] Alium Batteries. *Li-Polymer Battery – Shaped*. `http://aliumbatteries.com/products/secondary-batteries/li-polymer-battery/li-po-shaped/`. Accessed: 2021-07-19. 2017.

[143] *Customcells - Ahead in cell innovation*. `https://www.customcells.org/products-development/cell-prototyping/`. Accessed: 2021-07-05. 2021.

[144] J. P. Schmidt, H. Y. Tran, J. Richter, E. Ivers-Tiffée, and M. Wohlfahrt-Mehrens. "Analysis and prediction of the open circuit potential of lithium-ion cells". In: *J. Power Sources* 239 (2013), pp. 696–704.

[145] C. Weng, J. Sun, and H. Peng. "A Unified Open-Circuit-Voltage Model of Lithium-ion Batteries for State-of-Charge Estimation and State-of-Health Monitoring". In: *J. Power Sources* 258 (2014), pp. 228–237.

[146] L. Lavigne, J. Sabatier, J. M. Francisco, F. Guillemard, and A. Noury. "Lithium-ion Open Circuit Voltage (OCV) curve modelling and its ageing adjustment". In: *J. Power Sources* 324 (2016), pp. 694–703.

[147] H. Matsui, T. Nakamura, Y. Kobayashi, M. Tabuchi, and Y. Yamada. "Open-circuit voltage study on LiFePO4 olivine cathode". In: *J. Power Sources* 195.19 (2010), pp. 6879–6883.

[148] C. Y. Wang, G. Zhang, S. Ge, T. Xu, Y. Ji, X. G. Yang, and Y. Leng. "Lithium-ion battery structure that self-heats at low temperatures". In: *Nature* 529.7587 (2016), pp. 515–518.

[149] B. Suthar, P. W. C. Northrop, D. Rife, and V. R. Subramanian. "Effect of Porosity, Thickness and Tortuosity on Capacity Fade of Anode". In: *J. Electrochem. Soc.* 162.9 (2015), A1708–A1717.

[150] J. Smekens, R. Gopalakrishnan, N. Van den Steen, N. Omar, O. Hegazy, A. Hubin, and J. Van Mierlo. "Influence of electrode density on the performance of Li-ion batteries: Experimental and simulation results". In: *Energies* 9.2 (2016), pp. 1–12.

[151] M. Doyle and J. Newman. “The use of mathematical modeling in the design of lithium/polymer battery systems”. In: *Electrochim. Acta* 40.13-14 (1995), pp. 2191–2196.

[152] M. Doyle and J. Newman. “Modeling the performance of rechargeable lithium-based cells: design correlations for limiting cases”. In: *J. Power Sources* 54.1 (1995), pp. 46–51.

[153] W. Zheng, M. Shui, J. I. E. Shu, D. A. N. Gao S.and Xu, L. Chen, L. I. N. Feng, and Y. Ren. “GITT studies on oxide cathode LiNi 1 / 3 Co 1 / 3 Mn 1 / 3 O 2 synthesized by citric acid assisted high-energy ball milling”. In: *Bull. Mater. Sci.* 36.3 (2013), pp. 495–498.

[154] S. Franger, C. Bourbon, and F. Le Cras. “Optimized Lithium Iron Phosphate for High-Rate Electrochemical Applications”. In: *J. Electrochem. Soc.* 151.7 (2004), A1024.

[155] C. K. Park, S. B. Park, S. H. Oh, H. Jang, and W. I. Cho. “Li ion diffusivity and improved electrochemical performances of the carbon coated LiFePO4”. In: *Bull. Korean Chem. Soc.* 32.3 (2011), pp. 836–840.

[156] J. J. Wu and W. R. Bennett. “Fundamental investigation of Si anode in Li-ion cells”. In: *2012 IEEE Energytech, Energytech 2012* (2012), pp. 1–5.

[157] E. De La Llave, V. Borgel, K. J. Park, J. Y. Hwang, et al. “Comparison between Na-Ion and Li-Ion Cells: Understanding the Critical Role of the Cathodes Stability and the Anodes Pretreatment on the Cells Behavior”. In: *ACS Appl. Mater. Interfaces* 8.3 (2016), pp. 1867–1875.

[158] J. P. Meyers, M. Doyle, R. M. Darling, and J. Newman. “The Impedance Response of a Porous Electrode Composed of”. In: *J. Electrochem. Soc.* 147.8 (2000), pp. 2930–2940.

[159] Z. Liu, Y. Qi, Y. X. Lin, L. Chen, P. Lu, and L. Q. Chen. “Interfacial Study on Solid Electrolyte Interphase at Li Metal Anode: Implication for Li Dendrite Growth”. In: *J. Electrochem. Soc.* 163.3 (2016), pp. 592–598.

[160] J. Pan, Y.-T. Cheng, and Y. Qi. “General method to predict voltage-dependent ionic conduction in a solid electrolyte coating on electrodes”. In: *Phys. Rev. B* 91 (13 2015), p. 134116.

[161] S. L. Koch, B. J. Morgan, S. Passerini, and G. Teobaldi. “Density functional theory screening of gas-treatment strategies for stabilization of high energy-density lithium metal anodes”. In: *J. Power Sources* 296 (2015), pp. 150–161.

[162] Y. C. Chen, C. Y. Ouyang, L. J. Song, and Z. L. Sun. “Electrical and Lithium Ion Dynamics in Three Main Components of Solid Electrolyte Interphase from Density Functional Theory Study”. In: *J. Phys. Chem. C* 115.14 (2011), pp. 7044–7049.

[163] C. Bommier, W. Luo, W. Y. Gao, A. Greaney, S. Ma, and X. Ji. “Predicting capacity of hard carbon anodes in sodium-ion batteries using porosity measurements”. In: *Carbon* 76 (2014), pp. 165–174.

[164] B. Breitung, P. Baumann, H. Sommer, J. Janek, and T. Brezesinski. “In situ and operando atomic force microscopy of high-capacity nano-silicon based electrodes for lithium-ion batteries”. In: *Nanoscale* 47 (2016), pp. 2930–2946.

[165] C. R. Becker, K. E. Strawhecker, Q. P. Mcallister, and C. A. Lundgren. “In Situ Atomic Force Microscopy of Lithiation and Delithiation of Silicon Nanostructures for Lithium Ion Batteries”. In: *ACS Nano* 7.10 (2013), pp. 9173–9182.

[166] F. Wu and N. Yao. “Advances in sealed liquid cells for in-situ TEM electrochemial investigation of lithium-ion battery”. In: *Nano Energy* 11 (2015), pp. 196–210.

[167] X. Lu, E. R. Adkins, Y. He, L. Zhong, et al. “Germanium as a Sodium Ion Battery Material: In Situ TEM Reveals Fast Sodiation Kinetics with High Capacity”. In: *Chem. Mater.* 28.4 (2016), pp. 1236–1242.

[168] D. Chen, M. Indris S.and Schulz, B. Gamer, and R. Mönig. “In situ scanning electron microscopy on lithium-ion battery electrodes using an ionic liquid”. In: *J. Power Sources* 196.15 (2011), pp. 6382–6387.

[169] C.-Y. Chen, T. Sano, T. Tsuda, K. Ui, et al. “In situ Scanning Electron Microscopy of Silicon Anode Reactions in Lithium-Ion Batteries during Charge/Discharge Processes”. In: *Sci. Rep.* 6 (2016), p. 36153.

[170] M. L. Wasz. “Electrode Surface Area Characteristics of Batteries”. In: *7th International Energy Conversion Engineering Conference*. 2009.

[171] W. Chesworth. “Use of aluminum-amalgam in mineral synthesis at low temperatures and 1 atmosphere total pressure”. In: *Clays Clay Miner.* 19.5 (1971), pp. 337–339.

[172] L. Komsiyska, S. A. Garnica Barragan, M. Lewerenz, D. Ledwoch, and O. Osters. "Detecting Aging Phenomena in Commercial Cathodes for Li-Ion Batteries Using High Resolution Computed Tomography". In: *Adv. Sci. Tech.* 93 (2014), pp. 158–163.

[173] R. Baddour-hadjean. "Raman Microspectrometry Applied to the Study of Electrode Materials for Lithium Batteries". In: *Chem. Rev.* 110 (2010), pp. 1278–1319.

[174] C. Sole, N. E. Drewett, and L. J. Hardwick. "In situ Raman study of lithium-ion intercalation into microcrystalline graphite". In: *Faraday Discussions* 172.0 (2014), pp. 223–237.

[175] H. Vašková. "A powerful tool for material identification : Raman spectroscopy". In: *MMMAS* 5.7 (2011), pp. 1205–1212.

[176] K. Gotoh, T. Ishikawa, S. Shimadzu, N. Yabuuchi, et al. "NMR study for electrochemically inserted Na in hard carbon electrode of sodium ion battery". In: *J. Power Sources* 225 (2013), pp. 137–140.

[177] R. Clément, J. Billaud, R. Armstrong, G. Singh, T. Rojo, P. G. Bruce, and C. P. Grey. "Structurally Stable Mg-doped P2-$Na_2 3Mn_{1-y}Mg_y$ O_2 Sodium-ion Battery Cathodes with High Rate Performance: Insights from Electrochemical, NMR and Diffraction Studies". In: *Energy Environ. Sci.* (2016), pp. 3240–3251.

[178] E. Talaie, V. Duffort, H. L. Smith, B. Fultz, and L. F. Nazar. "Structure of the high voltage phase of layered P2-$Na_{\frac{2}{3}-z}$ $Mn_{\frac{1}{2}}Fe_{\frac{1}{2}}O_2$ and the positive effect of Ni substitution on its stability". In: *Energy Environ. Sci.* 8.8 (2015), pp. 2512–2523.

[179] A. K. Stephan. "Standardized Battery Reporting Guidelines". In: *Joule* 5.1 (2021), pp. 1–2.

[180] A. Ponrouch, E. Marchante, M. Courty, J.-M. Tarascon, and M. R. Palacín. "In search of an optimized electrolyte for Na-ion batteries". In: *Energy Environ. Sci.* 5.9 (2012), p. 8572.

[181] M. Keller, C. Vaalma, D. Buchholz, and S. Passerini. "Development and Characterization of High-Performance Sodium-Ion Cells based on Layered Oxide and Hard Carbon". In: *ChemElectroChem* 3.7 (July 2016), p. 1030.

[182] B. Scrosati, J. Garche, and W. Tillmetz. *Advances in Battery Technologies for Electric Vehicles*. Elsevier, 2015, p. 546.

[183] N. Ogihara, Y. Itou, T. Sasaki, and Y. Takeuchi. “Impedance Spectroscopy Characterization of Porous Electrodes under Different Electrode Thickness Using a Symmetric Cell for High-Performance Lithium-Ion Batteries”. In: *The Journal of Physical Chemistry C* 119.9 (Mar. 2015), pp. 4612–4619.

[184] O. O. Taiwo. “3D and 4D Characterisation of Lithium Ion Battery Electrode Microstructures using X-ray Tomography”. PhD thesis. University College London, 2016, p. 219.

[185] P. Bai, J. Li, F. R. Brushett, and M. Z. Bazant. “Transition of lithium growth mechanisms in liquid electrolytes”. In: *Energy and Environmental Science* 9.10 (Oct. 2016), pp. 3221–3229.

[186] L. Sannier, R. Bouchet, S. Grugeon, E. Naudin, E. Vidal, and J.-M. Tarascon. “Room temperature lithium metal batteries based on a new Gel Polymer Electrolyte membrane”. In: *Journal of Power Sources* 144.1 (June 2005), pp. 231–237.

[187] C. Wang, D. Wang, and C. Dai. “High-Rate Capability and Enhanced Cyclability of Rechargeable Lithium Batteries Using Foam Lithium Anode”. In: *Journal of The Electrochemical Society* 155.5 (2008), A390.

[188] M. Valvo, F. Lindgren, U. Lafont, F. Björefors, and K. Edström. “Towards more sustainable negative electrodes in Na-ion batteries via nanostructured iron oxide”. In: *Journal of Power Sources* 245 (2014), pp. 967–978.

[189] L. Wu, D. Buchholz, D. Bresser, L. Gomes Chagas, and S. Passerini. “Anatase TiO2 nanoparticles for high power sodium-ion anodes”. In: *Journal of Power Sources* 251 (2014), pp. 379–385.

[190] W. Luo, C. Bommier, Z. Jian, X. Li, et al. “Low-surface-area hard carbon anode for Na-ion batteries via graphene oxide as a dehydration agent”. In: *ACS Applied Materials and Interfaces* 7.4 (2015), pp. 2626–2631.

[191] M. Okoshi, Y. Yamada, A. Yamada, and H. Nakai. “Theoretical Analysis on De-Solvation of Lithium, Sodium, and Magnesium Cations to Organic Electrolyte Solvents”. In: *Journal of the Electrochemical Society* 160.11 (2013), A2160–A2165.

[192] A. Ponrouch, D. Monti, A. Boschin, B. Steen, P. Johansson, and M. R. Palacín. “Non-aqueous electrolytes for sodium-ion batteries”. In: *Journal of Materials Chemistry A* 3.1 (2015), pp. 22–42.

[193] E. Jónsson and P. Johansson. "Modern battery electrolytes: Ion-ion interactions in Li+/Na+conductors from DFT calculations". In: *Physical Chemistry Chemical Physics* 14.30 (2012), pp. 10774–10779.

[194] F. Sagane, T. Abe, and Z. Ogumi. "Sodium-ion transfer at the interface between ceramic and organic electrolytes". In: *Journal of Power Sources* 195.21 (2010), pp. 7466–7470.

[195] Y. Mizuno, M. Okubo, D. Asakura, T. Saito, et al. "Impedance spectroscopic study on interfacial ion transfers in cyanide-bridged coordination polymer electrode with organic electrolyte". In: *Electrochimica Acta* 63 (2012), pp. 139–145.

[196] J. S. Weaving, A. Lim, J. Millichamp, T. P. Neville, et al. "Elucidating the sodiation mechanism in hard carbon by operando raman spectroscopy". In: *ACS Applied Energy Materials* 3.8 (2020), pp. 7474–7484.

[197] S. Alvin, H. S. Cahyadi, J. Hwang, W. Chang, S. K. Kwak, and J. Kim. "Revealing the Intercalation Mechanisms of Lithium, Sodium, and Potassium in Hard Carbon". In: *Advanced Energy Materials* 10.20 (May 2020), p. 2000283.

[198] D. Ledwoch, E. Kendrick, and P. Adamson. *Composite Electrode including microporous ionically conducting material, composite slurry, and methods of manufacturing same (Application)*. 2017.

[199] D. Ledwoch, J. B. Robinson, D. Gastol, K. Smith, P. R. Shearing, D. J. L. Brett, and E. Kendrick. "Hard Carbon Composite Electrodes for Sodium-Ion Batteries with Nano-Zeolite and Carbon Black Additives". In: *Batteries & Supercaps* 4.1 (Jan. 2020), pp. 1–11.

[200] V. Simone, A. Boulineau, A. de Geyer, D. Rouchon, L. Simonin, and S. Martinet. "Hard carbon derived from cellulose as anode for sodium ion batteries: Dependence of electrochemical properties on structure". In: *Journal of Energy Chemistry* 25.5 (2016), pp. 761–768.

[201] S. Alvin, D. Yoon, C. Chandra, H. S. Cahyadi, et al. "Revealing sodium ion storage mechanism in hard carbon". In: *Carbon* 145 (Apr. 2019), pp. 67–81.

[202] Kazuma Gotoh, Takahiro Ueda, Hironori Omi, Taro Eguchi, et al. "Observation of micropores in hard-carbon using 129Xe NMR porosimetry". In: *Journal of Physics and Chemistry of Solids* 69.1 (2008), pp. 147–152.

[203] J. M. Stratford, P. K. Allan, O. Pecher, P. A. Chater, and C. P. Grey. "Mechanistic insights into sodium storage in hard carbon anodes using local structure probes". In: *Chem. Commun.* 52.84 (2016), pp. 12430–12433.

[204] J. M. Bray, C. L. Doswell, G. E. Pavlovskaya, L. Chen, et al. "Operando visualisation of battery chemistry in a sodium-ion battery by 23Na magnetic resonance imaging". In: *Nature Communications* 11.1 (2020), pp. 1–10.

[205] E.-M. Hammer, B. Berger, and L. Komsiyska. "Improvement of the Performance of Graphite Felt Electrodes for Vanadium-Redox-Flow-Batteries by Plasma Treatment". In: *International Journal of Renewable Energy Development (IJRED)* 3.1 (Feb. 2014), pp. 7–12.

[206] I. Pivac, B. Šimić, and F. Barbir. "Experimental diagnostics and modeling of inductive phenomena at low frequencies in impedance spectra of proton exchange membrane fuel cells". In: *Journal of Power Sources* 365 (Oct. 2017), pp. 240–248.

[207] S. K. Roy, M. E. Orazem, and B. Tribollet. "Interpretation of Low-Frequency Inductive Loops in PEM Fuel Cells". In: *Journal of The Electrochemical Society* 154.12 (Oct. 2007), B1378.

[208] L. Wang, J. Zhao, X. He, J. Gao, J. Li, C. Wan, and C. Jiang. "Electrochemical Impedance Spectroscopy (EIS) Study of LiNi 1/3 Co 1/3 Mn 1/3 O 2 for Li-ion Batteries". In: *Int. J. Electrochem. Sci* 7 (2012), pp. 345–353.

[209] P. Yu, B. N. Popov, J. A. Ritter, R. E. White, et al. "Determination of the Lithium Ion Diffusion Coefficient in Graphite Anode Material". In: *Acta Physico - Chimica Sinica* 17.5 (2001), p. 388.

[210] Z. Liu, Y. Y. Hu, M. T. Dunstan, H. Huo, et al. "Local structure and dynamics in the Na ion battery positive electrode material Na3V2(PO4)2F3". In: *Chemistry of Materials* 26.8 (Apr. 2014), pp. 2513–2521.

[211] Y. Shi, M. Wang, Y. Qiao, A. V. Le, and D. J. Noelle. "Internal resistance and polarization dynamics of lithium-ion batteries upon internal shorting". In: *Applied Energy* (2017).

[212] British Standard ISO. *Electrically propelled road vehicles — Test specification for lithium-ion traction battery packs and systems*. 2014.

[213] R. Gogoana. “Internal Resistance Variances in Lithium-Ion Batteries and Implications in Manufacturing”. Master. Massachusetts Institute of Technology, 2012, pp. 1–87.

[214] T. Hein S.and Danner, D. Westhoff, B. Prifling, R. Scurtu, et al. “Influence of Conductive Additives and Binder on the Impedance of Lithium-Ion Battery Electrodes: Effect of Morphology”. In: *Journal of The Electrochemical Society* 167.1 (2020), p. 013546.

[215] V. Zinth, C. Von Lüders, M. Hofmann, J. Hattendorff, et al. “Lithium plating in lithium-ion batteries at sub-ambient temperatures investigated by in situ neutron diffraction”. In: *Journal of Power Sources* 271 (2014), pp. 152–159.

[216] L. Mandeltort and J. T. Yates. “Rapid atomic Li surface diffusion and intercalation on graphite: A surface science study”. In: *Journal of Physical Chemistry C* 116.47 (2012), pp. 24962–24967.

[217] A. Ponrouch, A. R. Goñi, and M. R. Palacín. “High capacity hard carbon anodes for sodium ion batteries in additive free electrolyte”. In: *Electrochemistry Communications* 27 (Feb. 2013), pp. 85–88.

[218] J. Jin, B. J. Yu, Z. Q. Shi, C. Y. Wang, and C. B. Chong. “Lignin-based electrospun carbon nanofibrous webs as free-standing and binder-free electrodes for sodium ion batteries”. In: *Journal of Power Sources* 272 (Dec. 2014), pp. 800–807.

[219] W. Haselrieder, S. Ivanov, D. K. Christen, H. Bockholt, and A. Kwade. “Impact of the Calendering Process on the Interfacial Structure and the Related Electrochemical Performance of Secondary Lithium-Ion Batteries”. In: *ECS Transactions* 50.26 (July 2013), pp. 59–70.

[220] C. Schilcher, C. Meyer, and A. Kwade. “Structural and Electrochemical Properties of Calendered Lithium Manganese Oxide Cathodes”. In: *Energy Technology* 4.12 (Dec. 2016), pp. 1604–1610.

[221] R. Xu, H. Sun, L. S. de Vasconcelos, and K. Zhao. “Mechanical and Structural Degradation of LiNi x Mn y Co z O 2 Cathode in Li-Ion Batteries: An Experimental Study”. In: *Journal of The Electrochemical Society* 164.13 (Nov. 2017), A3333–A3341.

[222] D. Antartis, S. Dillon, and I. Chasiotis. “Effect of porosity on electrochemical and mechanical properties of composite Li-ion anodes”. In: *Journal of Composite Materials* 49.15 (June 2015), pp. 1849–1862.

[223] Y. Orikasa, Y. Gogyo, H. Yamashige, M. Katayama, et al. “Ionic conduction in lithium ion battery composite electrode governs cross-sectional reaction distribution”. In: *Scientific Reports* 6 (May 2016).

[224] P. Verma, P. Maire, and P. Novák. *A review of the features and analyses of the solid electrolyte interphase in Li-ion batteries*. Sept. 2010.

[225] ACS Material. *Technical Data Sheet: ACS Material Mesoporous Molecular Sieve Nano H-ZSM-5*. `https://www.acsmaterial.com/media/catalog/product/t/d/tds-nano{_}h-zsm-5.pdf`. Accessed: 2019-09-02. 2019.

[226] C. C. Liang. *Separator and electrolyte material for solid electrolyte battery systems*. May 1973.

[227] V. Di Noto, S. Lavina, G. A. Giffin, E. Negro, and B. Scrosati. “Polymer electrolytes: Present, past and future”. In: *Electrochimica Acta*. Vol. 57. Elsevier Ltd, Dec. 2011, pp. 4–13.

[228] S. Sanada and Y. Sekine. *Lithium secondary Battery with a Laminate Housing Material*. 2008.

[229] Makihiro Otohata. *Nonaqueous electrolyte battery*. 2003.

[230] B. Lee, E. Paek, D. Mitlin, and S. W. Lee. “Sodium Metal Anodes: Emerging Solutions to Dendrite Growth”. In: *Chemical Reviews* 119.8 (Apr. 2019), pp. 5416–5460.

[231] S. Liu, S. Tang, X. Zhang, A. Wang, Q. H. Yang, and J. Luo. “Porous Al Current Collector for Dendrite-Free Na Metal Anodes”. In: *Nano Letters* 17.9 (Sept. 2017), pp. 5862–5868.

[232] Y. Zhao, K. R. Adair, and X. Sun. *Recent developments and insights into the understanding of Na metal anodes for Na-metal batteries*. Oct. 2018.

[233] Y. Zhao, X. Yang, L. Y. Kuo, P. Kaghazchi, et al. “High Capacity, Dendrite-Free Growth, and Minimum Volume Change Na Metal Anode”. In: *Small* 14.20 (May 2018).

[234] X. Bi, X. Ren, Z. Huang, M. Yu, E. Kreidler, and Y. Wu. “Investigating dendrites and side reactions in sodium-oxygen batteries for improved cycle lives”. In: *Chemical Communications* 51.36 (May 2015), pp. 7665–7668.

[235] A. Rudola, K. Saravanan, C. W. Mason, and P. Balaya. “Na2Ti3O7: An intercalation based anode for sodium-ion battery applications”. In: *Journal of Materials Chemistry A* 1.7 (Feb. 2013), pp. 2653–2662.

[236] M. Jäckle and A. Groß. “Microscopic properties of lithium, sodium, and magnesium battery anode materials related to possible dendrite growth”. In: *Journal of Chemical Physics* 141.17 (Nov. 2014).

[237] W. Weppner and R. A. Huggins. “Electrochemical investigation of the chemical diffusion, partial ionic conductivities, and other kinetic parameters in Li3Sb and Li3Bi”. In: *Journal of Solid State Chemistry* 22.3 (1977), pp. 297–308.

[238] R. Tian, S. H. Park, P. J. King, G. Cunningham, J. Coelho, V. Nicolosi, and J. N. Coleman. “Quantifying the factors limiting rate performance in battery electrodes”. In: *Nature Communications* 10.1 (Dec. 2019).

[239] Y. Zhu, T. Gao, X. Fan, F. Han, and C. Wang. “Electrochemical Techniques for Intercalation Electrode Materials in Rechargeable Batteries”. In: *Accounts of Chemical Research* 50.4 (Apr. 2017), pp. 1022–1031.

[240] W. Zhou, Y. Li, S. Xin, and J. B. Goodenough. “Rechargeable Sodium All-Solid-State Battery”. In: *ACS Central Science* 3.1 (Jan. 2017), pp. 52–57.

[241] R. Dugas, A. Ponrouch, G. Gachot, R. David, M. R. Palacin, and J. M. Tarascon. “Na Reactivity toward Carbonate-Based Electrolytes: The Effect of FEC as Additive”. In: *Journal of The Electrochemical Society* 163.10 (2016), A2333–A2339.

[242] R. Rodriguez, K. E. Loeffler, S. S. Nathan, J. K. Sheavly, A. Dolocan, A. Heller, and C. B. Mullins. “In Situ Optical Imaging of Sodium Electrodeposition: Effects of Fluoroethylene Carbonate”. In: *ACS Energy Letters* 2.9 (Sept. 2017), pp. 2051–2057.

[243] S. Wei, S. Choudhury, J. Xu, P. Nath, Z. Tu, and L. A. Archer. “Highly Stable Sodium Batteries Enabled by Functional Ionic Polymer Membranes”. In: *Advanced Materials* 29.12 (Mar. 2017).

[244] W. Luo, C. F. Lin, O. Zhao, M. Noked, Y. Zhang, G. W. Rubloff, and L. Hu. "Ultrathin Surface Coating Enables the Stable Sodium Metal Anode". In: *Advanced Energy Materials* 7.2 (Jan. 2017).

[245] Dequan Chen, Wen Zhang, Kangying Luo, Yang Song, et al. "Hard carbon for sodium storage: Mechanism and optimization strategies toward commercialization". In: *Energy and Environmental Science* 14.4 (2021), pp. 2244–2262.

[246] P. Thomas and D. Billaud. "Effect of mechanical grinding of pitch-based carbon fibers and graphite on their electrochemical sodium insertion properties". In: *Electrochimica Acta* 46.1 (2000), pp. 39–47.

[247] P. Thomas and D. Billaud. "Sodium electrochemical insertion mechanisms in various carbon fibres". In: *Electrochimica Acta* 46.22 (2001), pp. 3359–3366.

[248] C. M. Wu, P. I. Pan, Y. W. Cheng, C. P. Liu, C. C. Chang, M. Avdeev, and S. kang Lin. "The mechanism of the sodiation and desodiation in Super P carbon electrode for sodium-ion battery". In: *Journal of Power Sources* 340 (2017), pp. 14–21.

[249] P. C. Tsai, S. C. Chung, S. K. Lin, and A. Yamada. "Ab initio study of sodium intercalation into disordered carbon". In: *Journal of Materials Chemistry A* 3.18 (2015), pp. 9763–9768.